École doctorale des Sciences Chimiques
UMR 7140 - Chimie de la Matière Complexe

Hermann-Staudinger Graduiertenschule
Institut für Biochemie

THÈSE

en cotutelle entre l'Université de Strasbourg et l'Albert-Ludwigs-Universität Freiburg

présentée par

Tatjana Gerasimova

soutenue le **16 juin 2023**

pour obtenir le grade de : **Docteur de l'université de Strasbourg et de Doktor der Albert-Ludwigs-Universität Freiburg**

Discipline/ Spécialité : Chimie

Décryptage des mécanismes des complexes de la chaîne respiratoire par marquage IR et approches exaltées de surface

Deciphering mechanisms of respiratory chain complexes by IR labelling and surface enhanced approaches

THÈSE dirigée par :

Dr. Petra Hellwig	Professeur, Université de Strasbourg
Dr. Thorsten Friedrich	Professeur, Albert-Ludwigs-Universität Freiburg

RAPPORTEURS :

Dr. Sophie Lecomte	Directrice de recherche, Université Bordeaux
Dr. Christoph von Ballmoos	Professeur, Universität Bern

AUTRES MEMBRES DU JURY :

Dr. Frédéric Melin	Maître de Conférences, Université de Strasbourg

This study was carried out in the following laboratories:

Laboratoire de Bioélectrochimie et Spectroscopie (group of Prof. Dr. Petra Hellwig)
UMR 7140 Chimie de la Matière Complexe, Université de Strasbourg - CNRS
1 rue Blaise Pascal, 67070 Strasbourg, France

Institut für Biochemie (group of Prof. Dr. Thorsten Friedrich)
Albert-Ludwigs-Universität Freiburg
Albertstraße 21, 79104 Freiburg in Breisgau, Germany

Tatjana Gerasimova: *Deciphering mechanisms of respiratory chain complexes by IR labelling and surface enhanced approaches*, 2023

Chairman of the Doctoral Committee: Prof. Dr. Stefan Weber

Dean of the Faculty: Prof. Dr. Andreas Bechtold

1st Supervisor: Prof. Dr. Thorsten Friedrich

2nd Supervisor: Prof. Dr. Petra Hellwig

Oral Examination: 16 June 2023

"*If we knew what it was we were doing, it would not be called research, would it?*"

Albert Einstein

Dedication

I dedicate this work to my beloved grandmother Klavdija, who passed away when this manuscript was written.

In loving memory…

Table of content

Abbreviations and Acronyms

Abs	Absorbance
ACMA	9-Amino-6-chloro-2-methoxyacridine
ANTA	Nα,Nα-bis(carboxymethyl)-L-lysine
ATP	Adenosine triphosphate
ATR	Attenuated total reflection
Cryo-EM	Cryo-electron microscopy
DMSO	Dimethyl sulfoxide
DNA	Desoxyribonucleic acid
DTNB	5,5'- Dithio-bis-(2-nitrobenzoic acid)
DTSP	3,3-dithiodipropionic acid di(N-hydroxysuccinimide ester)
DTT	Dithiothreitol
Fe/S	Iron-sulfur cluster
FTIR	Fourier transform infrared spectroscopy
EPR	Electron paramagnetic resonance
FMN	Flavin mononucleotide
IPTG	Isopropyl-β-D-thiogalactopyranoside
IR	Infrared spectroscopy
LMNG	Lauryl-maltose-neopentyl-glycol
MES	2-*N*-(Morpholino)ethanesulfonic acid
MIR	Mid infrared
MOPS	3-*N*-(Morpholino)propanesulfonic acid
NADH	Nicotinamide adenine dinucleotide
Ni-NTA	Nickel-chelating nitrilotriacetic acid
OD	Optical density
OxPhos	Oxidative phosphorylation
PMSF	Phenylmethanesulfonyl fluoride
ROS	Reactive oxygen species
Q / QH_2	Quinone/quinol
SAM	Self assembled monolayer
SCN	Thiocyanate
SDS	Sodium dodecyl sulfate
SEIRAS	Surface enhanced infrared absorption spectroscopy
THF	Tetrahydrofuran
UV/vis	Ultra-violet/visible
WT	Wild type

1 Abstract

The respiratory chains of the gram-negative bacterium *E. coli* have a flexible composition that enables survival in various environments from aerobic to anaerobic conditions. The aerobic respiratory chain of *E. coli* consists of several primary dehydrogenases and terminal reductases. Energy-converting NADH: ubiquinone oxidoreductase, also called respiratory complex I is the largest enzyme of the respiratory chains and serves as a primary dehydrogenase. It has an L-shaped form and couples the transfer of two electrons from NADH to ubiquinone (Q) with translocation of four protons across the membrane. Complex I consists of a peripheral and a membrane arm, it contains nine iron-sulfur clusters and one flavin mononucleotide (FMN) as cofactors. All cofactors for the electron transfer reaction are located in the peripheral arm, while proton translocation takes place in the membrane arm. The coupling of both processes is still under debate. The membrane arm contains three antiporter-like subunits NuoL, NuoM, NuoN, each comprising a putative proton pathway. A fourth proton pathway is contributed by other subunits building the so-called E-channel. It is not clear how the four protons are translocated across the membrane. It was proposed that either the four protons are translocated by four pathways or just to the pathway of the distal subunit NuoL.

Conformational changes play an important role in proton translocation. These movements need to be visualized to obtain a comprehensive understanding of a mechanism. Fourier-transform infrared (FTIR) spectroscopy is one of the most versatile techniques for the non-destructive characterization of proteins. Good-quality spectra are rapidly obtained with a high signal-to-noise ratio. However, detecting an intense absorption signal from a protein monolayer using FTIR spectroscopy is challenging. Surface-enhanced infrared absorption spectroscopy (SEIRAS) is applied to enhance the IR absorbance. An IR label is required to visualize conformational changes by means of IR spectroscopy. Nitrile labels are attractive IR labels as they can provide valuable information about the local environment of the probe in a defined protein environment. They appear in the clear region of IR spectra and do not overlap with protein signals. They are small and can be easily incorporated into a protein structure at distinct positions. Signals of nitrile labels are sensitive towards hydrogen bond interactions making it possible to follow reaction-induced conformational changes.

To visualize a possible involvement of NuoM in proton translocation by complex I, a nitrile IR label was inserted in close proximity to its putative proton pathway. Individual residues were genetically changed to cysteine residues that were labelled with cyanides without blocking enzyme activity. Changes in the environment of the label were detected after addition of the substrates, NADH and Q

(ubiquinone). The pattern of conformational changes at the distinct positions in NuoM suggests that NuoM is taking part in proton translocation.

Cytochrome *bd*-I oxidase belongs to terminal reductases of respiratory chains. They catalyze oxygen reduction to water. This process is coupled with ubiquinone oxidation to ubiquinol. *bd*-I oxidase consists of four subunits and contains three hems: b_{558}, b_{595} and heme *d* that are all located in one subunit. Conserved glutamic acid residues are in close proximity of heme b_{595} and heme *d*. Previous biochemical and spectroscopical studies revealed the importance of these positions, which show untypically high pK_a values. Here, these residues were mutated to aspartic acid and glutamine residues. The midpoint potential of the two hemes groups were drastically altered by the mutations. Unexpectedly, some of the mutants were still active. These findings are discussed in relation to the physiological role of the enzyme.

1 Zusammenfassung

Die Atmungsketten des gramnegativen Bakteriums *E. coli* sind flexibel aufgebaut und ermöglichen ein Überleben bei verschiedenen Umgebungsbedingungen von aerob bis anaerob. Die aerobe Atmungskette von *E. coli* besteht aus einer Reihe primärer Dehydrogenasen und terminaler Reduktasen. Die NADH: Ubichinon Oxidoreduktase, der respiratorische Komplex I ist das größte Enzym der Atmungskette und dient als Eintrittsstelle für die Elektronen aus NADH. Komplex I besitzt eine L-Form und koppelt die Übertragung von zwei Elektronen von NADH auf Ubichinon (Q) mit der Translokation von vier Protonen über die Membran. Komplex I besteht aus einem peripheren Arm und einem Membranarm und enthält neun Eisen-Schwefel Zentren und ein Flavinmonokleotid als Kofaktoren. Alle Kofaktoren der Redoxreaktion befinden sich im peripheren Arm, während die Protonentranslokation im Membranarm stattfindet. Die Kopplung dieser Prozesse ist noch nicht geklärt. Der Membranarm enthält die drei antiporterähnlichen Untereinheiten NuoL, NuoM, NuoN, die jeweils einen Protonenweg enthalten. Ein weiterer Protonenweg, der sogenannte E-Kanal, wird von anderen Untereinheiten, gebildet. Es wird spekuliert, dass alle vier Protonen durch die vier Protonenwege transloziert werden. Eine andere Theorie sagt, dass vier Protonen durch den Weg auf der distalen Untereinheit NuoL transloziert werden.

Konformationsänderungen spielen bei der Protonentranslokation eine wichtige Rolle. Diese Bewegungen müssen visualisiert werden, um ein umfassendes Verständnis für den Enzym-Mechanismus zu erhalten. Die Fourier-Transformations-Infrarot-Spektroskopie (FTIR) ist eine der vielseitigsten Analysetechniken für die nicht destruktive Charakterisierung von Proteinen. Gute Spektren mit einem hohen Signal-Rausch-Verhältnis werden schnell gewonnen. Allerdings ist es schwierig, ein intensives Absorptionssignal von einer einzelnen Proteinschicht mit Hilfe der FTIR-Spektroskopie zu erhalten. Die oberflächenverstärkte Infrarot-Absorptionsspektroskopie (SEIRAS) ermöglicht eine Verstärkung des Signals. Um Konformationsänderungen bei der IR-Spektroskopie sichtbar zu machen, wird ein IR-Label benötigt. Nitrilmarkierungen sind attraktive IR-Markierungen, da sie wertvolle Informationen über die lokale Umgebung der Sonde liefern können. Sie erscheinen im klaren Bereich der IR-Spektren und überschneiden sich nicht mit Proteinsignalen. Nitrile sind klein und können an spezifichen Positionen in das Protein eingebaut werden. Die Position ihrer Signale ist empfindlich gegenüber Änderungen des Wasserstoffbrückennetzwerks und ermöglichen es, reaktionsbedingte Konformationsänderungen zu verfolgen.

Um die mögliche Beteiligung von NuoM an der Protonentranslokation zu untersuchen, wurden verschiedenen Positionen in unmittelbarer Nähe eines der mutmaßlichen Protonenwege in NuoM mit Nitril-Gruppen markiert. Einzelne Reste wurden zu Cysteinreste mutiert, die mit Cyaniden markiert wurden. Änderungen in der Umgebung der Sonden nach Zugabe der Substrate NADH and Q wurden nachgewiesen. Das Muster der Änderungen deutet darauf ein, dass NuoM an der Protonentranslokation beteiligt ist.

Die Cytochrom *bd*-I-Oxidase gehört zu den terminalen Reduktasen der Atmungsketten. Sie Katalysieren Sauerstoffreduktion zu Wasser. Hierfür wird Ubichinon zu Ubichinol oxidiert und vier Elektronen werden auf Sauerstoff übertragen. Die *bd*-I-Oxidase besteht aus vier Untereinheiten und enthält drei Häm-Gruppen: b_{558}, b_{595} und Häm *d*, die sich alle auf einer Untereinheit befinden. In der Nähe der Häme b_{595} und Häm *d* befinden sich konservierte Glutaminsäurereste. Biochemische und spektroskopische Studien wiesen auf die Bedeutung dieser Positionen ein, die einen untypisch hohen pK_a-Wert haben. In dieser Arbeit wurden diese Reste zu Asparaginsäure und Glutamin mutiert. Das Redoxpotential der beiden Häm Gruppen wurde durch die Mutationen dramatisch geändert. Gleichzeitig waren die Varianten aber enzymatisch aktiv. Diese Ergebnisse werden im Zusammenhang mit der physiologischen Rolle der *bd*-Oxidase diskutiert.

1 Résumé

1) Introduction

Les changements de conformation jouent un rôle important dans les études de la dynamique des protéines au cours des réactions catalytiques. Ces mouvements doivent être visualisés pour obtenir une compréhension globale du rôle fonctionnel des motifs structurels et des réarrangements. La spectroscopie infrarouge (IR) est une technique précieuse pour étudier les réactions des protéines car elle peut fournir des informations sur la structure des protéines, les réactions moléculaires, la dynamique et le repliement [1].

La protéine étudiée est le complexe I (NADH: ubiquinone oxydoréductase). C'est la plus grande enzyme de la chaîne respiratoire et elle sert de point d'entrée dans la chaîne respiratoire. Elle catalyse le transfert de deux électrons du NADH à la (ubi)quinone couplé à la translocation de quatre protons à travers la membrane [2]. Elle a une structure en forme de L composée d'un bras périphérique et d'un bras membranaire. Le transfert d'électrons a lieu dans le bras périphérique, tandis que le bras membranaire catalyse la translocation des protons [3]. Le bras hydrophobe d'*E. coli* a été visualisé à basse résolution par cryo-microscopie électronique et à plus haute résolution par diffraction des rayons X, ce qui a permis d'identifier et de déterminer les sous-unités du bras membranaire. Le bras membranaire a la forme d'un haricot et mesure environ 180 Å de long. Il comprend les sous-unités NuoL, M et N, qui sont impliquées dans la translocation des protons et sont homologues aux sous-unités de transport. Chacune des sous-unités contient 14 hélices transmembranaires (TM). La figure 1.1 montre la structure cristalline du complexe I d'*E. coli*.

Le complexe I bactérien est similaire au complexe I mitochondrial. Il peut servir de modèle pour étudier les maladies neurodégénératives associées à des mutations du complexe I. Une déficience en complexe I a été identifiée dans la maladie de Parkinson et la dystonie. Le complexe I est également considéré comme l'une des principales sources d'espèces réactives de l'oxygène conduisant à des lésions de l'ADN mitochondrial et au vieillissement [4].

La translocation de protons à travers la membrane est actuellement l'un des sujets les plus discutés dans le domaine de la recherche. Le mécanisme de translocation des protons par le complexe est encore débattu. Il existe de nombreuses théories et hypothèses. L'une d'entre elles, appelée 'ND5-only' (ND5 est l'homologue mitochondrial de la sous-unité NuoL), postule que seule la sous-unité distale NuoL est impliquée dans la translocation des protons, et que tous les protons sont transférés par cette sous-unité [5]. D'autres théories suggèrent que la translocation des protons à travers la membrane se produit

dans toutes les sous-unités du bras membranaire du complexe I. L'hypothèse a été émise que les changements de conformation à longue portée déclenchés par l'énergie libérée par la reaction redox entraînent la translocation de protons à travers ces sous-unités de type antiporteur [6]. Pour mieux visualiser le mouvement du bras membranaire pendant le transfert d'électrons et en présence des substrats naturels (NADH, ubiquinone), des sondes infrarouges ont été utilisées pour marquer différents résidus dans la sous-unité NuoM du bras membranaire. Des positions individuelles ont été génétiquement modifiées par des résidus de cystéine qui ont été marqués avec des cyanures pour obtenir des thiocyanates. Les thiocyanates sont des marqueurs IR attrayants car ils apparaissent dans une région peu encombrée du spectre IR et ne se superposent pas aux signaux des protéines. Les signaux des thiocyanates sont sensibles aux liaisons hydrogène, ce qui permet de suivre les changements de conformation induits par la réaction. La vibration d'étirement du thiocyanate [ν(SC≡N)] se situe entre 2175 et 2120 cm^{-1} [7].

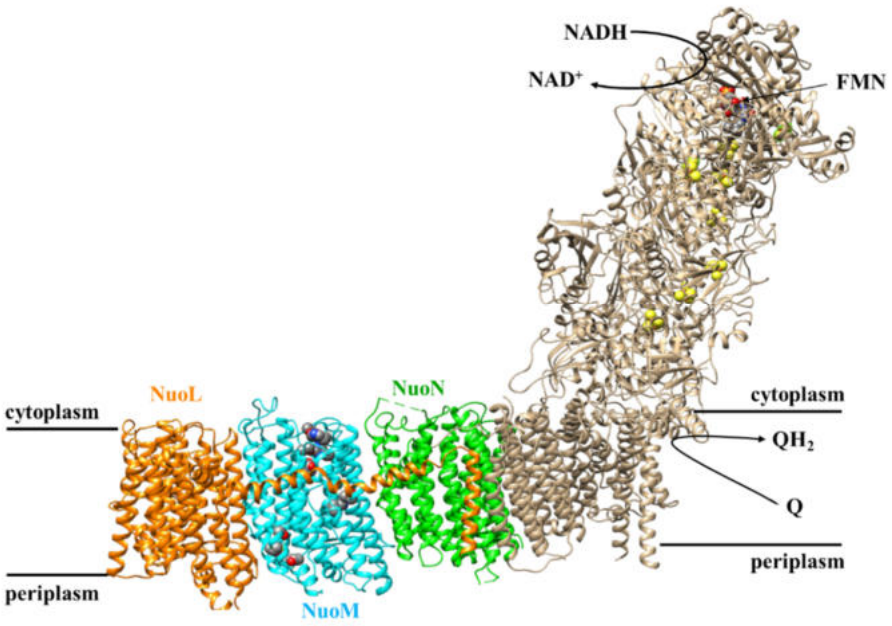

Fig.1.1 : Structure cristalline du complexe I d'*E. coli* à une résolution de 2,4 Å (entrée PDB : 7Z7S, Kravchuk *et al.*, 2022). Les sous-unités du bras membranaire en couleur ainsi que les réactions catalysées sont représentées. Les mutations créées dans la sous-unité NuoM sont indiquées.

2) Résultats et discussion

Les mutations insérées qui ont été marquées peuvent fournir des informations sur l'environnement local. La figure 1.2 montre les mutations créées dans la sous-unité NuoM.

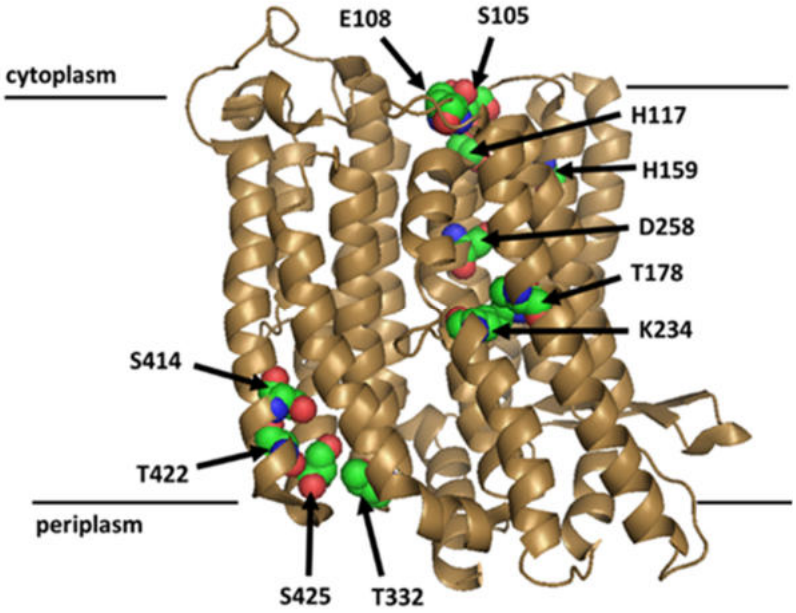

Fig. 1.2 : Localisation des mutations étudiées dans les sous-unités NuoM dans le bras membranaire (PDB : 3RKO, Efremov et Sazanov, 2011).

Les mutations ont été créées à proximité de l'un des chemins de protons putatifs dans du bras membranaire. La mutagenèse dirigée a été utilisée pour insérer des mutations dans des vecteurs d'expression déjà existants pBAD*nuo* qui codent pour le complexe respiratoire I d'*E. coli*. Après la croissance de cellules bactériennes dans des milieux nutritifs à grande échelle, les cellules ont été lysées et les membranes préparées à l'aide de différentes méthodes de centrifugation. Les activités de transfert d'électrons ont été déterminées pour les variants isolés du complexe I. Les activités NADH/ferricyanure oxydoréductase des variants ont été comparées à celle du complexe I de type sauvage. Les valeurs des activités de la NADH oxydase membranaire des échantillons ne diffèrent pas beaucoup de celles du type sauvage. Les données de photométrie de masse des protéines fraîchement purifiées ont prouvé l'assemblage complet et la stabilité des échantillons. La caractérisation par SDS-PAGE a révélé que toutes les sous-unités du complexe I sont présentes dans les variants.

Le marqueur thiocyanate (SCN) a été incorporé dans les protéines par modification chimique post-traductionnelle d'un résidu cystéine qui peut être placé par mutagenèse dirigée. Toutes les variantes ont été totalement marquées. Les activités NADH:decyl-Q oxydoréductase avant et après le marquage ont été mesurées. L'analyse SDS-PAGE après le marquage n'a pas non plus révélé de changements par rapport aux échantillons avant le marquage. Les mutations et le marquage ont donné lieu à des variants entièrement assemblés dont l'activité est légèrement diminuée (tableau 1.1).

Tableau 1.1: Activités NADH:decyl-Q oxydoréductase des variants du complexe I marqués.

Échantillon	Activités NADH:Décylubiquinone oxydoréductase (avant marquage)	Activités NADH:Décylubiquinone oxydoréductase (après marquage)	
	[U/mg]	[U/mg]	[%](par rapport aux produits non marqués)
Type sauvage	24.7 ± 1.3	-	**-**
S105C^{M}	17.8 ± 5.1	14.1 ± 2.2	**79**
E108C^{M}	19.9 ± 2.0	10.4 ± 0.8	**52**
H117C^{M}	13.4 ± 0.4	13.1 ± 0.7	**98**
H159C^{M}	18.9 ± 4.9	13.4 ± 1.8	**71**
T332C^{M}	15.7 ± 0.5	13.0 ± 1.9	**83**
S414C^{M}	12.3 ± 7.1	11.5 ± 1.2	**94**
T422C^{M}	13.7 ± 2.2	12.3 ± 2.8	**90**
S425C^{M}	23.1 ± 1.0	16.9 ± 1.8	**73**
T178C^{M}	19.6 ± 7.1	16.8 ± 0.7	**85**
K234C^{M}	3.4 ± 0.7	2.4 ± 0.2	**71**
D258C^{M}	8.8 ± 0.8	5.3 ± 0.3	**64**

La spectroscopie IR exaltée de surface (SEIRAS) a été utilisée pour suivre les changements de conformation du complexe I. Il s'agit d'une variante de la spectroscopie infrarouge dans laquelle l'amélioration du signal a été obtenue grâce à une couche métallique fine nanostructurée [8]. Il est possible d'observer les groupes qui participent activement à une réaction catalytique en obtenant des informations sur la structure et l'environnement des chaînes latérales d'acides aminés, du squelette des protéines et autres. Grâce à l'effet SEIRAS obtenu sur la surface de l'or, le signal SCN peut être directement observé à partir des spectres d'absorbance entre 2200 et 2000 cm^{-1}.

La liaison du NADH et de l'ubiquinone a conduit à des décalages spectraux différents. Il est intéressant de noter qu'une tendance caractéristique a été observée pour les résidus marqués sur les côtés cytoplasmique et périplasmique du chemin de proton proposé. Des décalages spectraux ont été observés pour tous les variants. Les changements de conformation révèlent des mouvements vers l'hydrophobie (valeurs d'ondes inférieures) ou l'hydrophilie (valeurs d'ondes supérieures). L'incubation avec du NADH et de la quinone a été réalisée pour tous les variants créés. Cependant, seuls certains résultats, plus représentatifs, des décalages spectraux pour les variants du complexe I sont décrits ici. La figure 1.3 montre quelques résultats pour des variants situés dans différentes positions du

complexe I, y compris ceux situés sur les côtés cytoplasmiques, périplasmiques et dans la cavité du complexe I.

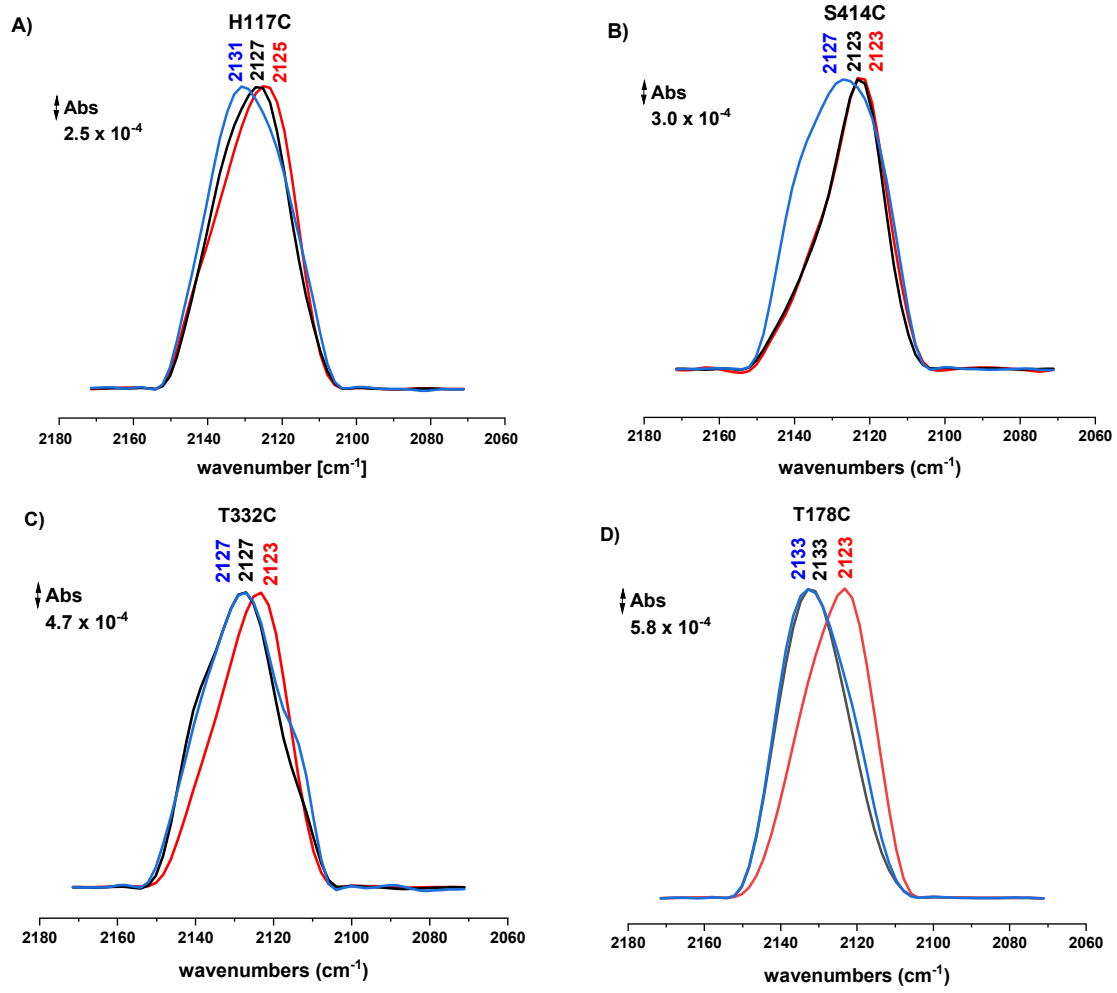

Fig. 1.3 : Position spectrale des bandes de thiocyanate de variants du complexe I (SCN). Le noir représente la bande SCN après marquage, le rouge après incubation avec du NADH et le bleu après incubation avec du NADH et de l'ubiquinone. A) Variant du complexe I NuoM H117C (côté cytoplasmique); B) Variant du complexe I NuoM S414C (côté périplasmique); C) Variant du complexe I NuoM T332C (côté périplasmique) ; D) Variant du complexe I NuoM T172C (côté périplasmique); E) Variant du complexe I NuoM S414C (côté périplasmique). variante du complexe I NuoM T178C (dans la cavité).

Le signal du groupe thiocyanate du variant du complexe I du côté cytoplasmique NuoM H117C est situé à la même position que celui du variant NuoM S105C à 2127 cm^{-1}. L'ajout de NADH a entraîné un léger déplacement de 2 cm^{-1} vers les nombres d'onde plus faibles, ce qui suggère un environnement légèrement plus hydrophobe. L'incubation avec l'ubiquinone a entraîné un déplacement de 6 cm^{-1} vers les nombres d'onde plus élevés (2131 cm^{-1}), donc le thiocyanate est maintenant dans un environnement plus hydrophile.

Le variant du complexe I marqué avec la mutation NuoM S414C située sur le côté périplasmique a donné un signal à un nombre d'onde plus faible (2123 cm^{-1}). L'ajout de NADH n'a pas produit de changement visible. Cependant, l'ajout d'ubiquinone a entraîné un déplacement de 4 cm^{-1} vers des nombres d'ondes plus élevés. En comparant la largeur des bandes, les bandes des protéines marquées et incubées avec du NADH ont une largeur plus petite que les bandes des protéines incubées avec de l'ubiquinone, car la bande peut contenir plusieurs conformères.

Après marquage, le variant du complexe I du côté périplasmique NuoM T332C a également produit une bande à 2127 cm^{-1}. Un petit épaulement autour de 2140 cm^{-1} peut être observé. L'incubation avec du NADH a déplacé la bande à 2123 cm^{-1}. Le traitement à l'ubiquinone a entraîné un retour vers la position initiale à 2127 cm^{-1}. Il y a également un épaulement visible autour de 2115 cm^{-1} qui est caractéristique d'une bande.

La bande du thiocyanate du variant du complexe I situé dans la cavité NuoM T178C est apparue à des nombres d'ondes plus élevés (par rapport aux autres variants du complexe I), à 2133 cm^{-1}. L'incubation avec du NADH a entraîné un déplacement significatif de 10 nombres d'ondes vers le bas (2123 cm^{-1}), donc vers un environnement plus hydrophobe. La bande est apparue à 2123 cm^{-1}. Le traitement à l'ubiquinone a entraîné un retour vers l'état initial de la protéine à 2123 cm^{-1}. Pour ces variants, des changements plus significatifs ont été enregistrés.

La fréquence de la liaison CN est déterminée par les molécules d'eau environnantes. Les déplacements SCN enregistrés peuvent indiquer des mouvements vers un environnement plus ou moins accessible au solvant [9]. Une modification de l'environnement des liaisons hydrogène, ou la présence ou l'absence de molécules d'eau après l'ajout d'ubiquinone peut également influencer la signature spectrale. Les déplacements observés des variants du complexe I lors de l'ajout de NADH et d'ubiquinone peuvent correspondre au mouvement du complexe I entre l'état ouvert et l'état fermé. Cela pourrait indiquer que la sous-unité NuoM du complexe I est impliquée dans la translocation des protons.

3) Conclusion générale

En conclusion, tous les variants créés et marqués dans cette étude sont entièrement assemblés avec des activités un peu réduites. La position de la bande SCN en IR varie selon les mutants, et l'analyse de déconvolution qui a été effectuée a révélé des pics multiples dans la plupart des cas. L'incubation avec du NADH et de l'ubiquinone a entraîné certains déplacements de la position de la bande ou de la distribution des pics. L'incubation avec le NADH a entraîné de plus petits déplacements vers l'environnement hydrophobe, tandis que le traitement avec l'ubiquinone a produit des changements plus importants vers l'environnement hydrophile. Dans l'ensemble, les études ont fourni des

informations précieuses sur la localisation et les changements du marqueur SCN dans les mutants du complexe I.

Les résultats obtenus dans cette étude pourraient être un signe que la translocation des protons dans la sous-unité NuoM se produit et que les positions marquées pourraient faire partie du canal des protons.

List of presentations

Tatjana Gerasimova, Ana Filipa Santos Seiça, Thorsten Friedrich, Petra Hellwig. Substrate-induced conformational changes in respiratory complex I. 21st edition of the European conference on Bioenergetics, Aix-en-Provence, France, 20.08.-25.08.22 (Poster).

Tatjana Gerasimova, Ana Filipa Santos Seiça, Thorsten Friedrich, Petra Hellwig. Substrate-induced conformational changes in respiratory complex I. Research Training Group 2202 symposium on Mechanisms of proton translocation. Freiburg, Germany, 17.08.-19.08.22 (Poster).

Tatjana Gerasimova, Ana Filipa Santos Seiça, Thorsten Friedrich, Petra Hellwig. Monitoring the conformational changes upon NADH binding in respiratory complex I by means of a nitrile label. 21st edition of the congres of Groupe Français de Bioénergétique, Online, France, 21.09.-24.09.21 (Oral communication).

Tatjana Gerasimova, Conformational changes of Complex I during reaction studied by SEIRAS and SCN labelling. Meeting of the Binational PhD college “Enzyme reactivities and their applications”. Strasbourg, France, 26.11.21 (Oral communication).

Tatjana Gerasimova, Following the conformational changes of respiratory complex I with the help of SCN labelling. Journée Doctorant et Master UMR 7140 (Unité Mixte de Recherche), Strasbourg, France, 10.05.22 (Oral communication).

List of publications

Schimpf, J.; Oppermann, S.; Gerasimova, T.; Santos Seica, A. F.; Hellwig, P.; Grishkovskaya, I.; Wohlwend, D.; Haselbach, D.; Friedrich, T. Structure of the Peripheral Arm of a Minimalistic Respiratory Complex I. *Structure* **2022**, 30 (1).

Makarchuk, I.; Kägi, J.; Gerasimova, T.; Wohlwend, D.; Friedrich, T.; Melin, F.; Hellwig, P. pH-Dependent Kinetics of NO Release from *E. coli bd*-I and *bd*-II Oxidase Reveals Involvement of Asp/Glu58^{B}. *Biochimica et Biophysica Acta (BBA) - Bioenergetics* **2023**, 1864 (2), 148952.

Makarchuk, I.; Gerasimova, T.; Kägi, J.; Wohlwend, D.; Melin, F.; Friedrich, T.; Hellwig, P. Mutating the Environment of Heme b_{595} of *E. coli* Cytochrome *bd*-I Oxidase Shifts Its Redox Potential by 200 mV without Inactivating the Enzyme. *Bioelectrochemistry* **2023**, 151, 108379.

Strotmann, L; Harter, C.; Gerasimova, T.; Ritter, K.; Jessen, H.J.; Wohlwend, D.; Friedrich, T. High H_2O_2 concentrations selectively damage the binuclear iron-sulfur cluster N1b of respiratory complex I. *Scientific Reports***,** (revised manuscript submitted).

2 Introduction

2.1 The aerobic respiratory chain of *E. coli*

Respiration is one of the essential energy transmission pathways in *Escherichia coli* and other bacteria that is realized *via* oxidative phosphorylation (OxPhos) [10]. It consists of a series of complexes transferring electrons from electron donors to electron acceptors, from organic substances to various terminal molecular acceptors [11]. This process is coupled to the generation of a proton gradient across the membrane. The power generated across the membrane is called the proton motive force [12]. It is used to produce the universal energy carrier adenosine triphosphate (ATP) [13]. Adenosine triphosphate is synthesized by the ATP-synthase [14]. In bacteria, such as *E. coli,* the enzymes of the respiratory chain are located in the cytoplasmic membrane [15]. For bacteria grown in neutral pH, the gradient is positive on the outside of the membrane and is usually about 100-180 mV [16].

Like other bacteria, *E. coli* has a flexible composition of the respiratory chains that enables prokaryotes to live under various growth conditions, from aerobic to completely anaerobic [17]. *E. coli* has at least 15 dehydrogenases and 10 terminal oxidases linked by electron-transferring ubiquinone derivatives [18]. Depending on growth conditions, *E. coli* has the ability to use different electron donors such as NADH, succinate or lactate linked to the terminal quinol reductases by ubiquinone (Q). NADH and succinate are mainly produced in the citric acid cycle [19]. The aerobic respiratory chain of *E. coli* contains three primary dehydrogenases and three terminal oxidases. The enzymes involved in the aerobic oxidative phosphorylation of *E. coli* are depicted in Figure 2.1.

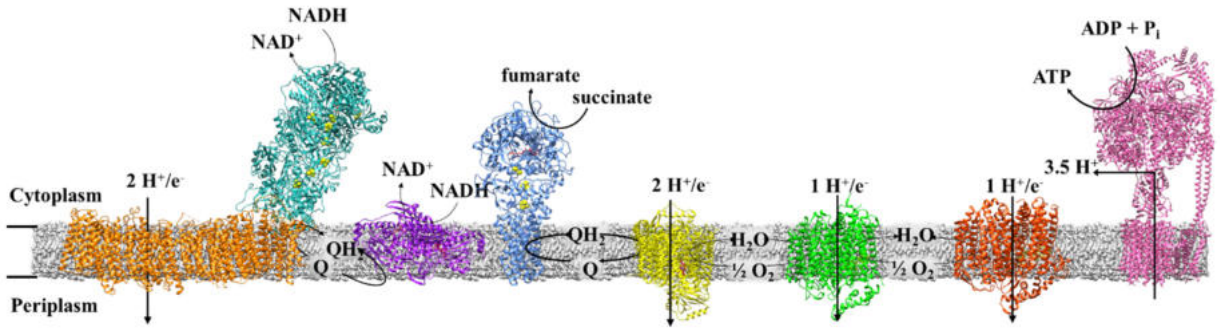

Fig. 2.1: Composition of the *E. coli* oxidative phosphorylation under aerobic conditions. The NADH:ubiquinone oxidoreductase is shown (peripheral arm in cyan, membrane arm – orange, PDB: 7Z7S) [20], the NDH-2 in violet (PDB: 4G6H) [21], succinate:ubiquinone oxidoreductase in blue (PDB: 1NEK) [22], cytochrome bo_3 oxidase in yellow (PDB: 7N9Z) [23], cytochrome *bd*-I oxidase in light green (PDB: 6RX4) [24], cytochrome *bd*-II oxidase in red (PDB: 7OSE) [25] and ATP-synthase in pink (PDB: 6OQR) [26].

Three primary dehydrogenases oxidize the substrate by using ubiquinol as an electron acceptor, namely NADH: quinone oxidoreductase (NDH-1), or complex I, NDH-2 (alternative dehydrogenase) and succinate: ubiquinone oxidoreductase (complex II). Terminal oxidases, such as cytochrome bo_3, cytochrome *bd*-I and *bd*-II oxidases transfer electrons from ubiquinol to the final electron acceptor of aerobic respiration oxygen.

Four of these enzymes from the *E. coli* respiratory chain contribute to a proton motive force: the proton-pumping complex I (NDH-1), cytochrome bo_3, the proton-pumping oxygen reductase that is a member of the superfamily of heme-copper oxidoreductases, and the cytochrome *bd*-I and *bd*-II oxidases [14, 27]. Cytochrome *bd* oxidases cannot actively pump protons but contribute to the proton-motive force by transmembrane charge separation [27]. Complex I couples NADH oxidation and quinone reduction with translocation of four protons across the membrane [28]. It serves as the main electron entry point to the aerobic respiratory chain [29]. Complex I has an L-shape and consists of a peripheral and a membrane arm [30]. It contains nine iron-sulfur clusters and a flavine mononucleotide (FMN) as cofactors. All cofactors of electron transfer are located in the peripheral arm [3]. Translocation of four protons occurs in the membrane arm consisting of antiporter-like subunits [31]. Complex I is described in more detail in Chapter 2.2.

E. coli also contains the alternative NADH dehydrogenase (NDH-2), which does not contribute to the proton gradient. It is much smaller, and its structure is much more simple compared to NDH-1 [32]. It is a single-subunit monotopic membrane protein with a flavin cofactor [33]. NDH-2 has a mass of 47 kDa and most likely exists in homodimeric form. NDH-2 uses NADH as a substrate and catalyzes the electron transfer to ubiquinone [34]. However, in contrast to complex I, this process is not coupled with proton translocation across the membrane. Due to its metabolic prominent function NDH-2 serves as a promising antimicrobial drug target [33]. Kinetic analyses from the bacterial enzymes revealed that there is a ping-pong mechanism in which the substrates bind, react and dissociate sequentially [35].

The reason why *E. coli* has two NADH dehydrogenases with similar functions, is their regulation in different growth conditions. Gene expression of *nuo* (NDH-1) and *ndh* (NDH-2) is regulated by oxygen concentration in the growing environment [36]. Under aerobic conditions, there is a tendency for *E. coli* to produce more NDH-1 (complex I). However, in anaerobic conditions, the expression of the *ndh* gene dominates [36, 37]. Having two NADH dehydrogenases allows to regulate the generation of the proton motive force and the reoxidation of NADH independently

from each other [37]. If the microbe lives in an environment with limited substrate availability, maximal growth yield can be a positive factor for survival. NDH-1 plays a significant role in electron transport. It was observed that a mutant of *E. coli* lacking NDH-1 showed diminished survival in the stationary phase. The activity of NDH-2 leads to a lower rate of energy generation, which could be detrimental under these circumstances [38]. The presence of two NADH dehydrogenases also helps to regulate the [NADH]/[NAD^+] ratio in aerobic organisms [39].

One more primary oxidoreductase is the succinate dehydrogenase (or succinate: ubiquinone oxidoreductase, complex II, Sdh), which does not generate a proton motive force across the membrane [40]. This enzyme is part of the Krebs cycle and of the respiratory chains, thus, connecting the citric acid cycle with respiration [22]. The function of complex II is to couple the oxidation of succinate to fumarate in bacterial cytoplasm with the reduction of ubiquinone [41]. Complex II comprises three iron-sulfur clusters and a covalently bound FAD [22]. It is mainly produced under aerobic conditions, and its production is suppressed under anaerobic conditions [42].

Terminal oxidases reoxidize ubiquinone, which was reduced by the primary dehydrogenases. These integral membrane proteins catalyze the four-electron reduction of oxygen to water coupled with the generation of a proton motive force [43]. There are three ubiquinol oxidoreductases in *E. coli*: bo_3, *bd*-I and *bd*-II.

Cytochrome bo_3 ubiquinol oxidase is the primary respiratory oxidase present in *E. coli* grown at high aeration [44]. This enzyme is a member of the heme-copper superfamily, which includes oxygen reductases and NO reductases [45]. The enzyme catalyzes the 2-electron oxidation of ubiquinol-8 and the 4-electron reduction of oxygen to water [46]. Four genes encode the bo_3 oxidase (*cyoABCD*). The redox groups heme *b,* heme o_3 and Cu_B are located in the largest subunits CyoA and B [47].

Cytochrome *bd*-type oxidases distinguish themselves from the other oxidases as having a high oxygen affinity and the reaction is insensitive to inhibitors like cyanide [36]. The content of *bd* oxidases increases not only in a low oxygen environment but also under some unfavorable conditions like alkaline pH and high temperatures [37]. Cytochrome *bd* oxidases do not contain copper in contrast to cytochrome bo_3 oxidases [48]. Cytochrome *bd*-I oxidase are expressed under microaerobic conditions [49]. Cytochrome *bd*-I oxidase consists of two major subunits, CydA and CydB, and two small subunits CydX and CydY [24]. It has several specific functions apart from

energy conservation. Cytochrome *bd*-I serves as an oxygen scavenger and inhibits the degradation of O_2-sensitive enzymes [50]. Cytochrome *bd*-I oxidase is described in Chapter 2.3 in more detail. The third terminal oxidase *bd*-II is expressed under anaerobic conditions, and upon entering the stationary phase and phosphate starvation [17, 51, 52]. Cytochrome bo_3 and *bd*-I are well studied, but less is known about *bd*-II [53]. It comprises the three subunits AppCBX and shows an architecture homologous to *bd*-I. The arrangement of the cofactors is similar to that in *bd*-I oxidase [25]. Functional similarities to *bd*-I were also identified [54]. However, some differences were found. For example, *bd*-II lacks one subunit resulting in heme b_{595} being more accessible from the membrane and from the active site [25].

Different inhibitors can affect the activities of bo_3- and *bd*-oxidases. Inhibitors are classified into two groups: heme ligands (cyanide, azide) that act at the oxygen-reducing site and compounds acting at the quinol-binding sites. For example, cytochrome bo_3 is more sensitive to cyanide and azide than *bd*-oxidases which might be due to the presence of heme *d* [55]. In contrast, quinolone-type compound aurachine D serves as an inhibitor of *bd*-oxidase but does not affect bo_3-oxidase [56].

The redundancy of NADH dehydrogenases and oxygen reductases may provide robustness and flexibility for bacteria to adjust to environmental conditions (temperature, availability of carbon source and oxygen). Under aerobic conditions, mostly complex I and succinate dehydrogenase are produced to reduce the quinone pool [57]. Under these conditions, mainly cytochrome bo_3 oxidase is the terminal oxidase that oxidizes quinol and reduces oxygen to water. On the other hand, in anaerobic environment, NDH-2 and *bd*-I are the dominant enzyme complexes [58].

2.2 NADH: ubiquinone oxidoreductase, complex I

2.2.1 Architecture of complex I

NADH: ubiquinone oxidoreductase (complex I) is crucial for cell energy metabolism and serves as an electron entry point to the respiratory chains in most eukaryotes and many prokaryotes [32]. It is a redox-driven proton pump that is one of the mammalian cells' largest and most complicated enzymes [59]. Mammalian complex I contains up to 45 subunits and has a molecular mass of 1 MDa [60]. Fourteen of these subunits are core subunits that house the catalytic machinery and are conserved from humans to bacteria [61]. 31 supernumerary subunits have functional and regulatory tasks but are not involved in the main catalytic machinery. The role of each accessory

complex I subunit in regulation, stability and functions remains to be determined [62]. It is assumed that some of them are related to complex I protection from reactive oxygen species (ROS) [63]. Studies indicated these subunits are essential for complex I assembly [64]. The supernumerary subunits are central to structural stability, and some of them play independent metabolic roles [61]. Mutations occurring in complex I are associated with human neurodegenerative diseases like Alzheimer's and Leigh syndrome [65–68]. In addition, a complex I deficiency was identified in Parkinson's disease, dystonia and Leber's hereditary optic neuropathy [69–71]. Complex I is also considered a main source of reactive oxygen species that can lead to DNA damage and ageing [72, 73]. Figure 2.2 shows the structure of mammalian complex I.

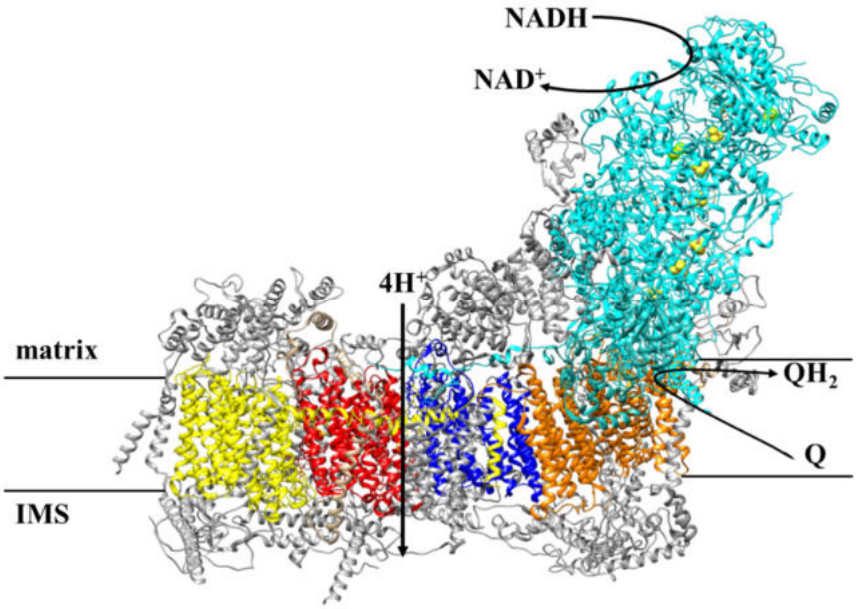

Figure 2.2: Structure of the mitochondrial complex I from *Homo sapiens* (PDB: 5XTD) [74]. The core subunits are shown in color (peripheral arm – light blue, membrane arm – yellow, red, blue, orange). Supernumerary subunits are shown in grey. Binding sites of NADH and Q are shown with the black arrows. Translocation of four protons across the membrane is indicated by the black arrow.

Bacterial complex I can serve as a minimal structural model to study different neurodegenerative diseases as it contains homologous core subunits that are essential for complex I catalysis. It catalyzes the same reaction and is inhibited by the same inhibitors [75]. In *E. coli*, complex I is encoded by 14 genes, *nuoA-N* [76, 77], derived from the enzyme terminology (NADH:ubiquinone oxidoreductase), building an 550 kDa enzyme consisting of 13 subunits as subunits NuoC and NuoD are fused. Complex I consists of a peripheral and a membrane arm. In the electron transfer reaction, two electrons are transferred from NADH to Q. This process is coupled with the translocation of four protons across the membrane. Electron transfer occurs in the peripheral arm,

and proton translocation across the membrane from the negative inner side (N-side) to the external positive side (P-side) takes place in the membrane arm [28]. This process can be described with the following equation 1 [29]:

$$NADH + Q + H^+ + 4H^+_{in} \rightarrow NAD^+ + QH_2 + 4H_{out} \quad (1)$$

Figure 2.3 shows the structure of bacterial complex I from *E. coli.*

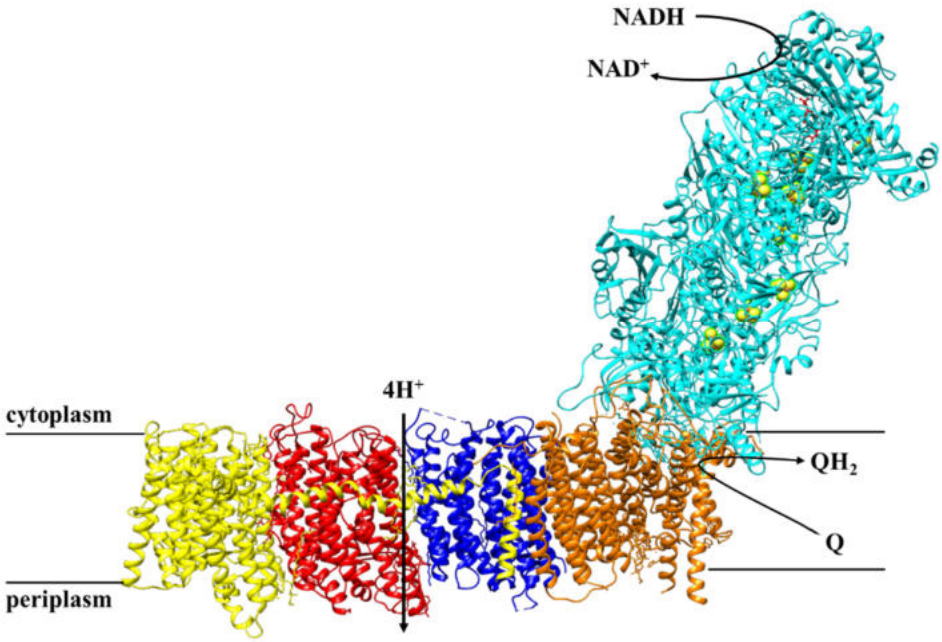

Figure 2.3: Complex I crystal structure from *E. coli* at 2.4 Å resolution (PDB-entry: 7Z7S) [20]. The core subunits are shown in color (peripheral arm – light blue, membrane arm – yellow, red, blue, orange). Binding sites of NADH and Q are shown with the black arrows. Translocation of four protons across the membrane is indicated by the black arrow.

The peripheral arm has a length of 140 Å and comprises subunits NuoB, CD, E, F, G and NuoI [78]. All cofactors needed for electron transfer are located there [79]. It includes the flavin mononucleotide (FMN) and the iron-sulfur clusters [80]. The number of iron-sulfur clusters may vary according to the species, but only seven are involved in electron transfer from NADH to Q over a distance of 95 Å [81, 82].

2.2.2 Electron transfer in *E. coli* complex I

Electrons are transported from NADH to the electron acceptor Q through the FMN and seven iron-sulfur (Fe/S) clusters [83]. The electron transfer from NADH to Q proceeds *via* the FMN and clusters in the following way: FMN→N3→N1b→N4→N5→N6a→N6b→N2, here the clusters are named according to Ohnishi [84]. Seven Fe/S clusters are tetranuclear [4Fe/4S], and two are

binuclear [2Fe/2S]. Figure 2.4 shows the cofactor arrangement in the peripheral arm of *E. coli* complex I.

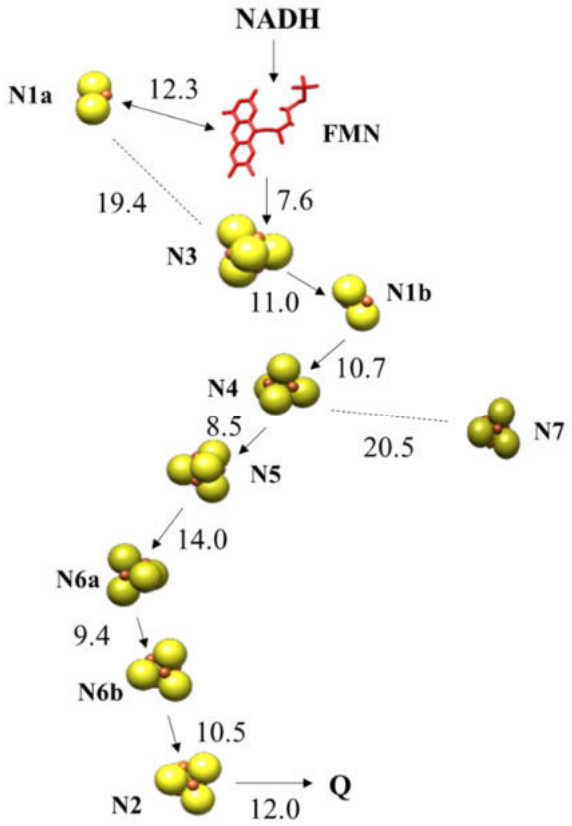

Figure 2.4: Arrangement of cofactors in *E. coli* complex I (PDB: 7Z7S) [20]. The Fe/S clusters are shown as yellow/brown spheres, and FMN is in red. The electron pathway is shown with arrows. The edge-to-edge distances are indicated.

The binuclear Fe/S cluster N1a, which is located in close proximity to FMN, is strictly conserved. It was supposed that it might regulate the reduction of flavosemiquinone, thus preventing the production of ROS [85]. It was shown to be important for the stability of the subunits NuoE, F and G [86]. N1a cluster is not reduced by NADH in many species [87], but might be involved in the regulation of NADH reduction [88]. The tetranuclear Fe/S cluster N7, present only in some species, is not involved in electron transfer. It is located 20.5 Å from the closest Fe/S cluster and thus is not within the electron transfer distance of 14 Å [89]. However, it is also essential for the stability and assembly of complex I [90]. Available data from microsecond freeze-hyper quenching electron paramagnetic resonance (EPR) showed a detailed picture of electron distribution after reduction by NADH according to the midpoint potentials of Fe/S [91, 92]. After the binding of NADH, FMN is reduced by hydride transfer, and the first electron is transferred to the tetranuclear

cluster N3. The second electron is “parked” on cluster N1a. The electron is transferred to the binuclear Fe/S cluster N1b and then through the tetranuclear Fe/S clusters N4, N5, N6a and N6b to the distal tetranuclear Fe/S cluster N2. After reoxidation of N3, the second electron from cluster N1a is transferred to the chain of clusters *via* the FMN. Reduction of N1a initiates structural rearrangements that prevents binding of NADH to the reduced complex I and keeps NAD^+ in the binding pocket [93]. This might prevent ROS production.

EPR studies revealed that after reduction by NADH, only five Fe/S clusters were detectable [84]. Upon the reduction of NADH, signals from N1a, N1b, N3, N4 and N2 clusters were identified [94]. Cluster N7 was detected only after reduction with dithionite as this cluster is located too far to be reduced by NADH. The EPR signal of the sixth cluster N5 was detected only at 3 K [95]. The Fe/S clusters are almost isopotential, and the values were around -250 mV [78, 84, 87]. However, more positive values were determined for N2 with -200 mV [96]. This cluster’s potential is also pH-dependent, contrary to most of the other Fe/S clusters [97]. One more salient feature of this cluster is the coordination with two adjacent cysteine residues as ligands, which is observed in very few Fe/S clusters. These specific features led to the assumption that N2 might play a role in coupling electron transfer with proton translocation [98]. There is a significant energetic drop of about +100 mV between the midpoint potential of the distal N2 cluster and the Q/QH_2 couple [96]. Ultra-fast freeze quench experiments showed that N2 is reduced in around 90 µs, which is very close to the rate proposed by electron transfer theory [99, 100]. The high midpoint potential of N2 assures that it has the maximum electron occupancy for further reacting with Q.

2.2.3 Quinone binding site

Molecular dynamics simulations suggest that the redox energy from NADH is almost completely transferred to Q, which was confirmed experimentally [96, 101]. The quinone binding site is located 25-30 Å above the membrane plane in a tight tunnel, at around 12 Å from the cluster N2 [83, 102]. It is formed by the subunits NuoB and NuoCD from the peripheral arm and by subunits NuoH and NuoA from the membrane arm [103]. The quinone binding pocket is 25-40 Å long, has an L-shape, and offers at least five binding positions for Q according to quantum mechanical simulations and cryo-electron microscopy data [104, 105]. It is long and heterogeneously lined up, where the top and bottom are hydrophobic, while many charged residues were found in the central section of the cavity [106]. One feature of Q binding is that it is enclosed from solvents and has a

narrow entry site for Q [83]. Previous mutagenesis studies proved the importance of $H224^{CD}$ and $Y273^{CD}$ in the mitochondrial complex I for Q binding [107]. Head groups of Q coordinate to these amino acids [108] by hydrogen bonds [109, 110]. Figure 2.5 shows quinone binding site of complex I.

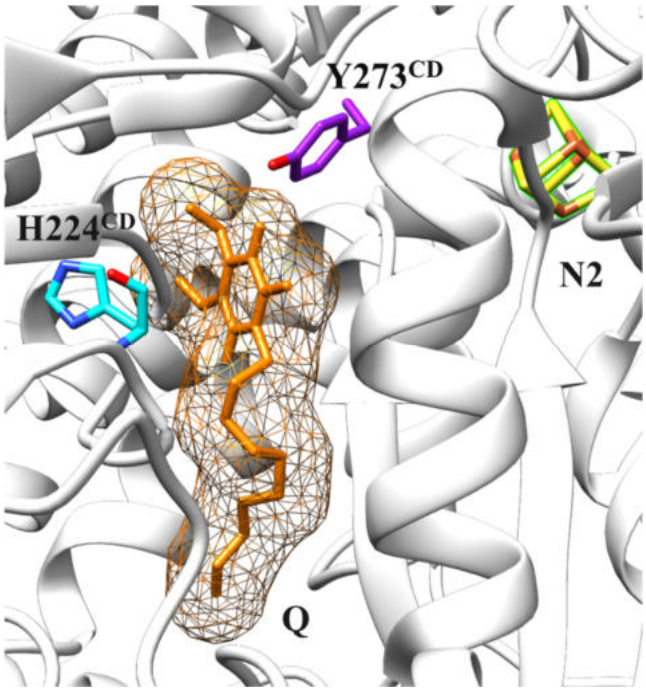

Figure 2.5: Quinone binding site of *T. thermophilus* complex I (PDB: 6I0D) [111]. Fe/S cluster N2 is shown in yellow and brown. Decyl-ubiquinone and its electron density are shown in orange. Both coordinating amino acids are shown (*E. coli* nomenclature).

The Q-binding tunnel is lined with the charged amino acids of the NuoH subunit. Reduction of Q occurs by the transfer of an electron from the distal N2 cluster and a putative protonation by the amino acid residues. A network of charged residues around the central region of the ubiquinone connected to the E-channel may therefore be functionally relevant in the mechanism by which ubiquinone reduction is coupled to proton translocation [106]. Reprotonation of both amino acids occurs probably by a water channel, which is directed to that position [112]. Conformational changes in the direction of conserved and charged amino acids [101] drive the movement of QH_2, which might change dipolar interactions in the cavity and probably causes proton translocation in the membrane arm [113]. Area of charged amino acids connects the Q-binding site with the so-called E-channel, the proton pathway located closest to the peripheral arm of complex I [101]. The name E-channel derives from the presence of several conserved glutamate residues [108]. It was proposed that the negative charge of the reduced Q might lay the foundation of the proton pumping

mechanism [94]. QH^- might be produced as an intermediate [114]. There are two theories regarding the further way of QH_2. According to one theory, reduced QH_2 leaves complex I, and a new Q molecule enters to start a new catalysis cycle [113]. The other theory states that the quinone molecule stays inside the cavity and moves between two sites, transferring electrons to an additional Q molecule that do not fully enter the Q cavity [104]. The advantage of such a mechanism, as it is coupled to reoxidation of QH_2, is that it can provide local protons in a controlled manner to annihilate the original negative charge that triggered the pump mechanism. To achieve the same coordination with the other model, undefined gating or timing mechanisms are required [115].

2.2.4 Structure of the membrane arm

The membrane arm of complex I has a length of 180 Å and a height of 30 Å. It consists of the subunits NuoA, NuoH and NuoJ-N [82]. There is no cofactor found in the membrane arm of complex I [29]. NuoH is located between the peripheral and membrane arm of complex I. The structural arrangement of the membrane arm was visualized by X-ray diffraction.

The distance between the NADH binding site and the distal subunit NuoL is around 300 Å. Proton pumping occurs over a distance of 200 Å to the Q binding site. So, proton-coupled electron transfer in complex I is catalyzed over a long distance. The difficulty of solving the coupling process is caused by its location at the junction of the peripheral and membrane arm, which is structurally the most complicated part of the enzyme [83]. It is generally accepted that per oxidation of one NADH, four protons are translocated across the membrane resulting in a stoichiometry of $4H^+/2e^-$ [116].

The E-channel is the closest to the Q-cavity proton pathway that is made of the subunits NuoH, NuoJ and NuoK [90]. Subunits NuoL, M and N are homologous to each other and can be described as antiporters-like subunits [113, 117]. Each of the antiporter-like subunits has an internal symmetry and comprises five transmembrane helical bundle segments [118]. They contain two pseudo symmetrically located half-channels, where the N terminus is open to the N-side and the C terminus to the P-side [119]. Each of the antiporter subunits has a hydrophilic axis containing charged amino acid residues like conserved lysine/glutamate or lysine/aspartate residues that are located in the middle of the lipid bilayer. This charged polar axis is assumed to be essential for proton translocation [120, 121]. There is a conserved lysine residue in each of the antiporter subunit and a distal lysine (NuoL and NuoN) or glutamate (NuoM) residue [122]. The distribution of

conserved titratable amino acids is asymmetric as a central subunit NuoM contains a conserved distal glutamate. Molecular simulations suggest that the proton pathways are located around the broken helix motifs, and several mutagenesis experiments proved that suggestion [123]. Proton transfer starts from the negative N-side, which is connected to the membrane's central axis, to the positive P-side.

The structure of the complex I membrane arm indicated the location of putative proton pathways which can be found in each antiporter subunits. Figure 2.6 shows putative proton channels in antiporter-like subunits (A) and more specific in subunit NuoM (B).

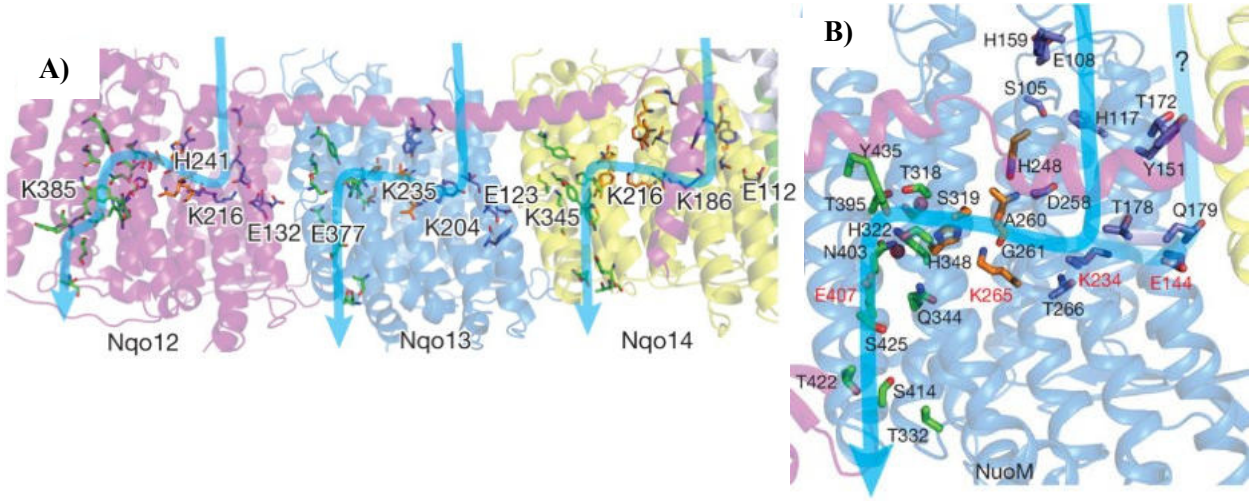

Figure 2.6: A) Putative proton-translocation channels in the antiporter-like subunits of complex I from *T. thermophilus* (PDB: 3M9C) [124]. Polar residues lining the channels are shown as sticks. Approximate proton-translocation paths are indicated by blue arrows [83]. **B) Putative proton channel in NuoM of *E. coli* membrane arm (PBD: 3RKO) [119].** Polar residues lining the channels are shown as sticks, with carbon in green and in orange for the connecting residues [119].

The coupling mechanism of electron transfer with the translocation of protons across the membrane is currently the most discussed topic in the research area of complex I [125–128]. There are several theories to explain how protons are translocated across the membrane and how this process is driven and coupled with electron transfer in the peripheral arm. Many theories were proposed to explain the coupling mechanism, comparing the function of complex I, for example, to a wave-spring [129], a piston [130], a steam engine [131] and a semi-automatic shotgun [132]. There were many suggestions for coupling principles including direct (electrostatics), indirect (conformational) or a combination of both [6, 129, 133, 134].

2.2.5 Proton translocation catalyzed by $1H^+$ per proton pathway

According to this mechanism of proton translocation, one proton is translocated through each of the subunits NuoL, NuoM and NuoN and one through the E-channel [113, 135]. Charged amino acid residues located on the central axis form a wire on which an electrostatic wave caused by Q reduction propagates from the quinone binding site to the distal subunit NuoL in the membrane arm and is reflected back to the Q site [113, 135]. The propagation of the wave is based on conformational changes, electrostatic interactions and changes in the hydration state of channels along the membrane arm [129]. Subunits NuoL, M and N contain a conserved Lys/Glu ion pair at the interface to the next subunit. In the closed ion pair conformation, the protonated state of the central lysine is favorable. Opening of the ion pair triggers a proton transfer from the central lysine to the distal lysine and glutamate residues. Protonation of these residues leads to the opening of the ion pair in the next subunit [136]. The progression of the electrostatic wave, triggered by the movements of QH_2-species in the Q-channel, induces protonation of residues of the E-channel, which leads to the opening of the central titratable ion pair in NuoN. MD simulations and pK_a calculations showed that the protonated central Lys induces an electric field that pulls in water molecules along the broken helix from the N-side [118]. The protonated amino acid $K247^N$ transfers the proton to the distal $K345^N$ which leads to the opening of the ion pair in NuoM ($E144^M/K234^M$). Accordingly, the wave would pass further to NuoL and would propagate through the entire membrane arm. Stepwise opening of ion pairs and lateral proton transfer leads to the charge redistribution in the distal subunit NuoL. Accordingly, a proton is released to the P-side, which in turn stabilizes ion-pair formation in the distal subunit NuoL [137]. This leads to the deprotonation of distal Glu residue on NuoM and the transition of the NuoN ion pair to the closed state. Deprotonation induces the back wave that causes the closing of the ion pairs of the central axis and proton release on the P-side. This proposed mechanism involves opening and closing of the central ion pair and the proton redistribution from the N- to the P-side. The wave reaches the E-channel close to the Q-binding site, where the reduced Q-species moved to its second Q-binding site in contact with titratable amino acids of the E-channel. The formation of QH^- from QH_2 triggers proton pumping along the membrane arm [138]. The back wave initiates a protonation of QH^- to QH_2 that is either released or stays in the cavity in accordance with the Q-shuttle mechanism [11, 104]. This theory of proton translocation was supported by experimental observations, as deletion of the distal subunit NuoL leads to a decrease in the stoichiometry of proton translocation [139].

The coupling of the ion-pairs between subunits of the membrane arm as proposed from molecular simulations is consistent with the forward/backward electrostatic wave-propagation model. The back wave arises from principles of microscopic reversibility, where the back-propagation is similar, as in Newton's cradle device, initiated by a pulse from the terminal unit [138]. Figure 2.7 shows a schematic representation of this kind of proton translocation mechanism.

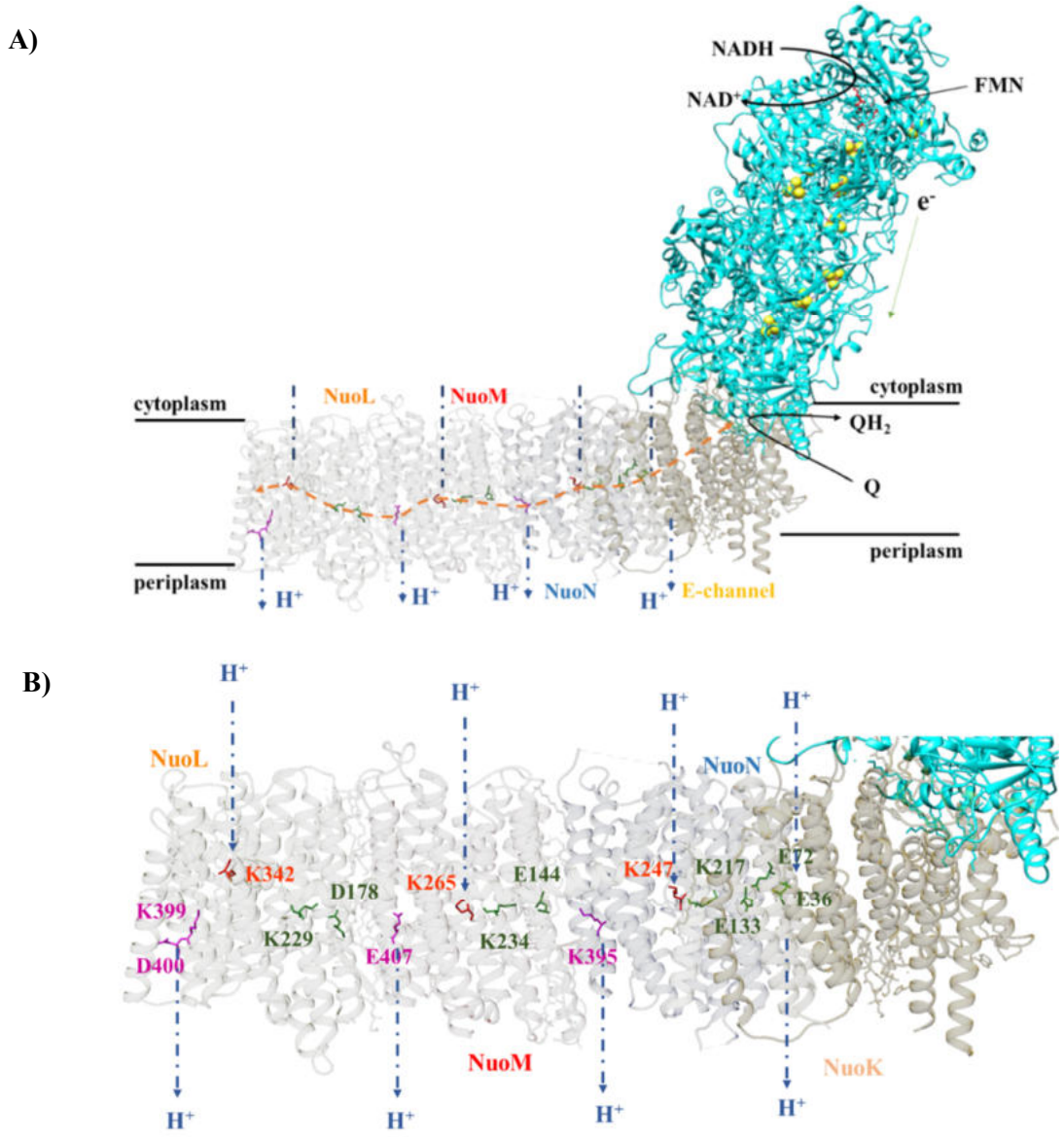

Figure 2.7: A) Structure of *E. coli* complex I (PDB: 7Z7S) [20]. The peripheral arm is shown in blue, Fe/S clusters as yellow and brown spheres, FMN is shown is red. Binding sites of NADH and Q indicated by the black arrows. Direction of electrons is indicated by the green arrow. Putative proton channels are indicated with the blue broken arrows. The central axis of charged amino acids is shown as the orange arrow. Three antiporter subunits and the E-channel are shown. **B) Structure of the membrane arm of *E. coli* complex I (PDB: 7Z7S) [20].** Three antiporter subunits and the E-channel are shown. Putative proton channels are indicated with the blue broken arrows. Polar residues building the central axis are indicated: central lysine residues are shown in red, the ion pairs are shown in green, distal lysine/glutamate residues are shown in magenta. Reproduced from [122].

2.2.6 Proton translocation according to the "ND-5 only" theory

Based on cryo-EM structures, another mechanism of proton translocation was suggested [5]. The mechanism described in 2.2.5 was criticized as the proposed conformational states of individual amino acid residues were not detected in cryo-EM experiments. However, it can be possible that the lifetime of the conformational states is too short to be detected by cryo-EM [122].

The "ND-5 only" theory proposes that two electrostatic forward waves propagate to the distal subunit [140, 141]. According to this mechanism, opening and closing movements of the entire complex I occur. Quinone can enter the cavity only in the open state of complex I. The proton pumping cycle is initiated by quinone binding, accompanied by the transition to the closed state with the reordering of NuoH into a so-called retraced conformation allowing quinone reduction. The distribution of charge is asymmetric, so the opening and closing of ion pairs happen asynchronically. Two forward electrostatic waves drive the proton pumping that occurs in the distal subunit NuoL. Structural cryo-EM investigations revealed that only the distal subunit NuoL is sufficiently hydrated among all antiporter-like subunits of the membrane arm, to allow proton exit from NuoL (ND-5 is mitochondrial homologue in mammalians) to the P-side [5]. The other antiporter subunits are not applicable for proton translocation according to these observations as they lack the appropriate hydrated channels. A 'domino effect' mechanism of complex I was proposed, where electrostatic interactions initiate a series of proton transfers along the central axis for 'vacancy' towards NuoL and 'electrostatic pressure' from the upcoming protons [20]. The forward wave 'dominoes stacking' is assumed to prime the pump, and the reverse wave 'dominoes falling' could results in the ejection of all pumped protons. As a result, all four protons are ejected from the distal subunit NuoL. This mechanism requires that all protons are transferred to the neighboring subunits and not to the periplasm, as otherwise the process will not be initiated, explaining the exit of all four protons *via* NuoL [20]. However, this theory does not agree with the observation that proton translocation is still observed when the distal subunit is removed [142]. It is also difficult to interfere with the directionality of electrostatic waves from structural data [138].

2.3 Cytochrome *bd*-I oxidase

Cytochrome *bd* oxidases belong to the superfamily of proteins that catalyze oxygen reduction to water [143]. They are found in prokaryotes, including several pathogens. Therefore, they can serve as a prospective drug target as their presence in mammalian cells was not observed [144]. Besides

energy conversion, they play an essential role in protection against oxidative stress, adaptability and bacterial virulence [145]. Usually, they are produced under low oxygen concentrations and oxidative stress [146, 147]. They couple (ubi)quinol (QH_2) oxidation with proton uptake from the cytoplasmic side and proton release on the periplasmic side. Cytochrome *bd* oxidases are not proton pumps, but they contribute to the generation of proton motive force across the membrane by a vectorial charge transfer [148]. The electrons from QH_2 are transferred *via* three heme groups to oxygen. Oxygen is reduced to water in a four-electron process. The reaction is expressed in the following equation [53]:

$$2QH_2 + O_2 + 4H_{in} \rightarrow 2Q + 2H_2O + 4H_{out} \quad (2)$$

Structures of *bd*-I oxidase are available from *Geobacillus thermodenitrificans* [149], *E. coli* [24] and some other organisms like *Corynebacterium glutamicum* [150], *Mycobacterium tuberculosis* [151], *Mycobacterium smegmatis* [152]. The overall architecture is similar. However, slight differences are present, which results in subtle differences of mechanistic features [24].

E. coli bd-I oxidase consists of two major subunits CydA and CydB and two small subunits CydX and CydY [24, 153]. CydA and CydB have 9 transmembrane helices, each, comprising two four-helix bundles and an additional cytoplasmic helix. The molecular mass of these subunits is 58.2 and 42.5 kDa, respectively [143]. However, CydX and CydY contain only one transmembrane helix and have 37 and 26 residues, respectively [24]. The fourth subunit CydY is also called CydH and it is not encoded within the *cyd* operon [24, 154].CydA contains a globular domain located between helices 6 and 7, the 'Q-loop', which is expected to be involved in QH_2 binding and oxidation [155]. Due to the presence of long (L) and short (S) domain loops, the family of *bd* oxidases is classified into S- and L-subfamilies.

Cytochrome *bd*-I oxidase comprises three hemes: b_{595}, b_{558} and heme *d*. All of them are located in subunit CydA. The low-spin heme b_{558} serves as an electron input device, and high-spin heme b_{595} delivers electrons to high-spin heme *d*, which is located in the active site, where oxygen is reduced to water [156]. This assumption was supported by several experiments, including EPR and pulse radiolysis studies [157–159]. Hemes in CydA are arranged in the triangle [149]. Earlier, it was supposed that heme b_{595} and heme *d* could work as di-heme site [160], but the structures revealed that oxygen is reduced exclusively at heme *d* [149] and that the other hemes are located too far away [24]. The triangle of hemes with consistent distances between the central iron atoms shows the same orientation towards the membrane plane in all organisms [24]. The close interactions

between the three hemes in *bd*-I result in highly cooperative properties [161]. Heme b_{558} is hexacoordinated with the central iron by H186 and M193. Heme b_{595} and heme *d*, have glutamic acids as axial ligands E445 and E99, respectively. These positions are conserved. Figure 2.8 shows the structure of *bd*-I oxidase (A) and its heme arrangement (B).

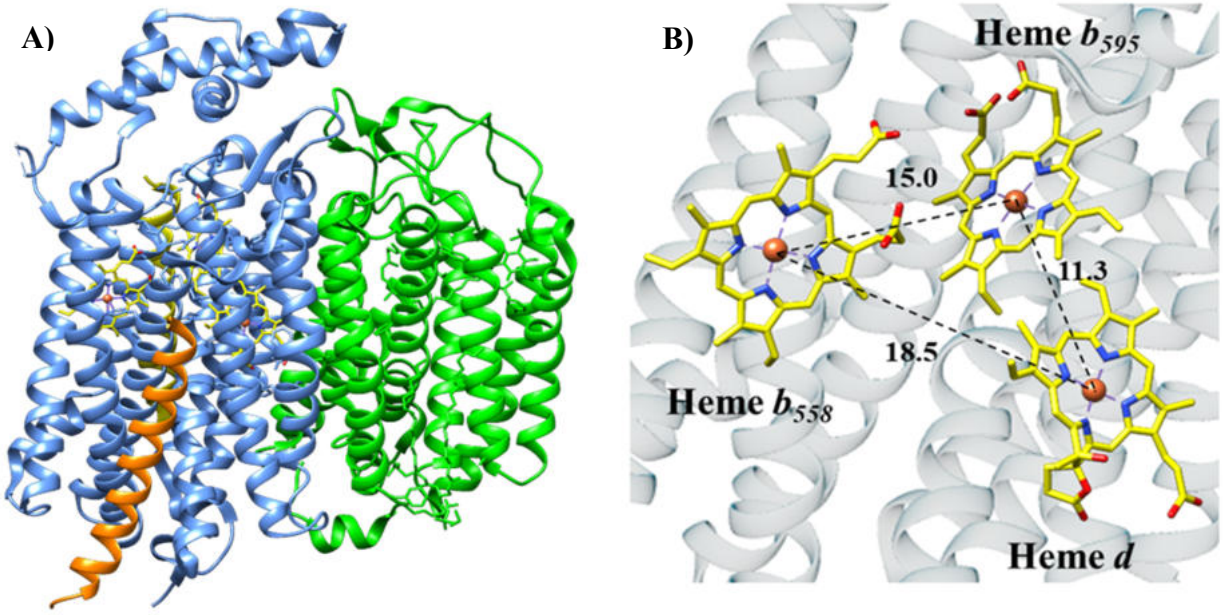

Figure 2.8: A) Structure of *E. coli bd*-I oxidase (PDB: 6RX4) [24]. CydA is shown in blue, CydB in green, CydX in orange and CydY in yellow**.** CydY is not visible in the projection of *bd*-I. Hemes are shown in the yellow and brown. B) Location of hemes in the subunit CydA. Heme ring is shown in the yellow, the iron atom in brown, nitrogen in blue, and oxygen in red.

Two more residues, R448 and E107, that are not axial ligands of the hemes are located in close vicinity and appeared to be important for reactivity [162]. Figure 2.9 shows the position of essential residues near both hemes.

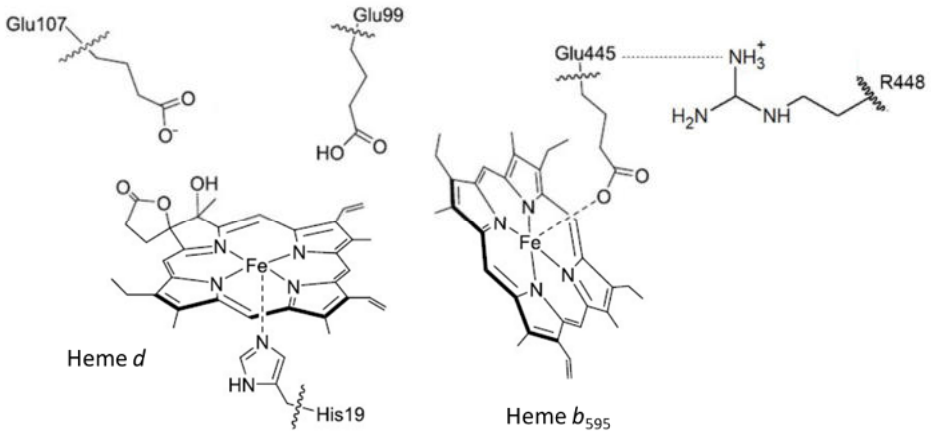

Figure 2.9: Sketch of the essential residues located in the proximity of hemes b_{595} and *d*. Reproduced from [163].

E445 is located at a 2.1 Å distance to heme b_{595} and E99 at a 2.7 Å distance to heme *d* [149]. Previous studies showed the functional importance of E445 as ligand of b_{595} [164]. The mutation E445A was characterized in detail, and the results show that IR-signals of heme b_{595} are essentially perturbed or missing in most preparations of the variant. The purified E445A variant was not functional [164]. The UV/vis spectrum showed the absence of the signal at 595 nm, which is associated with heme b_{595}. The absorbance of the Soret band was strongly decreased [164]. However, the isolated variant was stable [161]. Later studies showed that the heme is not reduced by dithionite, thus, explaining the absence of its signals in Raman spectra. EPR spectroscopy revealed the presence of the heme b_{595} in the ferric state even after reduction with dithionite [148]. The role of b_{595} was controversially discussed due to the peculiar behaviour of E445 [165]. The structure finally revealed that E445 is one of the ligands of heme b_{595} [24]. Therefore, the presence of a titratable residue at position 445 of CydA is essential for the function of *bd*-I oxidase [166]. Mutations E445C, E445Q and E445H were generated to investigate the influence of a small (cysteine), isoelectronic (glutamine) or bulkier residue (histidine) at this position. It was shown that E445C and E445H appeared inactive, while E445Q variant retained 15% of specific activity. Variant E445C had less heme b_{595}, E445H and E445Q had less heme *d*. However, variant E445H showed the lowest heme b_{595} content. The E445Q mutation affected the potential of heme b_{558} [161].

R448 was assumed to build a salt bridge with the E445 [161]. The R448A mutation diminished the level of heme *d* binding [164]. It was assumed that both residues, E445 and R448, are essential to stabilize the oxygenated state of heme *d*, by H-bond formation and electrostatic interaction [161]. Mutations around E99 can eliminate or severely reduce both hemes b_{595} and *d* contents [167]. Recent FTIR studies identified E107 as one of the protonated carboxylate residues which undergo environmental changes [168]. Mutations in these positions severely diminished the oxidase activity and eliminated heme *d* binding. Replacement of E99 and E107 with Asp resulted in nonfunctional enzymes [169]. Mutations E99A, E99Q and E99H resulted in variants containing heme *d*. However, only the E99A variant showed activity, although at diminished rates, while the other mutants appeared to be inactive [161]. Therefore, position E99 dramatically influences heme *d* stability and properties [168]. Figure 2.10 shows the positions of the residues described above.

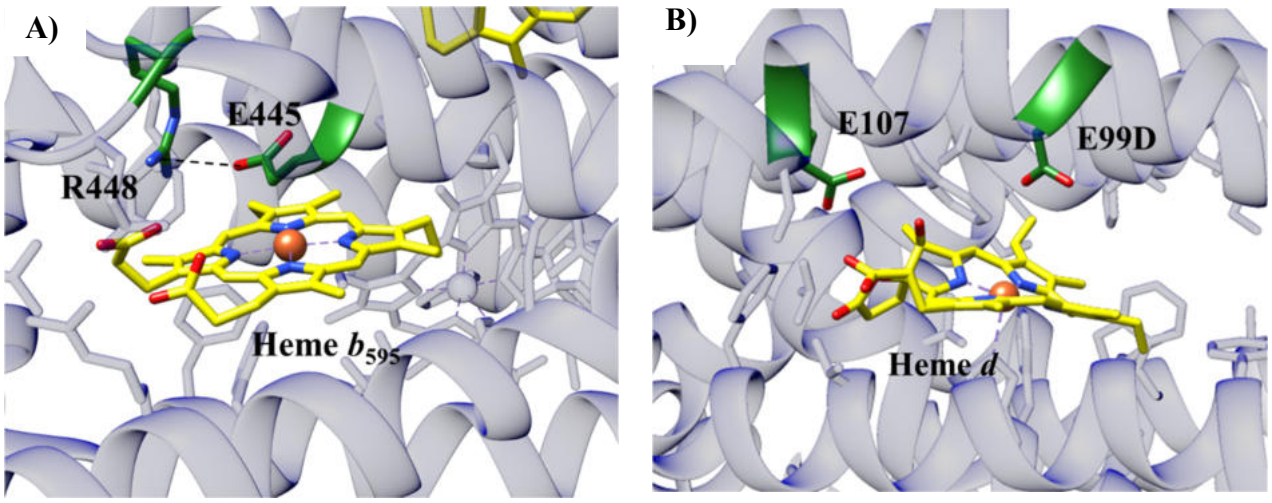

Figure 2.10: A) Coordination of E445 and R448 with heme b_{595}, B) Coordination of E107 and E99 with heme *d* of the *E. coli bd*-I oxidase. The heme ring is shown in the yellow, the iron atom in brown, nitrogen in blue, oxygen in red, and substituted amino acids are shown in green (PDB: 6RX4).

2.4 Spectroscopic techniques

2.4.1 Spectroscopy in general

Spectroscopy is the study of matter interaction with electromagnetic radiation. Electromagnetic radiation can be described as a particle and as a wave. Maxwell's law describes it as two oscillating fields perpendicular to each other. Planck's equitation describes the relation between the energy (E) and frequency (ν):

$$E = h\nu = h\frac{c}{\lambda} \tag{3}$$

where c is the light speed, and h is Planck's constant [170]. The electromagnetic spectrum is a broad and continuous spectrum, which can be divided into seven regions according to the energy level. The interaction with matter produces transitions to another energy levels. In the process of interaction with the matter, the photon energy has to move between two states:

$$\Delta E = E_2 - E_1 = h\upsilon \tag{4}$$

Figure 2.11 shows the electromagnetic spectrum.

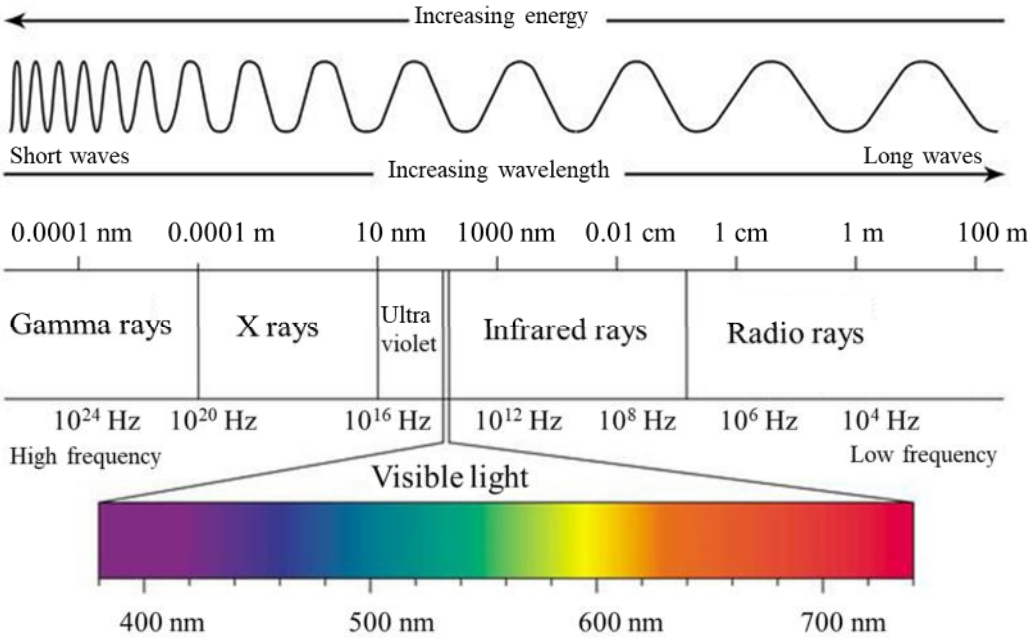

Figure 2.11: Electromagnetic spectrum with different energy levels. Reproduced from [171].

Spectroscopy occupies a particular position in general sciences. Spectroscopic methods are helpful for solving different analytical problems and studying biological systems [172] as they are informative and can be applied to both qualitative and quantitative analyses [173]. Spectroscopic techniques can be classified into absorption, emission, scattering, and diffraction according to the nature of interaction between matter and radiation [174]. Other type of classification is based on a range of the light (from microwave to x-rays). Also, spectroscopy can be classified by the studied species (atomic or molecular). Spectroscopy techniques have found a wide application in studying different biological systems and samples as they can provide valuable information.

2.4.2 UV/vis spectroscopy

UV/visible spectroscopy (UV-vis or UV/vis) is related to spectroscopy which concerns the ultraviolet and visible part of the electromagnetic spectrum. The UV/vis range of the electromagnetic spectrum corresponds to the wavelength range of 800-200 nm. In this range, the light excites electrons from the ground to an excited state. Most molecules and ions absorb energy in the ultraviolet or visible range as they contain chromophores, the functional group in the molecule that is responsible for the absorption of UV/vis light. The absorbed photon excites an electron in the chromophore to a higher energy molecular orbital [175]. For organic molecules, four different types of energy transitions are observed: π–π^*, n–π^*, σ–σ^*, and n–σ^* [176].

The Beer-Lambert law or Beer-Lambert-Bouguer law relates the attenuation of light with properties of matter through which the light is travelling and refers to the following equation:

$$A = \lg\left(\frac{I_0}{I}\right) = \log T = \varepsilon l c \quad (5)$$

where A is the absorbance, ε is the molecular attenuation coefficient (or molecular extinction coefficient), I is the transmitted intensity, I_o is the incident intensity, l - path length in cm, c is the concentration of attenuated species.

UV/vis spectroscopy is a standard tool for measuring various protein samples. Proteins absorb light in the region 260-280 nm of the UV spectrum, primarily due to tryptophan and tyrosine. Peptide bond also absorbs weakly at 210-220 nm [177]. Prosthetic groups (such as flavin and hemes) in proteins frequently have strong absorption bands [178]. The intense bands are produced due to π-π* in conjugated systems and metal-to-ligand charge transfers in the coordination complexes [179]. Heme is a coordination complex consisting of an iron ion coordinated to a porphyrin acting as a tetradentate ligand, and to one or two axial ligands. Hemoproteins have found wide applications and have a variety of biological functions, such as the transport of gaseous molecules [180]. Hemes found in *bd*-oxidases are studied with UV/vis spectroscopy as they act as chromophores and their absorption depends on the redox state of the central atom. In redox chemistry, the central iron serves as an electron source or sink. Hemes produce mainly three different bands: Soret-band (400-450 nm), α-band (540-630 nm) and β-band (500-560 nm). Table 2.1 shows the UV/visible characteristic bands of *bd*-oxidase hemes.

Table 2.1: UV/Visible characteristic bands of hemes in the reduced state observed in the cytochromes *bd* [181].

Type of heme	**Soret-band**	**β-band**	**α-band**
Heme *b*	426−430, 439	528−532	555−566, 595
Heme *d*	430	-	620−630

Figure 2.12 shows a reduced-minus-oxidized UV/vis difference spectrum of *bd*-oxidase in the α- and β-bands regions. Signals for the b_{558} heme are detectable at 531.5 and 561.5 nm. The heme b_{595} shows bands at 561.5 and 594 nm. The characteristic heme *d* band is found at 629 nm.

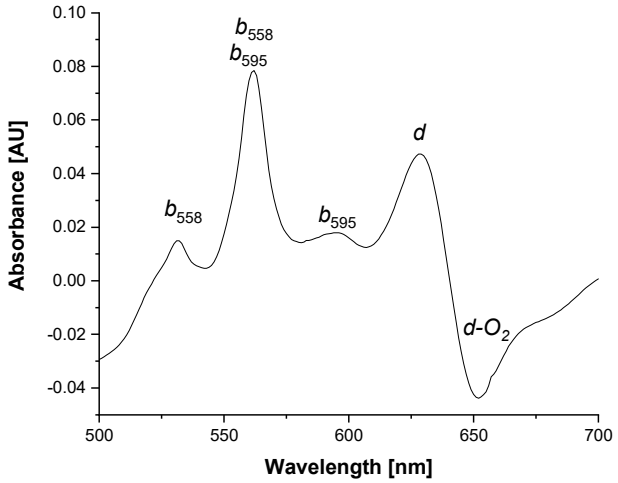

Figure 2.12: Reduced-minus-oxidized UV/vis difference spectra of isolated *E. coli bd*-oxidase.

2.4.3 Infrared spectroscopy

Infrared spectroscopy is a valuable technique for qualitative and quantitative analysis of different varieties of samples. Unlike UV/vis spectroscopy, which relies on larger energy absorptions, infrared (IR) spectroscopy uses much smaller energy absorbance, light, and concerns the vibrational and rotational states of the molecule. IR bands represent transitions between the vibrational ground state (ν=0) and vibrational first excited states (ν=1) or second excited state (ν=2). Molecules that undergo a net change in dipole moment can absorb IR light [182]. The range of infrared spectra is between 780 nm and 1 mm, corresponding to a frequency range from 300 GHz to 400 THz [183]. The infrared portion of electromagnetic absorption is usually divided into three groups: near-infrared (14000-4000 cm^{-1}), mid-IR (4000-400 cm^{-1}) and far infrared (400-10 cm^{-1}). The mid-IR (MIR) is usually used to study vibrational and rotational structures [184].

An IR spectrum can be visualized in a graph of infrared light absorbance (or transmittance) on the vertical axis *vs* wavenumber on the horizontal axis. Typical units of wavenumber used in IR spectra are reciprocal centimeters, with the symbol cm^{-1} [185].

Molecular vibrations can be classified as either stretching or bending modes. Stretching is a result of continuously changing distances in a bond between two atoms. Bending refers to a change in the angle between two bonds. Bending motions include scissoring, rocking, wagging, and twisting [186]. The various types of vibrations and rotations are excited at different frequencies within the infrared region, thus resulting in unique spectral properties for different molecular

species [187]. A molecule can vibrate in many ways, and each way is called a vibrational mode. For molecules with N number of atoms, geometrically linear molecules have 3N – 5 degrees of vibrational modes, whereas nonlinear molecules have 3N – 6 degrees of vibrational modes (also called vibrational degrees of freedom). Figure 2.13 shows the different types of stretching and bending vibrations.

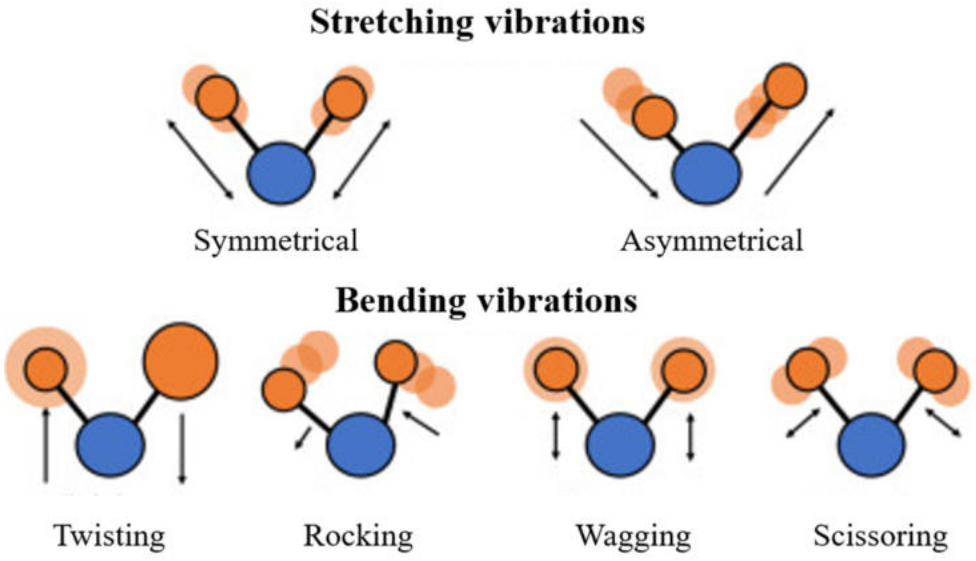

Figure 2.13: Normal mode vibrations observed in IR spectroscopy. Reproduced from [188].

For a diatomic molecule, the the frequency of the vibration is described with Hooke's law for a periodic harmonic oscillator:

$$\nu = \frac{1}{2\pi}\sqrt{\frac{k}{M}}, \qquad M = \frac{m_1 \cdot m_2}{m_1 + m_2} \tag{6}$$

where k is the force constant, m_1 and m_2 represent the mass of each atom participating to the interaction of diatomic molecules, and M is the reduced mass of the atoms.

Infrared spectroscopy can provide various amounts of information, including the chemical structure of the vibrating group, redox state, bond parameters, conformational states, hydrogen bonds and electric fields. Infrared spectroscopy has shown to be a powerful tool for the study of biological molecules, including proteins, lipids, carbohydrates, and nucleic acids [189]. spectroscopic approach enables such molecules to be identified and changes to their chemical structures to be characterized [177].

2.4.4 Infrared spectroscopy of proteins

The high information content from infrared spectrum can be applied to biological systems [190]. It makes infrared spectroscopy a valuable tool for studying protein structure, reactions and functions [191]. The quantity of obtained information can be applied from small to large proteins. Further advantages of using infrared spectroscopy are a high time resolution, short measuring times, low amount of required sample and relatively low costs [192]. Figure 2.14 shows a typical spectrum of a protein in MIR range.

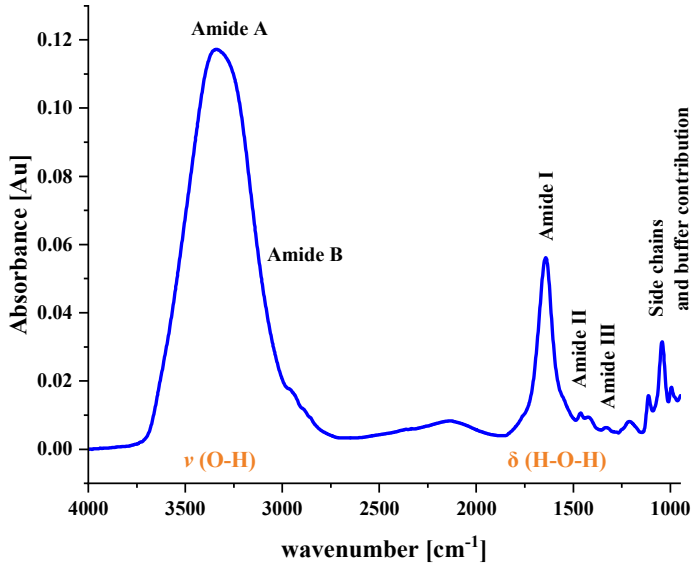

Figure 2.14: Typical spectrum of a protein in a buffer in IR range.

Proteins possess a complex chemical structure, so in the infrared spectrum combination of many overlapping bands is visible. Proteins are studied in mid-IR as this part of the spectrum contains the most valuable information about amino acids side chains and protein backbone [193]. Amide A, amide I and amide II regions characterize the spectrum of proteins. Amide stretching vibrations give rise to the amide A band between 3310 and 3270 cm^{-1}. The amide I vibrations can be observed from 1600 to 1700 cm^{-1} and arise mainly from C=O stretching modes [194]. Amide I band is sensitive to the structure of protein backbone mainly due to the coupling between transition dipoles [195]. The amide II band is located at 1550 cm^{-1}, it is an out-of-phase combination of NH in plane bending and CN vibrations with smaller contributions from CO in-plane bending and CC and NC stretching vibrations [192].

Table 2.2 shows the location of the amide bands in the IR spectrum. ν describes stretching vibrations and δ describes bending vibrations.

Table 2.2: Location of the amide bands and their contribution to the IR spectrum [192].

Region	Frequency, cm^{-1}	Vibrational mode
Amide A	3310-3270	ν(N-H)
Amide B	3100-3030	ν(N-H) resonance with Amide II overtone
Amide I	1610-1695	ν(C=O) 80%, ν(C-N) 10%, δ(CCN), δ(N-H) 10%
Amide II	1480-1575	ν(C-N), δ(N-H) (60%), δ(C=O), ν(C-C), ν(C-N) (40%)
Amide III	1220-1320	ν(C-N), δ(C=O), ν(C-C), δ(N-H),

As amide I frequencies depend on polypeptide bonds and are hardly affected by the chemical nature of side-chain, they can provide information about the secondary structure of the protein. Proteins usually fold into complex three-dimensional structures consisting of various domains containing polypeptides folded into different types of secondary structure [196]. The secondary structure elements absorb at different positions of the amide I band. Each of conformational components is assigned to different structural components: α-helices, β-sheet, turns and non-ordered structures. The fundamental difficulty in detecting secondary structure is that the width of the bands is usually more significant than the separation between maxima of peaks [196]. It leads to a considerable overlap of the individual components, making the identification problematic. The extraction of structural information from experimentally obtained spectra requires mathematical manipulation. The most common procedure to identify the amount of the various secondary structures is deconvolution analysis with Gaussian fitting [197]. The position, amplitude and width at the half-height of each component are optimized for each band. Afterwards, the area under the individual bands is calculated to determine the contribution of each secondary structure component to the amide I band's total surface. Finally, bands of individual components are assigned to the secondary structure. Table 2.3 shows assignments of amide I positions to secondary structure of proteins [198].

Table 2.3: Frequencies for secondary structure assigned from amide I band [199].

Secondary structure	Band position in ^1H_2O, cm^{-1}		Band position in ^2H_2O, cm^{-1}	
	Average	Extremes	Average	Extremes
α-helix	1654	1648-1657	1652	1642–1660
Parallel β-sheet	1633	1623-1641	1630	1615–1638
Antiparallel β-sheet	1684	1674-1695	1679	1672–1694
Turns	1672	1662-1686	1671	1653–1691
Disordered	1654	1642-1657	1645	1639–1654

The α-helical structure appears in the 1648-1657 cm^{-1} range, β-sheets have peaks at 1623-1641 and 1674-1695 cm^{-1}. Random coil structure has an average at around 1654 cm^{-1} (in ^1H_2O). A fundamental problem of the assignment of secondary structure is that it is not straightforward [196]. α-helices overlap with random coils in ^1H_2O. It can lead to mistakes for proteins with high α-helical content [200]. The major problem is that in an aqueous solution individual bands of protein secondary structure bands overlap with the H_2O bending mode. By using D_2O this problem can be solved. However, this might also have an effect on protein secondary structure [201]. Modern Fourier transform spectrometers include a function for water subtraction. However, this procedure should be performed carefully to avoid signal over-subtraction and not lose valuable information in the amide I band [198]. Despite all the advantages of infrared spectroscopy to study proteins, it is challenging to assign correctly obtained bands due to interaction with lipids, protein buffers, other molecules and water contributions. It is possible to overcome these problems by introducing deuterated solvents, infrared labelling and working with infrared difference spectra.

2.4.5 Fourier Transform Infrared Spectroscopy (FTIR)

Fourier Transform Infrared Spectroscopy (FTIR) is a common form of infrared spectroscopy. An FTIR spectrometer collects spectral data of high resolution over a wide spectral range. The term originates from the mathematical operation Fourier transform that allows the transfer of raw spectrum to the actual spectrum [202]. Fourier Transform spectrometer uses a polychromatic beam of light containing many frequencies. The core of an FTIR spectrometer is a Michelson interferometer which consists of two perpendicular mirrors and a beam splitter [203]. One mirror is stationary, and another one is moving. The beam splitter splits the beam into two parts: one goes

to the movable mirror, and the other is reflected in a fixed mirror. The two beams reflected from the mirrors are recombined at the beam splitter, generating an interference pattern that is transmitted to the detector. The signal is subjected to the the Fourier Transformation function, and a spectrum is generated [204]. Fourier transform infrared spectroscopy has three main advantages over dispersive infrared spectroscopy:

1. Fellgett's advantage - all the resolution elements are measured at all times during the measurements. It takes less time to collect a spectrum.
2. Jacquinot's advantage - the increase of throughtput of FTIR devices compared to traditional spectrometers that need slits to achieve resolution.
3. Conne's advantage - the resolution is more extensive, enabling spectral subtraction [205].

The advantages of FTIR spectroscopy are the quality of spectra that can be rapidly obtained with a high signal-to-noise ratio. Some minor disadvantage of using FTIR spectrometers is sensitivity to changes in atmospheric conditions [206]. Modern spectrometers are purged with dry gas to reduce the contribution of water molecules from the environment.

In FTIR spectrometers, different radiation sources and beam splitters are used depending on the range of infrared needed. However, FTIR has found a wide application in mid-IR. Figure 2.15 show the schematic representation of a FTIR spectrometer.

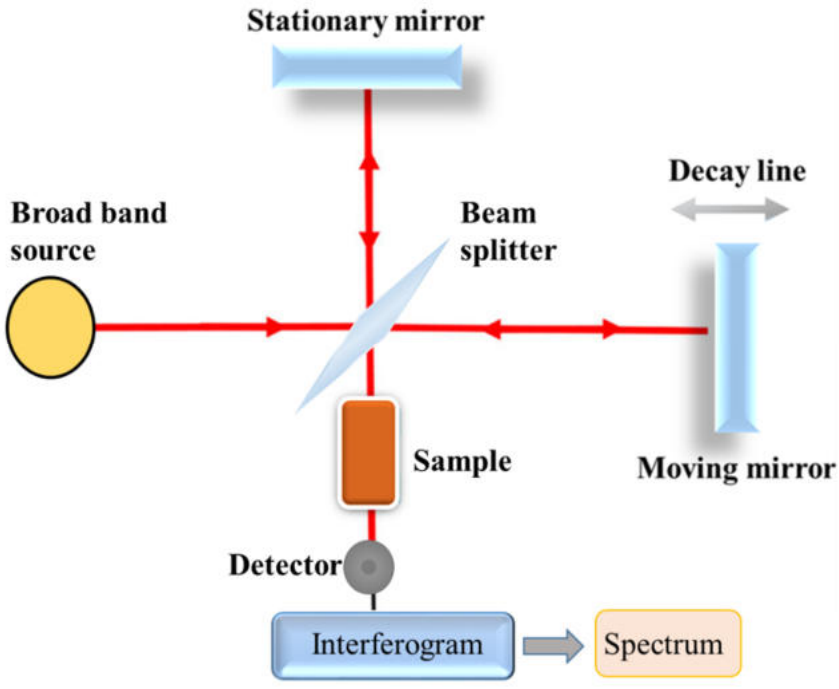

Figure 2.15: Schematic representation of a FTIR spectrometer. Reproduced from [207].

Attenuated Total Reflectance (ATR) in FTIR spectroscopy has become the primary sampling method for FTIR spectroscopy. It uses the phenomenon of total internal reflection. The angle of incidence of an interface between the sample and the crystal is bigger than the critical angle, so all incidents rays go through total internal reflection. This reflection forms an evanescent wave which extends into the sample. The depth of penetration is calculated according to the following equation:

$$d_p = \frac{\lambda}{2\pi\sqrt{n_1^2 \sin^2 \Theta - n_2^2}} \tag{7}$$

where d_p is the penetration depth, n_2 is the crystal's refractive index, Θ is the angle of incident radiation, n_1 is the sample's refractive index, λ is the function of wavelength.

Figure 2.16 shows a schematic representation of the ATR principle.

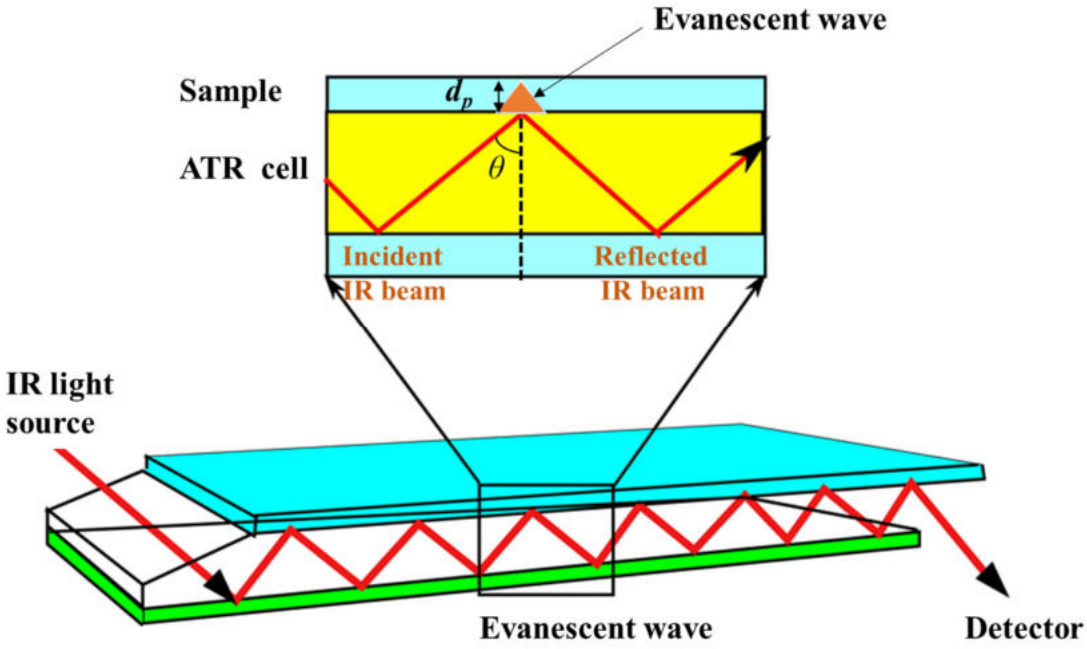

Figure 2.16: Schematic representation of the ATR principle. Reproduced from [208].

In ATR, crystals with a high refractive index are used. The most common crystals are diamond, zinc selenide, silicon and germanium. Attenuated Total Reflection Fourier Transform Infrared (ATR-FTIR) is a non-destructive technique that can be used to determine protein content and protein secondary structure composition [209].

2.4.6 Surface Enhanced Infrared Absorption Spectroscopy (SEIRAS)

Surface Enhanced Infrared Absorption Spectroscopy (SEIRAS) represents a variation of infrared spectroscopy. Detecting the signal from the protein monolayer using FTIR is challenging as the signal strength is low. The absorption of light by molecules, however, can be enhanced when they are located near the rough nanostructured metal surface [210]. The metal film structure is designed to show broad and intense absorption in the mid-IR enhanced at specific frequencies resonant with the transition dipole moments of vibrations from the nearby molecules. Typically, gold is used for SEIRAS experiments. Using SEIRAS, the adsorbed monolayer on nanostructured metal film provides a signal enhancement factor of 100-500 [211]. The absorption enhancement is restricted to the molecules near the metal surface [212], and it arises from a local electromagnetic field enhancement, due to the excitation of plasmons at the surface of the metal [213]. The short range of the enhancement is particularly beneficial for studying protein monolayers in contact with bulk water as the absorption of proteins and not the one of bulk water is enhanced [214]. An essential feature of SEIRAS is the surface selection rule. Bands that arise from vibrations with a transition dipole moment perpendicular to the metal surface are the most enhanced, while those parallel to the surface are not enhanced at all [215]. SEIRAS is commonly used in combination with ATR. A silicon crystal is mainly used because of its refractive index and stability. The gold nanostructured surface morphology deposited on silicon critically affects the enhancement and reproducibility of protein signals in the infrared spectra [216]. Generally, a gold film with a thickness of 10-200 nm is formed on the surface of silicon crystal after gold deposition. Afterwards, the gold surface can be chemically modified to allow the binding of proteins [214]. The immobilization of membrane proteins on the surface is more complex than that of soluble proteins. Proteins can adsorb on the surface through different interactions, such as electrostatic, hydrogen bonds and hydrophobic interactions [217]. One major challenge is controlling the protein orientation on the surface [218]. Figure 2.17 shows a complex I immobilization approach.

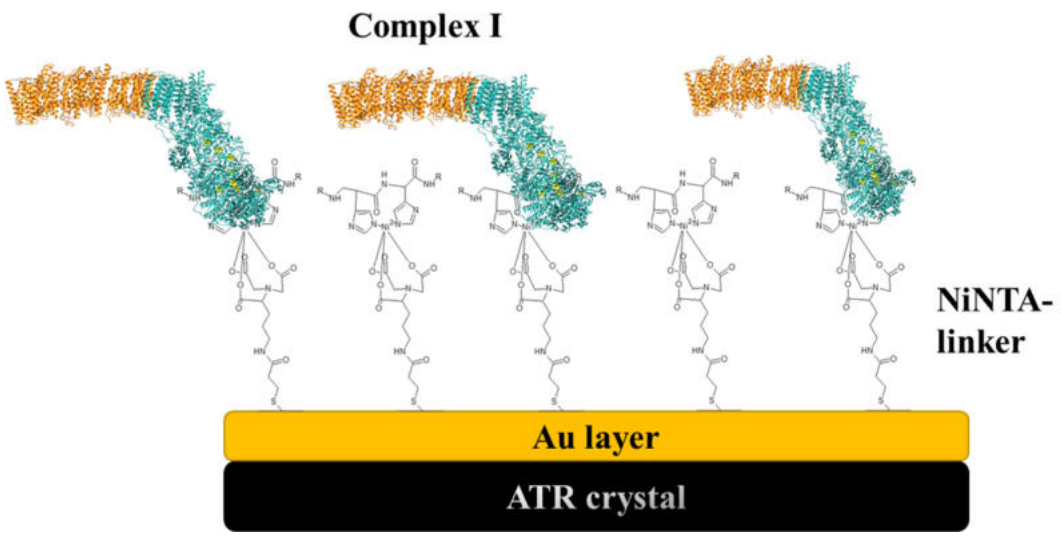

Figure 2.17: Complex I immobilization on SAM (self assembled monolayer).

Complex I can be successfully immobilized on the Au layer using the Ni-NTA-SAM approach and studied by SEIRAS [219]. The most common strategy for protein immobilization is a genetic introduction of a His-tag on the protein surface that selectively binds to a nickel chelating nitrilotriacetic acid Ni-NTA self-assembled monolayer (SAM) created on a gold-modified surface [204]. An immobilizing agent can be synthesized directly on the surface. Protein immobilization based on this technique is highly versatile [205]. The modified surface is produced by immersing the metal surface in the solution that contains a cross-linker molecule. The SAM of the cross-linker is formed spontaneously, based on the quasi-covalent binding of the sulfur atom to the metal surface [202]. After the linker with Ni^{2+} is formed, a protein with the His-tag can be attached to the surface through its His-tag [220]. His-tags are usually used for protein purification, which makes them accessible for this kind of interaction [206]. The His-tag immobilization with Ni-NTA has the advantage of directing the protein orientation on the surface [221]. The affinity of His-tag to Ni-NTA is usually low. However, due to the high density of immobilized Ni-NTA, multiple linkages can provide higher affinity [207].

2.4.7 SCN labelling

A spectroscopic reporter that can monitor conformational changes, binding and folding in proteins is very important in complex protein studies. There is an interest in non-natural functional groups that can provide structural specificity, and that react to the local environmental changes.

Fluorophores, such as dyes, that have been used for these purposes are large relative to the size of amino acids [222]. As a result, attachment of the fluorophores to the protein molecules can cause undesirable perturbations leading to changes in the native structure. The SCN^- group is an attractive infrared probe due to its smaller size, compared to other site-directed probes, such as, for example, nitroxide spin label. Thiocyanates have been shown as attractive IR probes as they can be easily incorporated into proteins without perturbing their structure [223]. The nitrile group can serve as an atomic substitution within an amino acid side chain [224]. The nitrile group has a polarity between the amide group and methylene, so it can be introduced in the hydrophobic interior of the protein as well as on the hydrophilic surface of water-soluble protein [223].

The frequency of the stretching mode appears in a region of the IR spectrum (ν(C≡N) ~ 2100-2240 cm^{-1}) that is not prone to overlap with other signals [225]. Experiments indicated that the C≡N stretching mode of an aliphatic thiocyanate is quite sensitive to particular dynamics, solvent polarity and H-bond properties [209]. Its stretching frequency is influenced by hydrogen-bonding interactions, σ-bonding and π-bonding of water [9]. The frequency of the SCN band depends on the character of the hydrogen bond in the local environment, the frequency undergoes a blue shift upon accepting a hydrogen bond (or σ-bond from the water molecule) at the nitrogen [7]. The interaction of water molecules with π-bond from SCN will lead to a red shift [7]. Studies have proved that nitriles are good candidates for studying various types of interactions regarding environmental changes. It is well-known that acetonitrile stretching vibration C≡N is sensitive to the solvent [226]. It was found that the CN stretching mode of the acetonitrile vibration had a maximum of 2260 cm^{-1} in water and 2252 cm^{-1} in THF [227].

Cyanoalanine and cyanophenylalanine are useful reporters to monitor electrostatic changes in the environment [223, 228, 229]. These C≡N modified amino acids showed bands at different spectral positions according to the solvent. Phe_{CN} has a band with the center at 2237 cm^{-1}, whereas in THF it shifts to 2228.5 cm^{-1}. Similar spectral behavior was recorded for Ala_{CN} [223]. Methyl thiocyanate was dissolved in different solvents, and the resulting IR spectra were compared. Figure 2.18 shows the different IR absorbances of KSCN towards different solvents.

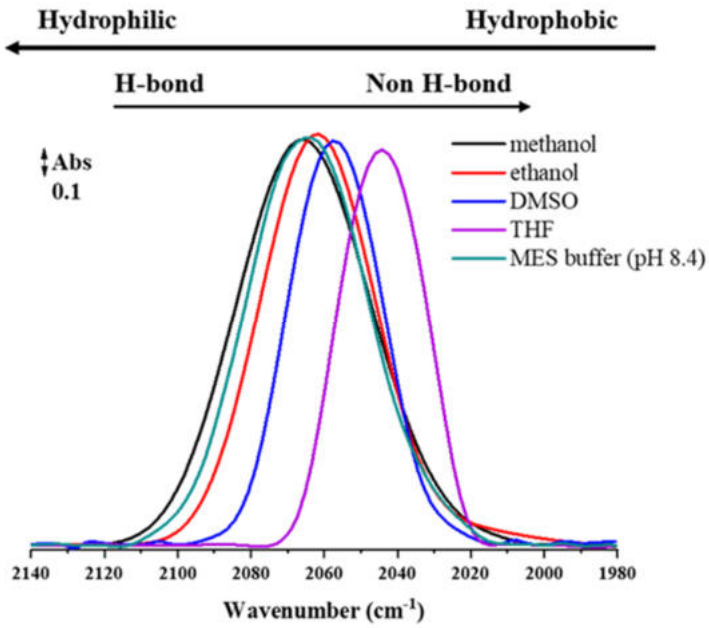

Environment	Frequency, cm^{-1}
Methanol	2066
Ethanol	2061
DMSO	2057
THF	2044
MOPS buffer, pH 7.0	2064

Figure 2.18: IR absorbance spectrum of KSCN dissolved in methanol (black), ethanol (red), DMSO (blue), THF (violet) and MOPS buffer (green) (pH 7.0) Reproduced from [9]**.**

Depending on the solvent, experimental line widths of SCN bands varied from 8.5 to 13.2 cm^{-1}. A clear dependence of CN line shape on solvent dynamics was observed [207]. The line width of the signal depends on the structural heterogeneity of the probe's environment and fluctuations in the time scale of that environment. For the solvent-exposed group, it depends only on solvent dipolar fluctuations [230]. The line width of the groups that are not solvent-exposed is evidence of the local distribution of the probe environment [231]. It has been shown that local helical secondary structure leads to a broadening of SCN signal due to faster water motions around the structure [232]. The Stark effect was found to influence signal's line width. The full width at half maximum (fwhm) is the parameter that can characterize changes in line width of the shape. The vibrational lifetime of the SCN group is quite long [233]. It must be admitted that the signal strength of these bands is weak.

Nitrile probes found a wide application not only applied to IR spectroscopy or 2D IR but also as probes of electric field used in vibrational Stark effect spectroscopy (VSE) [230]. VSE refers to the position of the peak in the IR spectrum caused by an external electric field.

In biologically relevant environments the signal of SC≡N appears in the IR spectrum at around 2153-2164 cm^{-1} [7]. Relatively few functional groups naturally present in proteins or DNA can absorb in this region of the IR spectrum [231].

Nitrile probes have found application in studies of ligand binding. They showed sensitivity to the nature of bound ligands and changes in the local electric field [232]. Nitrile-derivatized amino acids can be used to provide detailed information about peptide-membrane interaction, hydration state and orientation of individual side chains [233]. Nitrile groups found an application in various kinds of studies applied to biological molecules [234–236], as, for example, they were used to probe the structure of amyloid fibers [237], to examine the binding of anesthetic halothane to a protein [238] or probe the dynamics of an HIV-1 reverse transcriptase inhibitor [239]. They can be used to study DNA structural changes and site-specificity. It was demonstrated by labelling model DNA oligomers that the coupling between two nitrile groups is strong [240].

Nitriles must be either incorporated into proteins synthetically or through novel expression approaches. One of the approaches is by using a post-translational chemical modification of cysteines that can be placed into protein by site-directed mutagenesis [241]. It was reported that cysteine residues can be cyanylated directly and selectively under very mild conditions [242, 243]. The conversion of cysteines to thiocyanates occurs in reaction with Ellman's reagent (DTNB) where the mixed protein nitrobenzoic acid disulfide (PS-TNB) is being formed. It is displaced by cyanide (CN^-) to form thiocyanate [241]. The electronic absorbance of (TNB) anion byproduct is monitored at 412 nm and its molar extinction coefficient is 13'600 $M^{-1}cm^{-1}$ [244].

The versatility and scope of this method were checked using different systems. Cyanylated cysteine derivatives were obtained, for example, in the S-peptide bound to ribonuclease S-protein (RNase S), the human aldose reductase (*h*ALR2), which has multiple cysteine residues and a multi-subunit, integral membrane protein, and the bacterial photosynthetic reaction center (RC) [241]. It was observed that some obtained PS-CN samples were stable while stored at 4°C for 4 days at pH 7 [245].

The S-peptide was synthesized, modified with a nitrile label and attached to S-protein to form labeled RNase S complex. This process was visualized by recording a shift of the SCN band from 2161 cm^{-1} (for a labelled peptide) to 2155 cm^{-1} for the obtained complex. For human aldose reductase (*h*ALR2), it was possible to reach the selective nitrile labelling on the active site, which appeared at 2159 cm^{-1} in the FTIR spectrum, producing a narrow peak. Further reaction over a longer time with an excess of reagents resulted in the appearance of an additional peak at 2151 cm^{-1}, the area under the initial peak increased, and the absorbance was higher [241]. The final test was conducted with the RC where the native cysteines were removed, a single cysteine was

introduced and labelled with two isotopic labels –S^{13}CN and –S^{12}CN, appearing at different wavenumbers at 2110 and 2159 cm^{-1}, respectively, with the equal intensity [241]. This is an example of selective isotopic labelling of cysteines in a protein.

In one of the studies, dynamics of CN^- ligated cytochrome *c* (CytCN) was followed in D_2O and two bands (one main band (82%) at 2122 cm^{-1} with a 23cm^{-1} fwhm and the other (18% at 2116 cm^{-1} with a 7 cm^{-1} fwhm) were recorded [246]. Frequency shifts of the SC≡N stretching mode indicated changes in water exposure at specific protein sites bound to membranes and other proteins and in a dynamically opening enzymatic active site [247, 248].

The absorbance of nitrile is narrow and intense, and nitrile groups are also chemically stable [212]. Thus, nitrile-derivated amino acids have become valuable infrared environmental probes due to the sensitivity of vibrations.

2.5 Aim of research

Complex I from *E. coli* belongs to one of the functionally well-characterized enzymes that couples the transfer of two electrons with the translocation of four protons across the membrane. However, the exact coupling of these two processes is still under debate. The membrane arm of complex I comprises a central axis of conserved titratable amino acids that are assumed to play an important role in proton translocation. One theory proposes the presence of four proton pathways, each translocating one proton across the membrane. This process is driven by an electric wave that propagates along the membrane arm causing conformational changes that enable proton translocation. Another theory, the so called “ND-5 only”, states that all four protons are translocated only by the distal subunit NuoL, while the other subunits of the membrane arm e.g. NuoM are not participating in this process.

This research aims to study conformational changes occurring in NuoM that might be involved in proton translocation. To indirectly detect these changes, an infrared nitrile should be inserted at distinct positions in close proximity of the putative proton pathway. Nitrile labels are attractive IR probes as they do not overlap with protein signals. These labels are sensitive towards hydrogen bond interactions making it possible to follow reaction-induced conformational changes. Cysteine residues were introduced at individual positions in NuoM that were activated and labelled with cyanides. IR spectra of the labelled variants should be obtained by surface-enhanced IR absorption spectroscopy (SEIRAS). Reduction of complex I with NADH and subsequent re-oxidation of the

same sample with ubiquinone should indicate possible conformational changes around mutated positions. Conformational changes along the putative proton pathway should help to clarify whether NuoM is involved in proton translocation.

In a second project, the role of two conserved amino acid residues for activity of cytochrome *bd*-I oxidase should be determined. Cytochrome *bd*-I has a heterotetrameric structure, build up by two major subunits, CydA and CydB, and two small subunits, CydX and CydY. Subunit CydA contains heme b_{558}, heme b_{595} and heme *d* cofactors. The ligands of these heme groups were identified by biochemical, spectroscopic, and structural studies. They play a crucial role for the redox potential of the hemes and their reactivity towards oxygen. Based on reaction-induced FTIR difference spectroscopy, it was shown that these residues have unusually high pK_a values. Various mutations should be generated to determine the role of two acidic amino acids that are ligands to hemes. The generated mutations should be characterized by biochemical methods and an electrochemical characterization should be performed. The pK_a value of these acidic residues might reveal important informations about the reaction mechanism and the physiological role of cytochrome *bd*-I.

3 Material and Methods

3.1 Chemicals

All chemicals used in this work are listed in Table 3.1.

Table 3.1: Index of chemicals.

Chemical	Manufacturer
Acetic acid, 100%	VWR
Acetone (technical)	Institute's stocks
Acrylamide/Bisacrylamide (29:1; w/w)	Serva
Agar *for bacteriology*	BioFroxx
Agarose *low* EEO	BioFroxx
9-Amino-6-chloro-2-methoxyacridine (ACMA)	Sigma Aldrich
Ammonium chloride (NH_4Cl)	Acros Organics
Ammonium fluoride (NH_4F)	Acros Organics
Ammonium persulfate (APS)	Merck
Ampicillin, sodium salt	AppliChem
L-(+)-Arabinose	Roth
Bovine serum albumin (BSA)	Sigma
Calcium chloride dihydrate ($CaCl_2 \cdot 2\ H_2O$)	Fluka
Carbonyl cyanide 3-chlorophenylhydrazone (CCCP)	Sigma Aldrich
Nα,Nα-bis(carboxymethyl)-L-lysine (ANTA)	Merck
Casein (hydrolyzed)	Roth
Chloramphenicol	Roth
Chloroform	J.T. Baker
Coomassie Brilliant Blue R250 (CBB R-250)	Serva
Copper sulfate pentahydrate ($CuSO_4 \cdot 5\ H_2O$)	Grüssing
L-Cysteine	Applichem
Dimethyl sulfoxide (DMSO)	Carlo Erba Reagents
Deoxynucleoside triphosphate mix (dNTPs)	ThermoScientific
5,5-dithiobis-(2-nitrobenzoic acid) (DTNB)	Sigma
3,3-dithiodipropionic acid di-(N-hydroxysuccinimide ester) (DTSP)	Sigma

Table 3.1; continued.

DNase I	AppliChem
n-Dodecyl-*β*-D-maltopyranoside (DDM)	AppliChem
Dithiothreitol (DTT)	Gerbu
E. coli polar lipids (powder or chloroform extract, 25 mg/mL)	Avanti Polar Lipids
Ethanol, abs. (EtOH)	VWR
Ferric ammonium citrate (Fe-NH_4-citrate, 14.5-16% (w/w) Fe)	Sigma-Aldrich
GeneRuler 1 kB Plus DNA Ladder	Thermo Scientific
Glucose monohydrate	Roth
Glycerol, 98%, p.a.	Roth
Hexanoic acid (C_6)	Sigma-Aldrich
Hydrochloric acid (36%; v/v)	VWR
Hydrofluoric acid (HF)	Sigma-Aldrich
4-(2-Hydroxyethyl)-1-piperizineethanesulfonic acid (HEPES)	Gerbu
Imidazole	AppliChem
Isopropanol	VWR
Isopropyl-β-D-thiogalactopyranoside (IPTG)	Roth
Kanamycin sulfate	Roth
Lauryl-maltose-neopentyl-glycol (LMNG) (2,2-didecylpropane-1,3-bis-*β*-D-maltoside)	Anatrace
Loading Dye 6×	Thermo Scientific
Magnesium dichloride hexahydrate ($MgCl_2 \cdot 6\ H_2O$)	Sigma-Aldrich
Magnesium sulfate heptahydrate ($MgSO_4 \cdot 7\ H_2O$)	VWR
2-Mercaptoethanol (EtSH)	Roth
Methanol (MeOH)	Carlo Erba Reagents
MilliQ (deionized (dd) H_2O)	Institute's stock
2-*N*-(Morpholino)ethanesulfonic acid (MES)	BioFroxx
3-*N*-(Morpholino)propanesulfonic acid (MOPS)	BioFroxx
Nickel(II) perchlorate hexahydrate ($Ni(ClO_4)_2 \cdot 6\ H_2O$)	Sigma Aldrich
Nicotinamide adenine dinucleotide, di-sodium salt (NADH)	Roth
n-Octylglucoside (Octyl-*β*-D-Glucopyranoside)	Sigma-Aldrich

Table 3.1; continued.

Peptone from Casein (pancreatic digest)	Roth
Phenylmethanesulfonic fluoride (PMSF)	Roth
L-α-Phosphatidylcholine	Sigma
Potassium carbonate (K_2CO_3)	VWR
Potassium chloride (KCl)	Merck
Potassium cyanide (KCN)	Merck/Sigma
Potassium dihydrogenphosphate ($KH_2PO_4 \cdot 2H_2O$)	Fisher Chemicals
Potassium hexacyanoferrate(III) ($K_3[Fe(CN)_6]$)	AppliChem
Potassium hydroxide (KOH)	Sigma-Aldrich
Potassium iodide (KI)	Merck
Riboflavin (Vitamin B_2)	BioFroxx
RNase A	AppliChem
D-(+)-Saccharose	Roth
Sephadex G-50	Sigma-Aldrich
Serdolit MB	Roth
Sodium chloride (NaCl)	VWR
Sodium cholate	Sigma-Aldrich
Sodium dithionite ($Na_2S_2O_4$)	Merck
Sodium dodecyl sulfate (SDS)	Serva
di-Sodium hydrogenphosphate dihydrate ($Na_2HPO_4 \cdot 2\ H_2O$)	Roth
Sodium hydroxide (NaOH)	Serva
Sodium potassium tartrate tetrahydrate (Seignette salt)	Grüssig
Sodium sulfate (Na_2SO_4)	Roth
Sodium sulfite (Na_2SO_3)	Sigma-Aldrich
Sodium tetrachloroaurate(III) ($NaAuCl_4 \cdot 2\ H_2O$)	Merck
Sodium thiosulfate-5-hydrate	Riedel-de Haën
SYBR Green	Sigma
Tetramethylethyldiamine (TEMED)	Sigma
Trichloroacetic acid (TCA)	Riedel de Haën
Tris(hydroxymethyl)-aminomethane (Tris)	Roth

Table 3.1; continued.

N-Tris-(hydroxymethyl)-methyl-glycine (Tricine)	Roth
L-Tryptophan	Merck
Unstained Protein Molecular Weight Marker	Thermo Scientific
Ubiquinone 0 (Q_0)	Sigma-Aldrich
Ubiquinone 2 (Q_2)	Sigma-Aldrich
Ubiquinone 10 (Q_{10})	Sigma-Aldrich
Yeast extract	AppliChem

3.2 Oligonucleotides

DNA oligonucleotides that were used in this work are listed in Tables 3.2-3.5. All oligonucleotides were ordered from Merck, formerly Sigma-Aldrich.

Table 3.2: DNA-oligonucleotide sequence for the site-directed mutagenesis of *nuoM*. Newly generated codons are depicted in bold and exchanged bases are shown in red. To prove the newly generated mutation by restriction analysis, silent mutations were introduced. The restriction sites are underlined and exchanged bases are shown in red. The corresponding restriction enzymes are listed, but not the complementary reverse oligonucleotides. The oligonucleotides were HPLC purified.

Oligonucleotide	**Sequence**	**Restriction enzyme**
nuoM_D258C_fwd	5'-CGACCGCCGGTTCCGTT**TG**CCTCGCGGGAATTC TGCTGAAAACTGCCGC-3'	EcoRI
nuoM_E108C_fwd	5'-GTACTATGTTCGTGGAAA**TGC**ATCGAAAAATAT CAGGGC-3'	NsiI
nuoM_H117C_fwd	5'-GAAAAATATCAGGGCTTCTTC**TGT**TTAAACCTG ATGTGGATCCTG-3'	DraI
nuoM_H159C_fwd	5'-CTGATCGCACTGTGGGGG**TGT**AAAGCTTCTGAC GGTAAAACGCG-3'	HindIII
nuoM_K234C_fwd	5'-CTTCTTCATCGCCTTCGCAGTC**TGT**ATGCCGGT GGTACCGCTGCATGG-3'	KpnI
nuoM_S105C_ fwd	5'-CGGTGTGCTAGCGGTACTATGT**TGC**TGGAAAGA GATCGAAAAATATC-3'	NheI
nuoM_S414C_ fwd	5'-GAATTTATGATTCTGTTCGGC**TGC**TTCCAGGTG GTACCGGTGATTACCGTTATC-3'	KpnI
nuoM_S425C_fwd	5'-GTACCGGTGATTACCGTCATA**TGT**ACCTTTGGG CTGGTCTTTGC-3'	NdeI
nuoM_T178C_fwd	5'-GCAACCAAGTTCTTCATTTAC**TGC**CAAGCTTCT GGCCTGGTGATGTTGATTG-3'	HindIII
nuoM_T332C_fwd	5'-GTTTCCCACATGGGCTTCGTATTAATTGCTATCT AC**TGC**GGCAGCCAGTTGGCCTAC-3'	VspI

Table 3.2; continued.		
nuoM_T422C_fwd	5‘-CTTCCAGGTTGTACCGGTCATATGCGTTATCTC TACCTTTGGGCTG-3’	NdeI

Table 3.3: DNA-oligonucleotide sequence for the site-directed mutagenesis of other *nuo*-genes. Newly generated codons are depicted in bold and exchanged bases are shown in red. The restriction sites are underlined and exchanged bases are shown in red. The corresponding restriction enzymes are listed; oligonucleotides were HPLC purified.

Oligonucleotide	Sequence	Restriction enzyme
nuoCD_H355A_fwd	5’-GTGGAAGCAATCACTGGTTTTCGAATGGCG CCGGCGTGGTTCCGTATTGG-3’	-
nuoCD_H355M_fwd	5’- GAAGCAATCACTGGTTTCCGTATGATGCCG GCGTGGTTCCGTATTGG -3’	-
nuoI_C74A_fwd	5’- CGCGGTAGCCTGCCCGGTCGGCGCCATCTC GCTGCAAAAAGCAGAAAC -3’	EheI
nuoI_C74S_fwd	5‘-GTAGCCTGCCCGGTCGGCTCTATAAGCTTG CAAAAAGCAGAAACCAAAGACGG-3’	HindIII
nuoG_A582C_fwd	5‘-CGCTTCTGCTATCCGCGTGAATTGCGCGCT AGCTAAAGCACCGCTGGTGATGG-3’	NheI

Table 3.4: DNA-oligonucleotide sequence for the site-directed mutagenesis on the plasmid of *cydA*. Newly generated codons are depicted in bold and exchanged bases are shown in red. The restriction sites are underlined and exchanged bases are shown in red. The oligonucleotides were HPLC purified.

Oligonucleotide	Sequence	Restriction enzyme
cydA_E99D_fwd	5’-CTTCGGTGCGCCGCTGGCGATCGACGGTCTGAT GGCCTTCTTC-3’	PvuI
cydA_E99Q_fwd	5’-CTTCGGTGCGCCGCTGGCAATCCAAGGATTAAT GGCCTTCTTCCTCGAATC-3’	VspI
cydA_E107D_fwd	5’-GGTCTGATGGCCTTCTTTCTAGACTCCACCTTTG TAGGTCTGTTC-3’	XbaI
cydA_E107Q_fwd	5‘-GGTCTGATGGCCTTCTTCCTCCAGTCGACCTTTG TAGGTCTGTTC-3’	SalI
cydA_E445D_fwd	5‘-GAAGCGGGCTGGTTCGTGGCTGATTATGGGCGC CAACCGTGGGCTATC-3’	EheI
cydA_E445Q_fwd	5‘-GAAGCGGGCTGGTTCGTGGCTCAATATGGGCGC CAACCGTGGGCTATC-3’	EheI
cydA_R448N_fwd	5‘-CTGGTTCGTGGCTGAATATGGCAACCAACCATG GGCTATCGGTGAAGTG-3’	NcoI

Table 3.5: DNA-oligonucleotide sequence to sequence the pBAD*nuo* plasmid. Oligonucleotides were purified by desalting.

Oligonucleotide	Mutations	Sequence
Seq-pBAD-25	nuoM_E108, S105	5‘-GAGAACGGCTATCTGCGCTG-3’

Table 3.5; continued.		
Seq-pBAD-25a	nuoM_H159, H117, T178, D258, K234	5‘-GCTGGATCGCGCTGATCAC-3’
Seq-pBAD-26	nuoM_S414, T332, T422, S425	5‘-CGATGTACTTCCTGATCGCAC-3’
Seq-pBAD-10	nuoCD_H355A, H355M	5‘-TCTATCGATCGTAACCGCGAC-3’
Seq-pBAD-16a	nuoG_A582	5‘-CAGGCTGTGAAAGGTAAAGC-3’
Seq-pBAD-19a	nuoI_C74A, C74S	5‘-GTTGCCGACCTGAACATCGG-3’

3.3 Plasmids

Plasmids used in this work, their characteristics and references are listed in tables 3.6 and 3.7.

Table 3.6: pBAD plasmids, characteristics, and references.

Plasmids	Genotype	Reference
pBAD*nuo* His*nuoF*	cam^R, ori_{p15a}, *araC*, P_{araBAD}, *nuoA-N*, *his6-nuoF*	[249]
pBAD*nuo* *His*nuoF nuoCD* H355A	pBAD*nuo nuoF*$_{His}$, *nuoCD* H355A	This work
pBAD*nuo* *His*nuoF nuoCD* H355M	pBAD*nuo nuoF*$_{His}$, *nuoCD* H355M	This work
pBAD*nuo* *His*nuoF nuoG* A582C	pBAD*nuo nuoF*$_{His}$, *nuoG* A582C	This work
pBAD*nuo* *His*nuoF nuoI* C74A	pBAD*nuo nuoF*$_{His}$, *nuoI* C74A	This work
pBAD*nuo* *His*nuoF nuoI* C74S	pBAD*nuo nuoF*$_{His}$, *nuoI* C74S	This work
pBAD*nuo* *His*nuoF nuoM* E108C	pBAD*nuo nuoF*$_{His}$, *nuoM* E108C	This work
pBAD*nuo* *His*nuoF nuoM* H117C	pBAD*nuo nuoF*$_{His}$, *nuoM* H117C	This work
pBAD*nuo* *His*nuoF nuoM* H159C	pBAD*nuo nuoF*$_{His}$, *nuoM* H159C	This work
pBAD*nuo* *His*nuoF nuoM* K234C	pBAD*nuo nuoF*$_{His}$, *nuoM* K234C	This work
pBAD*nuo* *His*nuoF nuoM* S105C	pBAD*nuo nuoF*$_{His}$, *nuoM* S105C	This work
pBAD*nuo* *His*nuoF nuoM* S414C	pBAD*nuo nuoF*$_{His}$, *nuoM* S414C	This work
pBAD*nuo* *His*nuoF nuoM* S425C	pBAD*nuo nuoF*$_{His}$, *nuoM* S425C	This work
pBAD*nuo* *His*nuoF nuoM* T178C	pBAD*nuo nuoF*$_{His}$, *nuoM* T178C	This work
pBAD*nuo* *His*nuoF nuoM* T332C	pBAD*nuo nuoF*$_{His}$, *nuoM* T332C	This work

Table 3.6; continued.		
pBAD*nuo* $_{His}$*nuoF nuoM* T422C	pBAD*nuo nuoF*$_{His}$, *nuoM* T422C	This work

Table 3.7: pET plasmids, characteristics, and references.

Plasmids	**Genotype**	**Reference**
pET28b(+) *Ec_cydA*$_h$*BX*	P_{T7} *ori*$_{pBR322}$ *Kan*^{r} *Ec_cydA*$_{his}$ *Ec_cydB Ec_cydX*	[153]
pET28b(+) *Ec_cydA*$_h$*BX cydA* E99D	pETcydABX	This work
pET28b(+) *Ec_cydA*$_h$*BX cydA* E99Q	pETcydABX	This work
pET28b(+) *Ec_cydA*$_h$*BX cydA* E107D	pETcydABX	This work
pET28b(+) *Ec_cydA*$_h$*BX cydA* E107Q	pETcydABX	This work
pET28b(+) *Ec_cydA*$_h$*BX cydA* E445D	pETcydABX	This work
pET28b(+) *Ec_cydA*$_h$*BX cydA* E445Q	pETcydABX	This work
pET28b(+) *Ec_cydA*$_h$*BX cydA* R448N	pETcydABX	This work

3.4 Bacterial strains

E. coli strains, their characteristics and references are listed in Table 3.8.

Table 3.8: *E. coli* strains, genotypes, and references.

Strain	**Genotype**	**Reference**
BW25113	Δ(araD-araB)567 ΔlacZ4787(::rrnB-3) λ$^-$ rph-1 Δ(rhaD-rhaB)568 hsdR514	[249]
BW Δ*ndh nuo::nptII*_FRT (abbreviated as BWΔΔ in this work)	BW25113, Δ*ndh*, *nuo::nptII_FRT*	[250]
DH5α	F$^-$ Φ80*lacZ*ΔM15 Δ(*lac*ZY A-*arg*F) U169 *recA1 endA1 hsdR17* (rk$^-$ mk$^+$) *gal- phoA supE44* λ- *thi-1 gyrA96 relA1*	Invitrogen
DH5α *Δnuo*	DH5α, *Δnuo*	[90]
CBO	F$^-$ *ompT hsdS*$_B$ (r$_B$-m$_B$-) *gal dcm* λ(DE3)Δ(*cyd-app*) + unknown mutations	[153]
BL21*(DE3) Δ*cyo*A-D	F$^-$ *ompT hsdS*$_B$ (r$_B$-m$_B$-) *gal dcm rne131* (DE3) Δ*cyoA-D*	S. Oppermann, unpubl. data

3.5 Enzymes, media, solutions, buffers and columns

Enzymes, media, solutions and buffers used in this work are listed in tables 3.9-3.17.

Table 3.9: Restriction enzymes, their working temperatures, concentrations and manufacturer. The enzymes were all used in concentration of 10 U/µL at 37°C optimal temperature. They were all from Thermo Fischer Scientific.

Enzyme	Buffer	Manufacturer
DpnI	Tango	Thermo Fischer Scientific
DraI	Tango	Thermo Fischer Scientific
EcoRI	EcoRI	Thermo Fischer Scientific
EheI	Tango	Thermo Fischer Scientific
HindIII	R	Thermo Fischer Scientific
KpnI	KpnI	Thermo Fischer Scientific
NcoI	Tango	Thermo Fischer Scientific
NdeI	O	Thermo Fischer Scientific
NheI	Tango	Thermo Fischer Scientific
NsiI	R	Thermo Fischer Scientific
PvuI	R	Thermo Fischer Scientific
SalI	O	Thermo Fischer Scientific
VspI	O	Thermo Fischer Scientific
XbaI	Tango	Thermo Fischer Scientific

Table 3.10: Media for bacterial cultivation and their components.

Medium	Components	Concentration
LB medium	Yeast extract Peptone NaCl	0.5% (w/v) 1% (w/v) 1% (w/v)
LB agar plates	LB medium with agar	2% (w/v)
eM9 medium	Na_2HPO_4 KH_2PO_4 NaCl NH_4Cl	0.6% (w/v) 0.3% (w/v) 0.05% (w/v) 0.1% (w/v)
eM9 medium additives	$CaCl_2$ $MgSO_4$ Caseine Tryptophane Glycerol Thiamine hydrocloride	0.1 mM 1 mM 0.1% (w/v) 5‰ (w/v) 25 mM 100 µg/mL
SOC medium	Yeast extract Peptone NaCl KCl $MgSO_4$ $MgCl_2$ Glucose	0.5% (w/v) 2% (w/v) 10 mM 2.5 mM 10 mM 10 mM 20 mM

Table 3.10; continued.		
Autoinduction medium	Yeast extract	0.5% (w/v)
	Peptone	1% (w/v)
	Glycerol	0.4% (w/v)
	Glucose	0.05% (w/v)
	L-Arabinose	0.2% (w/v)
	KH_2PO_4	25 mM
	Na_2HPO_4	25 mM
	NH_4Cl	50 mM
	Na_2SO_4	5 mM
	$MgSO_4$	2 mM
	$Fe(NH_4)$ citrate	30 mg/mL
	L-Cysteine	0.5 mM
	Riboflavine	50 mg/mL

Table 3.11. Antibiotics stock solutions and their final concentration in media.

Antibiotics	Stock solution	Final concentration
Kanamycin	50 mg/mL, in H_2O	50 µg/mL
Chloramphenicol	34 mg/mL, in EtOH	34 µg/mL in liquid medium
		20 µg/mL in solid medium

Table 3.12: Buffers for agarose gel electrophoresis und their compositions. During this work, the TBE buffer was switched to a TAE buffer due to potentially health-endangering ingredients.

Buffer	Components	Concentration
TBE-buffer	Tris/borate	89 mM, pH 8.3
	EDTA	1 mM
TAE-buffer	Tris	40 mM
	EDTA	1 mM
	Acetic acid	20 mM

Table 3.13: Buffers, solutions and gel compositions for SDS-polyacrylamide gel electrophoresis (SDS-PAGE) according to Schägger and Jagow [251].

	Components	Concentration
Schägger sample buffer (4x)	Tris/HCl	150 mM, pH 7.0
	SDS	12% (w/v)
	Glycerol	30% (w/v)
	Coomassie Brilliant Blue R250	0.05% (w/v)
	2-Mercaptoethanol	6% (v/v)
Schägger gel buffer	Tris/HCl	3 M, pH 8.45
	SDS	0.3% (w/v)
Schägger separating gel	Acrylamide/bisacrylamide (29:1, w/v)	34% (v/v)
	Schägger gel buffer	34% (v/v)
	Glycerol	11% (v/v)

Table 3.13; continued.		
Schägger separating gel	TEMED	0.1% (v/v)
	APS	0.1% (w/v)
Schägger stacking gel	Acrylamide/bisacrylamide (29:1, w/v)	13% (v/v)
	Schägger gel buffer	23% (v/v)
	TEMED	0.2% (v/v)
	APS	0.1% (w/v)
Cathode buffer	Tris	100 mM
	Tricine	100 mM
	SDS	0.1% (w/v)
Anode buffer	Tris/HCl	200 mM, pH 8.9
Staining solution	EtOH	40% (v/v)
	Acetic acid	10% (v/v)
	Coomassie Brilliant Blue R250	0.02% (w/v
Destaining solution	EtOH	20% (v/v)
	Acetic acid	10% (v/v)

Table 3.14: Buffers for membrane preparation and complex I purification.

Buffer	Composition	Concentration
A_{KI}-buffer	MES/NaOH	50 mM, pH 6.0
	NaCl	50 mM
A_{KI}*-buffer	MES/NaOH	50 mM, pH 6.0
	NaCl	50 mM
	$MgCl_2$	5 mM
$A^*_{pH\ 6.8}$-buffer	MES/NaOH	50 mM, pH 6.8
	NaCl	50 mM
	$MgCl_2$	5 mM
	Glycerol	10% (v/v)
Binding buffer (KI)	MES/NaOH	50 mM, pH 6.8
	NaCl	50 mM
	$MgCl_2$	5 mM
	Imidazole	20 mM
	Glycerol	10% (v/v)
	LMNG	0.005% (w/v)
Elution buffer (KI)	MES/NaOH	50 mM, pH 6.8
	NaCl	50 mM
	$MgCl_2$	5 mM
	Imidazole	500 mM
	Glycerol	10% (v/v)
	LMNG	0.005% (w/v)
A^*_{LMNG}-buffer	MES/NaOH	50 mM, pH 6.0
	NaCl	50 mM
	$MgCl_2$	5 mM
	Glycerol	10% (v/v)

Table 3.14; continued.		
A^*_{LMNG}-buffer	LMNG	0.005% (w/v)

Table 3.15: Buffers for membrane preparation and *bd*-I oxidase purification.

Buffer	Components	Concentration
A_{bd}-buffer	MOPS/NaOH	20 mM, pH 7.0
	NaCl	20 mM
B-buffer	MOPS/NaOH	20 mM, pH 7.0
	NaCl	350 mM
Binding buffer (*bd*)	MOPS/NaOH	50 mM, pH 7.0
	NaCl	500 mM
	Imidazole	20 mM
	LMNG	0.003% (w/v)
Elution buffer (*bd*)	MOPS/NaOH	50 mM, pH 7.0
	NaCl	500 mM
	Imidazole	500 mM
	LMNG	0.003% (w/v)
A^*_{LMNG}-buffer (*bd*)	MOPS/NaOH	20 mM, pH 7.0
	NaCl	20 mM
	LMNG	0.003% (w/v)

Table 3.16: Chromatography columns for protein purification.

Type of chromatography	Column material	Column volume, [mL]	Manufacturer
Affinity chromatography	Probond (Ni^{2+}-IDA)	35	Life Technologies
	HisTrap FF (Ni^{2+} Sepharose 6 Fast Flow)	20	GE Healthcare
Size exclusion chromatography	Superose 6	297	GE Healthcare
	HiPrep 16/60 (Sephacryl S-300 High Resolution)	120	GE Healthcare
Desalting chromatography	HiTrap Desalting (Sephadex G-25)	55	Life Technologies
Anion-exchange chromatography	ResourceQ (SOURCE 15Q)	6	GE Healthcare

Table 3.17: Buffers and solutions for protein analytical methods.

Buffer	Components	Concentration
Liposome-buffer	MES/NaOH	5 mM, pH 7.0
	NaCl	50 mM
ACMA-buffer	KH_2PO_4/KOH	5 mM, pH 7.5

Table 3.17; continued.		
ACMA-buffer	KCl	50 mM
	$MgCl_2$	5 mM
Reconstitution buffer	HEPES	20 mM, pH 7.5
	KCl	200 mM
	Saccharose	73 mM
	$MgSO_4$	5 mM
	L-α-Phosphatidylcholine	0.05% (w/v)
	n-Octylglucosid	1.1% (w/v)
Biuret-reagent	Na/K tartrate	0.5% (w/v)
	$CuSO_4$	0.3% (w/v)
	KI	0.5% (w/v)
	NaOH	0.2 mM

Table 3.18: Solutions for gold layer creation.

Solution	Components	Concentration
A	$NaAuCl_4 \cdot 2H_2O$	15 mM
B	Na_2SO_3	150 mM
	$Na_2S_2O_3$	50 mM
	NH_4Cl	50 mM
	HF	2% (w/v)
C	NH_4F	40% (w/v)

Table 3.19: Solutions for gold layer modification.

Solution	Components	Concentration	Solvent
DTSP	3,3' – Dithiodipropionic acid di(N-hydroxysuccinimide ester)	10 mM	DMSO
Lysine	Nα, Nα-Bis (carboxymethyl)-L-lysine hydrate	10 mM, pH 9.8	H_2O
	K_2CO_3	500 mM	
Nickel	Nickel(II) perchlorate hexa-hydrate	50 mM	H_2O

3.6 Molecular biology methods

3.6.1 Preparation of plasmid DNA

For the isolation of plasmid DNA, the *Wizard Plus SV Minipreps DNA Purification System* (Promega) was used and the purification procedure was performed following the manufacturer's protocol. The spin columns were incubated with 30-50 µL MilliQ before DNA was eluted (55°C, 2 min, 750 rpm, Thermomixer compact, Eppendorf). Isolated DNA was stored at -20°C.

3.6.2 Purification of DNA

DNA fragments from agarose gels or PCR products were purified using *Wizard SV Gel and PCR Clean up System* (Promega) according to the manufacturer's instructions. Spin columns were incubated with 30 µL MilliQ before DNA was eluted (55°C, 2 min, 750 rpm, Thermomixer compact, Eppendorf).

3.6.3 Determination of DNA concentration

DNA concentration was determined in 1:10 (v/v) dilutions using the *Qubit Fluorometer High Sensitivity Assay Kit* (Invitrogen) according to the manufacturer's instructions.

3.6.4 Restriction analysis

150-250 ng of the isolated plasmid DNA was incubated at 37°C for 1.5 h (Thermomixer compact, Eppendorf) with 2-5 U of the appropriate restriction enzyme in the corresponding buffer (1×) in a total volume of 20 µL (MilliQ was added to reach the final volume). The fragments were analyzed by agarose gel electrophoresis. To digest the methylated template DNA after a PCR, the PCR mixture was covered with 1× Tango buffer and DpnI (excess, 1 µL) was added. The restriction mixture was incubated at 37°C for 1.5 h and the DNA was purified using agarose gel extraction or electrophoresis.

3.6.5 Agarose gel electrophoresis

DNA fragments obtained by PCR or restriction analysis were analyzed using agarose gel (0.8% (w/v) in TAE-buffer) electrophoresis. The samples were mixed with 1× *Loading Dye* (Thermo Fisher Scientific) and 0.5 µL SYBR Green (SYBR Green 1:1000 (v/v) in DMSO). The *Gene Ruler 1 kB Plus DNA Ladder* (Thermo Fisher Scientific) was used as a reference. The fragments were separated with 10 V/cm (EPS 601, Amersham Pharmacia Biotech) and visualized on a LED Illuminator (470 nm, UltraSlim LED Illuminator, Maestrogen). The results were documented using Bio-1000F, Microtek, Serva. When agarose gel electrophoresis was used for preparative purposes, the DNA was isolated after separation by gel extraction. For this purpose, the fluorescence of the DNA/SYBR Green complex was excited at 470 nm on an LED screen (Maestrogen), the desired band was cut out of the agarose gel and the DNA was purified with the *Wizard SV Gel and PCR Clean-Up Kit* (Promega) (see 3.6.2).

3.6.6 Sequencing of DNA

Purified DNA (20 µL, ≥ 20 ng/µL) and corresponding oligonucleotides (20 µL, 10 µM) were sent to Eurofins Genomic (Konstanz, Germany) or Genewiz (Leipzig, Germany) for DNA sequencing.

3.6.7 Polymerase Chain Reaction

The polymerase chain reaction (PCR) was performed in 0.2 mL PCR tubes (Biozym) in the volume of 10, 25 or 50 µL. MilliQ H_2O was added to reach the desired volume. The mixture was cooled on ice before the DNA polymerase was added. Temperature gradients were run in a thermocycler (LifeTouch, Biozym). For site-directed mutagenesis, the *Quick-Change* protocol from Agilent Technologies was used. For this, the PCR mixture was prepared in a 50 µL volume. 70-100 ng template DNA, 0.2 µM DNA-oligonucleotides, 20 µM dNTPs-mix, 1 x KOD *Hot start* buffer, 2.25 mM $MgSO_4$, 0.02 U/µL KOD *Hot start* DNA-polymerase were mixed together. The optimal annealing temperature for the oligonucleotides was determined via screening PCR.

For screening PCR, different gradient temperatures were applied to find out optimal conditions. For this purpose, 10 µL of a PCR mixture with or without DMSO was applied to a temperature program with annealing temperatures between 50 to 72°C at the annealing step (Tab. 3.20). To estimate the successful amplification, 5 µL of the whole reaction was analyzed or purified by agarose gel electrophoresis. For this, 2 µL 1× *Loading dye* (Thermo Fischer Scientific) and 0.5 µL SYBR-Green was added. The rest of the PCR mixture was then treated with 1 U DpnI in 1× Tango buffer at 37°C for 1.5 h to digest the template DNA. The mixture was purified with *Wizard SV Gel* and *PCR Clean-Up Kit* (Promega). The concentration of the purified DNA was determined (see 3.6.2) and the sample was stored at -20°C until further use.

Table 3.20: Temperature programs used in PCR for site-directed mutagenesis *via* the Quick change protocol.

	Temperature [°C]	Time	Cycles
Initial denaturation	95	2 min	1
Denaturation	95	20 s	25
Annealing	50-72	10 s	
Elongation	70	20 s/kb	
Storage	4	-	

3.6.8 Transformation by electroporation

For transformation by electroporation, 50 µL of electro-competent cells that were freshly prepared or thawed on ice were mixed with 10-30 ng DNA. The suspension was transferred into an electroporation cuvette (d=0.1 cm, Biozyme) that was cooled on the ice beforehand and a voltage pulse of 1700 V (Electroporator 2510, Eppendorf) was applied for transformation. The mixture was immediately resuspended in 1 mL SOC-medium, transferred to a sterile 2 mL Eppendorf tube and incubated for 1-2 h (37°C, 750 rpm, Eppendorf Thermomixer compact). 50-100 µL or the whole cell suspension was plated on agar plates with the corresponding antibiotics. The plate was incubated for 16-18 h at 37°C.

3.7. Microbiological methods

3.7.1 Bacterial cultivation

Precultures were made in a 4 mL or 400 mL scale. LB medium, autoinduction medium or eM9 minimal medium, containing the appropriate antibiotics and additives, were inoculated with a preculture, a culture stored in glycerol (1:1000, v/v) or a single colony picked from an agar plate. The preculture was grown aerobically while shaking (Innova 44, Incubator Shaker Series, New Brunswick Scientific) for 16-18 h at 37°C.

3.7.2 Determination of optical density

Bacterial growth was followed by measuring the optical density at 600 nm (Greiner, Ultrospec 1100 pro, Amersham; OD_{600}). 1 ml of cell culture was transferred into a cuvette with a light path of 1 cm (d= 1 cm, 1.5 mL halfmicro, Brand; Ultrospec 1000, Pharmacia Biotech). The appropriate medium was used as a reference. To measure OD_{600} values above 0.5, the samples were diluted 1:10 with the medium.

3.7.3 Bacterial cell growth

For the preparation of complex I, autoinduction medium (12×800 mL) was prepared the day before the cell growth and sterilized in the autoclave. Chloramphenicol (1:2000 (w/v)) was added and the medium was inoculated with a preculture (60 mL added to each flask, 1:14 (v/v)). Cultures were grown aerobically while shaking (Innova 44, Incubator Shaker Series, New Brunswick Scientific) at 37°C at 180 rpm. Bacterial growth was followed by measuring the OD_{600} every 60 min. At an

optical density of 3.5-3.8, cells were harvested by centrifugation (4ºC, 4800 rpm, 15 min, Rotor JLA 81000, Avanti J-26 XP, Beckman Coulter). The sediment was frozen in liquid nitrogen and stored at -80°C.

For preparation of *bd*-I oxidase, LB medium (12×800 mL) was prepared and sterilized. On the day of bacterial cultivation, kanamycin (1:2000 (w/v)) was added. 60 mL of preculture (1:13 (v/v)) was added to each flask. Cultures were grown aerobically while shaking (Innova 44, Incubator Shaker Series, New Brunswick Scientific) at 37°C and 180 rpm. Bacterial growth was followed by measuring the OD_{600} every 60 min. At an optical density of around 2.0 IPTG (0.4 M) was added to each flask in a ratio of 1:1000. The cells were incubated for 2 h. Afterwards, the cells were harvested by centrifugation (4ºC, 4800 rpm, 15 min, Rotor JLA 81000, Avanti J-26 XP, Beckman Coulter). The sediment was frozen in liquid nitrogen and stored at -80°C.

3.7.4 Bacterial glycerol stocks

To produce bacterial glycerol stocks, 150 µL of glycerol (80%; v/v) were mixed with 250 µL of a fresh 4 mL preculture. The mixture was mixed on a vortex and shock frozen immediately in liquid nitrogen. The bacterial glycerol stocks were stored at -80°C.

3.7.5 Generation of electro-competent cells

All steps for electro-competent cells production were carried out sterile and on ice. For the production of electro-competent cells, 50 or 100 mL of LB medium were, if necessary, mixed with the appropriate antibiotics and inoculated with a preculture in a ratio of 1:100 (v/v). Cells were grown at 37°C while shaking (180 rpm, New Brunswick Innova 44, Incubator Shaker Series, Eppendorf) and cell growth was followed by measuring OD_{600}. At an OD_{600} of 0.5-0.7, cells were placed on ice for 15 min to slow down growth. Afterwards, centrifugation (4°C, 10 min, 3800×g, Rotor A-4-44, Eppendorf centrifuge 5804 R) was performed to sediment the cells. The supernatant was discarded and the sediment was resuspended in 50 mL MilliQ. This step was repeated twice with 50 mL glycerol (10%, v/v). The sediment was resuspended in 150 or 300 µL glycerol (15%, v/v). The cell suspension was aliquoted to 50 µL, shock-frozen in liquid nitrogen and stored at -80°C.

3.8. Protein chemical methods

3.8.1 Preparation of *E. coli* cytoplasmic membranes

All steps were carried out on ice or at 4°C. 30-70 g of frozen cells (wet weight) were mixed with 4-5 fold (w/v) of A-buffer, 0.1 mM PMSF (0.1 M stock solution in 2-propanol) and a few grains of DNAse I. The suspension was homogenized with a teflon-in-glas homogenizer and cells were disrupted in three rounds with an HPL-6 (*Maximator*, 1000-1500 bar). The lysate was centrifuged (4°C, 20 min, 9500 × g, Rotor JA25.50, Beckman, Avanti J-26S XP, Beckman) to separate non-disrupted cells. The sediment was discarded, and the supernatant was centrifuged at a higher speed (4°C, 70 min, 257'000 ×g, Rotor 60Ti, Beckman, Optima LE80-K, Beckman). The supernatant was retained and the sedimented membranes were homogenized in A*-buffer (pH 6.0 for complex I and pH 7.0 for *bd*-I (1:1, w/v) and 0.1 mM PMSF. For complex I preparations, membranes were suspended in A*-$_{pH\ 6.8}$-buffer if further chromatographic purification was planned. For *bd*-I oxidase preparations, membranes were suspended in A$_{bd}$-buffer (pH 7.0). Sedimented membranes were homogenized with teflon-in-glas homogenizer. Membranes were aliquoted, shock frozen in liquid nitrogen and kept in the freezer at -80°C. 100 µL samples from cytoplasmic membranes containing overproduced complex I were frozen separately to determine the NADH oxidase activity and determine protein concentration.

3.8.2 Preparation of respiratory complex I from *E. coli*

Complex I produced from pBAD*nuo* was prepared according to the following procedure. All chromatographic steps were performed at 4°C or on ice. Buffers used for the chromatographic system are listed in Table 3.14 and chromatographic columns in Table 3.16. PMSF (30 µM) was added to all the buffers right before usage. All buffers used for chromatographic purification were degassed for at least 20 min before usage. The chromatography systems NGC Quest 10 Plus (BioRad) and ÄKTA Go (Cytiva) were used for the preparations.

Frozen membranes were kept on ice till they were thawed, A*-$_{pH\ 6.8}$- buffer (1:5, (v/v)) was added to dilute the membranes. 5% (v/v) LMNG (final concentration 2%) was slowly added while stirring. The extract was left stirring slowly for 1 h at room temperature. The suspension was diluted with approximately 100 mL A*-$_{pH6.8}$-buffer, centrifuged (4°C, 15 min, 50'000 rpm, 257'000 × g, Rotor 60Ti, L8-M Ultrafuge, Beckman) and filtrated (0.45 µm pore size; Filtropur S 0.45, Sarstedt) to remove remaining particles. The cleared extract was mixed with imidazole to a

final concentration of 20 mM and loaded on an affinity chromatography column (35 mL, Ni^{2+}-IDA), equilibrated in binding buffer at pH 6.8, with a flow rate of 2 mL/min. The column was run at a rate of 3 mL/min. Weakly bound proteins were eluted at an imidazole concentration of 116 mM (20% elution buffer). Bound proteins were eluted with 60% elution buffer corresponding to an imidazole concentration of 308 mM. The eluate was collected in 4 mL fractions and the NADH/ferricyanide oxidoreductase activity of every fraction was determined. Fractions with the highest activity were pooled and concentrated (4°C, 3800 × g, Amicon Ultra-15, MWCO: 100 kDa, Millipore; Rotor 4-44, Centrifuge 5804 R, Eppendorf) to a volume of less than 1 mL.

400-800 µL of the concentrated protein was centrifuged (17'500×g, 10 min, 4°C, Rotor F-45-30-11, Centrifuge 5417 R, Eppendorf) to remove aggregated proteins. The supernatant was loaded on a size exclusion column (297 mL, Superose 6 10/300 GL), equilibrated in A^*_{MNG} –buffer (pH 6.0), with a flow rate of 0.3 mL/min and eluted in the same buffer. Fractions were collected at a retention volume from 80 to 240 mL. The peak was collected, and the NADH/ferricyanide oxidoreductase activity of fractions was determined. Fractions with the highest activity were concentrated (4°C, 3800 × g, Amicon Ultra-15, MWCO: 100 kDa, Rotor-4-44, Eppendorf Centrifuge 5804R) to a concentration higher than 20 mg/mL. The NADH/ferricyanide oxidoreductase activity as well as the protein concentration of the concentrated sample was determined. The protein sample was aliquoted, shock frozen in liquid nitrogen and stored at -80°C till further usage.

3.8.3 Preparation of *E. coli bd*-I oxidase

All steps were carried out at 4°C using the chromatography systems NGC Quest 10 Plus (BioRad) and Äkta Go (Cytiva). Buffers and solutions are listed in Table 3.15 and all columns used for chromatography are listed in Table 3.16. PMSF (30 µM) was added to all the buffers just before usage. All buffers used for chromatographic purification were degassed for at least 20 min before usage.

The membrane suspension was diluted with A_{bd}-buffer (pH 7.0) in a ratio of 1:6 (w/v), PMSF (1:200 (w/v)) and 5% (v/v) LMNG (final concentration 1%) were added. The extract was stirred for 75 min at 4°C. Protein aggregates were removed by centrifugation (4°C, 50'000 rpm, 257'000 × g, 15 min, Rotor 60Ti, L8-M Ultrafuge, Beckman). The extracted membrane proteins were mixed with elution buffer to a final imidazole concentration of 68 mM. The mixture was

loaded onto a HisTrapFF (20 mL, Ni^{2+} Sepharose 6 Fast Flow) affinity chromatography column pre-equilibrated in binding buffer (pH 7.0) at a flow rate of 3 mL/min. The column was washed with 68 mM imidazole binding buffer until absorption at 280 nm reached the baseline level. Bound proteins were eluted by applying a gradient from 68 to 500 mM imidazole within two column volumes. The eluate was collected in 3 mL fractions, and *bd*-I oxidase containing fractions were pooled and concentrated (Amicon Ultra - 15, 100,000 MWCO, Merck) to 2 mL by centrifugation at 3800 rpm (4°C, Centrifuge 5804 R, rotor A-4-44, Eppendorf). The concentrated fractions were loaded on a HiTrap Desalting chromatography column that was pre-equilibrated in A_{bd}-buffer at a flow rate of 3 mL/min. The eluate was collected in 2 mL portions, peak fractions of absorbance were pooled and concentrated (Amicon Ultra - 15, 100,000 MWCO, Merck) to 2 mL by centrifugation at 3800 rpm (Centrifuge 5804 R, rotor A-4-44, Eppendorf, 4°C). The concentrated solution was loaded on a MonoQ 10/100 GL ion exchange chromatography column pre-equilibrated in A_{bd}-buffer (pH 7.0) at a flow rate of 2 mL/min. The column was washed with A-buffer until the absorption at 280 nm reached the baseline level. Bound proteins were eluted by applying a gradient from 20 to 350 mM NaCl within 15 column volumes at a flow rate of 2 mL/min and the eluate was fractionated in 2 mL portions. Fractions containing *bd*-I oxidase were pooled and concentrated (Amicon Ultra - 15, 100'000 MWCO, Merck) to approximately 0.5 mL by centrifugation at 3800 rpm (4°C, centrifuge 5804 R, rotor A4-44, Eppendorf). To remove aggregated proteins, the concentrated protein solution was centrifuged (4°C, 10 min, 17'500×g, Rotor F-45-30-11, centrifuge 5417 R, Eppendorf) and applied to size-exclusion chromatography and Superose 6 Increase 10/300 GL (120 mL) size exclusion chromatography column. The column was pre-equilibrated in A^*_{MNG}-buffer and the protein were eluted at a flow rate of 0.3 mL/min. The eluate was collected in 0.5 mL portions, peak fractions were pooled and concentrated (Amicon Ultra - 15, 100'000 MWCO, Merck) by centrifugation at 3800 rpm (4°C, Centrifuge 5804 R, rotor A-4-44, Eppendorf,). Protein concentration was determined and a redox-difference spectrum was recorded. The preparation was aliquoted, frozen in liquid nitrogen and stored at -80°C.

3.8.4 Reconstitution of complex I into liposomes

Purified complex I was reconstituted into preformed *E. coli* liposomes to produce proteoliposomes for proton pumping experiments. To obtain *E. coli* liposomes, 1 mL of dissolved lipids in chloroform (*E. coli* polar lipids, Avanti) were evaporated under a stream of N_2 and the lipid layer

was then dissolved in the 5-fold volume of liposome buffer (Tab. 3.17). To obtain vesicles, the suspension was frozen seven times in liquid nitrogen and thawed again at 29°C (750 rpm; Thermomixer compact, Eppendorf). 250 µL liposomes were extruded through at least 21 passes with an extruder (0.1 µm polycarbonate membrane, mini extruder; Avanti) and brought to a uniform size. To this mixture 8 µL sodium cholate solution (20%, w/v) was added. For reconstitution, 0.5 mg of complex I (20 mg/mL) was mixed 1:3 (v/v) with reconstitution buffer (table 3.17) and incubated on ice for 5 min. The freshly extruded liposomes were mixed with complex I in reconstitution buffer and incubated for 20 min at room temperature. Liposomes were suspended to size exclusion chromatography column (PD-10 Desalting Column, 8.3 mL; Sephadex G-25, GE Healthcare) equilibrated in liposome buffer. The coloured eluate was collected and centrifuged (4°C, 2 bar compressed air, 150,000×g, 30 min; Rotor, A-100, Airfuge, Beckman). The sedimented proteoliposomes were resuspended in 500 µL liposome buffer and stored on ice for further use. The orientation and amount of reconstituted complex I in the proteoliposomes were determined by NADH/ferricyanide oxidoreductase activity (see 3.9.2). Membranes are impermeable to NADH. In the liposomes only complex I with an outward facing peripheral arm contributes to activity. The liposomes were dissolved by adding 0.04% DDM (w/v). Thus, the NADH/ferricyanide oxidoreductase activity of the total amount of reconstituted complex I was determined due to the now resulting unrestricted availability of NADH. The NADH/ferricyanide oxidoreductase activity was determined in both intact and solubilized liposomes. A comparison of both activities provides information about the complex I orientation in intact liposomes.

3.9. Protein analytical methods

3.9.1 Determination of protein concentration

The concentration of isolated complex I was determined by the UV/vis absorbance at 280 nm (precision cuvette, Helma QS, d = 1cm; TIDAS S, J&M Analytik AG). The corresponding buffer (A^*_{MNG}-buffer, pH 6.0) was used as a reference and measured at the same wavelength. To correct light scattering by lipids and detergent micelles, the absorbance at 310 nm was subtracted from the value at 280 nm. The protein concentration was calculated according to Lambert-Beer's law with the molar extinction coefficient of complex I calculated from the amino acid sequence ε_{280}=781 $mM^{-1}cm^{-1}$ [252] assuming a molecular mass of M_r = 535 kDa.

Biuret method was applied to determine protein content in membranes, detergent extracts or protein eluates after affinity chromatography. 10, 15 and 20 µL of protein samples or membrane suspensions were mixed with 1 mL trichloroacetic acid (TCA, 6%, w/v) and centrifuged (room temperature, 16'100×g, 1 min, Rotor F45-24-11, Eppendorf centrifuge 5415D, Eppendorf). 20 µL MilliQ water was used as blank and treated the same way. The supernatant was discarded, the sediment was dried shortly and 1 mL biuret-reagent was added. Samples were incubated at 37°C for 30 min while shaking (1400 rpm, 30 min, Eppendorf Thermomixer compact). The absorbance was measured at 546 nm (Ultrospec 1100 pro, Amersham Biosciences) before and after destaining the solution with a few grains of KCN. The difference was calculated to correct the influence of lipids and detergents on the absorbance. The protein concentration was calculated by comparison to a standard curve, obtained from bovine serum albumin (BSA, 0.1-1 mg).

Protein concentration of the *bd*-I oxidase was determined after chromatographic purification. The absorbance of a *bd*-I oxidase sample was measured by a diode array spectrometer in UV cuvettes (precision cuvette, Helma QS, d = 1cm; TIDAS S, J&M Analytik AG) according to [252]. The corresponding buffer (A-$_{MNG}$ buffer, pH 7.0) was used as a reference. 3 µL *bd*-I oxidase was diluted with 297 µL A-$_{MNG}$ buffer (pH 7.0). The absorptions at 278, 279, 280 and 282 were measured and the extinction coefficient was calculated using the Protein Calculator v3.4 (Scripps Research Institute) (Tab. 3.21). The protein concentration was calculated according to Lamber Beer´s law.

Table 3.21: Calculated molar extinction coefficients for the *E. coli* cytochrome *bd*-I oxidase [252].

Wavelength [nm]	**Molar extinction coefficient ε [M^{-1} cm^{-1}]**
278	219.800
279	219.845
280	218.630
282	213.200

3.9.2 Activity measurements

The NADH/ferricyanide oxidoreductase activity was determined by electron transfer from NADH to $K_3[Fe(CN)_6]$ and measured as a decrease in $K_3[Fe(CN)_6]$ concentration at 410 nm (Ultrospec 1100 pro, Amersham Bioscience). To 1 mL $K_3[Fe(CN)_6]$ solution (1 mM in A*-buffer) 0.2 µM NADH was added and the enzymatic reaction was started by the addition of 0.1-5 µL protein. For the activity calculation according to the Lambert-Beer's law, a molar extinction coefficient of ε_{410}

($K_3[Fe(CN)_6]$) = 1 mM^{-1} cm^{-1} was used [253]. Alternatively, this value was determined with a diode array spectrometer (UV cuvette, Macro QS, Hellma, d=1 cm; TIDAS S, J&M Analytik AG). To 979 µL $K_3[Fe(CN)_6]$ (1 mM in A* buffer, 30°C) 1 µL of protein sample (diluted with A^*_{MNG}-buffer, 1:10 (v/v)) was added and incubated while stirring for approximately 1 min. 0.2 µM NADH solution was added to activate the electron transfer. The decrease in absorbance was recorded over time before and after sample addition and the value of the enzymatically catalyzed reaction was corrected for the value of the non-enzymatic reaction.

The NADH oxidase activity of cytoplasmic membranes was determined as the decrease of the oxygen concentration using a Clark-type electrode (Oxygraph+, DW 1, Hansatech Instruments). The electrode was calibrated by filling 2 mL H_2O at 30°C in the chamber. A few grains of sodium dithionite were added to fully reduce the dissolved oxygen in the chamber. The signal was recorded and the difference between the oxidized and reduced state corresponds to an oxygen concentration of 237 µM [254]. For the NADH oxidase measurement, 2 mL A*-buffer (pH 6.0) at 30°C was used and 5 µL membrane suspension was incubated until the signal was stable. The reaction was started with the addition of 5 µL (d-) NADH (0.5 M stock solution, 1.25 mM final concentration). The activity of bo_3 was inhibited by adding 10 µM KCN (0.5 mM stock solution).

The activity of *bd*-I oxidase was measured as decrease of oxygen concentration by a Clark-type electrode. The electrode was calibrated in the same way as for NADH oxidase activity measurements. 10 µL of a 1 M DTT solution was added into 2 mL A_{MNG}-buffer (pH 7.0) at 30°C. 5 µL of 1 M duroquinone (freshly prepared solution) was added and the solution was incubated for 1 min. The reaction was started by the addition of 10 µL *bd*-I oxidase (2 mg/mL).

The physiological NADH:decyl-ubiquinone oxidoreductase activity (NADH:decyl-Q oxidoreductase activity) of complex I was determined spectroscopically at 340 nm by electron transfer from NADH to decyl-Q and the resulting decrease in the NADH concentration was recorded over time (macro cuvette QS, d = 1 cm, Hellma Analytics; TIDAS S, J&M Analytik AG). The activity was calculated using the Lambert-Beer law with a molar extinction coefficient for NADH of $\varepsilon_{340}(NADH) = 6.178$ $mM^{-1}cm^{-1}$ [255].

The NADH:decyl-Q oxidoreductase activity of complex I in lipids was measured according to the following method. Complex I sample (10 mg/mL) was incubated with polar lipids (in $lipid_{LMNG}$-buffer, c = 10 mg/mL) in an equal mass ratio (5 µg complex I + 5 µg polar lipids) for 30 min on ice. For the measurement, 981 µL of A*-buffer (pH 6.0, 30°C) was placed in the cuvette, 3 µL of decyl-Q (60 µM, 20 mM stock solution in EtOH) 1 µL of complex I (5 µg) incubated with lipids was added. The decrease in absorbance at 340 nm was recorded for 1 min and 15 µL NADH (150 µM, 10 mM stock solution in H_2O) was added to start the reaction.
The NADH:decyl-Q oxidoreductase activity of complex I in the presence of terminal oxidases was performed by adding an excess of *bo*$_3$ oxidase. The terminal oxidase ensures that the QH_2 generated by complex I is reoxidized and is available to the complex as a substrate. Complex I was diluted with A^*_{MNG} buffer to a concentration of 1 mg/mL. Protein was incubated on ice for approximately 30 min. For the measurement 981 µL of the A*-buffer (pH 6.0, 30°C) was placed in the cuvette, 3 µL of decyl-Q (60 µM, 20 mM stock solution in EtOH) was added, 0.3 µL *bo*$_3$ oxidase (4 µg) and 1 µL of complex I (2 µg, 1 mg/mL) were mixed in the cuvette. After 60 sec incubation under stirring, the reaction was initiated with the addition of 15 µL NADH (150 µM, 10 mM stock solution in H_2O).

The proton translocation activity of complex I in proteoliposomes was determined by fluorescence spectroscopy *via* the decrease in fluorescence of the pH-sensitive dye ACMA [256]. For proton translocation measurements, liposomes were obtained as described in 3.8.4, the measurements were performed on the same day. The build-up of a proton gradient (ΔpH) across the membrane was monitored *via* the decrease in ACMA fluorescence. The excitation wavelength was set to 430 nm and the emission wavelength to 480 nm (macro cuvette Spezial OS, d = 1 cm, Hellma Analytics; 2.5 nm slid width, LS 45 Luminescence Spectrometer, Perkin Elmer). ACMA was diluted in absolute EtOH to the concentration of 20 µM. Test measurements for the right amount of ACMA were conducted (985 µL ACMA buffer + 15 µL ACMA). To 1 mL ACMA-buffer (30°C; 5 mM KH_2PO_4/KOH, pH 7.5, 50 mM KCl and 1 mM $MgCl_2$) 0.2 µM ACMA, decylQ (60 µM, 20 mM stock solution in EtOH) were added and 50 µL proteoliposomes. The compounds were incubated for 2 minutes, and the reaction was started by adding NADH (150 µM, 10 mM stock solution in H_2O). To stop the reaction, 3 µL of the uncoupler CCCP (100 µM, 10 mM stock solution in EtOH) were added to dissipate the ΔpH.

3.9.3 UV/vis redox-difference spectroscopy

UV/vis spectra were recorded with a diode array spectrometer (UV cuvette Halbmicro QS, Hellma, d=1 cm, TIDAS S, J&M Analytik AG). To calculate the dithionite-reduced-minus-air-oxidized UV/vis difference spectra, a spectrum of a protein sample oxidized by atmospheric oxygen was subtracted from the spectrum of a sample reduced by sodium dithionite. For this, 20 µL of *bd*-I oxidase (20 mg/mL) was diluted with 280 µL of A-buffer (pH 7.0) and an UV/vis spectrum of the oxidized sample was recorded. The solution was then reduced by a few grains of dithionite and an UV/vis spectrum of the reduced sample was recorded. The absorbances of the heme-groups in the redox UV/vis-difference spectrum were determined and compared to the ones described in the literature [181].

3.9.4 SDS-PAGE (SDS-polyacrylamide gel electrophoresis)

The purities of the preparations were analyzed by SDS-polyacrylamide gel electrophoresis (SDS-PAGE). A discontinuous gel system with a 3.9% stacking gel and a 10% separation gel was used [251]. 50 µg protein were mixed with sample buffer and incubated while shaking (37°C, 750 rpm, 30 min, Eppendorf Thermomixer compact). The samples and 10 µL unstained protein marker were loaded on the gel and proteins were separated at 30 mA (EPS 600, Pharmacia Biotech) for 2 h. The protein bands were stained with staining solution and visualized by destaining the background with a destaining solution.

3.9.5 Mass photometry

Mass photometric measurements were performed on a One^{MP} mass photometer (Refeyn Ltd, Oxford, UK) [257]. A new, freshly cleaned glass slide was used and a new flow chamber was used for each measurement. To fix the focus, 15 µL of A*$_{KI}$-buffer (pH 6.0) were pipetted in drops into a flow chamber and the focus position was identified. The focus position for the subsequent measurement was fixed with an autofocus system based on total internal reflection. Immediately before the measurement, the protein sample was diluted to 500 nM with A*buffer (pH 6.0), added directly to the droplet in the flow chamber at a ratio of 1:10 (v/v) and, after autofocus stabilization, a film of 60 seconds length was recorded. To improve the signal-to-noise ratio of the measurement, a buffer without the appropriate detergent was used, since background signals from the detergent micelles are bypassed here. Data collection was done with AcquireMP (Refeyn Ltd, v1.2.1).

3.10 Nitrile labelling of complex I variants

3.10.1 Cyanide labelling

50 µL of complex I (10 mM) was incubated on ice with 0.5 µL dithiothreitol (0.5 µM, 1 M DTT stock solution in H_2O) for 30 min to reduce cysteine residues, followed by removal of DTT excess by consecutive size exclusion chromatography on Sephadex G50 (2.5 min, 1600 rpm, Centrifuge 5804 R, Eppendorf). Columns were prepared by dissolving 3.33 g Sephadex G-50 in 50 mL H_2O. Before usage, the columns were centrifuged (2 min, 1200 rpm, Centrifuge 5804 R, Eppendorf). After the protein was incubated at 4°C with a 44-fold molar excess of DTNB (30 mM stock solution in DMSO) for 1 hour and the excess of DTNB was removed with Sephadex G50 medium as described above. Finally, 6 mM potassium cyanide (30 mM stock solution of KCN in H_2O) was added to the protein and incubated for 2 h on ice.

3.10.2 Determination of label efficiency

The labelling efficiency of KCN was determined by UV/vis spectroscopy by following the absorption band of TNB^{2-} release at 412 nm after the addition of KCN. Absorbance spectra of the samples were recorded (1 cm path-length quartz cuvette, UV/Vis spectrometer Varian Cary 300). To determine the labelling efficiency, 50 µL labelled complex I were mixed with 400 µL buffer (50 mM MES, 50 mM NaCl, 5 mM $MgCl_2$, 0.05% MNG) and an UV/vis spectrum was recorded. The spectrum of the buffer was subtracted from the sample spectrum.

3.11 SEIRAS measurements

3.11.1 Gold layer formation

A silicon crystal was polished with 0.3 µm alumina and rinsed with distilled water. The crystal was dried under an argon stream and immersed with 40% NH_4F solution (v/w) for 1 min to remove the silicon oxide layer. The surface was rinsed with water and dried with argon. The gold solution was prepared from equal volumes of 15 mM $NaAuCl_4$, 150 mM Na_2SO_3, 50 mM $Na_2S_2O_3$, 50mM NH_4Cl, and 2% HF (w/v) solutions. The crystal and the solution were heated at 65°C for 10 min. The silicon surface was covered with the preheated solution for 40 s. The reaction was stopped by washing the crystal surface with water. The surface was dried in an argon stream.

3.11.2 Surface modification with Ni-NTA SAM and protein immobilization

The experimental procedure for the nickel nitrilotriacetic acid self-assembled monolayer (Ni-NTA SAM) was adapted from [219, 258]. 1 mg/mL of 3,3-dithiodipropionic acid di(N-hydroxysuccinimide) ester (DTSP) in dimethyl sulfoxide (DMSO) was allowed to self-assemble on the gold surface for 1 h. After the monolayer was formed, excess DTSP was washed away with DMSO and the crystal was dried under an argon stream. The modified surface was immersed in a solution of 100 mM Nα, Nα-bis (carboxymethyl)-L-lysine (ANTA) in 0.5 M K_2CO_3 at pH 9.8 for 3 h and then rinsed with water. Finally, the surface was incubated in 50 mM nickel(II) perchlorate hexahydrate ($Ni(ClO_4)_2$) for 1 h. After washing with water, 3 µL complex I (2-5 mg/mL) labelled wirh CN^- was dropped on the modified surface.

3.11.3 IR spectra

Infrared (IR) spectra were measured with a Vertex 70 FTIR spectrometer (Bruker, Karlsruhe, Germany; Globar source, potassium bromide (KBr) beamsplitter, mercury cadmium telluride detector (LN-MCT)) with 40-kHz scanner velocity, 256 scans and 4 cm^{-1} resolution). The spectrometer was purged with dried air to avoid the humidity. All experiments were performed in the MID IR range (400-4000 cm^{-1}). Typically, 50 spectra were recorded. The first 10 spectra were averaged for cyanide band analysis. For the amide I band analysis the last spectrum was taken to avoid the water contribution. A baseline correction was performed.

3.11.4 Incubation with NADH

5 µL labelled complex I (2-5 mg/mL) was mixed with 100 µM NADH and incubated for 5 min on ice. The absorbance spectra of the protein immobilized on the Ni-NTA surface were recorded.

3.11.5 Incubation with Q-2

10 µL labelled complex I (2-5 mg/mL) residue that was incubated with 100 µM NADH was mixed with 150 µM ubiquinone for 10 min on ice. The absorbance spectra of the protein immobilized on the Ni-NTA surface were recorded.

4 Results

4.1 Proton translocation by complex I

Proton translocation across the membrane is a highly discussed topic in the field [96, 113, 122, 259]. The mechanism of proton translocation by respiratory complex I is still under debate. One theory, the so called “ND5-only” mechanism (ND5 is mitochondrial homologue of *E. coli* NuoL) postulates that only the distal subunit NuoL is involved in proton translocation to the periplasm, and all the protons to be pumped are transfered *via* the central hydrophilic axis to this subunit [5]. Other theories suggest that proton translocation across the membrane occurs in all antiporter-like subunits of the membrane arm. It was hypothesized that long-range conformational changes triggered by Q chemistry, drives proton translocation through these antiporter-like subunits [6]. To indirectly visualize the movement of individual residues in the membrane arm in the presence of substrates, infrared probes were used to label different residues in NuoM subunit in the membrane arm. Individual positions were genetically changed to cysteine residues that were labelled with cyanide to obtain thiocyanates. Thiocyanates are attractive IR labels as their signals appear in the clear region of IR spectra and do not overlap with protein signals. These labels are sensitive towards hydrogen bond interactions and the hydrophobicity of the environment, enabling to follow reaction-induced conformational changes. The stretching vibration of thiocyanate [ν(SC≡N)] appears between 2175- 2120 cm^{-1} [7].

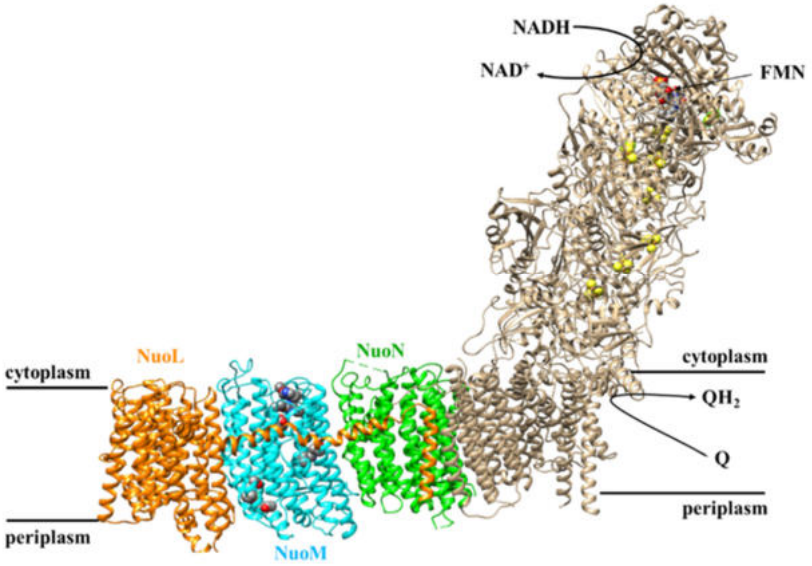

Fig. 4.1: Complex I crystal structure from *E. coli* at 2.4 Å resolution (PDB: 7Z7S) [20]. Membrane arm subunits are shown in color and the catalyzed reactions are shown. Mutations generated in the subunit NuoM are indicated.

4.1.1 Position of NuoM mutations

All mutations generated in this project were designed for the *E. coli* strain BWΔ*ndh nuo*::*npt*II on the plasmid pBAD*nuo*$_{his}$*nuo*F. NuoM, the central subunit in the membrane arm, was selected as the target for mutagenesis to test if it takes part in proton translocation to the periplasm for a better understanding of the mechanism. All selected positions were mutated to cysteines. 11 mutations were generated in NuoM to visualize possible helix movements. The mutated positions in NuoM are shown in Figure 4.2. Four mutations are located on the cytoplasmic side (E108, S105, H117 and H159), another four were generated on the periplasmic side (S425, T332, T422, S414) and three in the central part of the membrane (D258, T178 and K234).

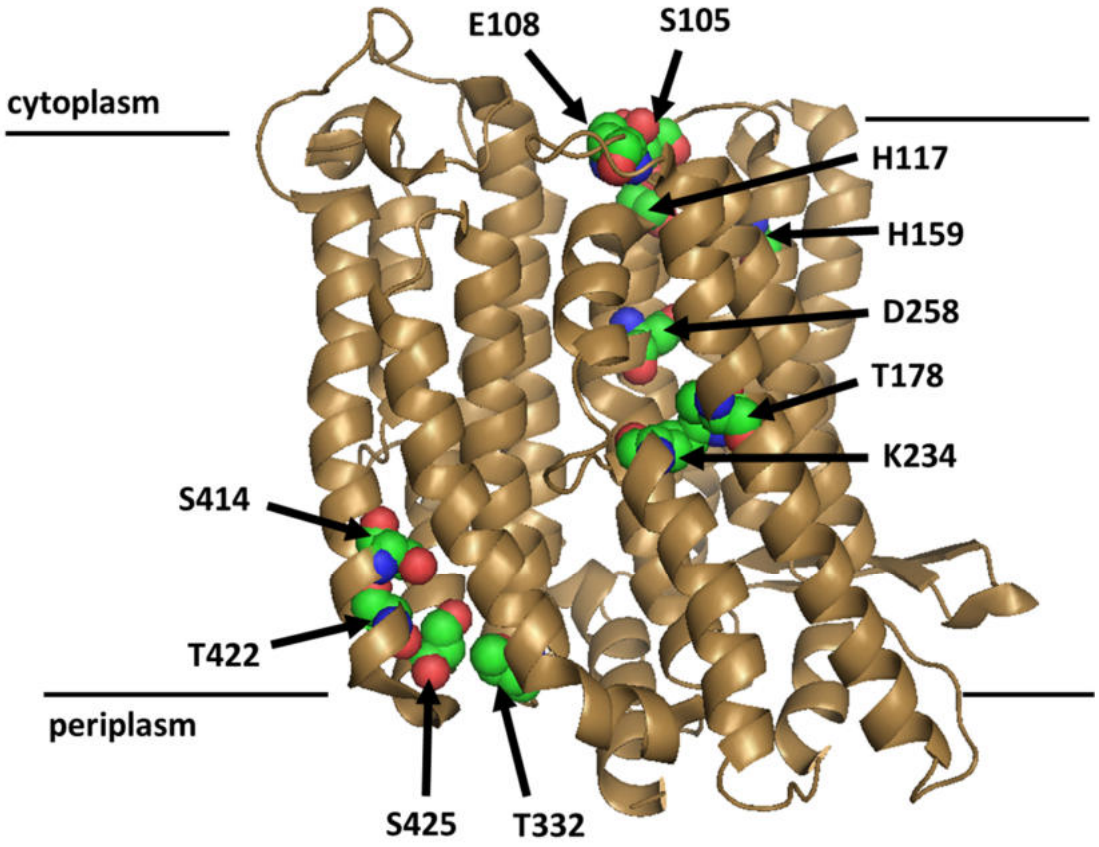

Figure 4.2: Location of NuoM mutations for labelling. PDB: 3RKO [119]. Mutated positions are shown in colour.

These positions were selected due to their location close to the membrane surface, but also in proximity to the putative proton pathway that is split into two half-channels [119]. It was assumed that proton translocation in NuoM involves these positions, resulting in local conformational changes or a change in the hydrophobicity of their environment, that would give a spectral shift of the label. All mutations were generated by site-directed mutagenesis.

4.1.2 Generation of NuoM mutations

Point mutations on NuoM were introduced into the pBAD*nuo* expression plasmid *via* site-directed mutagenesis. The plasmid encodes the complete *E. coli nuo* operon. A hexahistidine tag ($_{his}$*nuo*F) is added to the N-terminus of NuoF that allows protein purification by affinity chromatography. Corresponding oligonucleotides were used for mutagenesis (Tab. 3.2) by PCR. Different annealing temperatures from 50° to 72°C were tested. PCR was performed using KOD polymerase. Figure 4.3 shows the results of the PCR to introduce the E108C, H159C and S414C mutations.

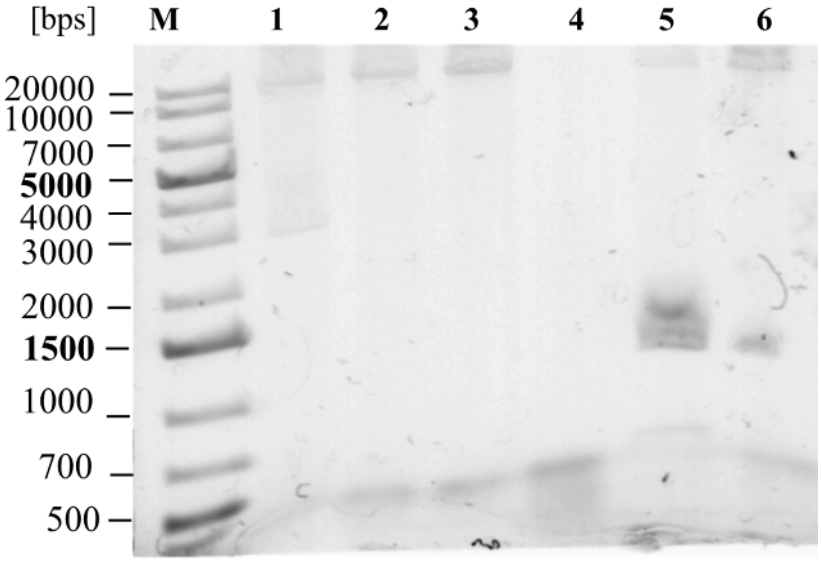

Figure 4.3: Gel of the PCR to generate the plasmids pBAD*nuo* $_{his}$*nuo*F E108C^{M} (lane 1, 2), H159C^{M} (lane 3, 4) and S414C^{M} (lane 5, 6). Lanes 1 to 3 and 5, 6 show expected bands at 21´326 bps of the parential plasmid. Lanes 1, 3 and 5 shows the band of the product obtained at 50° and lanes 2, 4 and 6 that of the product obtained at 72°C. The GeneRuler 1 kb Plus DNA Ladder (M) was used as a reference.

The band with the expected product (21´326 bps) was cut out, purified and transformed into electrocompetent BWΔ*ndh nuo*::*npt*II cells. Colonies were picked and cultivated, the plasmids were isolated. The variants carried the desired point mutation and also a silent mutation generating a new cleavage site, so the isolated plasmids were analyzed by restriction analysis (see 3.6.3). DNA sequencing (Eurofins or Genewiz) with the corresponding oligonucleotides (listed in Tab. 3.5) confirmed the success of site-directed mutagenesis. Figures 4.4 to 4.6 show the results of restriction analysis for all the generated mutations.

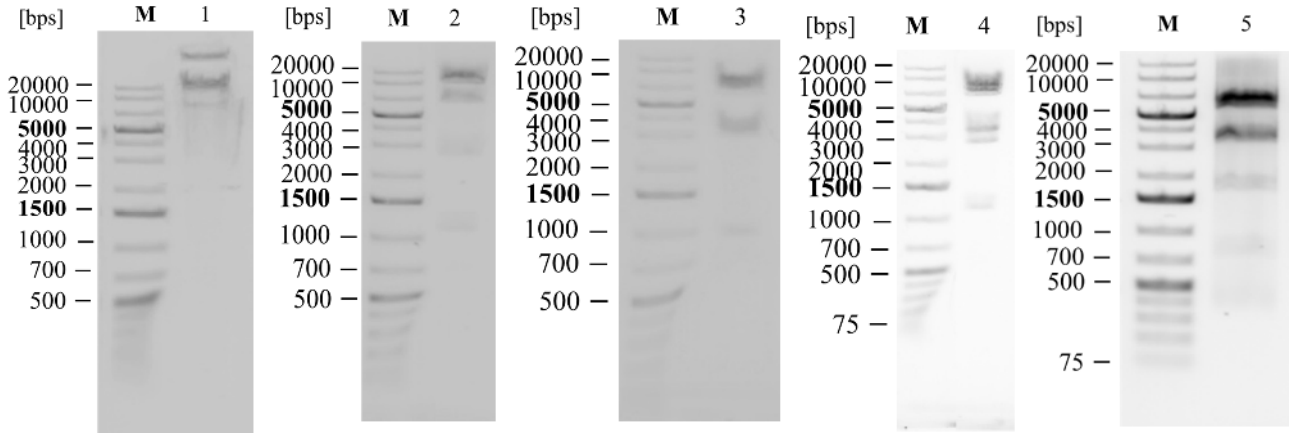

Figure 4.4: Restriction analysis of the mutations. The GeneRuler 1 kb Plus DNA Ladder (M) was used as reference. Lane 1: *nuoM* E108C (expected bands at 13761 and 7559 bps with NsiI), lane 2: *nuoM* S414C (expected bands at 8978, 7942 and 4400 bps with KpnI), lane 3: *nuoM* T332C (expected bands at 7232, 6396, 3588, 3147 and 957 bps with VspI), lane 4: *nuoM* H159C (expected bands at 7541, 6549, 3397, 2758 and 1075 bps with HindIII), lane 5: *nuoM* H117C (expected bands at 5619, 4959, 3453, 3212, 1662, 1335, 741 and 339 bps with DraI).

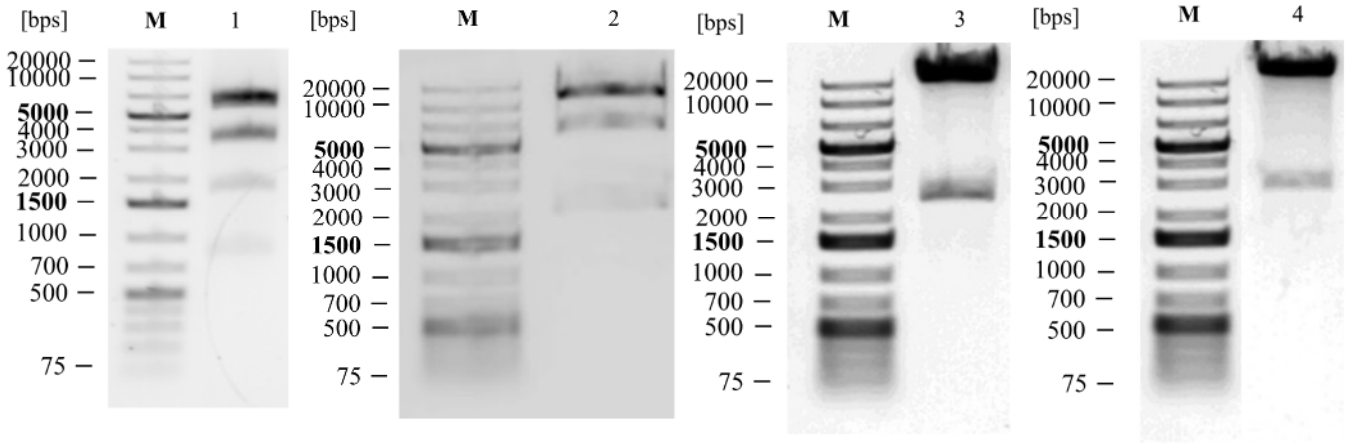

Figure 4.5: Restriction analysis for the mutations. The GeneRuler 1 kb Plus DNA Ladder (M) was used as reference. Lane 1: *nuoM* T178C (expected bands at 7598, 6549, 3340, 2758 and 1075 bps with HindIII), lane 2: *nuoM* S105 (expected bands at 12442, 6953 and 2285 bps with NheI), lane 3: *nuoM* T422C (expected bands at 18759 and 2561 bps with NdeI), lane 4: *nuoM* S425C (expected bands at 18768 and 2562 bps with NdeI).

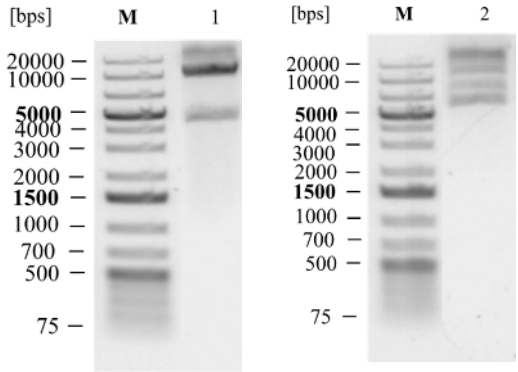

Figure 4.6: Restriction analysis for the mutations. The GeneRuler 1 kb Plus DNA Ladder (M) was used as a reference. Lane 1: *nuoM* K234C (expected bands at 8978, 8482, 3860, 2758 bps with KpnI), lane 2: *nuoM* D258C (expected bands at 7527, 5526, 2873, 2743, 1816, 586, 229 and 20 bps with EcoRI).

Positive clones identified by DNA sequencing were used to prepare bacterial glycerol stocks and cultures were stored at -80°C.

4.1.3 Cell growth

Cell growth of mutants was performed in auto-induction medium at a volume of 9.6 L. The OD_{600} was measured every hour. Cells were harvested at an OD_{600} between 3.5 and 3.8. Figures 4.7 and 4.8 show the growth curves of the mutant strains and that of the parental strain.

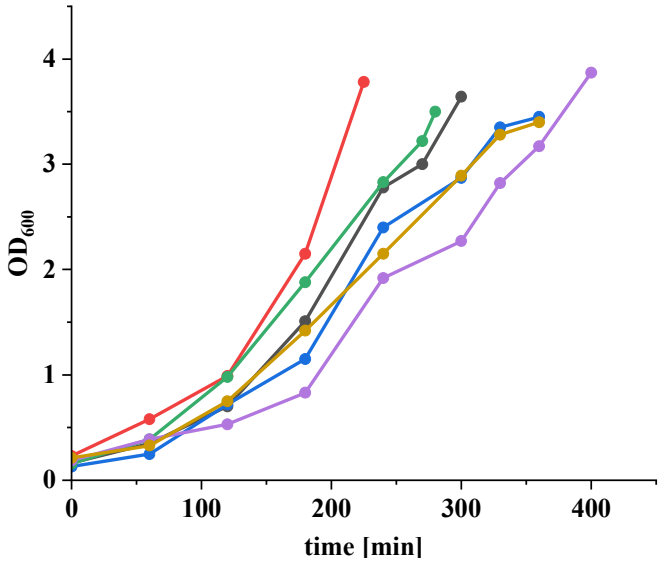

Figure 4.7: Growth of BWΔndhnuo::npt//pBADnuo$_{his}$*nuoF* (wild type, black); E108C^{M} (red); H117C^{M} (blue); H159C^{M} (green); S105C^{M} (magenta), and S425C^{M} (gold) in auto-induction medium.

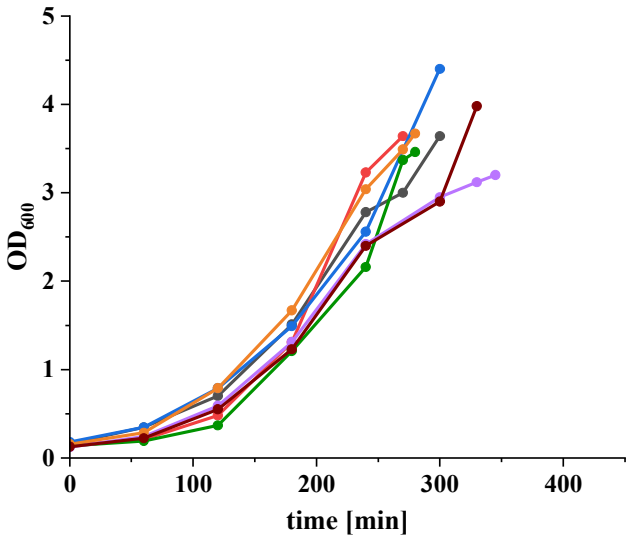

Figure 4.8: Growth of BWΔndhnuo::npt//pBADnuo$_{his}$*nuoF* (black); T332C^{M} (red); T422C^{M} (blue); T178C^{M} (green); S414C^{M} (orange); K234C^{M} (magenta) and D258C^{M} (brown) in auto-induction medium.

Growth of all mutant strains did not differ from that of the parental strain, thus, the mutations did not have any effect on complex I functions. The growth in 9.6 L medium yielded 50 to 75 g (wet weight) *E. coli* cells.

4.1.4 NADH oxidase activity of cytoplasmic membranes from *nuoM* mutants

Cytoplasmic membranes were prepared from the mutant strains. As a reference, the parental strain was grown and cytoplasmic membranes were prepared. The NADH oxidase activity of membranes was measured with a Clark-type oxygen electrode. 5 µL of membrane suspension was mixed with 2 mL A_{KI}-buffer (pH 6.0) and the reaction was started by the addition of 125 µM NADH. NADH oxidase activities are listed in Table 4.1. The activity of the parental strain was set to 100%. Its value (0.42 U/mg) was in accordance with the one described in the literature [260]. The NADH oxidase activity of the $H117C^M$, $S105C^M$, $S425C^M$, $D258C^M$ mutant were similar to that of the parental strain. Two mutants, $T422C^M$ and $T178C^M$, showed higher activity.

Table 4.1: NADH oxidase activity of cytoplasmic membranes from NuoM mutants. The data were acquired in triplicate measurements of each sample. The average was calculated, and the standard deviation is given. The parental strain was used as reference; its value was set to 100%.

Membranes from strain BWΔΔ/pBAD*nuo*$_{his}$*nuoF*	**Location**	**NADH oxidase activity**	
		[U/mg]	**[%]**
without changes	-	0.420 ± 0.029	100 ± 7
$S105C^M$	cytoplasmic side	0.404 ± 0.011	96 ± 3
$E108C^M$		0.226 ± 0.027	54 ± 12
$H117C^M$		0.396 ± 0.032	94 ± 8
$H159C^M$		0.328 ± 0.016	78 ± 5
$T332C^M$	periplasmic side	0.256 ± 0.029	61 ± 11
$S414C^M$		0.218 ± 0.004	52 ± 2
$T422C^M$		0.598 ± 0.026	142 ± 4
$S425C^M$		0.427 ± 0.034	101 ± 8
$T178C^M$	central part	0.626 ± 0.072	149 ± 12
$K234C^M$		0.075 ± 0.020	18 ± 27
$D258C^M$		0.436 ± 0.023	104 ± 5

The NADH oxidase activity of the E108C^{M}, H159C^{M}, S414C^{M} and T332C^{M} mutants were lower than that of the parental strain. The K234C^{M} mutant showed only 18% of complex I activity. The NADH oxidase activity of the H117C^{M} mutant is shown in Figure 4.9 and compared with that of the parental strain. Both activities run parallel indicating no change in the mutant due to the mutation.

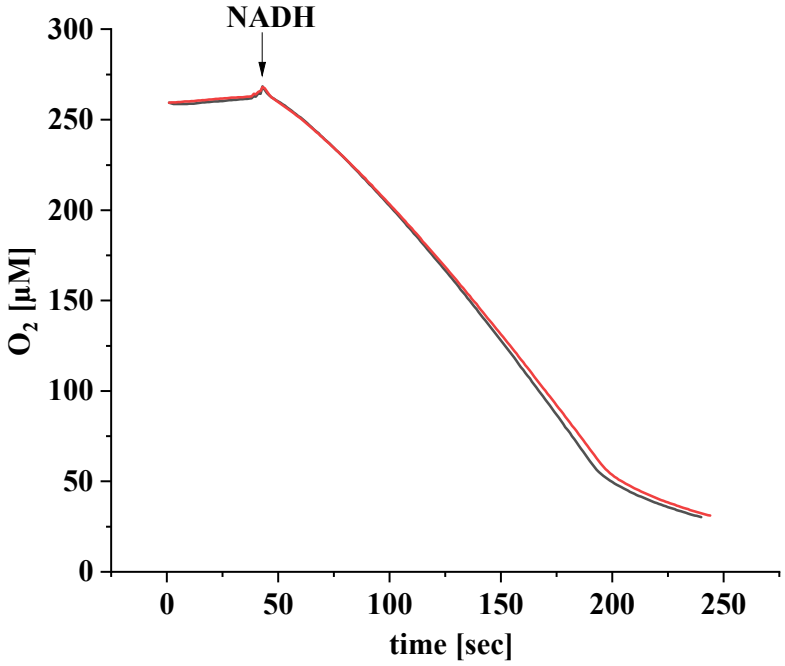

Figure 4.9: NADH oxidase activity of the parental strain (black) and the H117C^{M} mutant (red). The addition of NADH is marked with the arrow.

4.1.5 NADH/ferricyanide oxidoreductase activity of cytoplasmic membranes

The amount of complex I produced in the mutant membranes was determined by measuring the NADH/ferricyanide oxidoreductase activity. This activity is conferred by NuoF that carries the FMN cofactor (see chapter 2.2.1). It does not depend on participation of Fe/S clusters [261]. 2 µL of membranes were applied and protein concentration was determined using the biuret method. Membranes of the parental strain served as reference. The NADH/ferricyanide oxidoreductase activity of membranes are listed in Table 4.2. This activity is not linked with energy conversion and is commonly used to determine the complex I content in cytoplasmic membranes.

Table 4.2: NADH/ferricyanide oxidoreductase activities of cytoplasmic membranes from NuoM variants. The data were acquired in triplicate measurements of each sample. The average was calculated and standard deviation is given.

Membranes from strain BWΔΔ/pBAD*nuo*$_{his}$*nuo*F containing	**Location**	**NADH/ferricyanide oxidoreductase activity [U/mg]**	**[%]**
without changes	-	1.82 ± 0.19	100 ± 10
S105C^{M}	cytoplasmic side	3.36 ± 1.33	185 ± 40
E108C^{M}		0.59 ± 0.16	32 ± 27
H117C^{M}		1.34 ± 0.59	74 ± 44
H159C^{M}		0.62 ± 0.45	34 ± 73
T332C^{M}	periplasmic side	1.86 ± 1.31	102 ± 70
S414C^{M}		1.90 ± 0.94	104 ± 49
T422C^{M}		5.39 ± 2.93	296 ± 54
S425C^{M}		0.95 ± 0.50	52 ± 53
T178C^{M}	central part	3.17 ± 1.36	174 ± 75
K234C^{M}		1.11 ± 0.73	61 ± 66
D258C^{M}		4.20 ± 2.56	231 ± 61

The NADH/ferricyanide oxidoreductase activity of mutant membranes show that the complex I variants were produced in the mutants.

4.1.6 Preparation of NuoM variants

The parental and the *nuoM* mutant strains were cultivated in 9.6 L autoinduction medium and harvested at an OD_{600} between 3.5 and 3.8. 50-75 g cells (wet weight) were obtained and shock frozen. Membranes were obtained by differential centrifugation and cytoplasmic membranes were homogenized in A_{KI}-buffer (pH 6.8). Complex I and its variants were purified by two chromatographic steps. All complex I variants were obtained by the same procedure described in 3.8.1. Table 4.3 shows the yields of the preparations that varied from 4.7 to 18 mg.

Table 4.3. Yields of the performed steps to obtain proteins.

Residue (mutation)	Location	Cell mass, g	Membrane mass, g	Protein mass, mg
without changes	-	66.48	14.04	6.06
$S105C^M$	cytoplasmic side	62.94	16.10	18.00
$E108C^M$		66.78	13.91	4.72
$H117C^M$		68.08	18.50	7.51
$H159C^M$		73.53	16.35	6.49
$S414C^M$	periplasmic side	63.98	13.54	8.83
$T332C^M$		58.71	14.03	8.31
$T422C^M$		63.68	17.00	14.64
$S425C^M$		61.88	14.45	4.53
$T178C^M$	central part	59.34	17.01	13.00
$K234C^M$		56.47	13.84	6.60
$D258C^M$		52.90	12.03	7.40

Figures 4.10 and 4.11 show typical elution profiles obtained for the chromatographic steps of complex I.

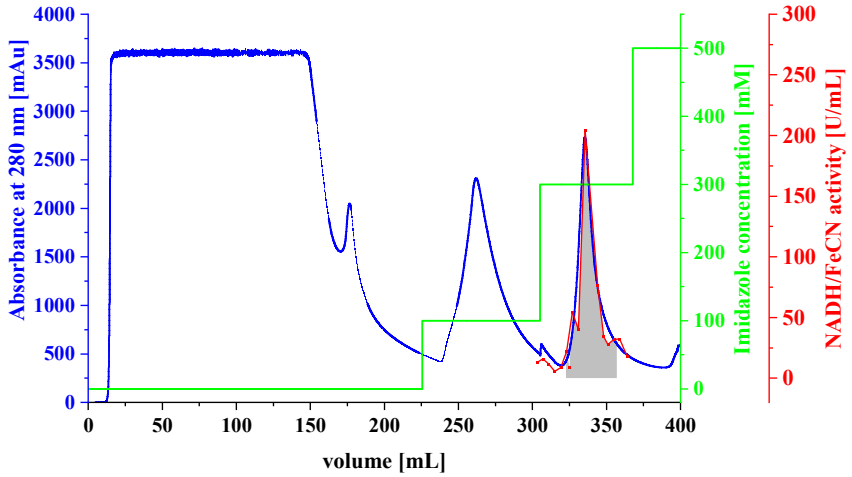

Figure 4.10: Elution profile of the Ni^{2+} affinity chromatography. The absorbance at 280 nm is shown in blue; the imidazole concentration in green. The NADH/ferricyanide activity is shown in red. Fractions that were pooled and concentrated are shown in grey.

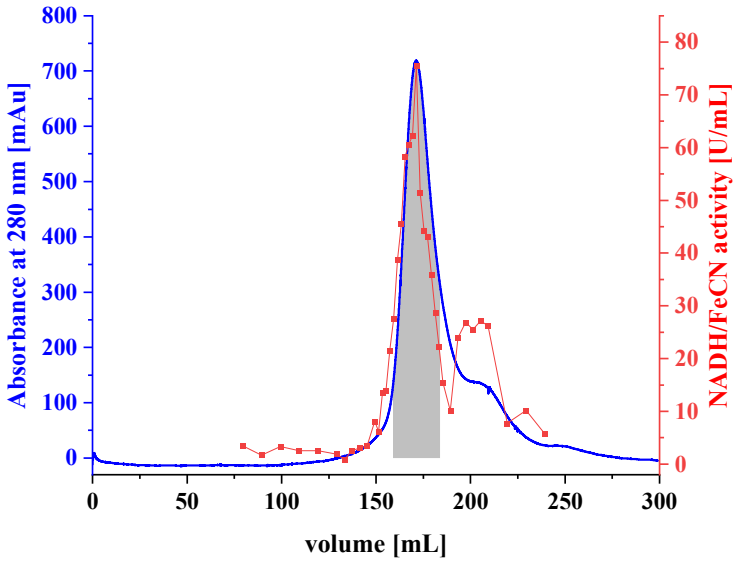

Figure 4.11: Elution profile of the size exclusion chromatography. The absorbance at 280 nm is shown in blue. NADH/ferricyanide activity is shown in red.

Table 4.4 shows the yields of individual purification steps for complex I. The table shows that the NADH/ferricyanide activity value is strongly increased after affinity chromatography. The yield of the complex I purification equals 25%, which corresponds to the literature value [260].

Table 4.4: Preparation of complex I from 68.5 g cells (wet weight).

Preparation step	Volume	Protein	NADH/ferricyanide activity		Yield
			total	specific	
	[mL]	[mg]	[U]	[U/mg]	[%]
Membrane suspension	13.64	1009.08	1839.90	1.82	100
Detergent extraction	125.00	1578.75	4376.25	2.77	238
Probond Ni^{2+}-IDA	0.80	20.15	2095.94	104.01	114
Superose 6	0.278	4.85	464.21	96.65	25

Preparation of the complex I variants resulted in similar values (data not shown).

4.1.7 SDS-PAGE of the NuoM variant preparations

The purity of the preparations of complex I and the NuoM variants was analyzed by SDS-PAGE (Figs. 4.12-4.14).

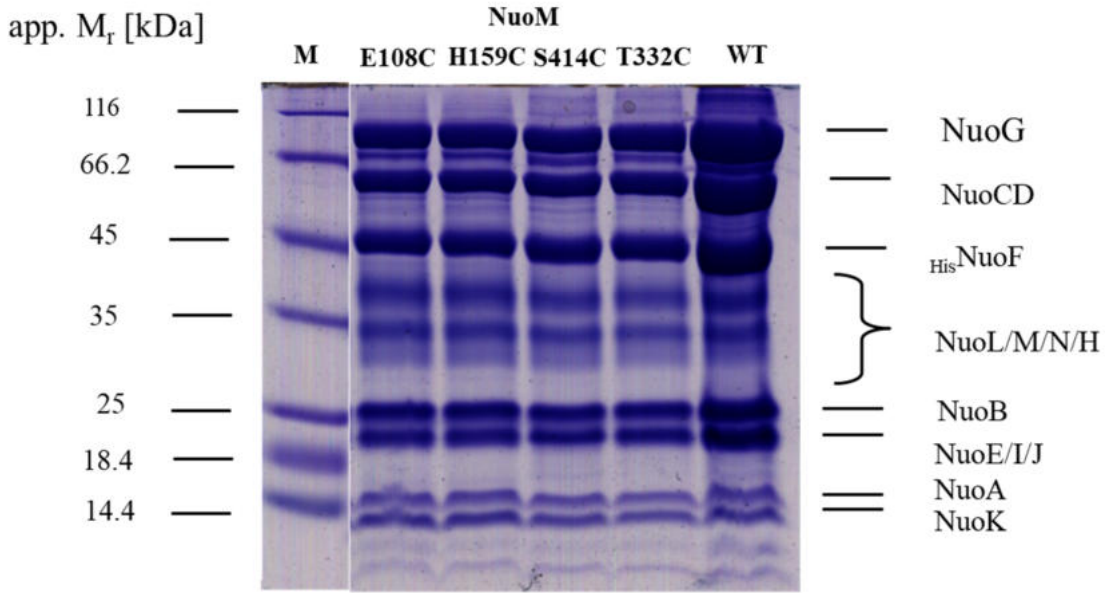

Figure 4.12: SDS-PAGE of preparations of complex I and its variants. The lane M shows the *unstained protein marker* (Thermo Fischer Scientific). The bands are assigned to individual complex I subunits according to their molecular mass. The faint band below NuoG at about 82 kDa corresponds to a proteolytic degradation product of NuoG [262].

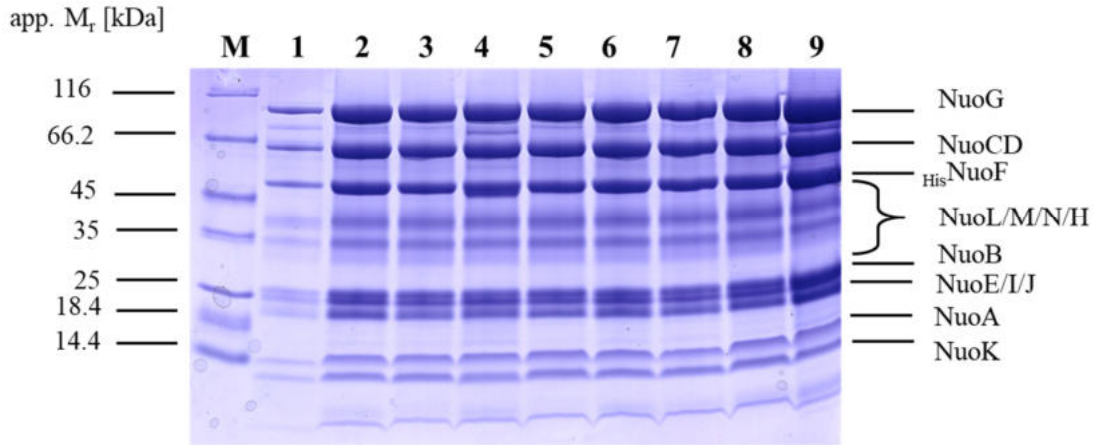

Figure 4.13: SDS-PAGE of preparations of complex I and its variants. The lane M belongs to the *unstained protein marker* (Thermo Fischer Scientific). Lanes are assigned as follows: complex I (1), NuoM S105C (2), NuoM H117C (3), NuoM T422C (4), NuoM S425C (5), NuoM T178C (6), NuoM K234C (7) and NuoM D258C (8), complex I (9, in higher concentration).

Several NuoM variants were purified a second time. The purity of the preparations obtained in a second round is shown in Figure 4.14. As in the first round, all complex I subunits are contained in the preparations of the NuoM variants.

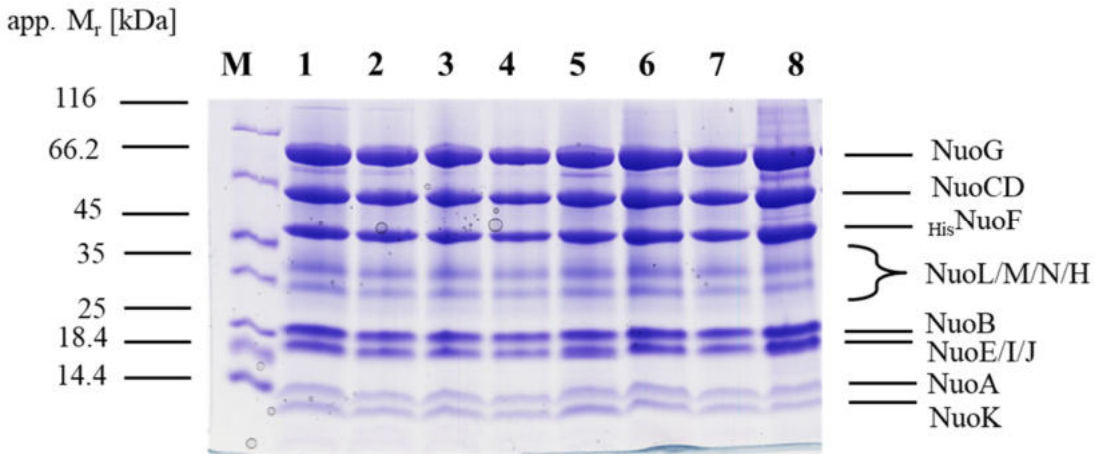

Figure 4.14: SDS-PAGE of preparations of complex I and its NuoM variants. The lane M shows the *unstained protein marker* (Thermo Fischer Scientific). Lanes are assigned as follows: NuoM E108C (1), NuoM H159C (2), NuoM T332C (3), NuoM S414C (4), NuoM T422C (5), NuoM S105C (6), NuoM H117C (7) and complex I (8).

4.1.8 Mass photometry of the preparations

Mass photometry was conducted to determine the stability of the variants preparations. Protein samples were diluted into a detergent-free buffer. The results are shown in Figures 4.15-4.18.

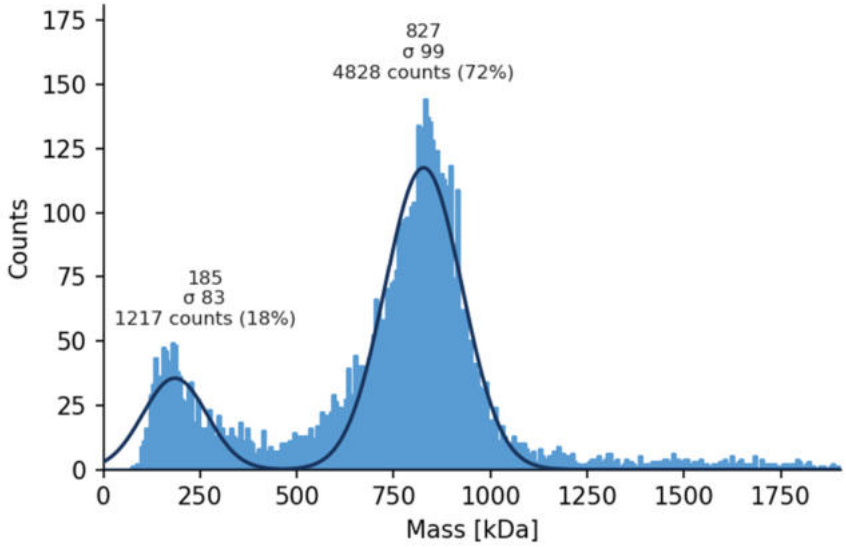

Figure 4.15: Mass distribution of the T332C^{M} variant. Scatter plots of the binding events with corresponding Gaussian adjustments are shown. The protein sample was diluted to 50 nM. The mass is given in kDa**,** binding events and percentages are given.

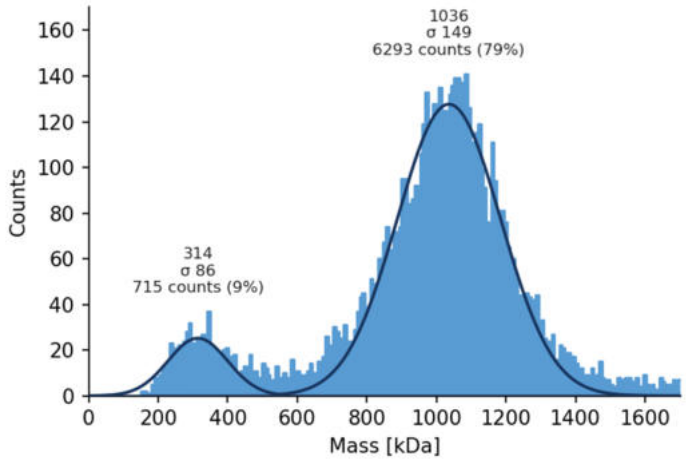

Figure 4.16: Mass distribution S414C^{M} variant. Scatter plots of the binding events with corresponding Gaussian adjustments are shown. Protein sample was diluted to 50 nM. The mass is given in kDa, binding events and percentages are given.

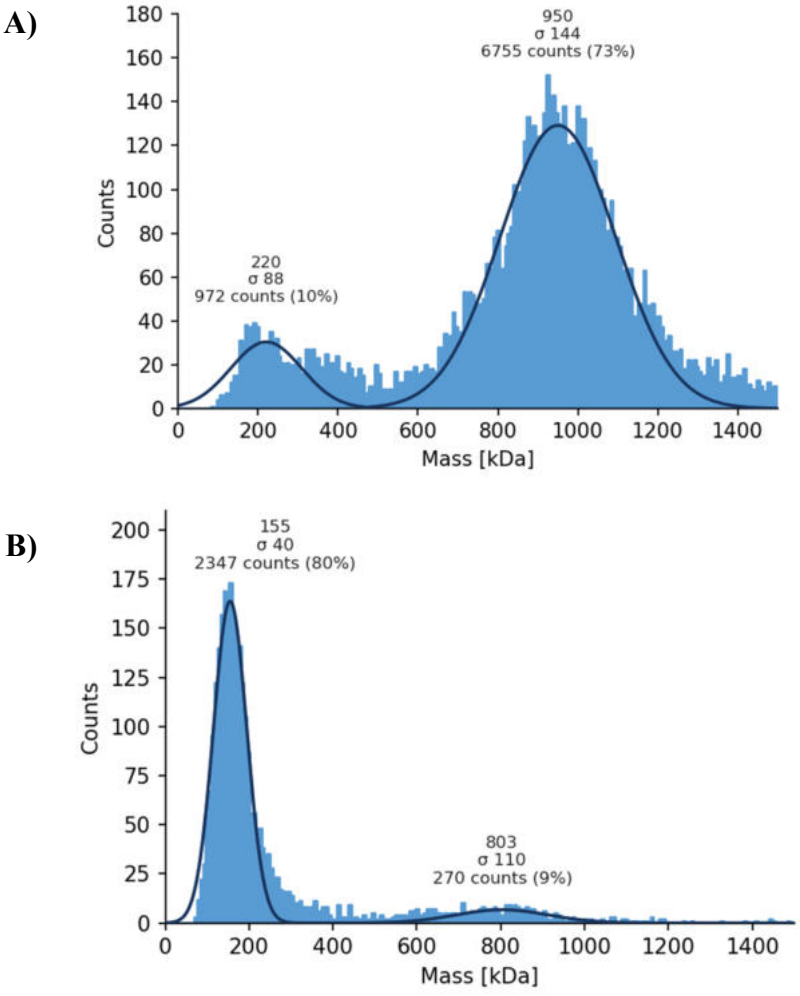

Figure 4.17: Mass distribution of H159C^{M} variant measured directly (A) and 5 min after dilution in detergent-free buffer (B). Scatter plots of the binding events with corresponding Gaussian adjustments are shown. Protein sample was diluted to 50 nM. The mass is given in kDa, binding events and percentages are given.

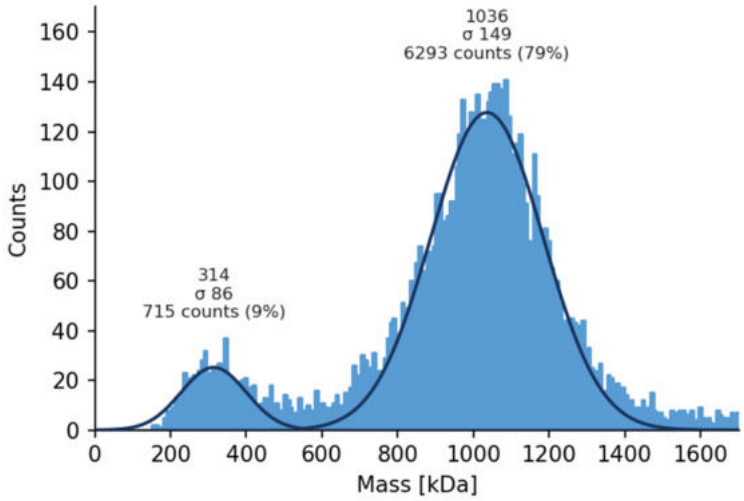

Figure 4.18: Mass distribution S414C^{M} variant. Scatter plots of the binding events with corresponding Gaussian adjustments are shown. Protein sample was diluted to 50 nM. The mass is given in kDa, binding events and percentages are given.

It was proven that the variant preparations were stable and appeared in a main peak around 827-1036 kDa. The mass of the peak may vary depending on the number of detergent molecules bound to the protein. The additional peak at around 185-314 kDa can be assigned to a soluble fragment of complex I containing subunits NuoEFG [257]. Complex I variants are not stable in the detergent-free buffer in which the measurements are performed. This was proven by mass photometric analysis 5 min after dilution of the sample (Fig. 4.17B). After 5 min in detergent-free buffer the major part of the complex I variant disassembled.

4.2. Activity of the preparations

4.2.1 NADH/ferricyanide oxidoreductase activity

The specific NADH/ferricyanide oxidoreductase activity of the variants were determined as described in 3.9.2. NADH/ferricyanide oxidoreductase activities were recorded at 410 nm as a decrease of $K_3[Fe(CN)_6]$ concentration. Table 4.5 shows NADH/ferricyanide activity of the preparations, complex I activity was set to 100%.

The NADH/ferricyanide oxidoreductase activity of the H117C^{M}, S414C^{M} and T332C^{M} variants was similar to or even higher (S105C^{M}) than that of the complex I. The E108C^{M}, T422C^{M}, T178C^{M} and D258C^{M} variants showed a slightly decreased activity (61-84%). The H159C^{M}, S425C^{M} and K234C^{M} variants showed an approximately halved activity.

Table 4.5: Specific NADH/ferricyanide activity of preparations of complex I NuoM variants.

Complex I variant	Location	NADH/ferricyanide oxidoreductase activity	
	-	[U/mg]	[%]
without changes		98.6 ± 5.3	100
S105C^{M}	cytoplasmic side	109.0 ± 5.6	111
E108C^{M}		59.8 ± 9.4	61
H117C^{M}		98.0 ± 15.6	99
H159C^{M}		50.7 ± 5.4	51
T332C^{M}	periplasmic side	93.0 ± 7.5	94
S414C^{M}		93.9 ± 5.2	95
T422C^{M}		68.2 ± 15.3	69
S425C^{M}		51.7 ± 2.9	52
T178C^{M}	central part	67.8 ± 0.8	69
K234C^{M}		49.4 ± 1.7	50
D258C^{M}		83.5 ± 13.5	84

4.2.2 NADH:decyl-Q oxidoreductase activity

NADH:decyl-Q oxidoreductase activities were measured for all NuoM variants to study the effect of the mutations on electron transfer. Table 4.6 shows NADH:decyl-Q oxidoreductase activities for all purified cysteine variants. The activity of complex I was set to 100%. Most variants showed a slightly decreased activity compared to complex I. The NADH:decyl-Q oxidoreductase activity of the H117C^{M} variant was identical to that of the complex I. For the other variants, the NADH:decyl-Q oxidoreductase activity was 64-94% of that of the complex I. Two mutations located in the central part of NuoM K234C^{M}, D258C^{M} had a noticeable effect on the NADH:decyl-Q oxidoreductase activity and decreased it to 14 and 36%, respectively. Thus, all variants with the exception of K234C^{M} and D258C^{M} exhibited a NADH:decyl-Q oxidoreductase activity similar to that of the parental complex I.

Table 4.6: NADH:decyl-Q oxidoreductase activity for complex I and NuoM variants. Measurements were performed in triplicates, mean value ± SEM is provided.

Complex I variant	Location	NADH:decyl-Q oxidoreductase activity	
		[U/mg]	[%]
without changes	-	24.7 ± 1.3	100
S105C^{M}	cytoplasmic side	19.7 ± 7.7	80
E108C^{M}		19.9 ± 2.0	81
H117C^{M}		25.0 ± 4.8	101
H159C^{M}		18.9 ± 4.9	77
T332C^{M}	periplasmic side	15.7 ± 0.5	64
S414C^{M}		17.1 ± 7.1	69
T422C^{M}		16.0 ± 3.7	65
S425C^{M}		23.1 ± 1.0	94
T178C^{M}	central part	19.6 ± 7.1	79
K234C^{M}		3.4 ± 0.7	14
D258C^{M}		8.8 ± 0.8	36

Figures 4.19-4.21 show the time course of the reaction.

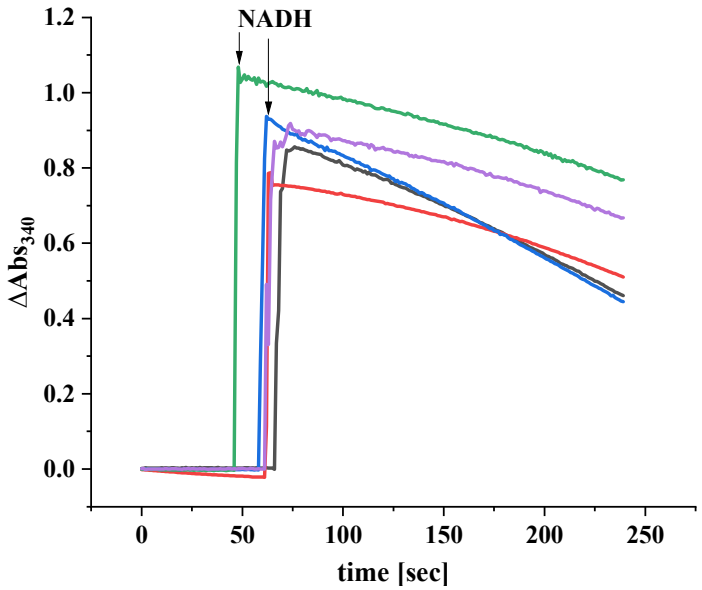

Figure 4.19: NADH:decyl-Q oxidoreductase activity of complex I and NuoM variants with mutations on the cytoplasmic side. The addition of NADH is marked with an arrow. Complex I (black), E108C^{M} (red), H117C^{M} (blue), H159C^{M} (green) and S105C^{M} (magenta) are shown.

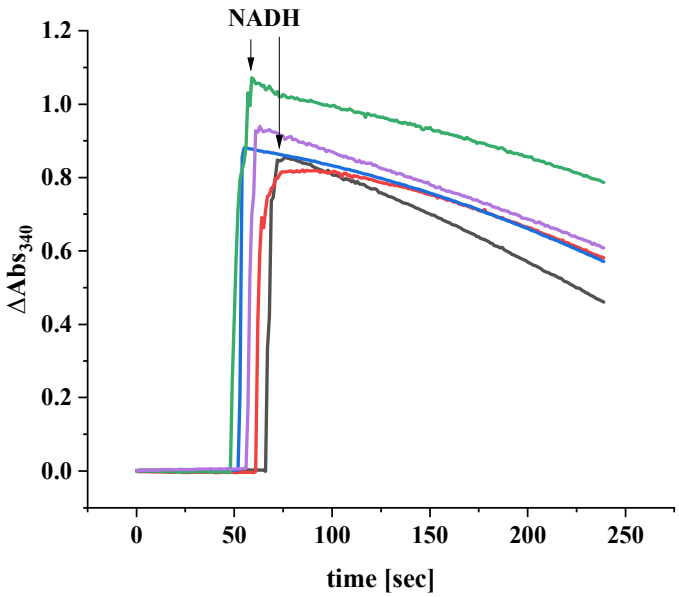

Figure 4.20: NADH:decyl-Q oxidoreductase activity of complex I and NuoM variants with mutations on the periplasmic side. The addition of NADH is marked with an arrow. Complex I (black), S414C^{M} (red), S425C^{M} (blue), T332C^{M} (green) and T422C^{M} (magenta) are shown.

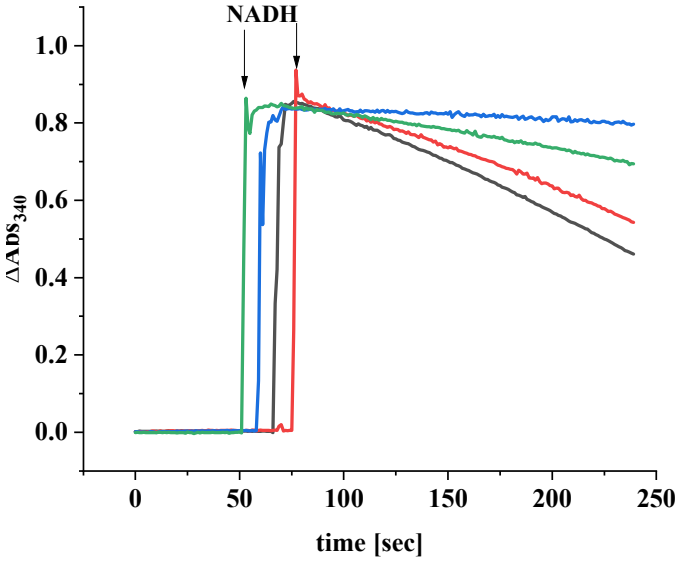

Figure 4.21: NADH:decyl-Q oxidoreductase activity of complex I and NuoM variants in the central part of NuoM. The addition of NADH is marked with an arrow. Complex I (black), T178C^{M} (red), K234C^{M} (blue) and D258C^{M} (green) are shown.

The K234C^{M} variant lost 86% of the wild-type NADH:decyl-Q oxidoreductase activity. This specific variant also had the lowest NADH oxidase activity in the membrane (50% compared to complex I).

4.2.3 Proton translocation activity

The proton translocation activity was determined to see if the mutations influenced proton translocation. The proton translocation activity was measured using ACMA fluorescence as an indicator of a pH gradient across the membrane. To perform the measurements, the variants were reconstituted into *E. coli* polar lipids, and proteoliposomes were obtained. The NADH/ferricyanide activity was determined for each proteoliposome to calculate the amount of reconstituted complex I. DDM was added to the proteoliposomes to open them, and NADH/ferricyanide activity was measured again. The ratio of activities before and after DDM addition describes the orientation of complex I in the proteoliposomes. Only complex I orientated with the peripheral arm outwards contributes to the activity as the membrane is not permeable for NADH. It was found that 30-60% of reconstituted complex I variants is located with its peripheral arm outwards. For the ACMA fluorescence measurements, proteoliposomes were mixed with ACMA buffer, and the reaction was started with the addition of NADH. The proton gradient was dissipated by adding CCCP. The kinetics shows generation of proton gradient upon addition of NADH. Quench of ACMA serves an indicator of proton translocation. Figure 4.22 shows the ACMA fluorescence for some of the variants.

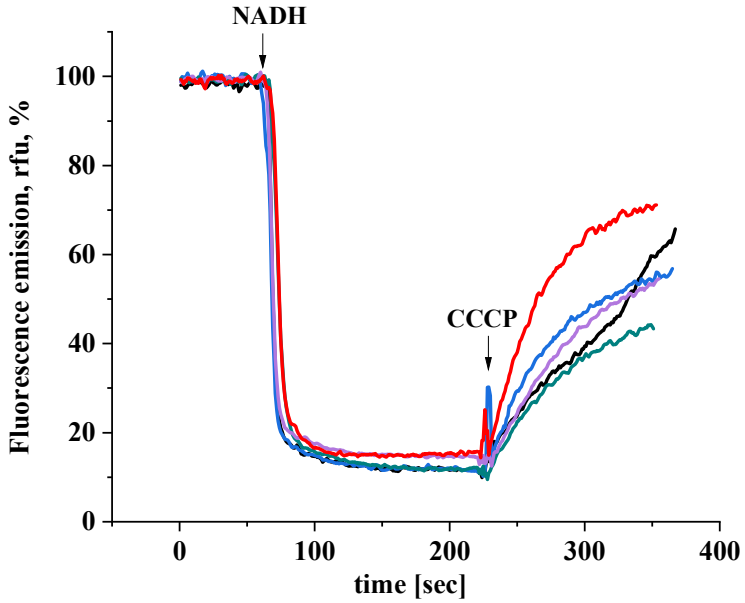

Figure 4.22: ACMA quench due to proton translocation by complex I and NuoM variants after reconstitution into liposomes. Quench of ACMA fluorescence was measured at an excitation wavelength of 430 nm and emission wavelength 480 nm for complex I (black), E108C^{M} (blue), H159C^{M} (green), S414C^{M} (magenta) and T332C^{M} (red). The addition of NADH and CCCP accordingly is indicated with arrows.

Results obtained for several complex I variants (E108C^{M}, S414C^{M}, H159C^{M} and T332C^{M}) revealed that all variant preparations were capable to perform proton translocation type complex I value. Table 4.7 shows the obtained values for ACMA fluorescence quench.

Table 4.7: ACMA fluorescence quench.

Sample	Quench, %
WT	74
E108C^{M}	77
T332C^{M}	69
H159C^{M}	71
S414C^{M}	70

4.3. Labelling of the variants

To perform IR-spectroscopic measurements, all variants were labelled with nitrile probes. The newly introduced cysteine residues were labelled according to the procedure as described in 3.10.1. The individual reaction steps are shown in Figure 4.23.

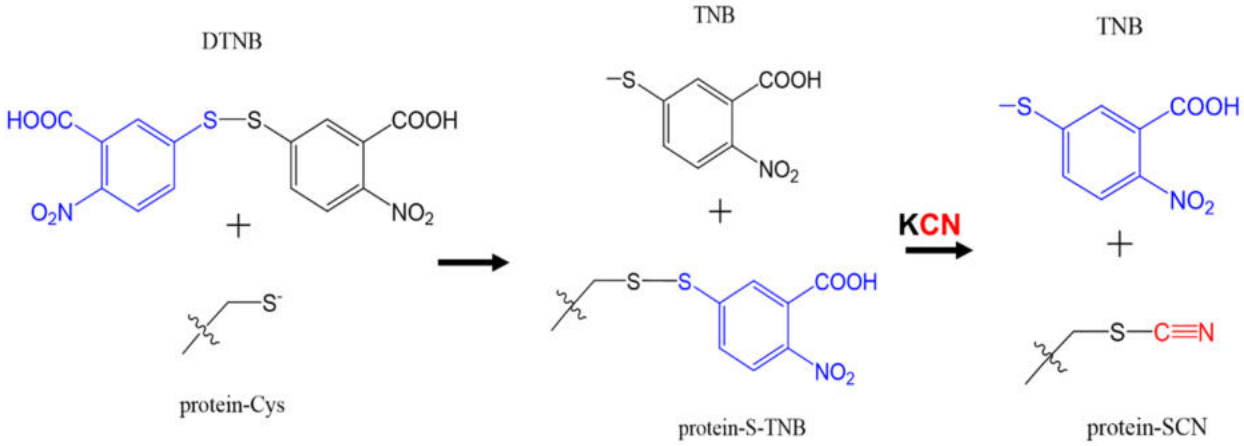

Figure 4.23: The procedure to attach cyanide residue to cysteine [211].

4.3.1 Label efficiency

The label efficiency of the preparations of the NuoM variants was calculated to determine whether the targeted cysteine residue was labelled with the nitrile group. Labelling efficiency was determined with UV/vis spectroscopy. Labelled variants showed a characteristic peak at 412 nm that was assigned to the release of TNB^{-} from the cysteines (Fig. 4.24). Table 4.8 shows label

efficiency of the individual variants.

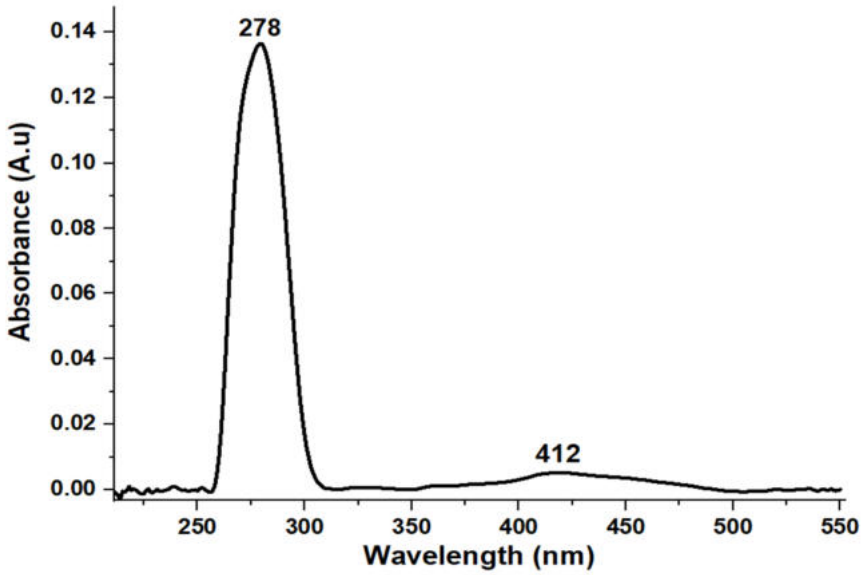

Fig. 4.24: UV/vis spectrum of labeled complex I E108C^{M} variant. The peak at 278 nm is assigned to complex I, the one at 412 nm belongs to the released TNB^- which is produced after treating complex I with KCN.

Example on label efficiency calculation in presented in Appendix 7.3.

Table 4.8: Label efficiency of the NuoM variants.

Variant	Location	Protein concentration, µM	[TNB^-], µM	Label efficiency, %
S105C^{M}	cytoplasmic side	5.87	5.7	~97
E108C^{M}		4.60	3.25	~71
H117C^{M}		4.99	5.02	~100
H159C^{M}		1.99	1.85	~ 93
T332C^{M}	periplasmic side	1.48	2.22	~100
S414C^{M}		1.70	3.72	~100
T422C^{M}		8.19	7.13	~ 87
S425C^{M}		11.86	16.21	~100
T178C^{M}	central part	9.40	9.52	~100
K234C^{M}		7.6	4.07	~ 77
D258C^{M}		7.92	7.39	~93

It was found that all variants were labelled with 71 to 100% efficiency.

4.3.2 NADH:Q oxidoreductase activities for labelled variants

To determine whether the label attached to a cysteine residue affected activity, NADH:decyl-Q oxidoreductase activity was determined for the variants after cyanide labelling. Table 4.9 shows the NADH:decyl-Q oxidoreductase activities of labelled variants compared to the non-labelled ones. Labelling of the variants resulted in a decreased NADH:decyl-Q oxidoreductase activity. The activities were diminished approximately by 30% due to the labelling. The loss of activity could partly also be explained by the fact that samples were frozen and thawed for this procedure. The loss of activity can also be also due to the loss of S-H bond. The E108C^{M} resulted in 52% activity, revealing the sensitivity of the mutated position to the changes introduced by insertion of the label. Attachment of the label causes structural changes that can result in diminished activity.

Table 4.9: NADH:decyl-Q oxidoreductase activity of labelled complex I variants.

Sample	Location	NADH:decyl-Q oxidoreductase activity (before labelling)	NADH: decyl-Q oxidoreductase activity (after labelling)	
		[U/mg]	[U/mg]	[%] (compared to non-labelled)
S105C^{M}	cytoplasmic side	17.8 ± 5.1	14.1 ± 2.2	**79**
E108C^{M}		19.9 ± 2.0	10.4 ± 0.8	**52**
H117C^{M}		13.4 ± 0.4	13.1 ± 0.7	**98**
H159C^{M}		18.9 ± 4.9	13.4 ± 1.8	**71**
T332C^{M}	periplasmic side	15.7 ± 0.5	13.0 ± 1.9	**83**
S414C^{M}		12.3 ± 7.1	11.5 ± 1.2	**94**
T422C^{M}		13.7 ± 2.2	12.3 ± 2.8	**90**
S425C^{M}		23.1 ± 1.0	16.9 ± 1.8	**73**
T178C^{M}	central part	19.6 ± 7.1	16.8 ± 0.7	**85**
K234C^{M}		3.4 ± 0.7	2.4 ± 0.2	**71**
D258C^{M}		8.8 ± 0.8	5.3 ± 0.3	**64**

4.3.3 SDS-PAGE of the labelled variants

SDS-PAGE of the labelled NuoM variants revealed that the labelling procedure had no influence on the subunit composition of the variants. Figure 4.25 shows the SDS-PAGE of the labelled

variants. All labelled variants comprised the same subunits than complex I. The label itself cannot be detected by SDS-PAGE due to its small size.

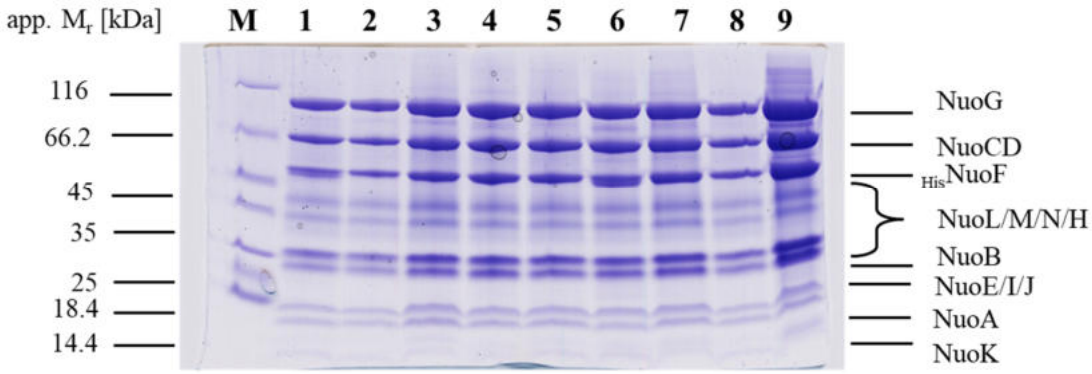

Figure 4.25: SDS-PAGE of the labelled NuoM variants. The lane M shows the pattern of the *unstained protein marker* (Thermo Fischer Scientific). Lanes are assigned as follows: E108C^{M}-CN (1) T332C^{M}-CN (2), S414C^{M}-CN (3), S105C^{M}-CN (4), H117C-CN^{M} (5), T422C^{M}-CN (6), T178C^{M}-CN (7), K234C^{M}-CN (8) and complex I (9).

4.3.4 Mass photometry of the labelled variants

Mass photometry was used to test the stability of the labelled variants. Figure 4.26 shows the results of mass photometry measurements for the T422C^{M}-CN variant.

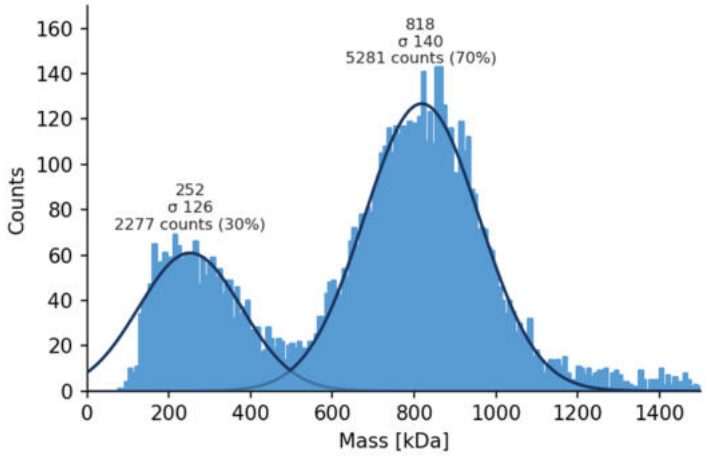

Figure 4.26: Mass distribution of the T422C^{M}-CN variant. Scatter plots of the binding events with corresponding Gaussian adjustments are shown. Protein sample was diluted to 50 nM. The mass is given in kDa**,** binding events and percentage are given.

Figure 4.26 was compared to Figures 4.15-4.18 showing the mass distribution of the variant preparations before the labelling and it turned out that labelling did not change mass distribution profile. This indicated that nitrile labelling did not influence the variants' stability.

4.4 IR-spectroscopic characterization of the NuoM variants

Changes in the molecular environment of the nitrile labels attached to the NuoM variants were followed by SEIRAS techniques. The infrared absorbance spectra were recorded for the labelled variants in the absence and presence of substrates NADH and Q-2. Spectroscopic shifts of the nitrile absorbances were analyzed.

4.4.1 Gold layer formation

A gold layer was formed on the silicon ATR crystal surface according to the following reaction:

$$3\ Si\ (s) + 18\ F^-\ (aq) + 4\ AuCl^{4-}\ (aq) \rightarrow 3\ SiF_6^{2-}\ (aq) + 4\ Au\ (s) + 16\ Cl^-\ (aq) \quad (8)$$

The procedure of obtaining a gold surface is described in 3.11.1. NH_4F is used in the first step for the activation of the surface.

4.4.2 Ni-NTA surface modification

Applying a protein sample on the gold surface of the crystal leads to protein denaturation by the metal. To prevent denaturation, a linker is inserted between the protein and the gold surface. Here, the Ni-NTA immobilization procedure was applied as it has the advantage of attaching complex I variant to the Ni-NTA immobilized surface by the His-tag fused to NuoF. Moreover, the Ni-NTA immobilization procedure has the advantage of orientating the complex towards the crystal. Figure 4.27 depicts the immobilization steps.

A)

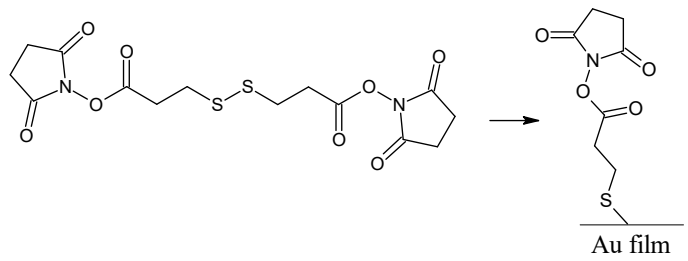

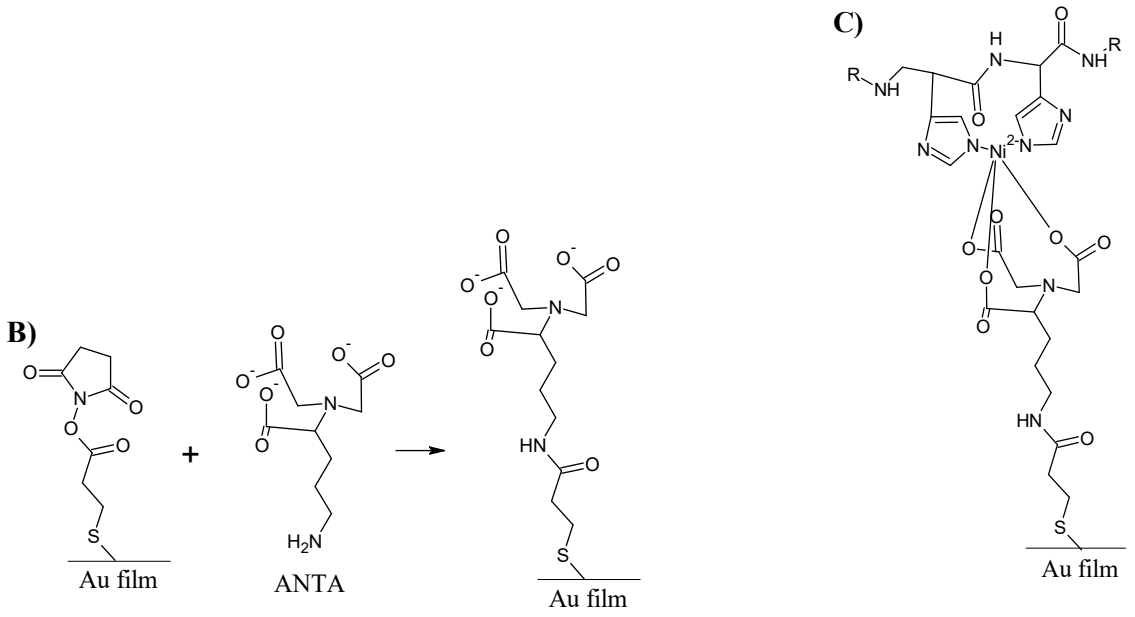

Figure 4.27: Reactions to build the Ni-NTA-SAM surface. A) Self-assembly of TSP on the gold monolayer; B) reaction of ANTA with TSP on the gold layer; C) complexation of Ni^{2+} on ANTA-TSP gold layer [263].

In the first step, di-N-hydroxysuccinimide ester (DTSP) was added to the gold surface and incubated for 1 hour. Typical DTSP bands were observed by IR-spectroscopy at 1811, 1782 and 1738 cm^{-1} (Fig. 4.28A). These bands are characteristic of the succinimidyl group after S-S bond cleavage. The excess DTSP was removed, the surface was covered with Nα,Nα-bis (carboxymethyl)-L-lysine (ANTA), and spectra were recorded for 3 hours. The reaction of lysine with the TSP moiety formed an amide bond. The formation of this bond was proved by the amide I peak at 1616 cm^{-1} (Fig. 4.28B). The peak at 1397 cm^{-1} corresponds to the symmetric stretching of $\upsilon(COO^-)$. In the end, the surface was covered with 50 mM nickel(II) perchlorate hexahydrate ($Ni(ClO_4)_2$) solution for 1 h. This process was visualized by the appearance of two bands at 1616 and 1402 cm^{-1} (Fig. 4.28C). These bands were assigned to the symmetric and asymmetric stretches of the ANTA carboxylate group that was deprotonated after complexation with Ni^{2+} [258].

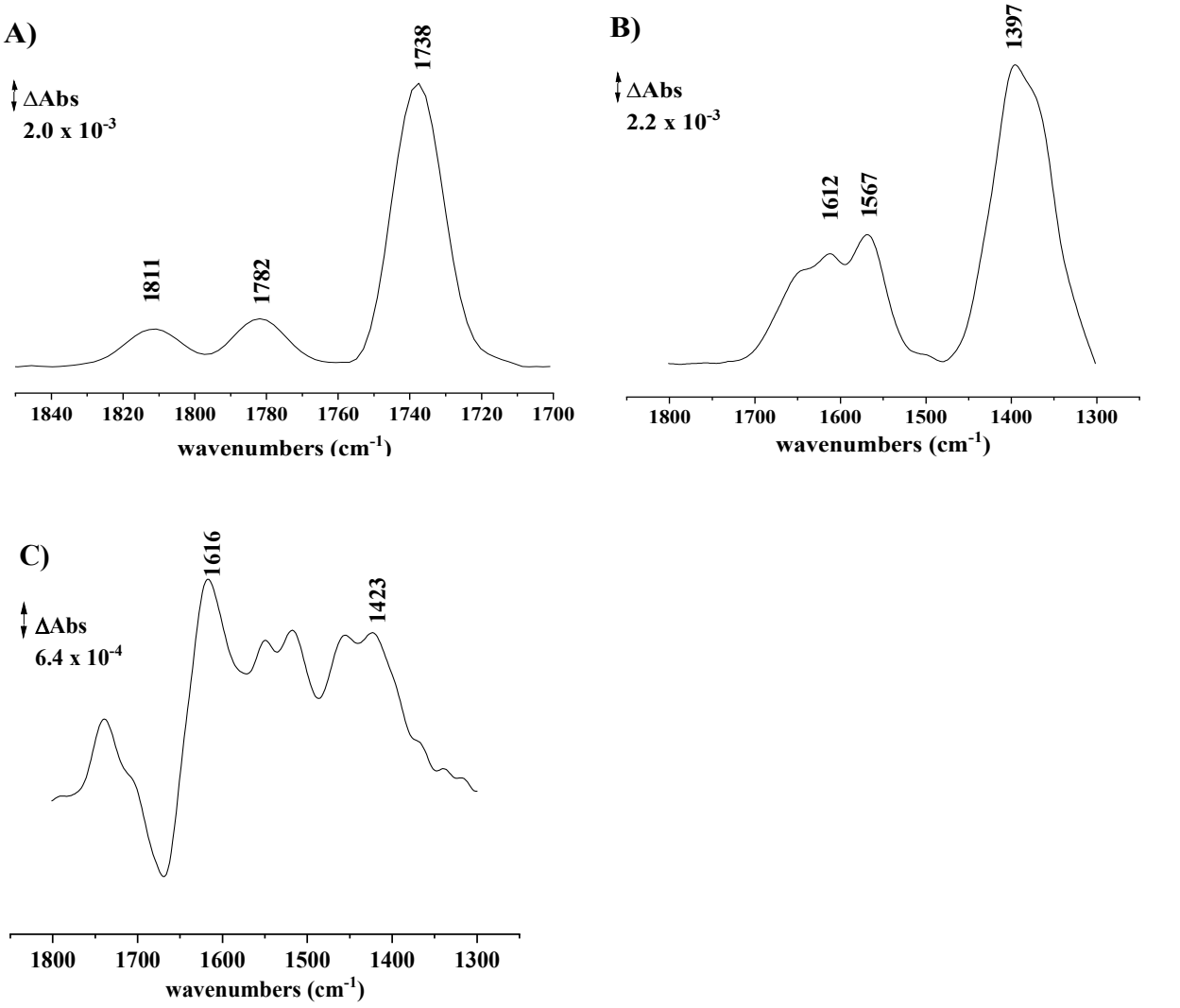

Figure 4.28: ATR-FTIR spectra following of the crystal surface modification steps. A) Self-assembly of the TSP monolayer on the bare Au surface (reference spectrum: gold layer covered with DMSO), B) cross-linking of ANTA with TSP monolayer (reference spectrum: DTSP SAM in water), C) complexation of Ni^{2+} by NTA (TSP-NTA SAM covered with water).

4.4.3 Amide I band

The amide I band is located between 1600 and 1700 cm^{-1}. It can be used to control the integrity of the protein after labelling and immobilization. The amide I band can also be used for secondary structure analysis. Figure 4.29 shows the amide I deconvolution band for the various complex I variants.

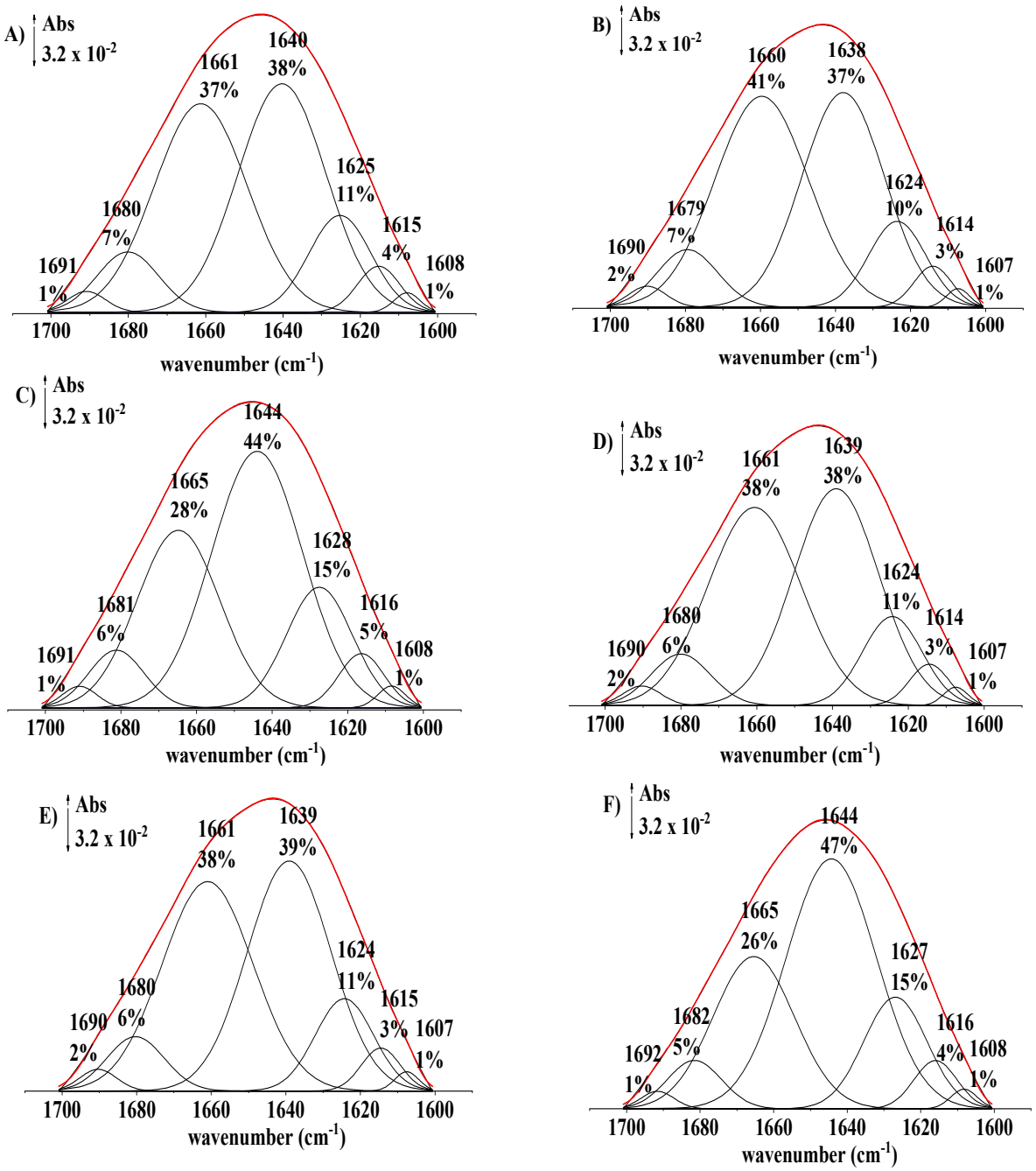

Figure 4.29. Deconvolution of the amide I band as observed in several NuoM variants. A) Labelled T332C^{M}; B) Labelled T332C^{M} incubated with NADH; C) Labelled H159C^{M}; D) Labelled H159C^{M} incubated with NADH; E) Labelled S414C^{M}; F) Labelled NuoM S414C^{M} incubated with NADH.

The amide I band is a characteristic peak in the FTIR spectra of proteins that reflects the secondary structure of the protein. In the case of complex I variants described above, the amide I band appears at around 1644 cm^{-1}, which is consistent with a predominant α-helical secondary structure, as observed in complex I. Deconvolution analysis was performed to further compare the amount of

distinct secondary structure elements of the NuoM variants before and after incubation with substrates. The data show that the peak positions of absorbances typical for secondary structure elements are found at the same wavenumbers for all variants after incubation with NADH and ubiquinone, indicating no significant changes in the secondary structure. The relative amount of the individual secondary structure elements did not also change significantly (Tab. 4.10-4.12). Overall, the results suggest that the mutations in the complex I variants do not significantly affect the secondary structure of the protein, and that the binding of NADH and ubiquinone does not cause major structural changes in the protein. It can be an evidence of the sample's stability and its structural integrity. This information is valuable for understanding the mechanism of complex I.

Table 4.10. Deconvolution distribution for the E108C^{M} variant before and after incubation with NADH and ubiquinone.

Conformation	Labelled	NADH	Q-2
α-helices	1643 (44%)	1640 (40%)	1644 (50%)
Antiparallel β-sheet	1626/1681 (21%)	1625/1682 (16%)	1627/1680 (25%)
β-turns	1664 (28%)	1663 (39%)	1665 (17%)
Intermolecular (aggregated β-sheets)	1615 (7%)	1615 (5%)	1617 (8%)

Table 4.11. Deconvolution distribution for the H159C^{M} variant before and after incubation with NADH and ubiquinone.

Conformation	Labelled	NADH	Q-2
α-helices	1644 (44%)	1645 (47%)	1646 (48%)
Antiparallel β-sheet	1628/1681 (21%)	1628/1682 (22%)	1628/1682 (22%)
β-turns	1665 (28%)	1666 (24%)	1667 (23%)
Intermolecular (aggregated β-sheets)	1616 (7%)	1617 (7%)	1617 (7%)

Table 4.12. Deconvolution distribution for the T332C^{M} variant before and after incubation with NADH and ubiquinone.

Conformation	Labelled	NADH	Q-2
α-helices	1641 (42%)	1643 (47%)	1639 (42%)
Antiparallel β-sheet	1626/1680 (20%)	1625/1682 (19%)	1623/1680 (18%)
β-turns	1662 (31%)	1665 (29%)	1660 (33%)
Intermolecular (aggregated β-sheets)	1615 (7%)	1615 (5%)	1612 (7%)

4.4.4 Technical problems while performing spectroscopy measurements

The challenges encountered in performing spectroscopy measurements on the complex I variants can be attributed to the intrinsic variability of the biological system and the sensitivity the technique. Moreover, the differences observed in the data after incubation with NADH or Q may be attributed to the complex biochemical interactions induced by the addition of the substrates. These interactions may be influenced by factors such as the stability of the variants, the presence of other cofactors, the presence of oxygen during sample preparation, the concentration and timing of the added substrates. The enhancement of the signal is achieved by immobilization on a nanostructured gold layer. However, it is hard to achieve a consistent and reproducible gold layer as slight variations in experimental conditions affect the thickness of the layer. Usage of the same protocol and maintenance of experimental conditions was important factor. Another challenge in this protocol is the difficulty in obtaining a consistent and reproducible signal from the thiocyanate band of the labelled variants directly after labelling. This variability may be due to the inherent heterogeneity of the protein sample (presence of conformers), as well as the sensitivity of the technique to small changes in the structure of the protein. Overall, these challenges highlight the importance of a careful experimental design and optimization in order to obtain reliable and meaningful results from spectroscopy measurements of complex biological systems. It is necessary to perform various experiments, find the average of the obtained signals, look at the specific region of the IR-spectrum and shorten the incubation times with substrates. Stability of the NuoM variants can also be an important factor. Figure 4.30 shows examples.

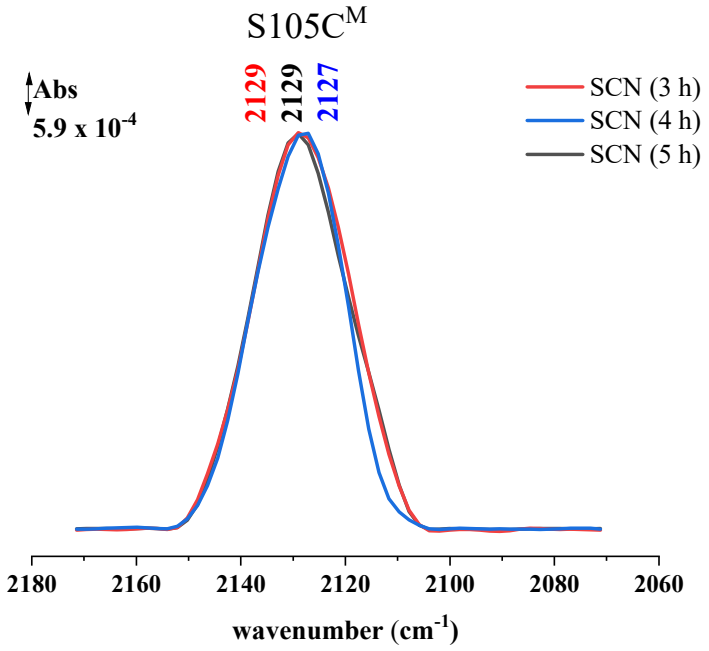

Figure 4.30: Positions of the nitrile band observed with the S105C^M variant after incubation on ice within 3 h (red); 4 h (blue) and 5 h (black).

The results from the experiments performed with the S105C^M variant suggest that the protocol used for labelling and incubation has a significant impact on the spectral position of the thiocyanate band. In this case, leaving the labelled sample on ice overnight resulted in a shift of 4 cm^{-1} towards a higher wavenumber (Fig. 4.31). Freezing the sample in liquid nitrogen and thawing on ice did not produce any significant change in the spectral position of the band. Incubation with NADH resulted in a shift towards a hydrophilic environment, but the shift was only 2 cm^{-1}. These results indicate that the labelling and incubation protocol need to be carefully optimized and consistently applied to obtain reproducible results. The slight shift (2 cm^{-1}) of the spectral position during the incubation process further highlights the need for careful and exact following of the protocol to ensure the reliability of the results.

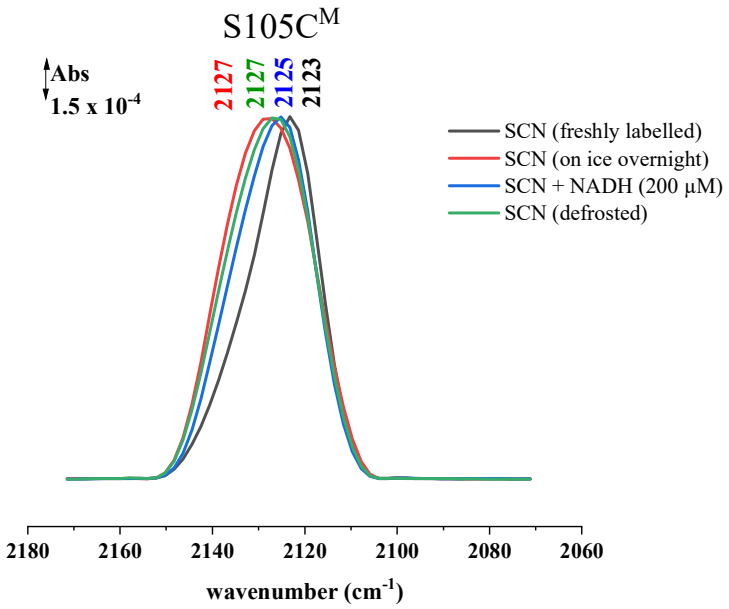

Figure 4.31: Position of the nitrile band observed with the S105C^{M} variant after immediate labelling (black); after leaving the labelled sample overnight (red), after freezing and thawing the sample (green), and after addition of a higher substrate concentration (blue).

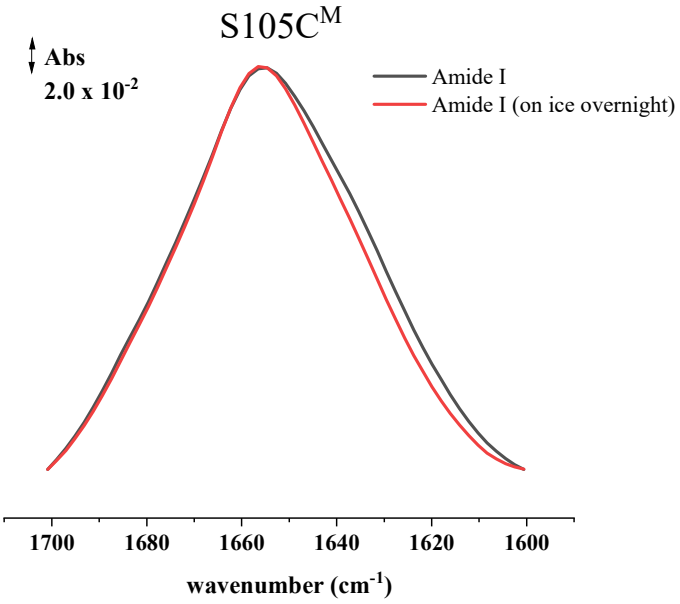

Figure 4.32: Position of the amide I band of the S105C^{M} variant directly after labelling (black) and after one night on ice (red).

The variability in the spectral positions of the thiocyanate bands of the different variants can be attributed to several factors, including differences in the local microenvironment of the labelled cysteine residue, stability of the protein, and variations in the experimental conditions. It is also

possible that the labelling specificity might vary for different cysteine positions, leading to differences in the position of the thiocyanate band.

The observed small difference in the amide I band for obtained with S105C^{M} after leaving it on ice overnight (Fig. 4.32) could indicate that a portion of the protein might have undergone structural changes, while the rest protein remained intact. Such changes could be due to conformational changes induced by labelling or variations in the local microenvironment around the labelled cysteine residue.

The variability in the position of the thiocyanate band for the T332C^{M} variant could be due to several factors, including variations in the local microenvironment around the labelled cysteine residue, differences in the stability of the protein, and variations in labelling efficiency and specificity. It is also possible that differences in the experimental conditions could have contributed to the observed variability in the position of the thiocyanate band (Fig. 4.33).

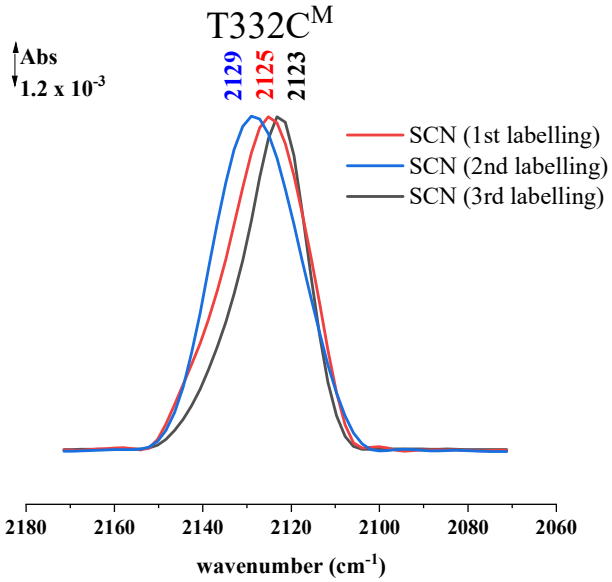

Figure 4.33: Position of the thiocyanate band after labelling the T332C^{M} variant several times. 1st labelling (red), 2nd labelling (blue), 3rd labelling (black).

Obtaining reproducible results is critical, and in this case, the variability of the data obtained in the experiments with complex I variants was a significant challenge. The shifts in the thiocyanate band position after incubation with NADH and Q are expected to provide insight into the conformational changes in the variants, but the irreproducible results made it difficult to interpret the data.

The long time required to obtain the labelled sample further complicated the measurements, as it may be affected by factors such as temperature, pH, and exposure to air, leading to variability in

the results. To overcome these challenges, it was necessary to perform multiple experiments to obtain reproducible data. The average values of the spectra were calculated, and comparisons were made to ensure the consistency of the results. In addition, it was necessary to optimize the experimental conditions, such as the concentration of the labeled protein, the concentration of NADH and ubiquinone, and the time required for incubation, to reduce the variability in the results. In conclusion, obtaining reproducible results is crucial and the variability in the data obtained for the NuoM variants presented significant challenges in this study. However, by performing multiple experiments, calculating average values, and optimizing experimental conditions, it was possible to obtain reproducible results and gain insights into conformational changes of the NuoM variants.

4.4.5 SCN bands analysis

The band of the SCN label appears in the infrared spectrum, between 2100 and 2240 cm^{-1} [241]. Absorbance spectra were recorded for each labelled NuoM variant before after incubation with NADH, and Q-2. For each variant, the procedure was repeated 3 to 5 times to obtain a clear reproducibility of the method. Figures 4.34 to 4.52 show the spectra of the NuoM variants including deconvolution of the thiocyanate bands. Deconvolution analysis was employed to analyze the thiocyanate bands of the NuoM variants after incubation with NADH and Q-2. It was used as a tool to identify various bands in the nitrile signal, which can be helpful to distinguish the conformers in the thiocyanate signal. It was performed by obtaining the second derivatives of the absorbances to detect and distinguish the different spectral populations. The most complex thiocyanate bands were observed for variants incubated with ubiquinone.

Complex I has no accessible cysteine residues on its surface [264], so that the ones generated at different positions in NuoM subunit can be used to follow conformational changes upon the addition of NADH and ubiquinone. Labelling the $S105C^{M}$, position on the cytoplasmic side variant located close to the surface, resulted in a band with a peak at 2127 cm^{-1} (Fig. 4.34). When NADH was added to the sample, the peak shifted towards lower wavenumbers, resulting in a peak at 2123 cm^{-1}. This shift may indicate a change in the hydrogen bonding or electrostatic interactions between the labeled residue and its environment. The addition of ubiquinone further affected the vibrational mode, resulting in a shift of 6 cm^{-1} towards higher wavenumbers, with the peak appearing at 2129 cm^{-1}. The broad shape of the thiocyanate band after treatment with ubiquinone may indicate that the labeled residue is involved in interactions with multiple components within

the complex, or that it is in a dynamic position where it can rapidly switch between multiple conformations.

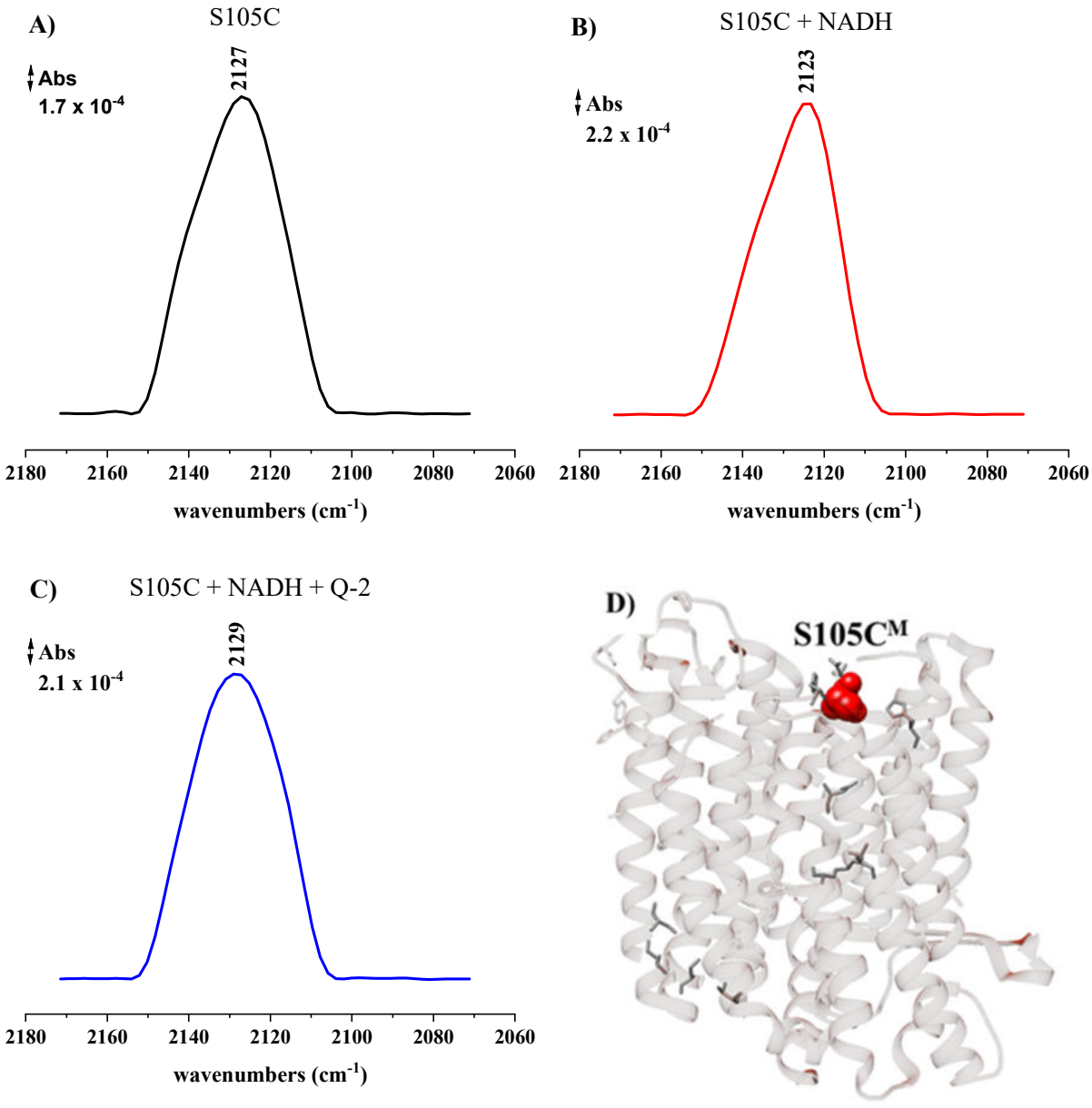

Figure 4.34. Spectra of the SCN bands of oxidized S105C^{M} (A, black), after reduction with 100 µM NADH (B, red) and re-oxidation with 150 µM Q-2 (C, blue). D) Position of the S105C^{M} residue in the NuoM structure.

The deconvolution analysis of the thiocyanate band of the S105C^{M} variant reveals interesting information about the distribution of thiocyanate bands at different redox states of the protein (Fig.4.35). In the oxidized sample, the majority of the signal appeared at 2125 cm^{-1}. After reduction by NADH, the band distribution shifted towards 2123 cm^{-1}, with 63% of the total signal appearing

at this wavenumber. The remaining 37% of the signal appeared at 2136 cm^{-1}, indicating that a fraction of the SCN-groups was experiencing a different environment. The deconvolution analysis for the reoxidized $S105C^M$ variant could not be performed due to the absence of significant peaks in the band.

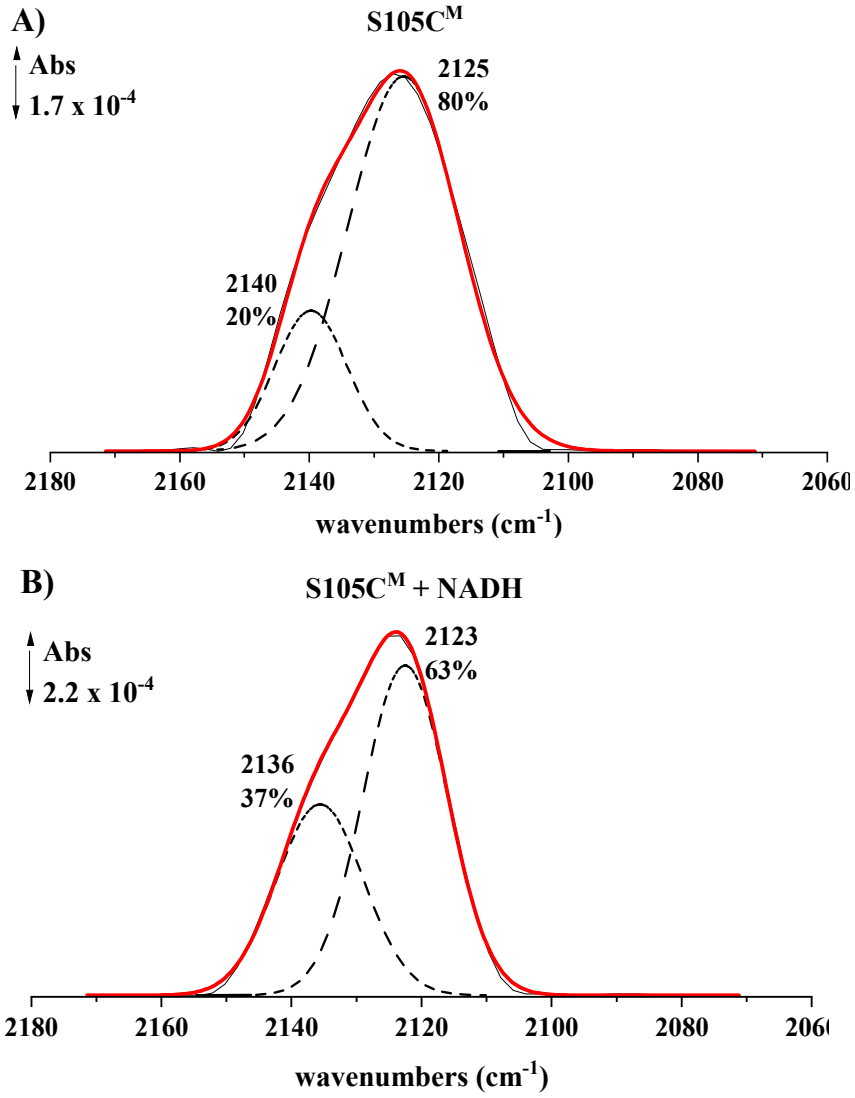

Figure 4.35: Deconvolution of the nitrile band obtained for the NuoM $S105C^M$ variant (A); after reduction by NADH (B).

$E108C^M$ located close to the surface of the cytoplasmic side, shows a characteristic thiocyanate signal appearing at 2125 cm^{-1} (Fig. 4.36). Incubation with NADH did not result in any changes of the spectral position. However, the band became narrower. Treating the sample with Q caused a shift towards a more hydrophilic environment, and the signal appeared at 2127 cm^{-1}.

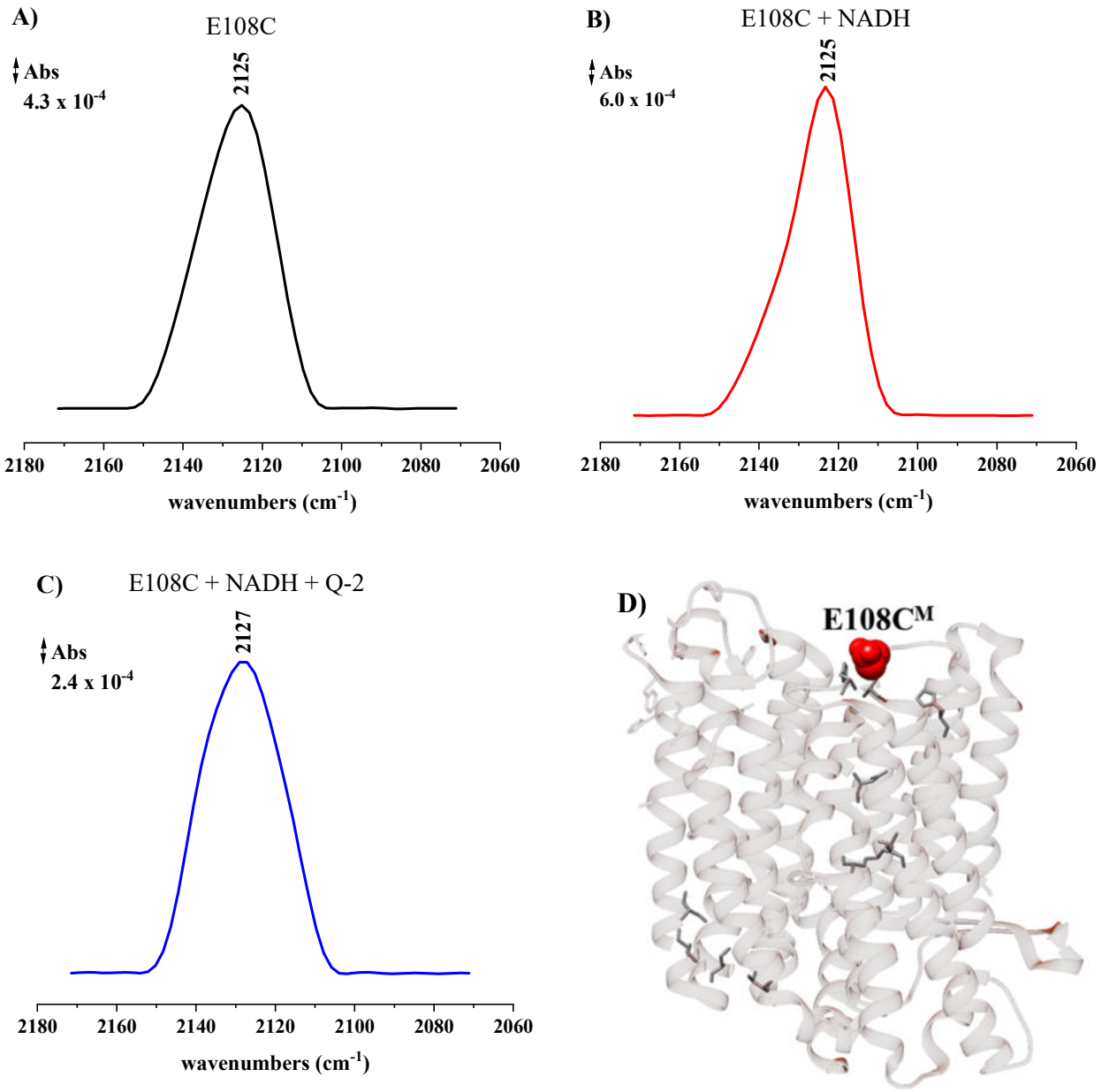

Figure 4.36: Spectra of the SCN bands of oxidized E108C^{M} (A, black), after reduction with 100 µM NADH (B, red) and after re-oxidation with 150 µM Q-2 (C, blue). D) Position of the E108C^{M} residue in the NuoM structure.

After deconvolution of the the band obtained for the reoxidized E108C^{M} variant two major peaks were always observed around 2136 and 2124 cm^{-1} (Fig. 4.37), which are likely indicative of specific structural features of the positions investigated on NuoM. They reflect the presence of different conformers.

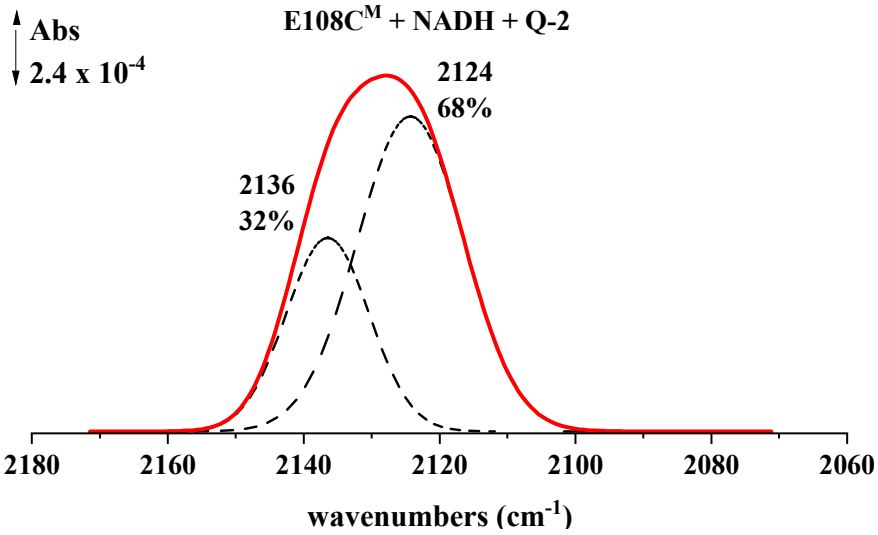

Figure 4.37: Deconvolution of the nitrile band of the E108C^M variant incubated with NADH and Q-2.

Another variant with a mutation on the cytoplasmic side, H117C^M, (Fig. 4.38) has the same thiocyanate band position as S105C^M at 2127 cm^{-1}. This suggests that the labeled residue in the H117C^M mutant may be in a similar local environment as in the S105C^M variant.

When NADH was added to the sample, there was a slight shift of the peak towards lower wavenumbers with a peak at 2125 cm^{-1}. This may suggest that the probe in the H117C^M variant is exposed to a more hydrophobic environment in the presence of NADH. The addition of ubiquinone resulted in a shift of 6 cm^{-1} towards higher wavenumbers, with the peak appearing at 2131 cm^{-1}. This shift is similar to the shift observed in S105C^M variant, and may indicate that the labeled residue in the H117C^M variant is also exposed to a more hydrophilic environment in the presence of Q.

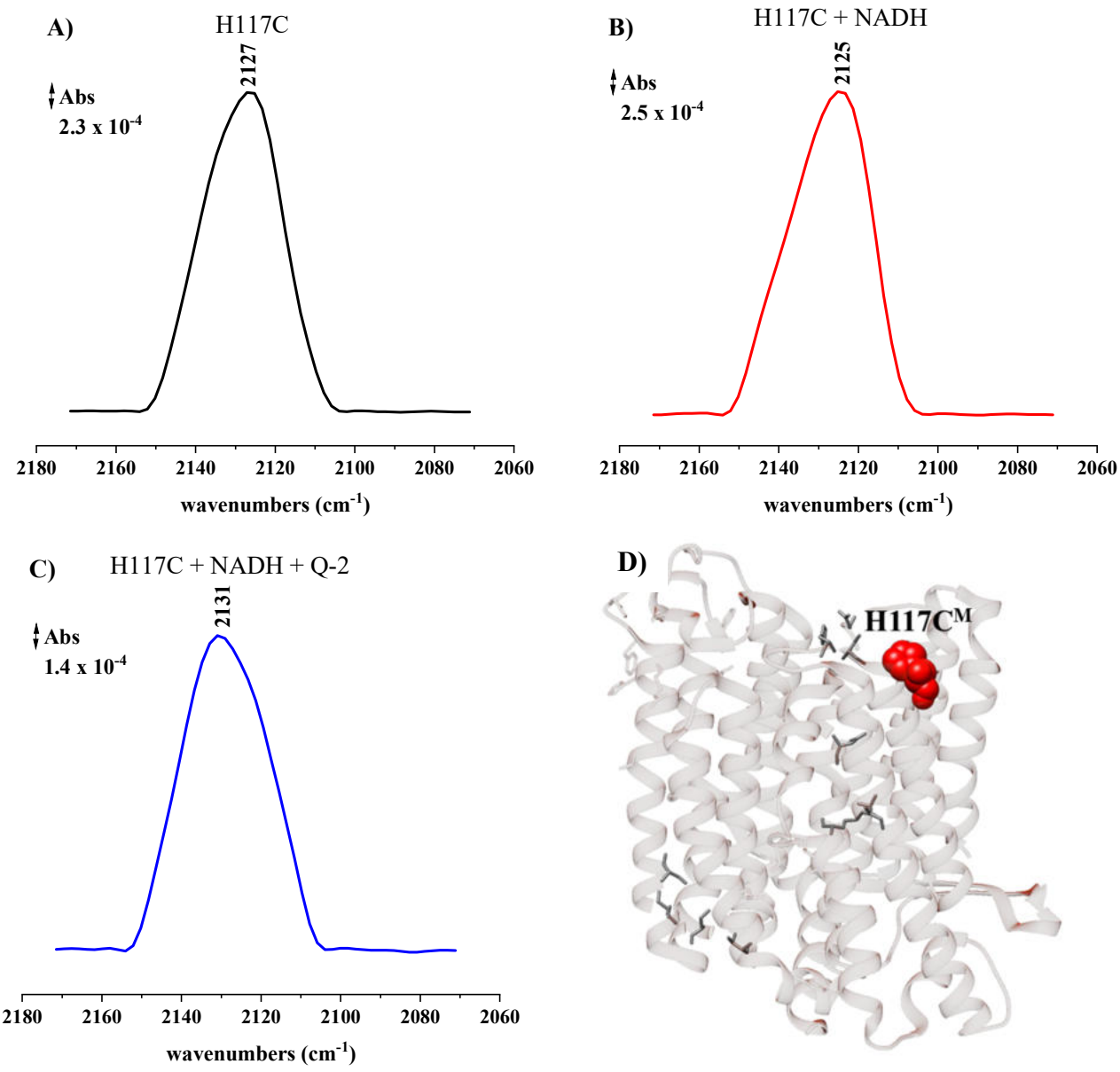

Figure 4.38: Spectra of the SCN bands of oxidized H117C^{M} (A, black), after reduction with 100 µM NADH (B, red) and re-oxidation with 150 µM Q-2 (C, blue). D) Position of the H117C^{M} residue in the NuoM structure.

The deconvolution of the band obtained with the H117C^{M} variant (Fig. 4.39) shows a band distribution between two peak located at 2125 and 2138 cm^{-1}. The majority of the band (72%) is located at the position 2125 cm^{-1}, which could indicate that this position is more favorable. Several conformers are present in the sample. However, deconvolution of the oxidized and reoxidized variants could not be performed due to their appearance as homogenous bands in the spectra.

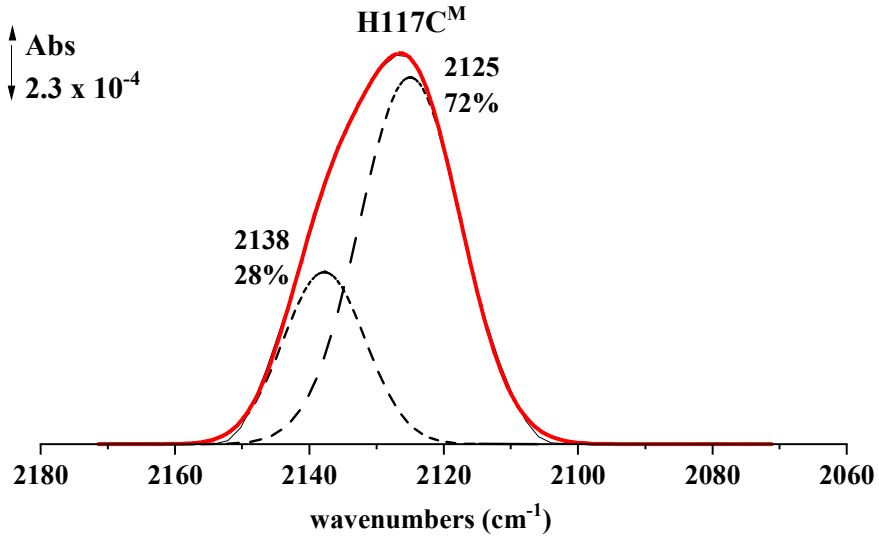

Figure 4.39: Deconvolution of the nitrile band of the H117C^M variant.

Labelling of H159C^M, a position that is located on the cytoplasmic side gave a band around 2123 cm^{-1} (Fig. 4.40). This variant is located close to the entrance to the putative proton channel. A shoulder is visible at around 2140 cm^{-1} for the labelled residue. The addition of NADH gave a slight shift of 2 cm^{-1} towards higher wavenumbers. The shape of the band remained the same, and the shoulder at 2140 cm^{-1} was still visible. However, the shoulder became smoother and its intensity decreased. The addition of Q resulted in a spectral position at 2129 cm^{-1}. The band moved towards higher wavenumbers. It indicated the change to a more hydrophilic environment. The width of the band became broader. The presence of different conformers of the label could be a possible explanation of the asymmetry of the signal. The increase of the width was significant, and further deconvolution of the bands revealed the presence of multiple peaks. It can be suggested that only a part reacted with NADH and Q-2. Another assumption would the presence of two substructures.

The deconvolution analysis of the SCN band of the H159C^M and that one incubated with NADH showed that the majority of the band (72%) appeared around 2122-2123 cm^{-1}, while the remaining 28% appeared around 2136-2138 cm^{-1} (Fig. 4.41). H159C^M and that one reduced by NADH look similar, showing 72% of absorbance around 2122-2123 cm^{-1}, while 28% appear around 2136-2138 cm^{-1}.

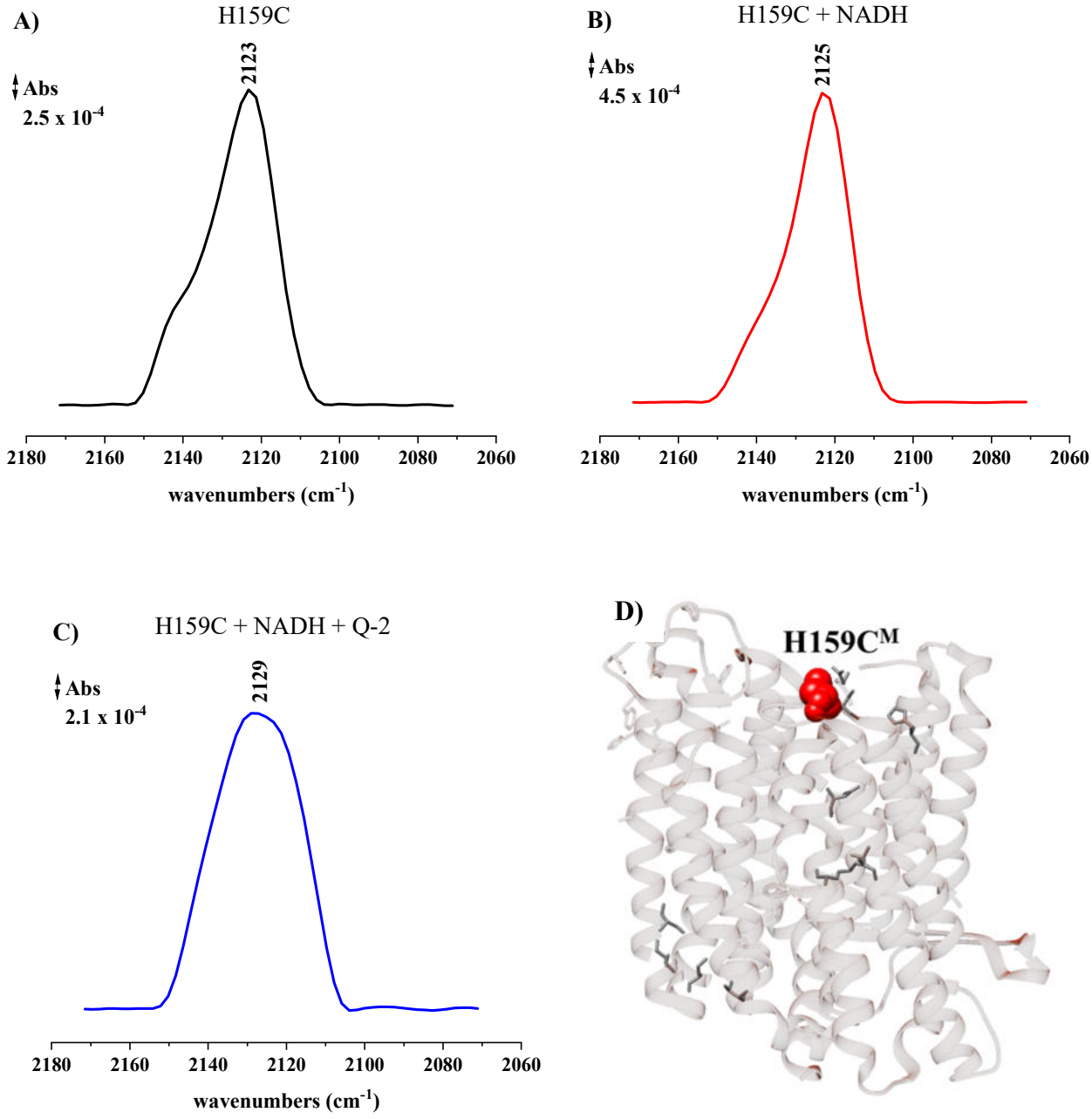

Figure 4.40: Spectra of the SCN bands of oxidized H159C^{M} (A, black), after reduction with 100 µM NADH (B, red) and after re-oxidation with 150 µM Q-2 (C, blue). D) Position of the H159C^{M} residue in the NuoM structure.

The shift in the distribution of SCN bands for the re-oxidized H159C^{M} variant compared to the reduced variant suggests that the addition of Q-2 has a major effect on the conformational freedom of the thiocyanate ligand. The shift towards lower wavenumbers (2119 cm^{-1}) suggests that Q-2 may alter the polarity of the microenvironment surrounding the ligand or alter the conformation of the protein. The band at 2132 cm^{-1} in the higher wavenumber region supports this assumption.

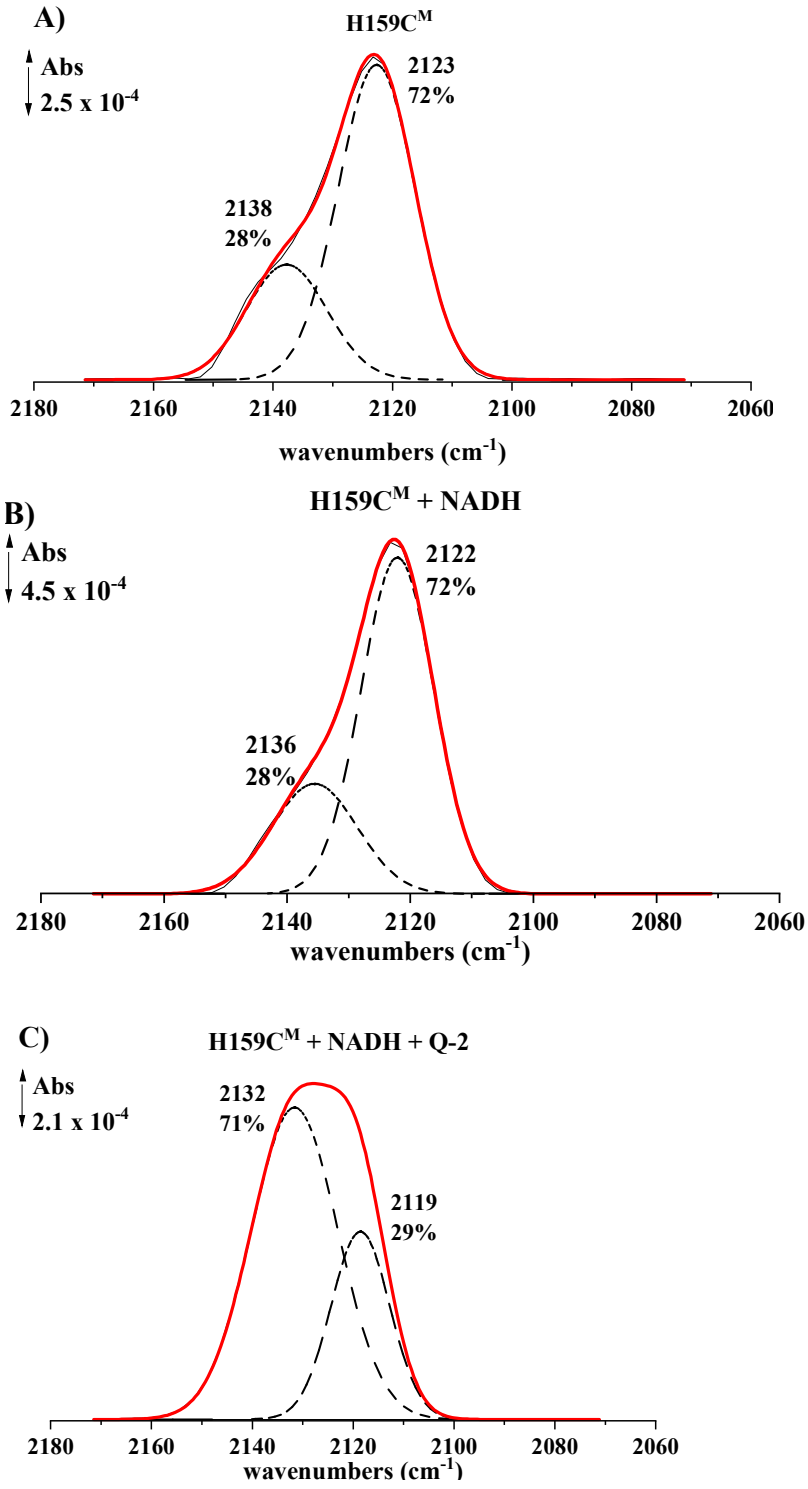

Figure 4.41: Deconvolution of the nitrile band of the H159C^M variant (A), after reduction with NADH (B) and after re-oxidation with Q-2 (C).

After labelling, the T332C^{M} variant with the mutation on the periplasmic side NuoM showed a band at 2127 cm^{-1}. A small shoulder at around 2140 cm^{-1} can be observed. Incubation with NADH changed the position of the band to 2123 cm^{-1}. Treatment with Q resulted in a shift towards higher wavenumbers to the initial state of the protein at 2127 cm^{-1}. There is also a shoulder visible around 2115 cm^{-1} that is characteristic of a band (Fig. 4.42).

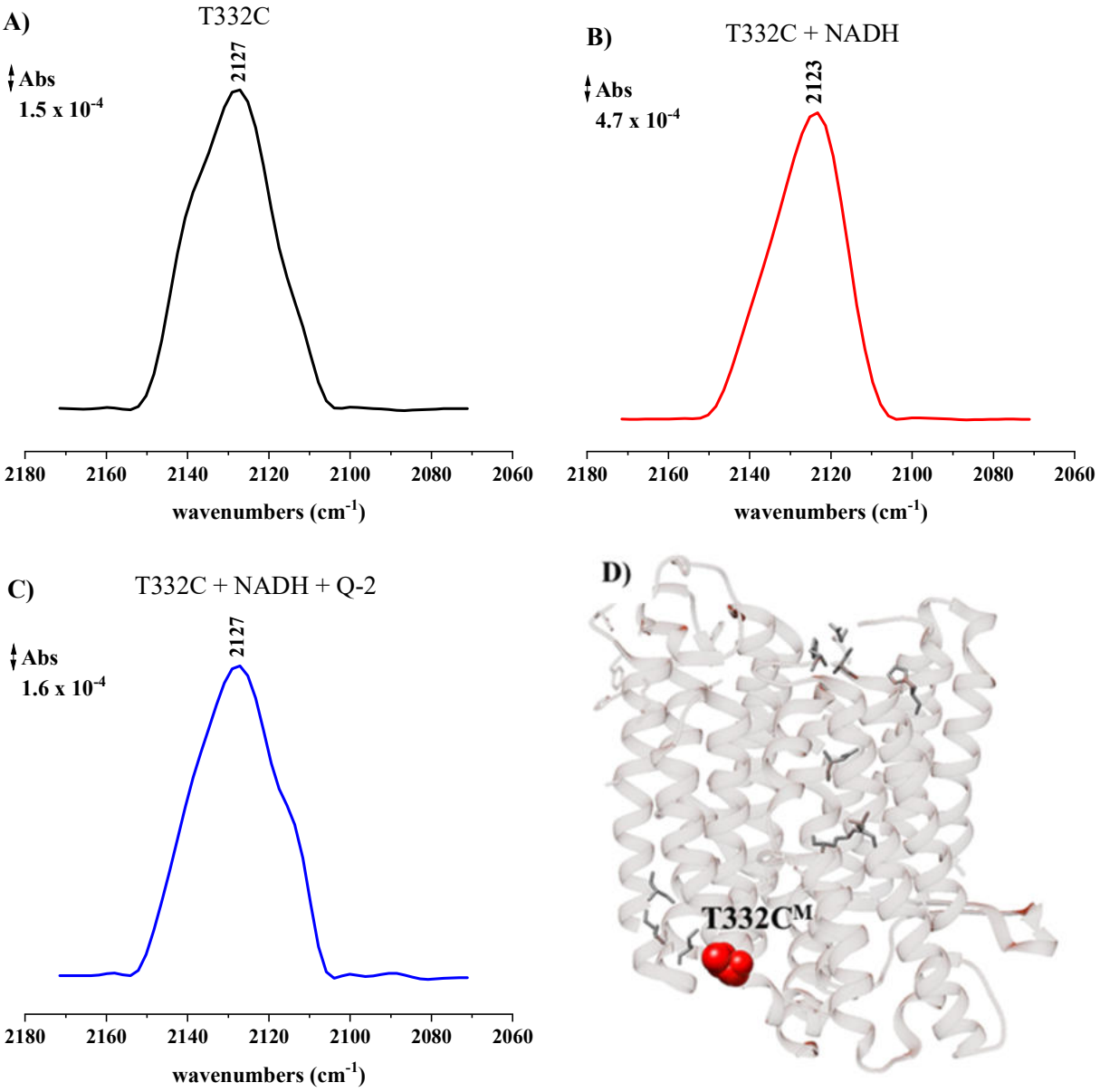

Figure 4.42: Spectra of the SCN bands of oxidized T332C^{M} (A, black), after reduction with 100 µM NADH (B, red) and after re-oxidation with 150 µM Q-2 (C, blue). D) Position of the T332C^{M} residue in the NuoM structure.

The deconvolution analysis of the band from the thiocyanate bound to the T332C^{M} variant shows that the majority of the peak appeared at 2128 cm^{-1}, pointing towards a homogenous environment

of this variant. Only a small fraction of the peak (8%) was found at higher wavenumbers (2141 cm^{-1}), indicating some conformational heterogeneity.

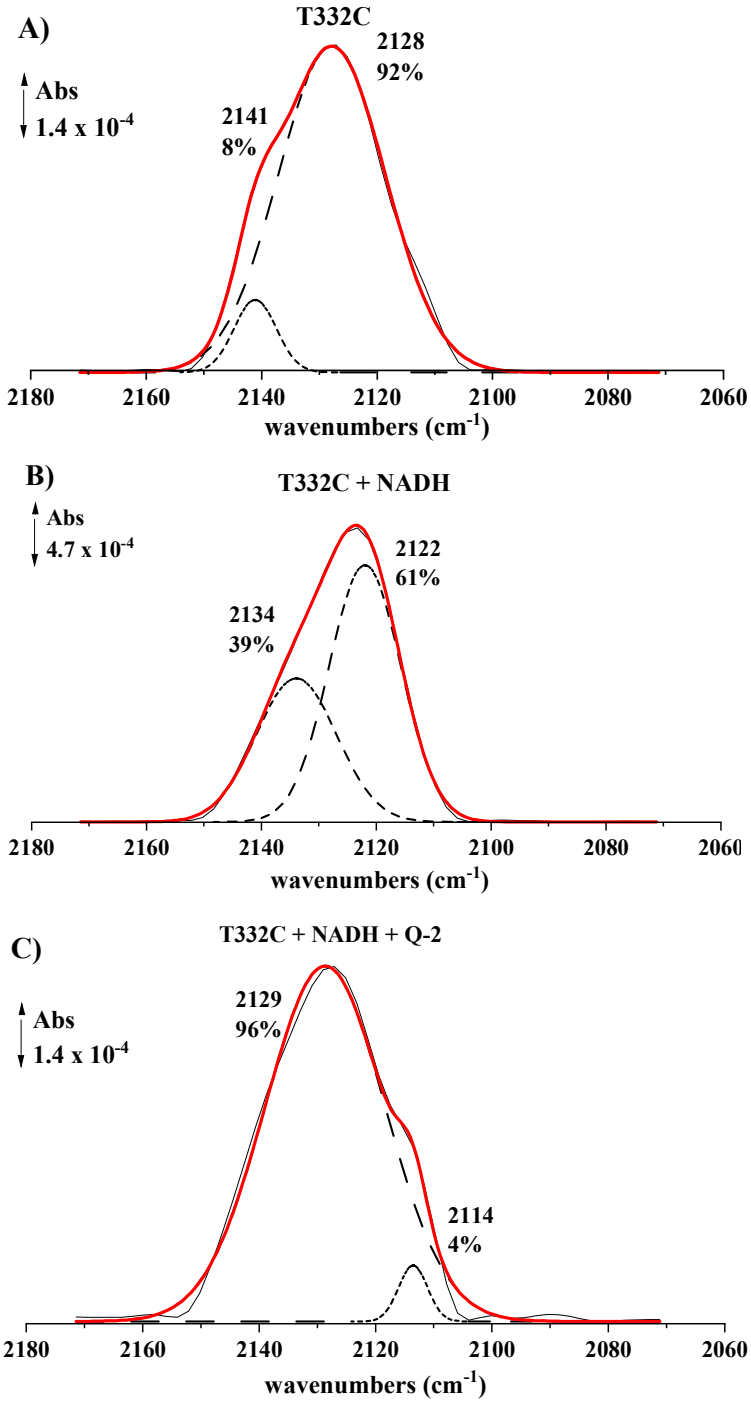

Figure 4.43: Deconvolution of the nitrile band of the T332C^{M} variant (A), after reduction by NADH (B) and after re-oxidation by Q-2 (C).

Upon incubation with NADH, there was an increase in the percentage of the peak at higher wavenumbers (now at 2134 cm^{-1}), indicating a change in the conformation around the label and a

different distribution between the conformers. Incubation with ubiquinone resulted in a main peak located at 2129 cm^{-1}, showing a different conformational change upon re-oxidation by ubiquinone. Only a small fraction of the peak was located at lower wavenumbers, pointing out that the label adopts a similar stable position in the oxidized and the re-oxidized state.

The band in the $S414C^M$ variant (Fig. 4.44) appeared at a lower wavenumber of 2123 cm^{-1}, indicating that the labeled residue is in a different local environment than in the previous mutant $H159C^M$ located on the periplasmic side. This residue ($S414C^M$) is located on the periplasmic side of the membrane close to the putative proton exit.

Interestingly, the addition of NADH did not result in any visible changes in the vibrational mode of the labeled residue, suggesting that NADH does not induce conformational changes at this position. The band remained at the same position of 2123 cm^{-1}. However, the addition of ubiquinone resulted in a shift of 4 cm^{-1} towards higher wavenumbers, indicating that the labeled residue is exposed to a more hydrophilic environment in the presence of ubiquinone. This shift is in the opposite direction compared to the shifts observed in the previous mutants, may indicate the same effect on the local environment of $S414C^M$, where the label moves to a more hydrophilic environment upon addition of ubiquinone.

It is also worth mentioning that the half-band width of the signal in the $S414C^M$ mutant is broader than those observed in the previous mutants indicating that the labeled residue may exist in multiple conformations or may be involved in interactions with multiple components within the complex.

The deconvolution for the $S414C^M$ nitrile signal after incubation with both NADH and ubiquinone showed two peaks with approximately equal distribution. Peaks at the same position are also detected with the oxidized and reduced variant (Fig. 4.45), while the relative amount of both contributions differs in different redox states. Thus, the label is present in two favorite positions, with the more stable one depending on the redox state of the complex.

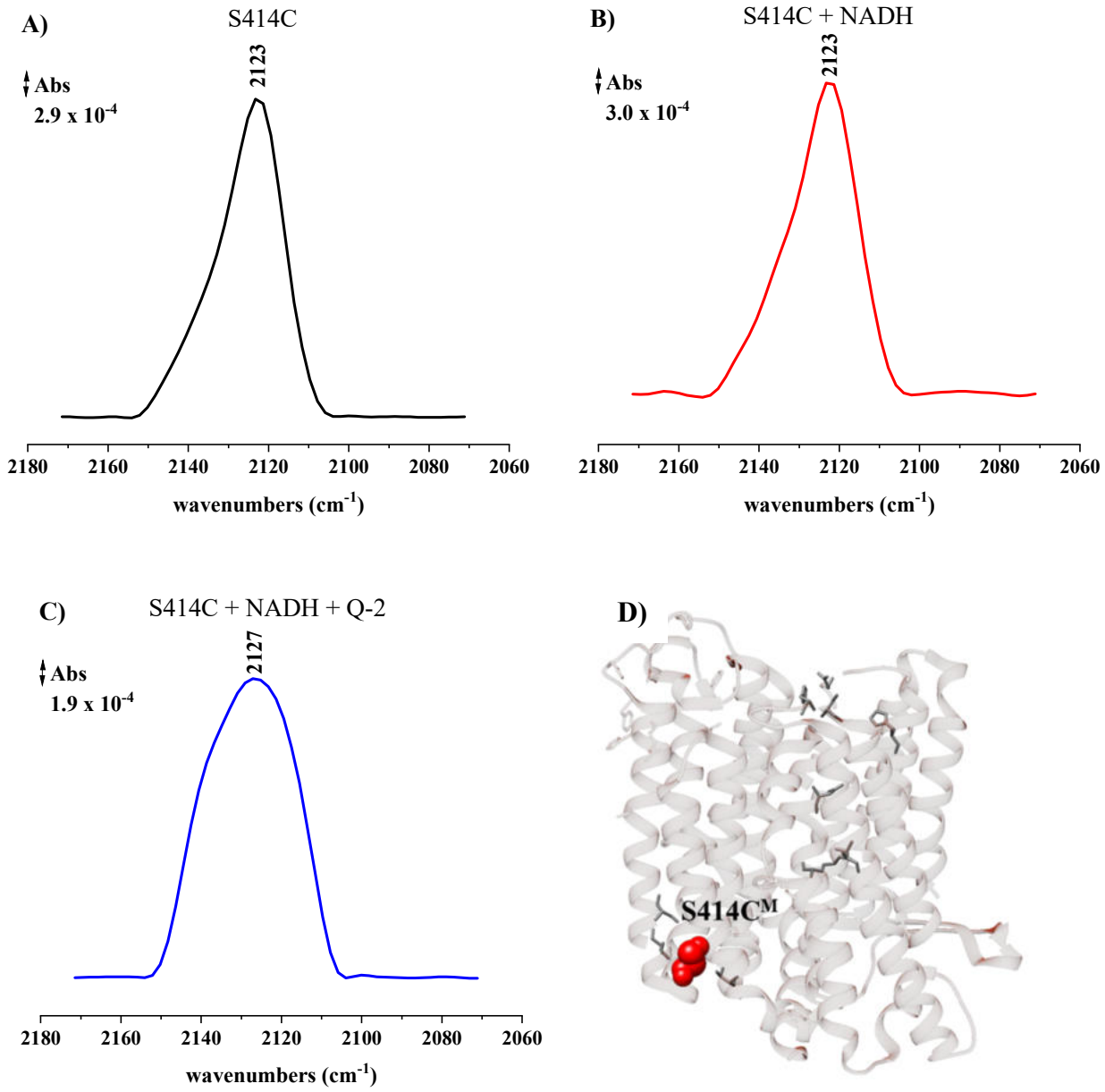

Figure 4.44: Spectra of the SCN bands of oxidized S414C^{M} (A, black), after reduction with 100 µM NADH (B, red) and re-oxidization with 150 µM Q_2 (C, blue). D) Position of the S414C^{M} residue in the NuoM structure.

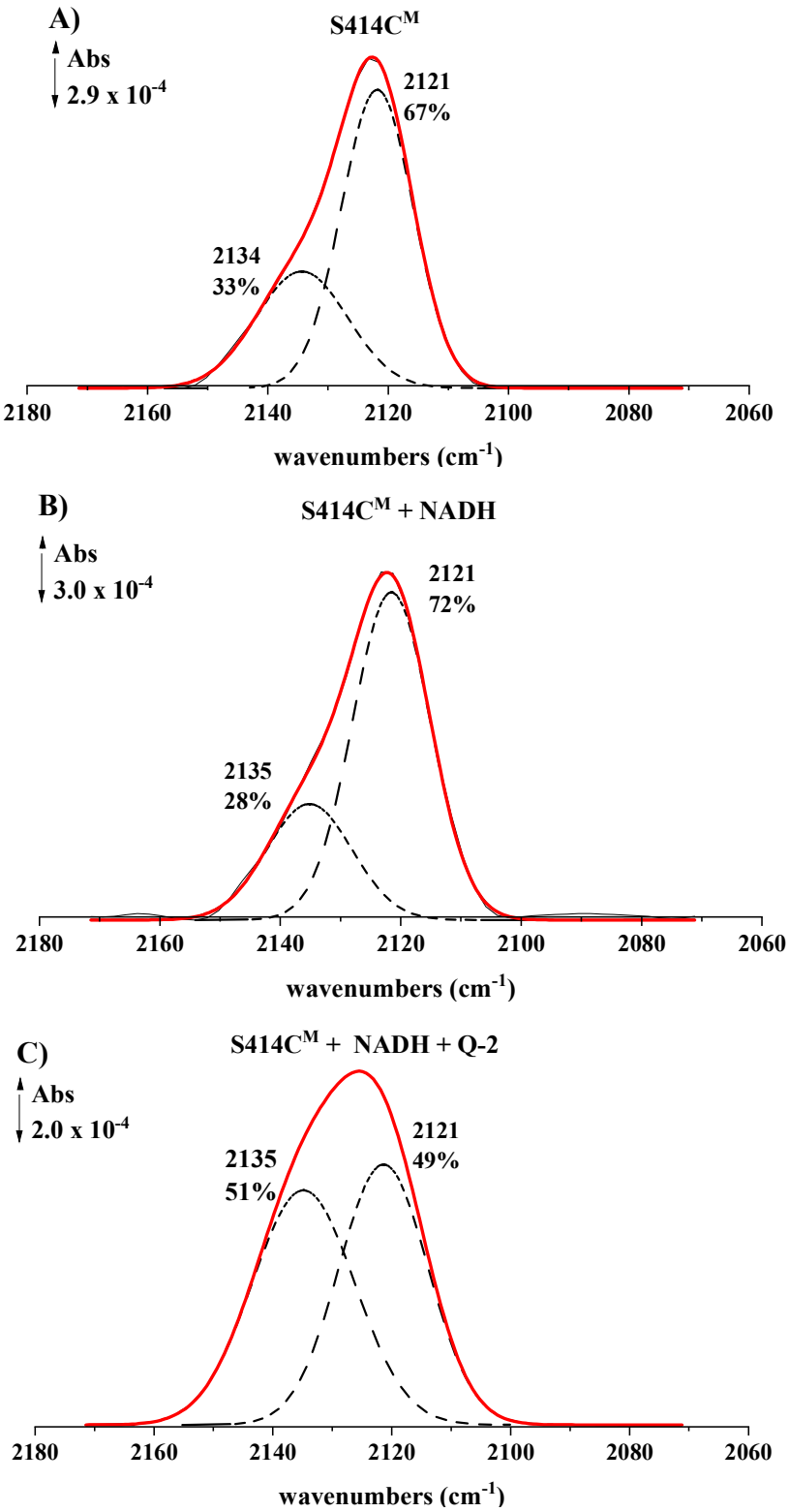

Figure 4.45: Deconvolution of the nitrile band of the S414C^M variant (A), after reduction with NADH (B) and after re-oxidation with Q-2 (C).

The T422C^{M} variant with the labelled residue on the periplasmic side shows a spectral position at 2123 cm^{-1} (Fig. 4.46). The shoulder at around 2140 cm^{-1} suggests that the probe may take several distinct conformations. The lack of significant changes upon treatment with NADH suggests that the position does not undergo a conformational change upon addition of NADH. The band remained at the same position of 2123 cm^{-1}.

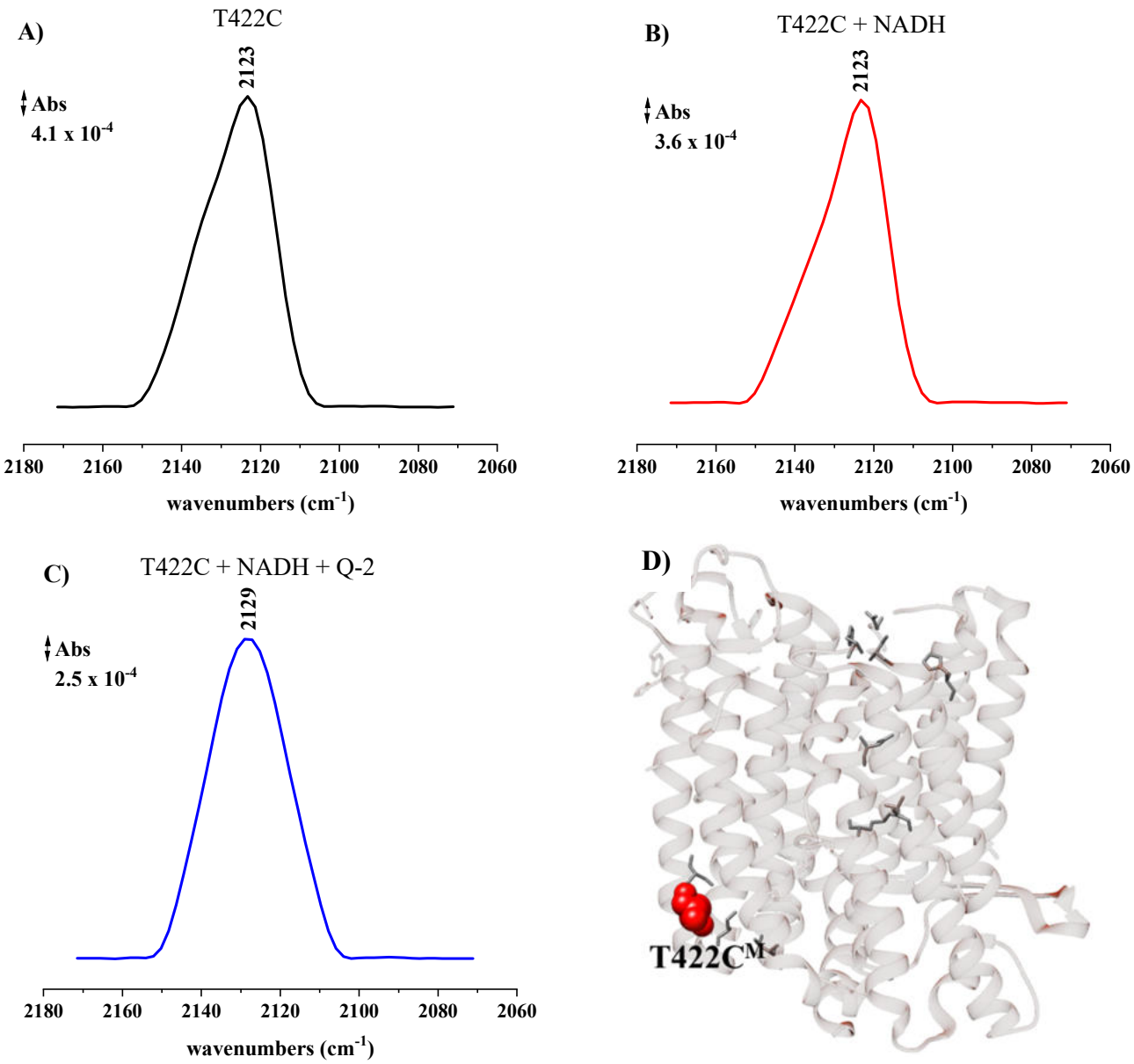

Figure 4.46: Spectra of the SCN bands of oxidized T422C^{M} (A, black), after reduction with 100 µM NADH (B, red) and incubation with 150 µM Q-2 (blue line). D) Position of the T422C^{M} residue in the NuoM structure.

In contrast, incubation with ubiquinone resulted in a significant shift of 6 cm^{-1} towards higher wavenumbers. This shift is consistent with the shifts observed with other variants with the probe

close to the periplasmic side. The lack of visible shoulders in the band suggests that the labelled T422C^{M} may not be involved in interactions with multiple conformations or components, as observed in the S414C^{M} mutant.

The observed changes in distribution of the thiocyanate signal of the T422C^{M} variant (Fig. 4.47) before and after incubation with NADH indicate that there are two major conformations taken by the label. Reduction with NADH only shifts the distribution of the label between these two positions. The slight increase in the the peak at 2121 cm^{-1} could suggest that the microenvironment of the cysteine residue has become less polar or hydrophobic. These changes could have an effect on the position of the thiocyanate band by altering the electron density around the sulfur atom of the thiocyanate group.

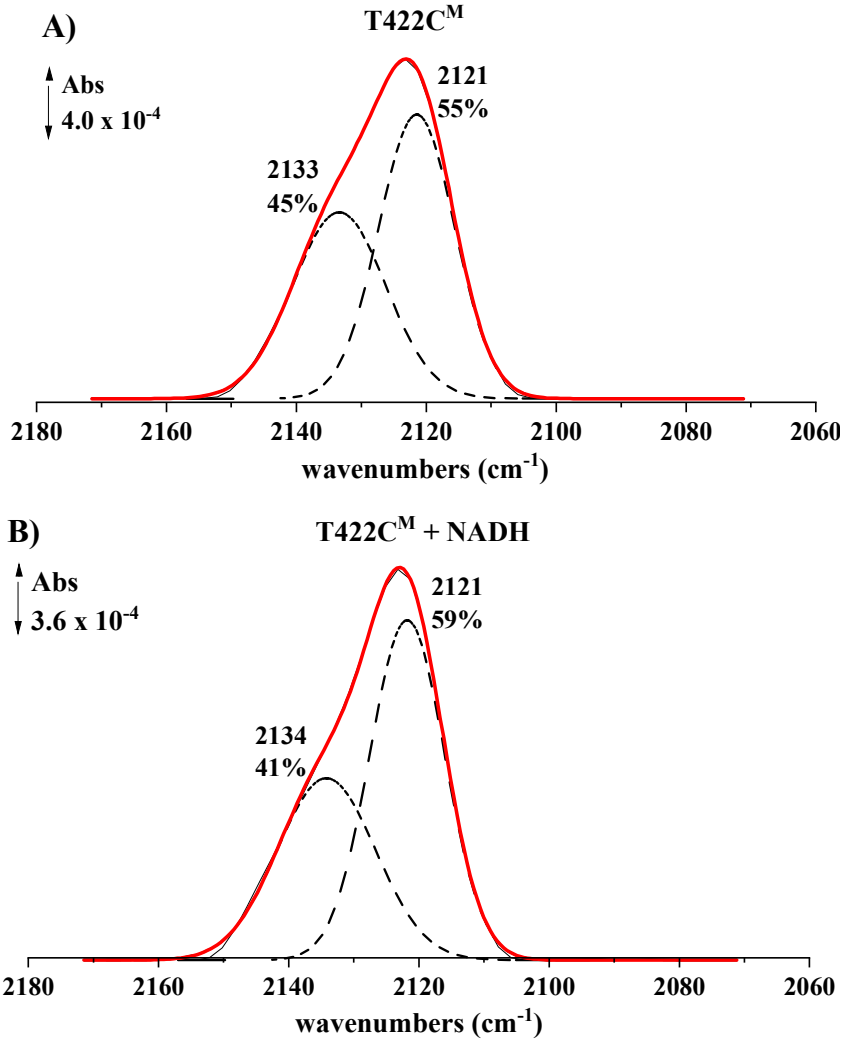

Figure 4.47: Deconvolution of the nitrile band T422C^{M} variant (A) and after reduction with NADH (B).

The spectral changes observed with the S425C^{M} variant suggest that the conformation and/or environment of the thiocyanate label is different in this mutant (Fig. 4.48). The higher wavenumber position of the thiocyanate band at 2129 cm^{-1} suggests that the label is in a more hydrophilic environment. The shift towards lower wavenumbers upon incubation with NADH suggests that the label is becoming more shielded from the solvent upon reduction. This could indicate a conformational change in NuoM that occurs upon NADH binding.

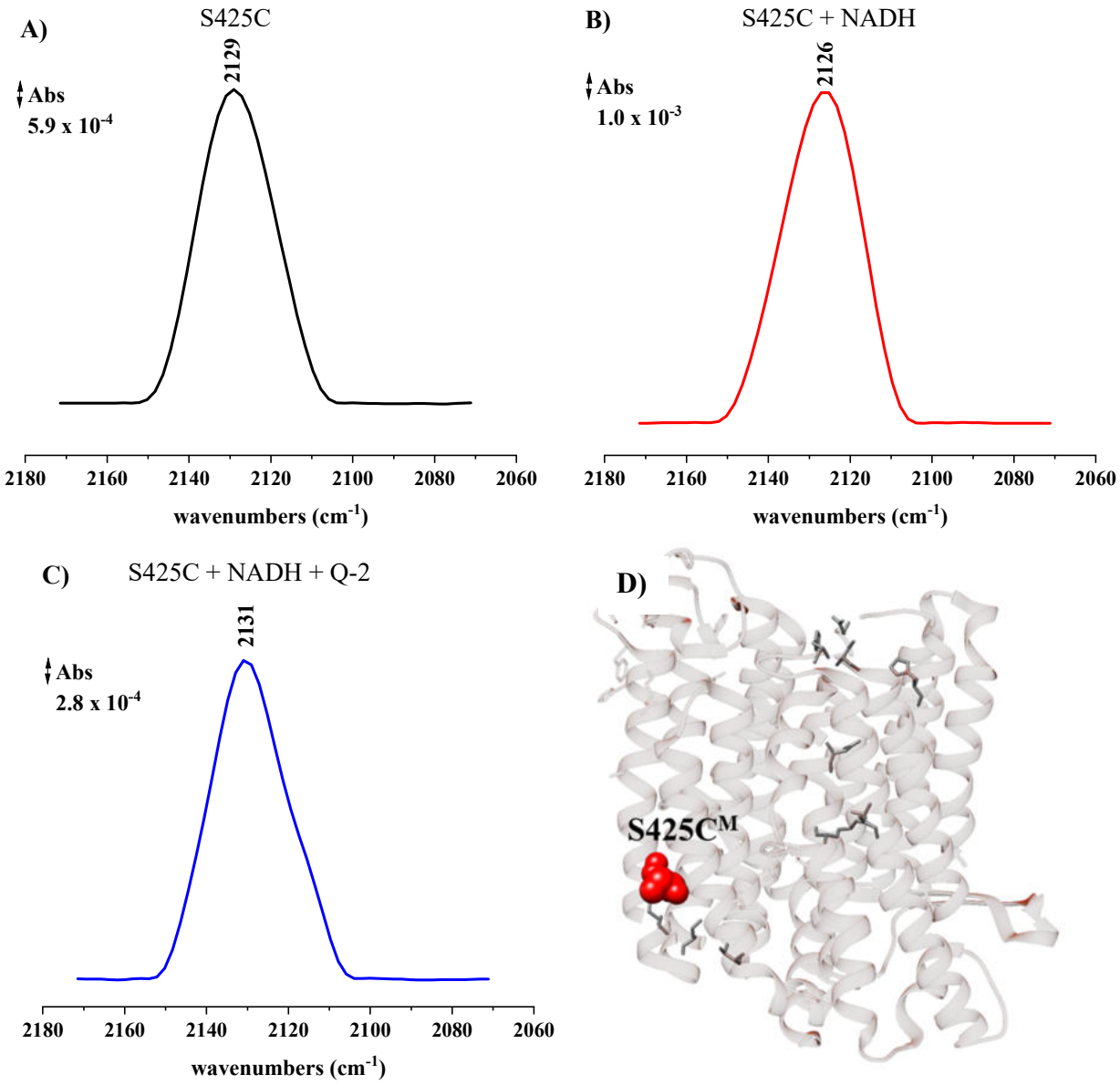

Figure 4.48: Spectra of the SCN band of oxidized S425C^{M} (A, black), after reduction with 100 µM NADH (B, red) and re-oxidation with 150 µM Q-2 (C, blue). D) Position of the S425C^{M} residue in the NuoM structure.

The shift towards a higher wavenumber upon incubation with Q suggests that the label is now in a more hydrophilic environment. This could indicate a conformational change in the protein that

occurs upon ubiquinone binding, leading to a different orientation of the label relative to the solvent.

The variant S425C^{M} variant shows a homogenous peak after labelling and incubation with NADH (Fig. 4.48A and B). However, the deconvolution analysis after incubation with ubiquinone shows that 92% of the peak appeared at 2131 cm^{-1}, and 8% was located at lower wavenumbers (2115 cm^{-1}) (Fig. 4.49). This could indicate the presence of a small fraction of the protein in a slightly different conformation or environment compared to the majority of the protein.

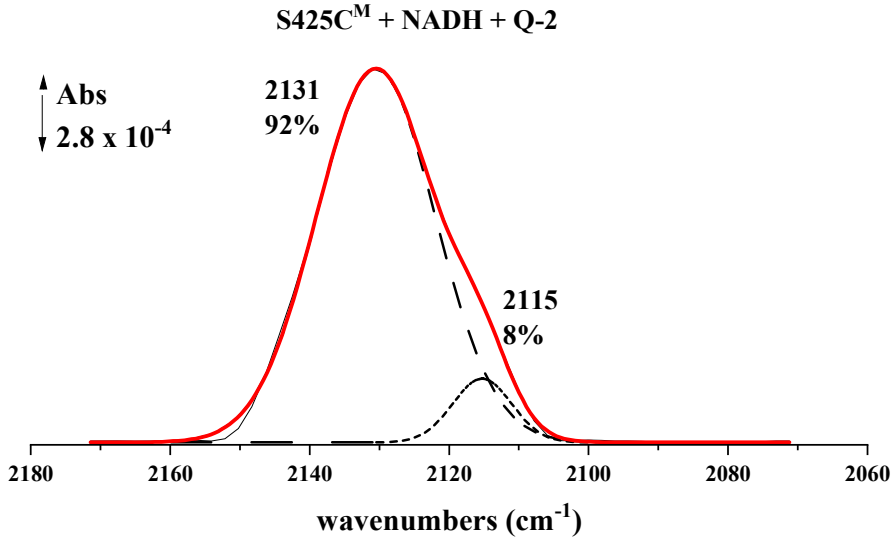

Figure 4.49: Deconvolution of the nitrile band of S425C^{M} variant incubated with NADH and Q-2.

The thiocyanate band of the T178C^{M} variant with a label in the central part of the protein appeared at higher wavenumbers compared to the other variants, at 2133 cm^{-1}. Incubation with NADH resulted in a significant shift of 10 cm^{-1} towards the lower wavenumbers, at 2123 cm^{-1}. Treatment with ubiquinone produced a shift towards the initial state of the protein at 2133 cm^{-1}. For this variant, more significant changes were recorded.

The data suggest that the labeled residue is exposed to a more hydrophobic environment in the presence of NADH. This shift is much larger than those observed with the other mutants, suggesting that position T178C^{M} is particularly sensitive to changes in the local environment induced by reduction of the complex.

The shift back to 2133 cm^{-1} upon treatment with ubiquinone indicates that position T178C^{M} returns to its original environment when ubiquinone is present. The shift to higher wavanumbers upon re-oxidation indicated that position T178C^{M} is similarly sensitive to changes in the local environment induced by Q binding.

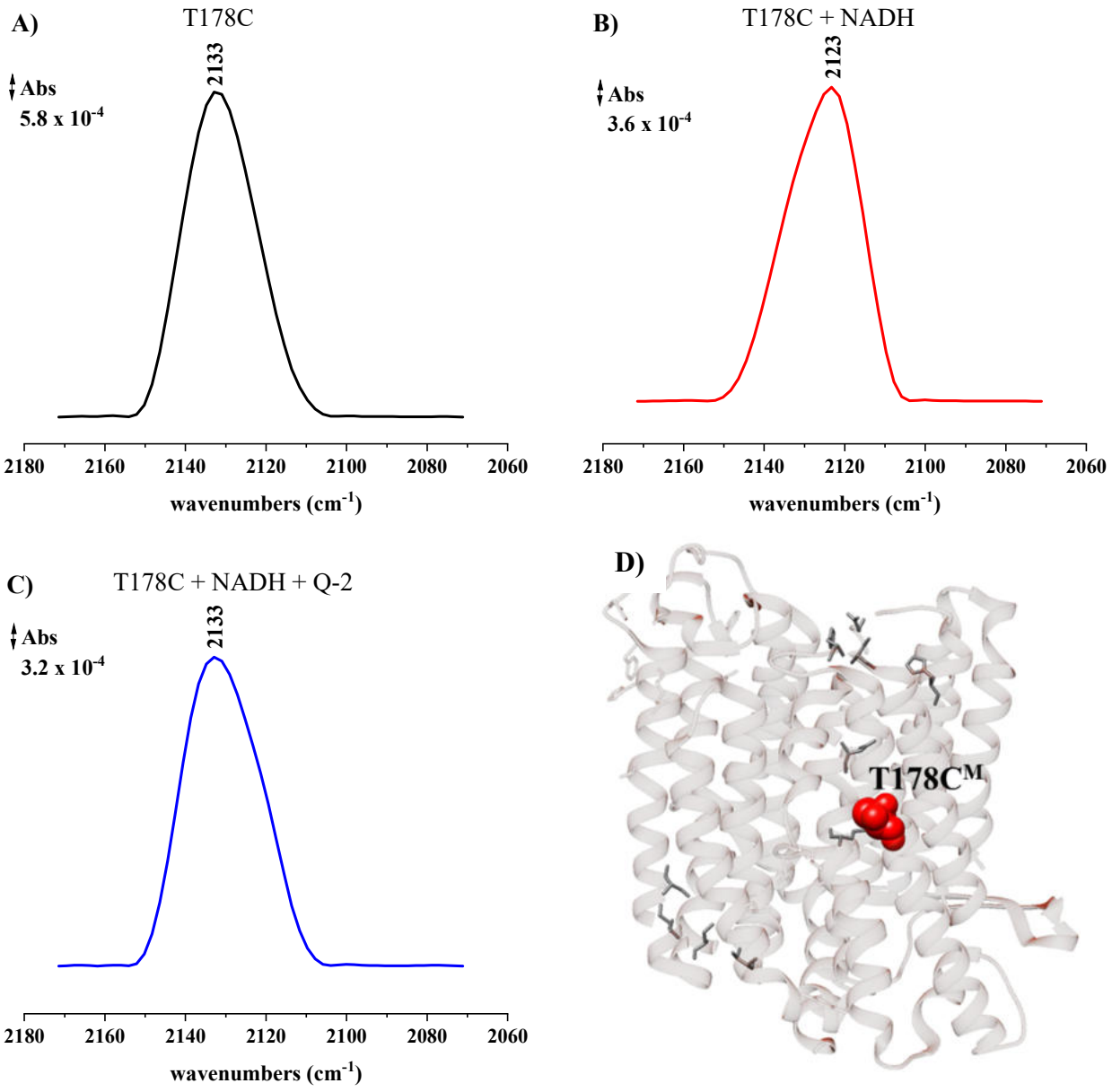

Figure 4.50: Spectra of the SCN bands of oxidized T178C^{M} (A, black), after reduction with 100 µM NADH (B, red) and re-oxidation with 150 µM Q-2 (C, blue). D) Position of the T178C^{M} residue in the NuoM structure.

Position K234C^{M} is also located in the central part of the protein. The NADH:decyl-Q oxidoreductase activity of this variant was less than 20% of that of complex I independent from labelling. The thiocyanate band of the labelled variant was observed at higher wavenumbers of 2131 cm^{-1} (Fig. 4.51). The addition of NADH resulted in a small shift of 2 cm^{-1} towards a more hydrophobic environment. Treatment with ubiquinone resulted in a signal at 2131 cm^{-1} that corresponds to the initial state of the thiocyanate signal directly after labelling.

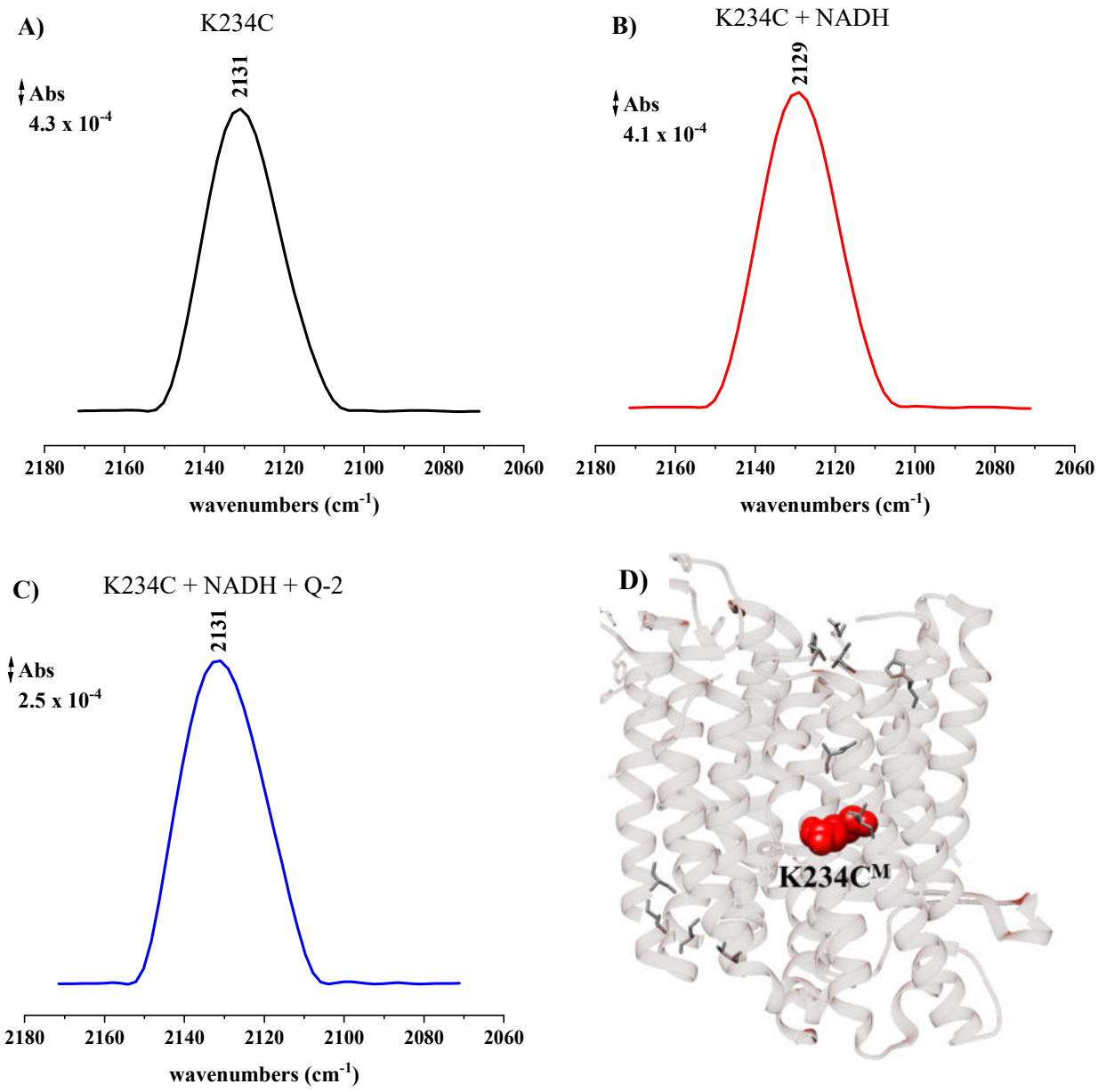

Figure 4.51: Spectra of the SCN bands of oxidized K234C^{M} (A, black), after reduction with 100 µM NADH (B, red) and re-oxidation with 150 µM Q-2 (C, blue). D) Position of the K234C^{M} residue in the NuoM structure.

The D258C^{M} variant is also mutated in the central part of the protein, and its NADH:decyl-Q oxidoreductase activity was significantly lower than that of the parent complex I. In the IR spectra, the thiocyanate signal appeared at 2125 cm^{-1} (Fig. 4.52), which is similar to the position of the signal of other variants with mutations located in the central part of NuoM. However, the reduction by NADH resulted in a small and insignificant shift of only 2 cm^{-1} towards higher wavenumbers, indicating that reduction did not significantly affect the environment around the labelled cysteine residue. The lack of significant changes in the spectral position of the label after re-oxidation with

ubiquinone also suggests that the environment of this position may not significantly be affected by redox reaction.

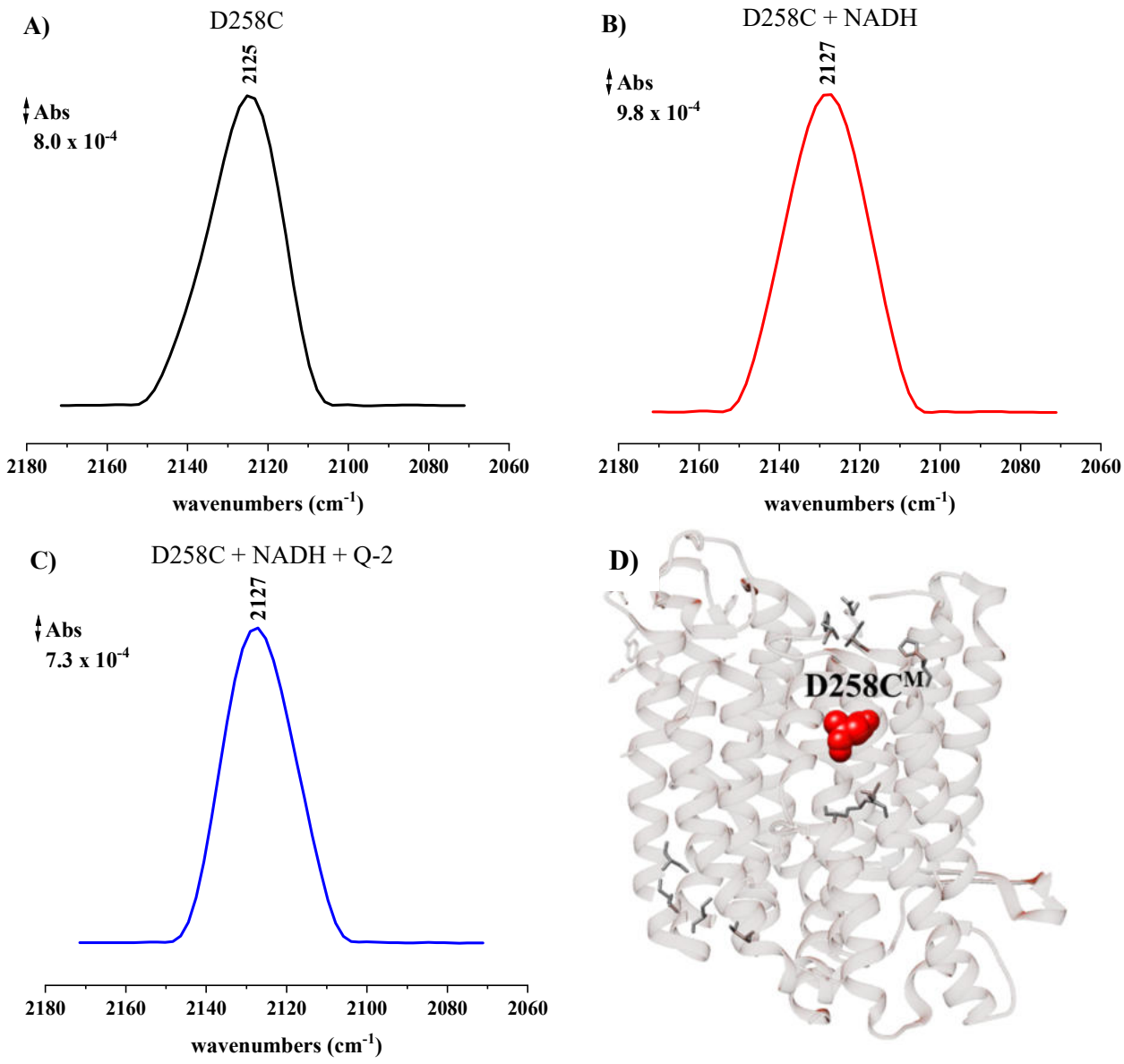

Figure 4.52: Spectra of the SCN bands of the oxidized D258C^{M} (A, black), after reduction with 100 µM NADH (B, red) and re-oxidation with 150 µM Q-2 (C, blue). D) Position of the D258C^{M} residue in the NuoM structure.

The results for the variants located in the central part of NuoM (except for T178C) D258C and K234C indicate that the thiocyanate band is not significantly affected by the reduction and reoxidation of the variants. Variant T178C^{M} resulted in a more significant shift. Deconvolution analysis was not performed for these mutants, because the peaks looked homogeneous and symmetric. It suggests that the surrounding environment does not provide conformational flexibility. It is possible that these residues do not directly interact with the thiocyanate molecule

and therefore do not cause any significant changes in the band distribution. Alternatively, the interactions between the thiocyanate molecule and these residues may be offset by interactions with other nearby residues or the solvent environment, resulting in a homogenous peak in the deconvolution analysis. Overall, the deconvolution analysis provides insight into the conformational changes of the complex I variants upon binding of substrates, which is useful for understanding the molecular mechanisms of complex I.

Table 4.13 summarizes all the spectral positions of label attached to newly inserted cysteine residues in the NuoM variants. All bands appeared in the range from 2123 to 2133 cm^{-1}. Bands after incubation with NADH tend to appear at lower wavenumbers and after incubation with Q at higher wavenumbers.

Table 4.13: Spectral positions of labelled complex I variants incubated with NADH and ubiquinone.

Variant	Location	CN (cm^{-1})	+NADH (cm^{-1})	Δ(NADH-CN), cm^{-1}	+Q-2 (cm^{-1})	Δ(Q-2-CN) cm^{-1}	Δ(Q-2-NADH) cm^{-1}
$S105C^M$	cytoplasmatic side	2127	2123	-4	2129	+2	+6
$E108C^M$		2125	2125	0	2127	+2	+2
$H117C^M$		2127	2125	-2	2131	+4	+6
$H159C^M$		2123	2125	+2	2129	+6	+4
$T332C^M$	periplasmatic side	2127	2123	-4	2127	0	+4
$S414C^M$		2123	2123	0	2127	+4	+4
$T422C^M$		2123	2123	0	2129	+6	+6
$S425C^M$		2129	2126	-3	2131	+2	+5
$T178C^M$	central part	2133	2123	-10	2133	0	+10
$K234C^M$		2131	2129	-2	2131	0	+2
$D258C^M$		2125	2127	+2	2127	+2	0

Table 4.14 shows a summary of all the conformers after deconvolution analysis. It was revealed that the band could be split into two peaks, where one of the contribution appeared at lower wavenumbers around 2125 cm^{-1} and another part was observed around 2140 cm^{-1}. It was found out that the contribution at higher wavenumbers increased for the re-oxidized variants. However, the presence of peaks at lower wavenumbers was still observed. This could be a sign that the variant was partially reoxidized, and some part of it remained reduced.

Table 4.14: Summary on the conformers after deconvolution analysis.

Variant	Location	CN (cm^{-1})	%	+NADH (cm^{-1})	%	+Q-2 (cm^{-1})	%
$S105C^M$	cytoplasmatic side	2125	80	2123	63	-	-
		2140	20	2136	37		
$E108C^M$		-	-	-	-	2124	68
						2136	32
$H117C^M$		2125	72	-	-	-	-
		2138	28				
$H159C^M$		2123	72	2122	72	2119	29
		2138	28	2136	28	2132	71
$T332C^M$	periplasmic side	2128	92	2122	61	2114	4
		2141	8	2134	39	2129	96
$S414C^M$		2121	67	2121	72	2121	49
		2134	33	2135	28	2135	51
$T442C^M$		2121	55	2121	59	-	-
		2133	45	2134	41		
$S425C^M$		-	-	-	-	2115	8
						2131	92

Table 4.15 shows the half-band widths of the nitrile label signals of the variants. The bands after incubation with Q were broader compared to those obtained directly after labelling or after reduction by NADH.

Table 4.15: FWHM of the variants.

Variant	Location	CN (cm^{-1})	+NADH (cm^{-1})	+Q-2 (cm^{-1})
$S105C^M$	cytoplasmatic side	27	23	26
$E108C^M$		23	18	25
$H117C^M$		23	24	27
$H159C^M$		20	19	28
$T332C^M$	periplasmic side	25	22	26
$S414C^M$		17	16	28
$T442C^M$		22	20	25
$S425C^M$		22	22	22
$T178C^M$	central part	22	21	23
$K234C^M$		22	24	25
$D258C^M$		22	25	22

4.4.4 Addition of ubiquinone

The spectra presented in Figure 4.53 demonstrate the importance of NADH in inducing a significant shift in the spectral position of the thiocyanate band after incubation with Q.

Specifically, incubation of the H117C^{M} variant, with Q directly after labelling resulted in a small shift of 2 cm^{-1}, suggesting a conformational change within NuoM. In contrast, treatment with NADH prior to incubation with Q led to a more substantial shift of 6 cm^{-1}, which is 4 cm^{-1} higher than the shift observed in the absence of NADH. These results suggest that electrotransfer to Q plays a crucial role in transmitting conformational changer to the membrane arm, leading to a more pronounced shift in the thiocyanate band's spectral position.

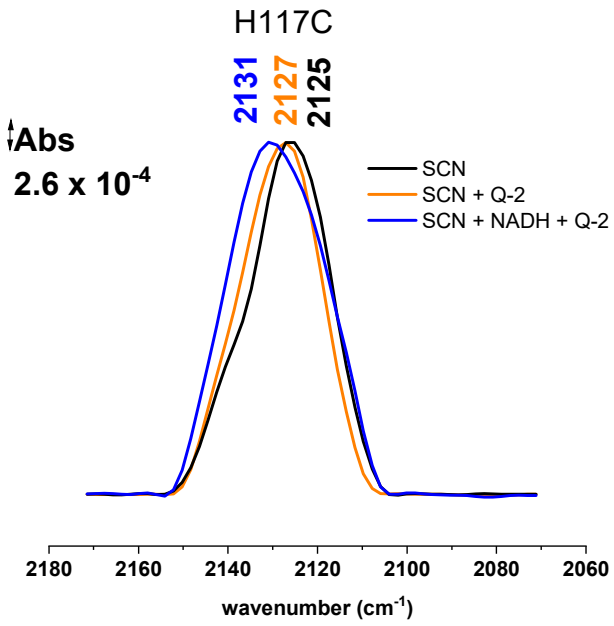

Figure 4.53: Spectra of the SCN bands of H117C^{M} (black), incubated with 150 µM Q-2 (orange) and first after reduction with 100 µM NADH and then re-oxidation with 150 µM Q-2 (blue).

4.5 Relevance of conserved amino acid residues for the mechanism of *bd* oxidase

Cytochrome *bd*-I oxidase contains three non-covalently bound heme groups in a 1:1:1 ratio, and catalyzes the reduction of oxygen to water with the help of hemes b_{558}, b_{595} and heme *d* [22]. Apart from contributing to energy conservation, cytochrome *bd* endows *E. coli* with several specific functions by acting as an oxygen scavenger and inhibiting the degradation of O_2-sensitive enzymes [23]. Cytochrome *bd*-I cryo-EM studies revealed that cytochrome *bd*-I is made up of two major subunits, CydA and CydB and the enzyme from some species contain additionally one or two accessory subunits called CydH (CydY) and CydX [24]. All heme groups are located in the catalytic subunit CydA.

Previous biochemical, spectroscopic, and structural studies revealed the presence of acidic amino acid residues as ligands to these heme cofactors, playing crucial roles in determining the redox potentials of the hemes, as well as their reactivity towards oxygen [25]. These studies demonstrated, based on reaction induced FTIR difference spectroscopy, that these residues have an untypically high pK_a value. Determining the exact pK_a value of these acidic residues can reveal important information about the reaction mechanism and physiological role of cytochrome *bd*-I oxidases. This work focusses on the four subunit *bd*-I oxidase from *E. coli*.

Mutations in CydA were generated in the proximity of the hemes. The mutated positions either serve as heme ligands or are found in close proximity to these residues (Fig. 4.54). The mutations E99D, E99Q, E107D, E107Q, E445D, E445Q, R448N were generated to study their influence on the *bd*-I oxidase activity and stability.

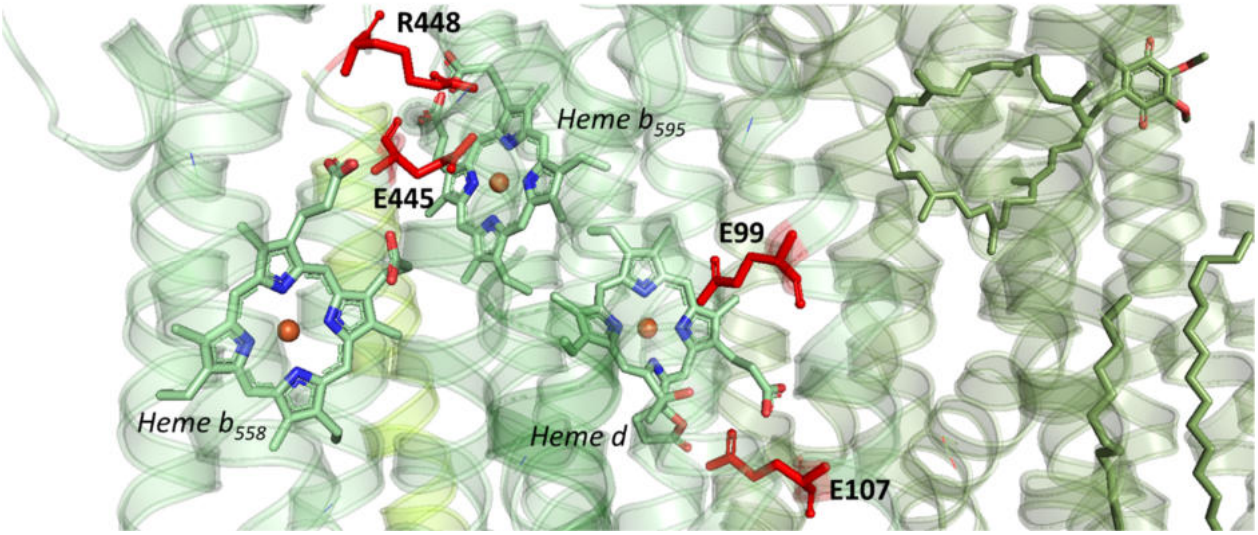

Fig. 4.54: Position of the mutated residues on CydA of *E. coli bd*-I oxidase. (PDB: 6RX4) [24].

4.5.1 Generation of mutations on CydA

All point mutations were generated on CydA *via* site-directed mutagenesis. To generate the mutations, polymerase chain reactions were applied. Mutations were introduced into the pET28b(+)cydA$_h$BX plasmid. Figures 4.55 to 4.57 show the products of the PCR reactions.

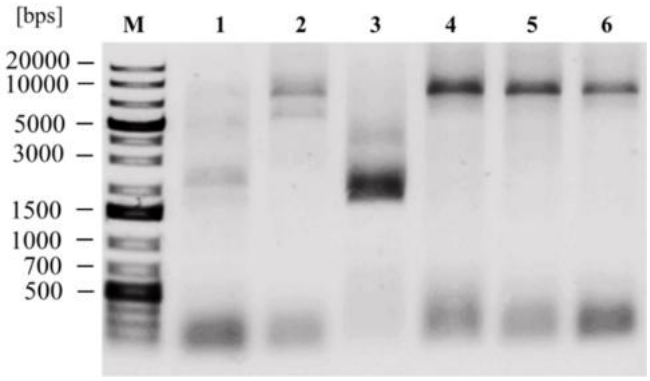

Figure 4.55: Agarose gel to identify the PCR products to generate the plasmid pET28b(+)cydA$_h$BX with mutations in *cydA*. Lane 1 and 2 show the pattern of the product E99D^A at 50° and 72°C, respectively. Lanes 3 and 4 show the pattern of the product E99Q^A at 50° and 72°C, respectively. Lanes 5 and 6 show the pattern of the reaction to generate E107D^A at temperatures 50° and 72°C, respectively. The GeneRuler 1 kb Plus DNA Ladder (M) was used as a reference. Lanes 1, 4, 5 and 6 show the expected bands at 8000 bps.

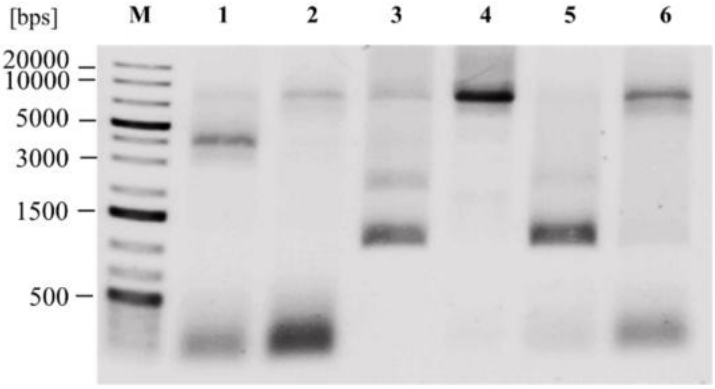

Figure 4.56: Agarose gel to identify the PCR products to generate the plasmid pET28b(+)cydA$_h$BX with mutations in *cydA*. Lane 1 and 2 show the pattern of the reaction to generate E107Q^A at 50° and 72°C, respectively. Lanes 3 and 4 show the pattern of the product E445D^A at 50° and 72°C, respectively. Lanes 5 and 6 show the pattern of the reaction to generate E445Q^A at temperatures 50° and 72°C, respectively. The GeneRuler 1 kb Plus DNA Ladder (M) was used as a reference. Lanes 2, 4 and 6 show the expected bands at 8000 bps.

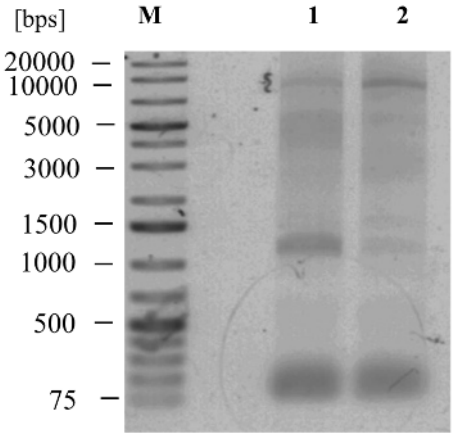

Figure 4.57: Agarose gel to identify the PCR products to generate the plasmid pET28b(+)cydA$_h$BX with a mutation in *cydA*. Lane 1 and 2 show the pattern of the reaction to generate R448N^A at 50° and 72°C, respectively. The GeneRuler 1 kb Plus DNA Ladder (M) was used as a reference. Lanes 2 shows the expected bands at 8000 bps.

For each mutation a band of the expected size around 8000 bps was obtained on the agarose gel. The bands were cut out, purified and strain CBO was individually transformed with the plasmid. Colonies were picked and cultivated, and their plasmids were isolated. The silent mutation was introduced into the plasmid in addition to the desired mutation to generate additional cleavage sites, so that successful mutagenesis could be tested by restriction analysis. DNA sequencing confirmed the success of site-directed mutagenesis. Figures 4.58 and 4.59 show the results of restriction analysis.

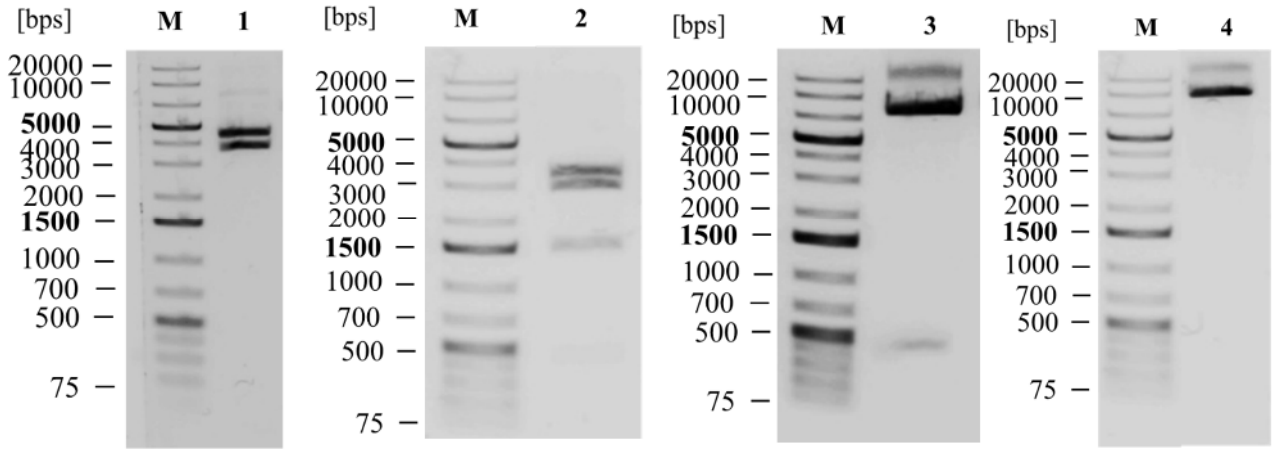

Figure 4.58: Agarose gels of restriction analysis to verify mutations on *cydA*. The GeneRuler 1 kb Plus DNA Ladder (M) was used as a reference. Lane 1: E99D^A (expected bands at 4420, 3663 bps with PvuI), lane 2: E99Q^A (expected bands at 3263, 2758, 1424, 390, 189 and 59 bps with VspI), lane 3: E107D^A (expected bands at 7726 and 357 bps with XbaI), lane 4: E107QA (expected bands at 8083 bps with SalI).

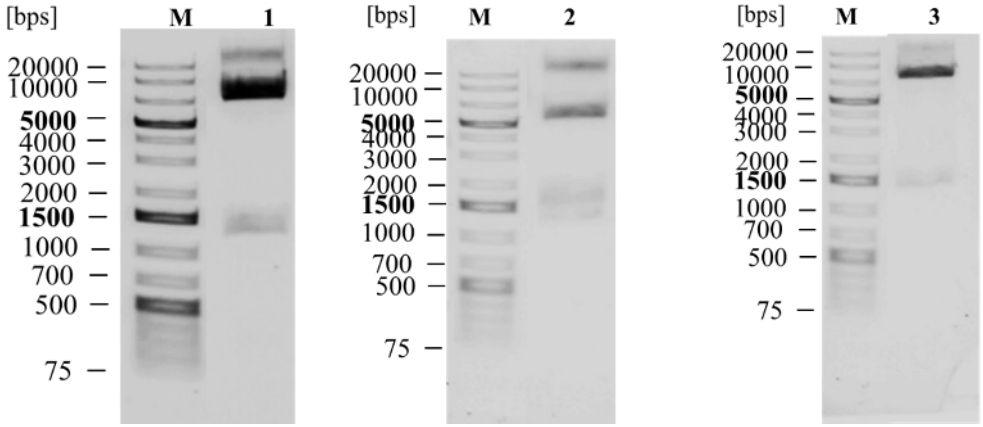

Figure 4.59: Restriction analysis to verify mutations on *cydA*. The GeneRuler 1 kb Plus DNA Ladder (M) was used as a reference. Lane 1: E445D^{A} (expected bands at 5274, 1492, 1182, 114, 21 bps with EheI), lane 2: E445Q^{A} (expected bands at 5274, 1492, 1182, 114, 21 bps with EheI), lane 3: R448N^{A} (expected bands at 6950 and 1133 bps with NcoI).

Positive clones were identified with DNA sequencing, bacterial glycerol stocks were produced and stored at -80°C.

4.5.2 Comparison of CBO and BL21*ΔcydA$_h$BXγ

To find out, which strain produces more *bd*-I oxidase, growth of CBO and BL21*ΔcydABXγ were compared. This procedure was performed with the strains transformed with the plasmid encoding *bd*-I oxidase. Both strains were grown in LB medium (Fig. 4.60). Membranes were extracted from cells of both strains, and membrane proteins were extracted and purified in parallel.

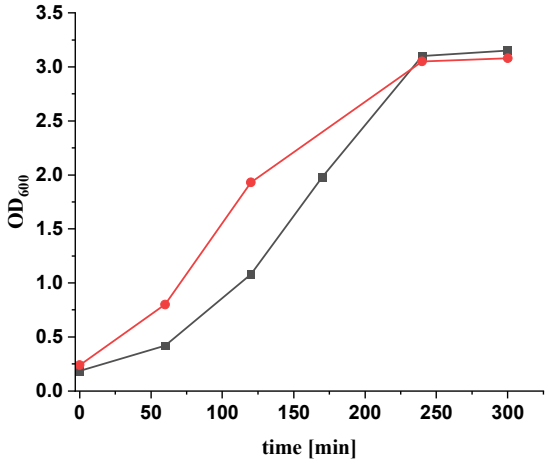

Figure 4.60: Growth of strains BL21*ΔcydABXγ (black) and CBO (red) in LB-medium.

At OD_{600} 2.0, IPTG was added to the cultures to induce the gene expression, and after 2 h cells were harvested. Membranes were purified from the cells, the membrane proteins were extracted,

and the *bd*-I oxidase was purified in a 4-step chromatography process. The obtained yields are depicted in Table 4.16.

Table 4.16: Protein yield of the preparations.

Strain	Cells, g	Membranes, g	Protein, mg
BL21*ΔcydABXγ	18.12	3.24	0.5
CBO	26.27	4.85	5.8

Strain CBO strain clearly produces more protein, so the mutated plasmids were used to transform strain CBO. Bacterial glycerol stocks were grown and kept at -80°C.

4.5.3 Bacterial cell growth

The strain CBO transformed with the plasmids containing a mutation in CydA were grown in LB medium to an OD_{600} of around 2.0, induced with IPTG (0.8 M), and cells were grown for 2 h more and then harvested. Figures 4.61 and 4.62 show the growth of the corresponding strains. All strains grew similar to the parental strain.

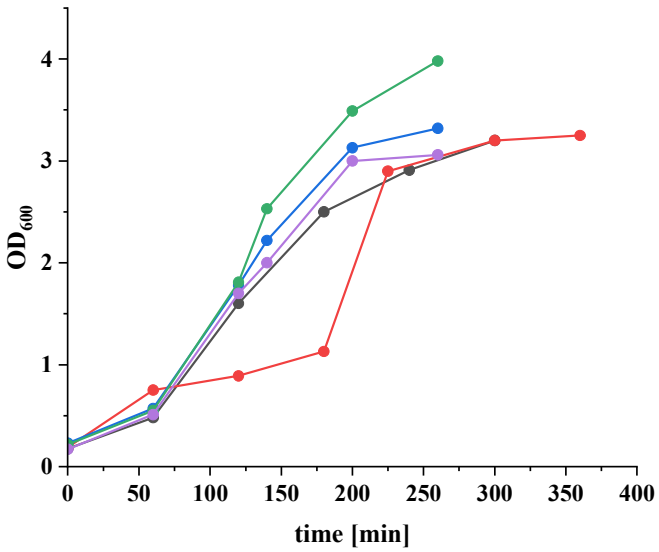

Fig. 4.61: Growth of CBO//pETcydA$_h$BX (black); E99D^A (red); E99Q^A (blue); E107D^A (green), E107Q^A (magenta).

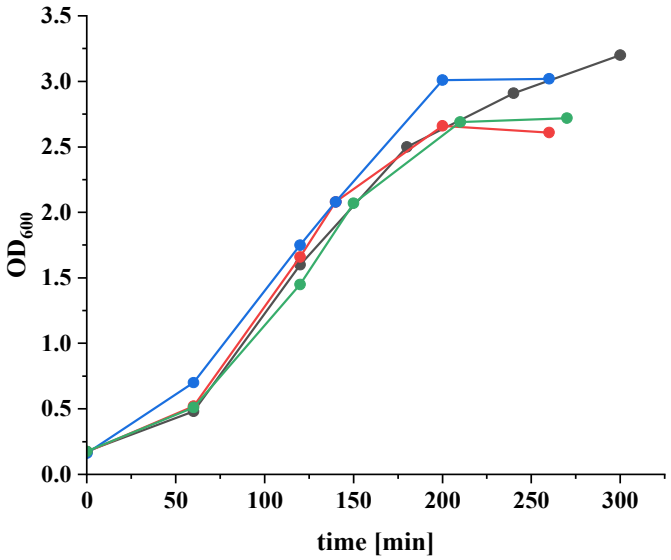

Fig. 4.62: Growth of CBO//pETcyd (black); E445D^{A} (red); E445Q^{A} (blue); cydA R448N^{A} (green).

4.5.4 Oxidase activity of cytoplasmic membranes

The NADH oxidase activity of the membranes was determined with a Clark-type electrode. 5 µL of membranes were incubated with 2 mL buffer (A_{bd}-buffer, pH 7.0). The reaction was started with the addition of 5 µL NADH (0.5 M). To inhibit the activity of *bo*$_3$, 1 mM KCN was added to the buffer.

Table 4.17: NADH oxidase activity of cytoplasmic membranes from CydA mutants. The data were acquired in triplicate measurements of each sample. The average and standard deviation was calculated. The parental strain was used as a reference and its value was set to 100%.

Membranes of CBOpETcydA$_h$BX variants	**NADH oxidase activity**	
	[U/mg]	**[%]**
no change	0.21 ± 0.025	100 ± 12
E99D^{A}	0.040 ± 0.001	18 ± 3
E445D^{A}	0.088 ± 0.003	41 ± 2
R448N^{A}	0.043 ± 0.002	20 ± 4

NADH oxidase activities of membranes from mutants with modifications on CydA were compared to the NADH oxidase activity of the parental strain that was set to 100%. The NADH oxidase activities of membranes from all variants were lower than the one measured for the parental strain. The NADH oxidase activity of the membrane carrying E99D^{A} variant resulted in 18% activity,

that carrying the R448N^{A} mutation had approximately the same value (20%) and that of the variant E445D^{A} variant had 41% of the activity of the parental strain.

4.5.5 Preparation of cydA variants

Cells were harvested, disrupted, and membranes isolated. Membrane proteins were solubilized with LMNG, and the extract was loaded on an affinity chromatography column. Weakly bound proteins were eluted with imidazole-containing buffer. The imidazole gradient was applied, and bound proteins were eluted. The eluate was collected, concentrated to 2 mL or less and loaded on a desalting column to remove the residual imidazole and salt before being subjected to ion exchange chromatography. The results of affinity and desalting chromatography are shown in Figure 4.63.

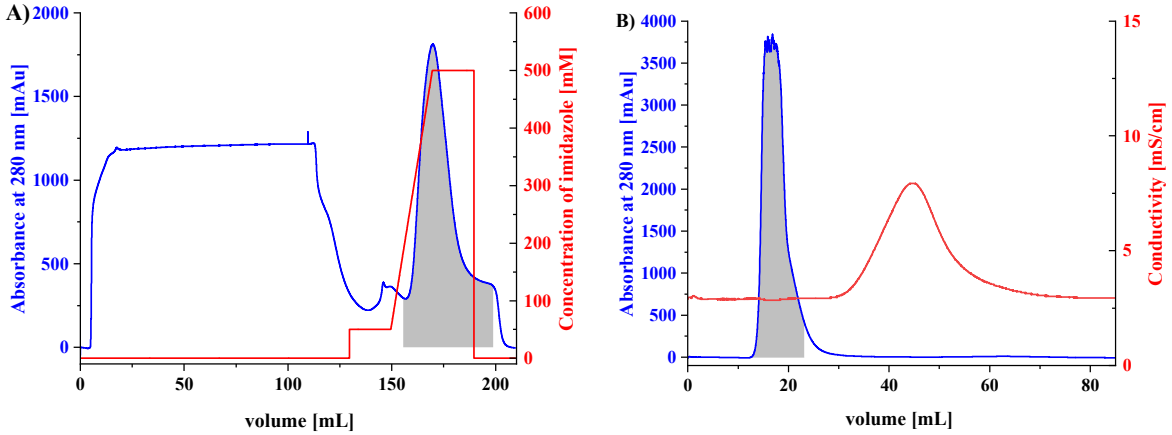

Figure 4.63: Elution profile of HisTrap affinity chromatography (A) and HiTrap Desalting column (B). A) Absorbance at 280 nm is shown in blue, concentration of imidazole in red. B) Absorbance at 280 nm is depicted in blue, conductivity is shown in red. The pooled fractions are indicated by the grey area.

The concentrated peak after desalting was subjected to MonoQ 10/100 GL anion exchange chromatography. The column was washed with buffer, and a gradient was applied with 20 to 350 mM NaCl. The eluate was collected, concentrated and applied to size exclusion chromatography. The eluate was collected and fractions containing cytochromes concentrated. The protein concentration was determined and the protein was stored at -80°C. Figure 4.64 shows the chromatograms of the anion exchange and size exchange chromatography.

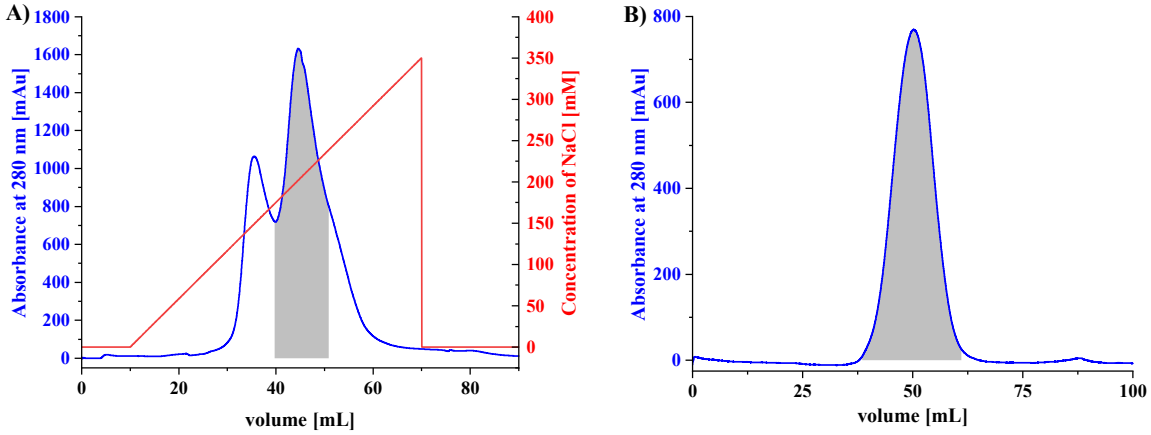

Figure 4.64: Elution profile of MonoQion exchange chromatography (A) and S300 size exclusion column (B). A) Absorbance at 280 nm is shown in blue, concentration of NaCl in red. B) Absorbance at 280 nm [mAu] is depicted in blue. The pooled fractions are indicated by the grey area.

This procedure was applied to all *bd*-I oxidase variants. Three variants were obtained successfully (E99D^{A}, E445D^{A} and R448N^{A}) according to this procedure. For the variant E99Q^{A} all the purification steps were performed and the elution profiles looked like the ones shown in Figures 4.63 and 4.64. However, the preparation was not stable, and the signals of the heme groups were lacking in the redox-difference spectrum. The variants E107D^{A} and E107Q^{A} were also not stable. The membrane proteins extracted from these variants were loaded on to affinity chromatography column, but both variants did not bind to the Ni^{2+} material. Figure 4.65 shows the elution profile of this purification step.

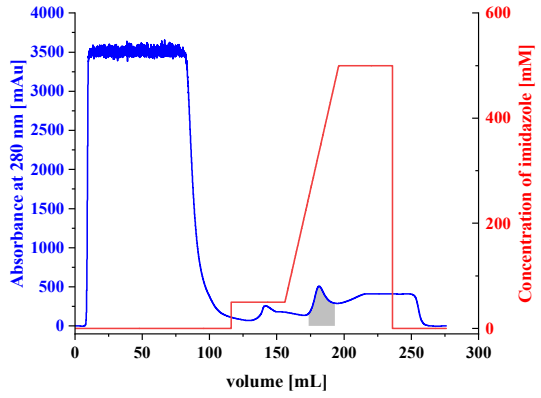

Figure 4.65: Elution profile of HisTrap affinity chromatography to purify the E107D^{A} variant. Absorbance at 280 nm is shown in blue, concentration of imidazole in red. The fractions that normally include the oxidase are shown in grey area.

The E445Q^{A} variant also appeared not stable, and purification was stopped after affinity chromatography.

Table 4.18: Yields of the preparations of the CydA variants.

Variant	Cells, g	Membranes, g	Protein, mg
E99D^{A}	57.68	10.12	5.96
E99Q^{A}	48.66	11.10	-
E107D^{A}	50.22	8.09	-
E107Q^{A}	50.72	8.91	-
E445D^{A}	40.19	6.91	3.00
E445Q^{A}	43.79	10.22	-
R448N^{A}	32.15	7.61	5.57

4.5.6 SDS-PAGE of the *bd*-I oxidase variant preparations

The SDS-PAGE analysis was performed for *bd*-I oxidase characterization to find out if all subunits were present in the mutated variants (Figure 4.66).

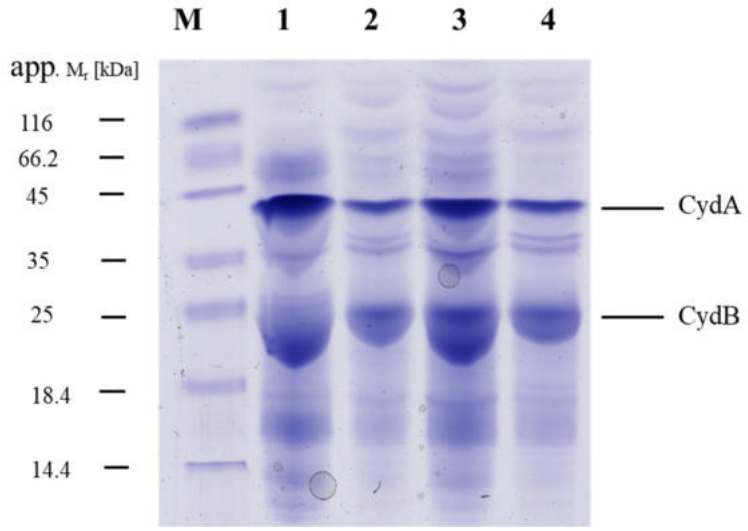

Figure 4.66: SDS-PAGE of the preparations of the *bd*-I oxidase variants. Lane M was loaded with the *unstained protein marker* (Thermo Fischer Scientific). Lanes are loaded with: *bd*-I oxidase (1), E99D^{A} (2), E445D ^{A} (3), R448N^{A} (4). The two major subunits were attributed according to their molecular mass.

The preparations of the variants are similar to that of the *bd*-I oxidase and the main subunits are visible on the SDS-PAGE gel (CydA, CydB).

4.5.7 Redox difference spectra of the preparations

The presence of the hemes b_{558}, b_{595} and heme *d* in the preparations was analyzed by recording UV/vis spectra of the reduced and oxidized state. The figure 4.67 shows the characteristic UV/vis

redox-difference spectrum of the wild type *bd*-I oxidase. The characteristic peaks were assigned to the heme groups. Heme b_{558} gives bands at 531 and 561.5 nm. For heme b_{595}, the peaks are visible at 561.5 and 595 nm. The characteristic peak for heme *d* was recorded at 628 nm. All characteristic peaks for hemes are present for the wild type.

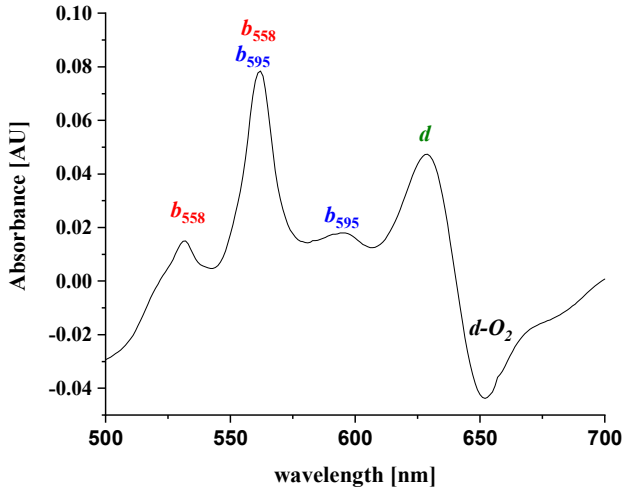

Figure 4.67: Reduced-minus-oxidized UV/vis difference spectra of *bd*-I oxidase. The wavelengths of the typical absorbances are indicated.

Figure 4.68 shows reduced-minus-oxidized difference spectra of the E99Q^{A} (A), E107D^{A} (B) E107Q^{A} (C) and E445Q^{A} (D) variants. In the spectrum of the E99Q^{A} variant the peak related to heme *d* at 628 nm is absent. Spectra of the E107D^{A} and E107Q^{A} variants also show only two peaks typical for heme b_{558}. The characteristic peak for b_{595} located at 595 nm is missing. Typical heme *d* peaks are absent from the spectra (Fig. 4.68A and B). The spectrum of the E445Q^{A} variant (Fig. 4.68D) show peaks at 531.5 and 561.5 nm. Other characteristic bands for the hemes are missing, this indicates that the hemes are absent from the sample.

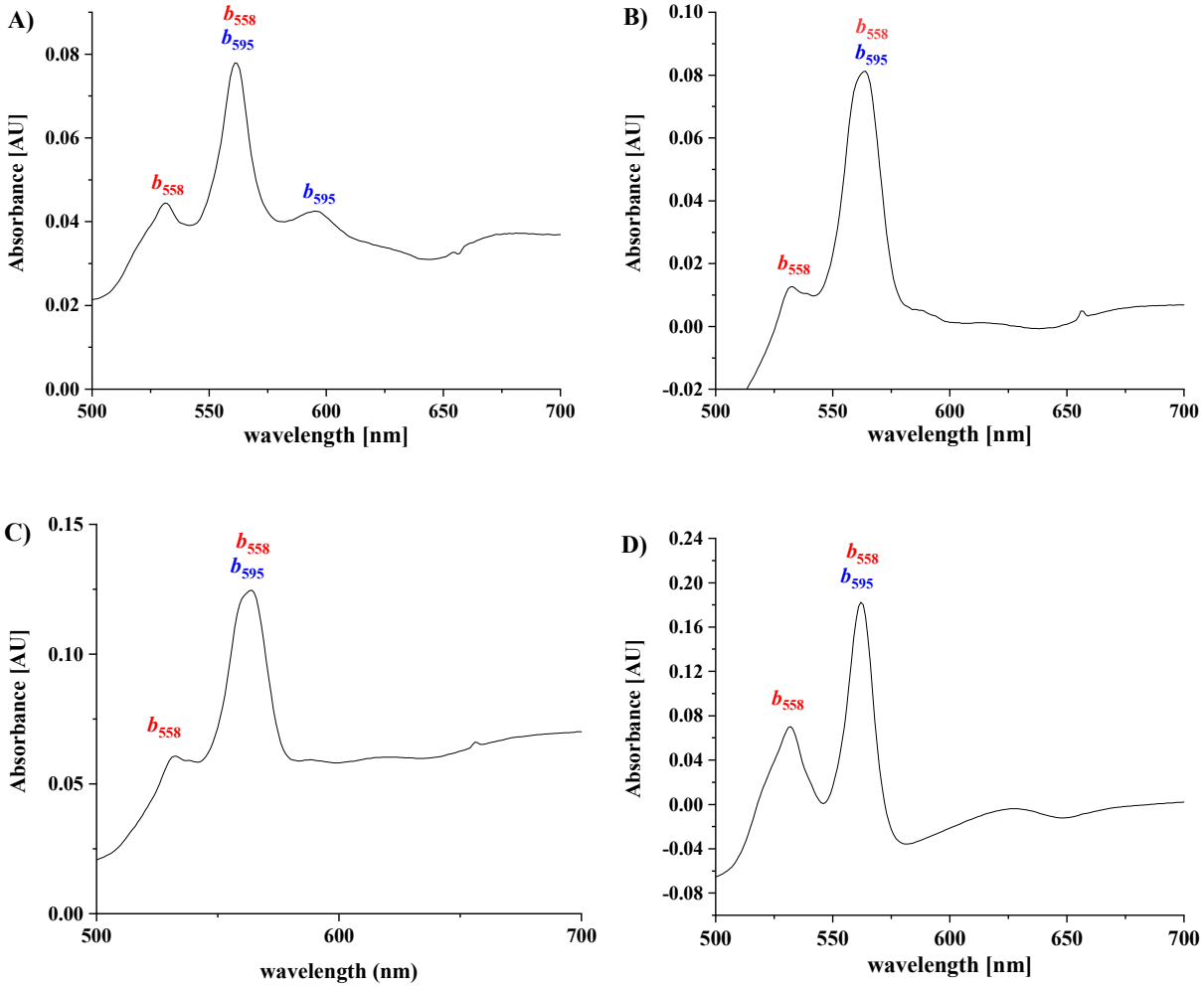

Figure 4.68: Reduced-minus-oxidized UV/vis difference spectra of the preparations of *bd*-I oxidase variants. A) E99Q^{A}, B) E107D^{A}, C) E107Q^{A} and D) E445D^{A}.

Further electrochemical and spectroscopical experiments were performed for the obtained *bd*-I oxidase variants to study to impact of inserted mutations on enzyme functions. These measurements were performed by Iryna Makarchuk, University Strasbourg. The redox properties of the heme groups in the mutated variants. The effect of the mutations on the catalytic dioxygen reduction by means of the electrocatalytic approach was examined to investigate the role of heme b_{595} [166]. UV-vis titration was performed to determine the redox potential groups. Table 4.19 shows the results of these measurements.

Table 4.19. Redox potentials of the bd-I heme groups determined by UV–vis titration [166].

Mutants of *bd*-I oxidase	Potential vs SHE, mV		
	heme b_{558}	heme b_{595}	heme *d*
WT	176	168	258
E445D	124	276	310
R448N	174	-86	446

The redox potential of heme b_{595} in the E445D variant, was up-shifted by 100 mV and that of heme *d* by 50 mV. R448N variant showed that the redox potential of heme b_{595} was down-shifted by 254 mV and that of heme *d* was up-shifted by 188 mV [166].

Cyclic voltammetry using a gold electrode was performed to check the ability of the preparations to reduce dioxygen. Figure 4.69 shows the results of these measurements.

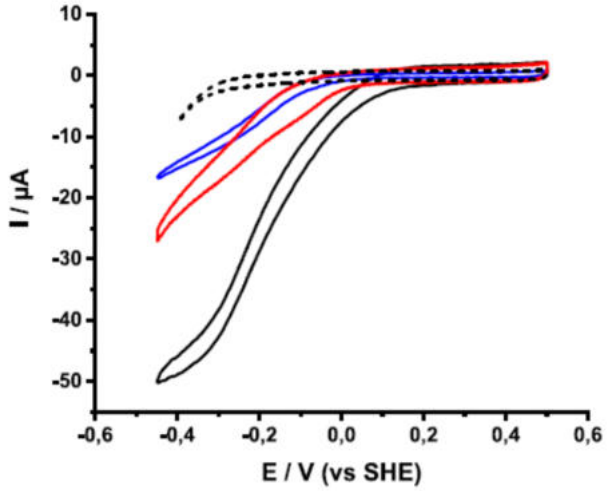

Fig. 4.69: Cyclic voltammograms of the *bd*-I wild-type (black) and the E445D (blue) and R448N (red) variants [166].

The cyclic voltammogram of wild-type *bd*-I showed a sigmoidal shape, while the curves obtained for both mutants were altered in shape and magnitude.

5 Discussion

5.1 Proton translocation by complex I

Complex I is functionally well-characterized. In addition, several structures of complex I from various species from 2.3 to 4.5 Å resolution were obtained. Complex I couples the electron transfer of two electrons to Q with the translocation of four protons across the membrane. The mechanism of electron transfer is reasonably well characterized. However, the mechanism of proton translocation across the membrane is still under discussion. The Q binding site is located in 200 Å distance from the distal subunit NuoL that comprises the proton pathway. The mechanism of proton translocation driven by the redox chemistry along such a long distance is still under debate.

The membrane arm of complex I comprises the three antiporter-like subunits NuoL, NuoM and NuoN that are homologous to each other. It was suggested that three protons go through each of the homologous subunits and the fourth proton is transported *via* E-channel. Due to the lack of cofactors, proton translocation is based on conformational changes within the membrane arm. The central axis of the membrane arm contains several conserved charged amino acids. Along this axis, an electrostatic forward and backward wave could propagate, allowing the opening and closing of proton pathway enabling proton translocation from the N-side to the P-side. There is another theory of proton translocation across the membrane, the so-called “ND-5 theory”, according to which all four protons are ejected through the distal subunit NuoL (ND-5 in mammals), by two electrostatic waves propagating in one direction along the central axis.

The idea of this study was to observe conformational changes that occur during protons translocation. As method to detect conformational changes, IR spectroscopy of complex I decorated with an IR label was chosen. Subunit NuoM the central antiporter subunit in the membrane arm was selected as target to introduce the label. Mutations were generated at the positions close to the putative proton pathway as postulated in [119]. NuoM shows a structural arrangement of two symmetrical parts along the central axis with a broken helix that could build up the proton channel, which comprises two half-channels. According to the structural data, NuoM as the other antiporter-like subunits connects the cytoplasmic and periplasmic side by this putative proton pathway.

It was experimentally found that complex I has no surface accessible cysteine residues [265]. Crucial positions of NuoM that were assumed to be part of the proton pathway and to be involved in proton translocation were mutated to cysteines for further labelling to cyanides by site-directed

mutagenesis. Cyanides are good candidates for infrared labelling as they are sensitive to changes of the local environment such as H-bonds and the electric field. Cyanides are small, can be easily incorporated into proteins and do not significantly perturb their structure. The signal appears in a spectroscopically clear region of the IR spectrum around 2120 cm^{-1} where signals of proteins are absent. To the complex bound to SAM, NADH and Q were added to monitor spectral changes in the absorbance of the infrared label. This might provide insights into transient structural changes occurring in NuoM during turnover.

It was stated that the SCN absorbance changes according to solvent exposure and can detect local changes in the environment. The frequency mode of the thiocyanate moiety experiences a blue shift in a polar environment compared to an aprotic solvent [7]. Quantum chemistry calculations showed that the peak frequencies of the SCN labels are not strongly affected by the side groups in proteins [7]. Thus, it is believed that frequencies depend mainly on the local environmental changes. The line width can describe also environmental fluctuation and give an idea of how fast the group would move between several conformational states.

5.2 Characterization of the NuoM variants

Mutations on subunit NuoM were generated by site-directed mutagenesis with the target amino acid substituted by cysteine. Mutations on the cytoplasmic side (E108, S105, H117, H159), on the periplasmic side (S414, T332, S425, T422) and in the cavity (K234, T178, D258) were designed and generated. These positions were assumed to be involved in building a putative proton pathway in NuoM [119]. Residues K234 and T178 are located in the center of the main cavity. Position D258 leads to the cytoplasmic half of the channels that comprises S105, H117, E108 and H159. Residues S414, S425, T422, and T332 are located in the periplasmic half channel of NuoM. Figure 5.1 shows the position of the mutated residues on NuoM. Figure 5.2 shows the environment of individual residues.

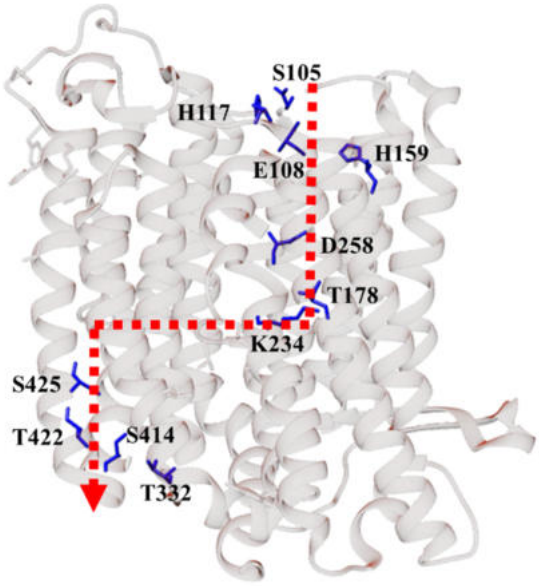

Figure 5.1: Position of mutated residues of NuoM (PDB:7Z7S) [20]. Mutated positions are shown in blue. The putative proton channel is indicated by the red broken arrow.

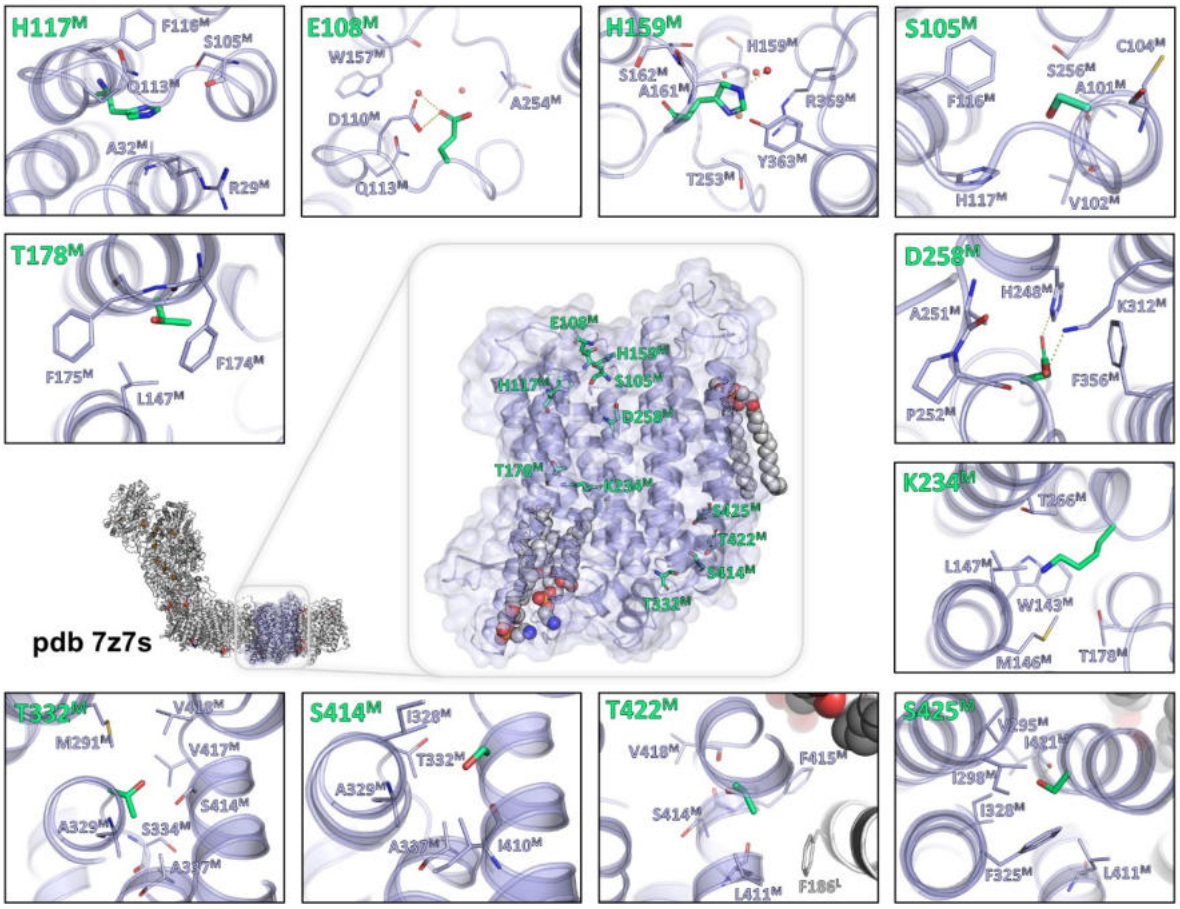

Figure 5.2: Position of individual residues of NuoM (PDB:7Z7S) [20].

All mutations were successfully introduced into the pBAD*nuo*$_{his}$*nuoF* plasmid. The success of mutagenesis was proven by sequence analysis. A strain lacking both membraneous NADH dehydrogenases were transformed with the respective plasmids. Mutant strains were grown, membranes were isolated and the complex I variants were isolated. Proteins were purified in yields of 4.7 to 18 mg. The NADH:decyl-Q oxidoreductase activity of the variants similar to that of the parental enzyme (Tab. 4.6). However, two variants showed a clearly diminished activity. The K234C variant had only 14% of the activity. Position K234C variant is conserved and it is located in the central part of the cavity that is assumed to be involved in charge transport according to all postulated mechanisms. The D258C variant had only 36% of the activity of the complex I. This loss of activity indicates that this residue might be essential for proton translocation. Other complex I isolated variants showed high NADH:decyl-Q oxidoreductase activity with ranging from 65 to 101% of that of complex I. The importance of position K234 is proved by NADH oxidase measurements (Tab. 4.1). The variant K234C showed 18% of the NADH oxidase activity of the complex I activity in the membrane. Membranes from the mutant strain K234C^{M} showed by far the lowest activity compared to the other mutants. Thus, the loss of activity was due to the mutation, which confirms the importance of this position. This data confirmed the ones described in the literature, where mutation of position K234^{M} resulted in an inactive complex I [121, 266]. Nevertheless, all variants were stable and fully assembled, active, and the mutations did not induce any significant changes, enabling their use for spectroscopic studies.

All cysteine residues were labelled with cyanide with high labelling efficiency. These data were acquired from UV/vis spectroscopy where the signal at 412 nm from TNB^- anion was followed as it was replaced by CN^- (Tab. 4.8). Based on the fact that complex I does not have any surface accessible cysteine residues, targeted and specific labelling of the variant residues was successful. Further biochemical characterization of the variants revealed that the activity of the variants was slightly diminished due to the labelling process (Tab. 4.9). However, the loss of activity was not significant. Mass photometry and SDS-PAGE showed that labelling did not affect complex I assembly and subunit composition. The SCN label size is too small to be detected by this kind of analysis. The SCN signal can be detected in the IR spectrum, due to its interaction with the protein structure, which is different from the band of free KCN that appears at position 2058 cm^{-1} [267]. The results show that the SCN label was successfully introduced into the complex I variants at the specific positions without perturbing protein structure. Its insertion affected complex I assembly

and activities to a minor extent. Each complex I variant had newly incorporated a cysteine labelled to SCN appearing in a unique local environment. Addition of substrates to the protein bound to the SAM (self-assembled monolayer) helped to obtain mechanistic insights on catalytic changes in complex I.

5.3 IR-spectroscopic characterization of the variants

Labelling of complex I variants resulted in the appearance of a specific band located at around 2123 cm^{-1}, that was not observed in the spectrum of the complex I. In biological systems, thiocyanate band is described to give a signal at around 2153-2164 cm^{-1}. However, there were peaks for labeled photoactive yellow protein (PYP) appearing at 2080 cm^{-1} [268]. For ribonuclease S a peak was observed at 2233 cm^{-1} that could be a sign of its location in the hydrophobic environment [269].

The significance of the shifts was proved by other studies. Shifts below 5 cm^{-1} appeared to be relevant [233]. In the literature, membrane-binding peptide, mastoparan x (MPx peptide), was studied by the IR spectroscopy using a PheCN probe. In water, the peptide showed a CN stretching vibration at 2235 cm^{-1}. However, attachment to the phospholipid bilayer caused a shift of 6 cm^{-1}, and the SCN band appeared at 2229 cm^{-1}, indicating a more hydrophobic or a less solvent-accessible environment [233].

In previous studies, complex I variants $K551C^{L}$ and $Y590C^{L}$ located in the horizontal helix were successfully labeled with cyanide and incubated with NADH [9]. It is the first time that such a big membrane protein as complex I acquired a cyanide label and movements were visualized with the help of an IR spectrum. It was observed that the initial position of the signal of each labelled residue is different from each other. That is due to the fact that all mutated positions are located in a unique local environment. They are located in different parts of NuoM, either at the entrance, in the middle of or at the exit of the putative proton pathway, experiencing a different local hydrophobicity and H-bond network structure.

SCN bands are sensitive to H-bond and their local environment. The changes in solvent exposure in the environment and the presence of water have an effect on the position of the band in the IR spectrum. The appearance of the signal at higher wavenumbers reflects a more hydrophilic environment or better solvent accessible environment. On the contrary, bands that show up at lower wavenumbers suggest that the label is located in less solvent exposed or hydrophobic environment.

Initial positions of the label at residues close to the cytoplasmic side (S105C and H117C) appeared at 2127 cm^{-1} (Fig. 4.34A and 4.38A), which could mean more hydrophilic or more solvent-accessible environment. Both residues are facing each other (Fig. 5.3), indicating a similar local environment. Position H159C is found in a more hydrophobic environment at 2123 cm^{-1} (Fig. 4.40A). The position of the glutamic residue E108C is observed at 2125 cm^{-1} (Fig. 4.36A). Both positions belong to different helices, although they are located at the same level in the membrane, in close proximity to each other (Fig. 5.3). This could explain the similar absorbances with a 2 cm^{-1} difference.

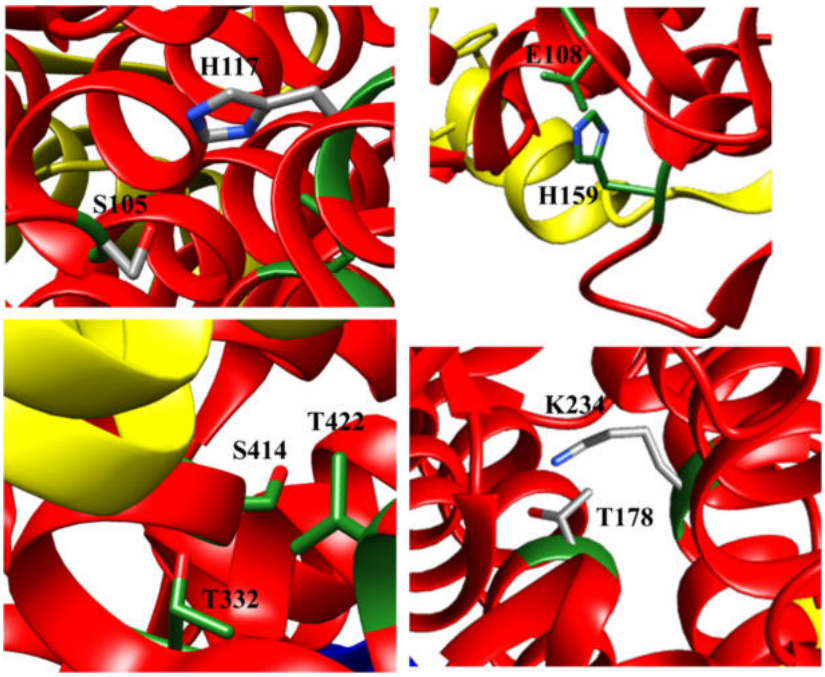

Figure 5.3: Positions used for labelling NuoM (PDB: 7Z7S) [20]. The side chain of the mutated residues is shown in different colours (green or silver). Nitrogen atoms are shown in blue, oxygen atoms are shown in red. HL helix is shown in yellow, helices of NuoM are shown in red.

On the periplasmic side, the signals of two residues (S414C and T422C) were observed at the same wavenumbers (2123 cm^{-1}) (Fig. 4.44A and 4.46A), in agreement with their location in a more hydrophobic or less solvent-accessible environment. Both residues are located at different sides of the exit of the putative proton channel (Fig. 5.3). The other two residues appeared at higher wavenumbers 2127 and 2129 cm^{-1} indicating a more hydrophilic environment (T332C and S425C), accordingly (Fig. 4.42A and 4.48A). Residue T332C is located closer to the periplasmic surface of complex I, where the proton exit site is expected to be located. Residue S425C is located in the inner part of the putative exit half-channel (Fig. 5.1).

Residues located in the centre of NuoM (T178C and K234C) tended to appear in a more hydrophilic environment at 2133 and 2131 cm^{-1}, respectively (Fig. 4.50A and 4.51A). Both residues are located in close proximity to each other (Fig. 5.3) as expected from the similar hydrophobicity of their environment. Residue D258C the signal of which appeared at 2125 cm^{-1} (Fig. 4.52A) is located at the inner end of the putative entry half-channel explaining its absorbance indicative for a rather hydrophilic environment. The presence of the water molecules within the half-channels will affect the local environment of these residues.

The study aimed to determine the position of the SCN label on various cysteine variants of complex I, as well as its changes upon incubation with NADH and ubiquinone. It turned out that the position of the SCN label varied among the variants as expected, and deconvolution analysis revealed the presence of multiple peaks in most cases, indicating the presence of several conformers.

Position $S105C^M$ had two peaks at 2125 cm^{-1} (80%) and 2140 cm^{-1} (20%) before incubation (Fig. 4.35A). After incubation with NADH, the position of the label signal shifted to 2123 cm^{-1} (63%) and 2136 cm^{-1} (37%) (Fig. 4.35B). Deconvolution of the second derivative of the signal of $S105C^M$ incubated with Q showed a mostly homogenous peak at 2127 cm^{-1} (Fig. 4.34C).

Position $E108C^M$ is located at the cytoplasmic side close to the entrance of the putative proton half-channel and showed a peak at 2125 cm^{-1} (Fig. 4.36A and D). Incubation with NADH did not lead to any significant changes of the peak position, however, the broadness of the band became narrower (Fig. 4.36B). Further treatment with Q resulted in a shift to 2127 cm^{-1} (Fig. 4.36C). Deconvolution revealed the presence of two overlapping peaks with 68% at 2124 cm^{-1} and 32% at 2136 cm^{-1} (Fig. 4.37).

The label at $H117C^M$ appeared at 2125 cm^{-1} (72%) and 2138 cm^{-1} (28%) (Fig. 4.39). Incubation with NADH produced a shift of 2 cm^{-1} towards lower wavenumbers and addition of Q resulted in a more significant shift of 6 cm^{-1} towards higher wavenumbers (Fig. 4.38).

The SCN label at position $H159C^M$ appeared around 2122-2123 cm^{-1}, with a small shoulder at 2136-2138 cm^{-1} (Fig. 4.40A). Reduction with NADH did not change the position of the label significantly (Fig. 4.40B). Re-oxidation by Q-2 led to a broad peak with a center around 2129 cm^{-1} (Fig. 4.40C).

The label of the $T332C^M$ variant, appeared mostly at 2128 cm^{-1} (92%), with a smaller portion at 2140 cm^{-1} (8%) (Fig. 4.43A). Incubation with NADH shifted the absorbance towards higher

wavenumbers, with a peak at 2134 cm^{-1} (Fig. 4.42B). Incubation with Q resulted in a peak located around 2129 cm^{-1}, with a small contribution at 2114 cm^{-1} (4%) (Fig. 4.43C).

For $S414C^{M}$ at 2121 cm^{-1} (67-72%) and 2134-2135 cm^{-1} (28-35%) (Fig. 4.45A). After incubation with NADH, the distribution of the signal shifted slightly towards higher wavenumbers. Incubation with Q resulted in two peaks located at 2121 cm^{-1} (49% contribution) and 2135 cm^{-1} (51% contribution) (Fig. 4.45C).

Deconvolution of the signal of the label at T422C showed two peaks at 2133 and 2121 cm^{-1} (45% and 55% respectively) (Fig. 4.47A). After incubation with NADH, the distribution shifted slightly towards the peak at 2121 cm^{-1} (Fig. 4.46B), while an addition of Q resulted in a backshift of the signal at around 2129 cm^{-1} (Fig. 4.46C).

The label at S425C showed a homogeneous absorbance before and after incubation with NADH. However, after incubation with ubiquinone, the label appeared mainly at 2131 cm^{-1}, with a small portion at 2115 cm^{-1} (Fig. 4.49).

Residues located in the cavity (T178C, D258C, K234C) resulted in homogenous peaks, for which deconvolution analysis was not performed.

Both variants with mutations located at the cytoplasmic side (E108C and H159C) showed a signal indicative of a more hydrophilic environment (2125 and 2123 cm^{-1}, respectively) (Fig. 4.36 and 4.40). After incubation with NADH, the signal appeared at 2125 cm^{-1}. Thus, a small shift towards a hydrophobic environment was observed for the label attached to H159C, while no significant change in its position was recorded when attached to E108C. For the other two residues on the cytoplasmic side (S105C and H117C) addition of NADH led to small shifts to lower wavenumbers (2 and 4 cm^{-1}, respectively) (Fig. 4.34 and 4.38), indicative of a movement to an environment with weaker hydrogen bonds, which is less solvent accessible.

The absorbances of residues located in the central part of NuoM were shifted towards wavenunumbers indicating a hydrophobic environment after treatment with NADH. For residue K234C a small shift (2 cm^{-1}) of the label absorbance towards the hydrophobic environment was observed (Fig. 4.51). Residue D258C showed the same shift of 2 cm^{-1} towards a more hydrophilic environment (Fig. 4.52). The addition of Q did not result in any spectral changes with the label attached to D258C. However, when bound to K234C, a small shift to its initial absorbance (2131 cm^{-1}) was observed (Fig. 4.51B). Both mutations showed a significant impact on complex I activity. However, the position of the label at T178C was significantly shifted by 10 cm^{-1} towards

the hydrophobic environment upon reduction with NADH (Fig. 4.50B). The addition of Q also resulted in a bigger shift, this time towards the hydrophilic environment and initial position of absorbance (Fig. 4.50C). Being located in the central axis of the protein, T178 could participate in conformational changes caused by quinone reduction that might be in accordance with the mechanism proposed by Kaila [113].

Interestingly, the absorbance of the label attached to residues at the periplasmic side (S414C and T422C) appeared at the same wavenumbers after labelling (2123 cm^{-1}), and the addition of NADH did not result in any spectral changes (Fig. 4.44 and 4.46). This could indicate that the local environment around these positions did not change, and there was no movement towards a more/less solvent-accessible environment. For the other two residues located at the periplasmic side (T332C and S425C), shifts of 3 and 4 cm^{-1} were observed indicating a local change towards a less solvent accessible environment (Fig. 4.42 and 4.48). Incubation with Q did not change the position of the peak for T332 label (Fig. 4.42C) and gave a small shift of 2 cm^{-1} towards hydrophilic environment for the position with the label at S425 (Fig. 4.48C).

Incubation with Q shifted the absorbances of the label bound to E108C and H159C, which are located at the cytoplasmic side by 2 and 4 cm^{-1}, towards higher wavenumbers or a hydrophilic environment respectively (Fig. 4.36 and 4.40). The other two residues at the cytoplasmic side (S105C and H117C) showed bigger absorbance shifts of 6 cm^{-1} indicating a more solvent accessible environment (Fig. 4.34 and 4.38).

The absorbances of the label bound to residues at the periplasmic side which did not move upon treatment with NADH (S414C and T422C), was shifted by the addition of Q produced by 4 and 6 cm^{-1}, respectively (Fig. 4.44 and 4.46). When bound to the other residues of the same environment (T332C and S425C), the treatment with ubiquinone resulted in shifts of 4 and 5 cm^{-1}, respectively (Fig. 4.42 and 4.48). In all cases, movements towards a more solvent accessible environment were detected. The label bound to the residue T332C, which is located in the proximity of the periplasmic side close to the exit of the putative proton channel, had an absorbance at its initial spectral position upon addition of Q (Fig. 4.42C). This could be explained by the opening and closure of the proton channel on the periplasmic side.

It was observed that labelling of two residues at the cytoplasmic (S105C and H117C) and two residues at the periplasmic side (T332C and S425C) the signal of the label appeared at higher wavenumbers (2127-2129 cm^{-1}). Signals of the label attached to residues on the cytoplasmic

(E108C and H159C) and on the periplasmic side (S414C and T422C) appeared at lower wavenumbers. Thus, there is pairing of residues, which are located as the entrance and exit for the putative proton channel. The absorbances of the label attached to residues in the cavity (K234C, T178C, D258C) appear mostly in a hydrophilic environment (2125-2133 cm^{-1}). The addition of NADH resulted in a tendency of the absorbance to move to lower wavenumbers (hydrophobic environment). Incubation with Q revealed the tendency of the residues to appear at higher wavenumbers or in a more hydrophilic environment. The spectroscopic shifts after treatment with Q were more significant than ones after the incubation with NADH, which could lead to the conclusion that Q plays an important role in the proton translocation. The observed spectral movements of the label described here are in line with the assumption that water channels are opening or closing. The opening of the channel enables water influt into the channel. The closing of the channel pushes water out.

The line width of the label's absorbance depends on the heterogeneity of the environment and fluctuation occurring in the environment [270]. Thus, line widths describe the dynamics of the local environment. The helical structure of NuoM leads to the broadening of the SCN signals [271]. Here, line widths of the labelled residues were found in the range of 17 to 27 cm^{-1} (Tab. 4.15). The values are higher than the ones described in the literature, where 7 to 16 cm^{-1} are described. The majority of the labels' line widths were here calculated to be 22 cm^{-1}. The broadest band was obtained for S105C (27 cm^{-1}), which is located on the cytoplasmic side, close to the entrance to the putative proton channel. It could indicate a high degree of conformational freedom around this position, enabling the residues to move between several states. The addition of substrates influenced the line widths of the residues. Incubation with NADH had only a small effect on the line widths of the obtained peaks. In most cases the bands were narrower. However, line widths upon the addition of Q showed more significant changes, giving broader peaks in most cases. This could be explained by the existence of several conformers, where changes in the local environment can cause equilibrium between several states of the residues. One example is the absorbance of the label found to S414C that is located at the periplasmic side of complex I. Its line width after labelling comprised 16 cm^{-1}. The addition of NADH did not have a significant effect on its line width. However, treatment with quinone increased its line width up to 28 cm^{-1}. Such a significant change of almost doubling the line width can give a hint on this specific residue existing in several states simultaneously.

Deconvolution analysis of the absorbances revealed multiple peaks that could indicate that the residues move between several states, and the existence of several conformers is predicted. It was observed that multiple inhomogeneous peaks were obtained for the label bound to residues at the surface E108C, H159C, S105C, H117C on the cytoplasmic side and S414C, T332C, T422C on periplasmic side. Residues located in the central part of the subunit resulted in more homogenous peaks. The peak of the residue S425C was almost homogenous (92%). These data indicate that the residues located closer to the surface have a higher conformational degree of freedom than the ones located in the cavity.

In conclusion, the position of the SCN label varied among the variants, and deconvolution analysis revealed multiple peaks in most cases. Incubation with NADH and ubiquinone caused some shifts in the label's position or distribution. Some labels, such as those bound to K234C and T178C (located in the central part of the membrane arm), showed homogenous peaks in the deconvolution analysis. Overall, the studies provided valuable insights into the dynamics of individual positions of NuoM.

5.4 Conclusions on the proposed mechanisms

Significant conformational changes occurred at the labelled positions. The spectral shifts describe the conformational flexibility of the individual residues in different redox states of the protein. They are indicators of movements towards a more hydrophobic or hydrophilic environment. Proton translocation involves proton entrance from the cytoplasmic side and exit to the periplasmic side. SCN shifts can be used as an indicator of H-bond networks and shifts towards more or less solvent accessible environment. However, to conclude on the mechanism of proton translocation based on the spectral changes observed in this study is rather hard due to limited information.

The observed local changes in the environment of the NuoM residues in question describe conformational and H-bond network changes as well as different degrees of hydratisation. The most likely explanation of the experiments is that the movements occurring at the specific labelled positions are due to structural rearrangements of the protein upon substrate binding. It supports the importance of conformational changes for the mechanism of complex I. The observed changes are in line with a mechanism, where NuoM is involved in proton translocation. The data support the mechanism, according to which all subunits of the membrane arm are taking part in the proton translocation including the presence of a proton channel in NuoM. Conformational changes

occurring upon the reaction of complex I with Q may be the indication for the opening and closing of a proton channel, proton uptake from the cytoplasmic and ejection towards the periplasmic side. Movements of helices and environmental changes in the subunit NuoM are likely during the reaction.

According to the "ND5-only" mechanism all four protons translocated by the oxidation of one NADH exit the membrane arm through the distal complex I subunit NuoL. The other homologous antiporter-like subunits NuoM and NuoN do not have a hydratized proton pathway to the periplasm. The conformational changes in NuoM indirectly observed by IR absorbance of the label render this mechanism unlikely. According to this mechanism, only the central axis of the membrane arm passes the protons to the distal subunit NuoL. The membrane subunits of the complex contain many conserved titratable amino acids that participate in this process. According to this mechanism, NuoM is not involved in proton translocation. However, if this would be the case, no conformational changes would be observed in the periplasmic half-channel of NuoM as it would not take part in proton ejection. However, all residues building the putative channel are involved in conformational changes during Q reduction. If protons were translocated across the membrane only by the distal subunit as it is according to the "ND-5 only" theory, there would not be any movements of the residues located close to the periplasm. The observations reported here are not in the agreement with the "ND-5 only" mechanism. This study can be useful in deciphering the mechanism of proton translocation and can be extended to studying the different positions of complex I that are likely to take part in proton translocation and Q reduction.

5.5 *bd*-I oxidase

Cytochrome *bd*-I oxidases belong to the terminal oxidases of respiration, reducing dioxygen to water and oxidizing ubiquinol to ubiquinone, thus, contributing to proton motive force (pmf) by this vectorial process. *bd*-I has three hemes: b_{595}, b_{558} and heme *d*, arranged in a triangle, enabling electron transfer through the enzyme. Previous biochemical and spectroscopic studies revealed the importance of acidic amino acids ligands situated in the proximity of the hemes [161, 164, 167–169]. These glutamic acid residues are conserved, underlying their importance for enzyme stability and functionality. Therefore, position R448 is important for *bd*-I oxidase functions. E445 and R448 are located in the proximity of the heme b_{595} and according to the structure build a salt bridge.

Previous studies revealed that mutations generated at position E445 resulted either in a stable, but non-functional enzyme (E445A) or in a variant with diminished activity (E445C) [161, 164]. Here, two different mutations were generated at this specific position: E445D and E445Q. Variant E445D was fully assembled and could be isolated. The redox-difference spectrum of the preparation revealed the presence of all hemes. It was described in the literature that this mutation resulted in a diminished activity of the variant [161]. However, here, the variant E445Q showed a loss of activity and resulted in a preparation where signals for heme b_{595} were absent. These data could confirm the importance of titratable amino acid's presence at position E445. Glutamic and aspartic acids share a similar structure, and both belong to polar amino acids that are negatively charged. However, glutamine is a neutral amino acid, and its insertion at this position results in the enzyme's instability. Keeping the acid group proved its importance. This result emphasizes the importance of the salt bridge between E445 and R448. Furthermore, this arginine was mutated to asparagine. In the literature, a R448A mutation is described, which resulted in a diminished level of oxygen binding [164]. The reduced-oxidized UV/vis difference spectrum revealed the presence of all hemes in the preparation. Variants E445D and R448N were isolated and purified. Activities of the E445D and R448N variants in the membrane were measured and compared to those of the wild-type. Cytochrome *bd*-I E445D had 20±4%, and R448N 41±2% activity compared to the wild-type. The diminished activity can be explained by a slow intramolecular electron transfer rate *via* b_{595} [166].

Electrochemical investigations and redox-potential titration performed by I. Makarchuk, University Strasbourg, revealed a 200 mV shift of the redox potential of b_{595} caused by the mutations compared to the wild-type. In the E445D variant, the redox potential of the heme b_{595} is up-shifted by 100 mV and that of the heme *d* by 50 mV. In the R448N variant, the heme b_{595} shifted by 250 mV and that of heme *d* by 190 mV [166]. However, both mutations did not block electron transfer. Previous studies revealed that H-bonds have an effect on the hemes' redox potential [272, 273]. The significant differences obtained with the R448N variant led to the assumption that this variant significantly slows down electron transfer to heme *d*. The ability of both variants to reduce oxygen, although the redox potential shifts decelerates the reaction, shows that heme b_{595} is involved in intramolecular electron transfer but does not contribute to oxygen binding. For these variants, the NADH oxidase activities were high, although both mutations are located in the close vicinity of heme b_{595}.

Four other mutations were designed in the CydA near heme *d* at positions E99 and E107. These glutamic acid residues were described in the literature as essential for enzyme stability and activity [161, 168, 169]. Mutations E99D and E99Q were generated. However, it was only possible to isolate the variant E99D, as the variant E99Q did not properly assembled as indicated by the mutants' cell growth. Position E99 is an axial ligand to heme *d*. Thus, mutating this glutamate can cause instability of the enzyme as the glutamate has a polar uncharged side chain. Substitution of the glutamate with aspartic acid residue was successful, as both amino acids are polar charged residues with an acid group. The redox-difference spectrum of the E99Q preparation revealed the absence of heme *d*. In the literature, this mutation was described as lacking heme *d* and heme b_{595}, and this mutant appeared inactive [168]. The mutation E99D resulted in a fully assembled protein, with all hemes groups. The variant had 18 ± 1% of the activity of the wild-type. This direct ligand to the heme *d* is thus essential in electron transfer.

Two mutations at position E107 were designed: E107D and E107Q. Both mutations resulted in slower cell growth, and the protein could not be isolated from the mutants. Redox-difference spectra revealed the absence of heme b_{595} and heme *d*. In the literature, both mutations were characterized as inactive, but the E107Q variant was assembled, and its UV/vis spectrum directly obtained after preparation was similar to the one obtained from the wild-type. However, the content of heme *d* was about 50%, and the heme b_{595} and *d* appeared labile upon storage. The isolated E107D lacked heme b_{595} and *d* and did not have any oxidase activity [168]. The data obtained here are in agreement with the ones described in the literature. E107 is not a direct ligand to heme *d*, and not involved in electron transfer. The absence of two hemes proves its structural importance. E107 seems to have essential functions and might be relevant for oxygen reduction [163].

6 References

[1] Hans-Ulrich Gremlich, G. H. 2003. *Handbook of Spectroscopy*. Wiley-VCH GmBH and Co. KGaA, Weinheim.

[2] Wirth, C., Brandt, U., Hunte, C., Zickermann, V. 2016. Structure and function of mitochondrial complex I. *Biochim. Biophys. Acta* 1857, 901–914.

[3] Kolata, P., Efremov, R.G. 2021. Structure of *Escherichia coli* respiratory complex I reconstituted into lipid nanodiscs reveals an uncoupled conformation. *eLife* 10, e68710.

[4] Nissanka, N., Moraes, C. T. 2018. Mitochondrial DNA damage and reactive oxygen species in neurodegenerative disease. *FEBS Lett.* 592, 5, 728–742.

[5] Kampjut, D., Sazanov, L. A. 2020. The coupling mechanism of mammalian respiratory complex I. *Science* 370, eabc4209.

[6] Wikström, M., Hummer, G. 2012. Stoichiometry of proton translocation by respiratory complex I and its mechanistic implications. *Proc. Natl. Acad. Sci. U. S. A.* 109, 12, 4431–4436.

[7] Choi, J. H., Oh, K. I., Lee, H., Lee, C., Cho, M. 2008. Nitrile and thiocyanate IR probes: quantum chemistry calculation studies and multivariate least-square fitting analysis. *J. Chem. Phys.* 128, 13, 134506.

[8] Ataka, K., Stripp, S. T., Heberle, J. 2013. Surface-enhanced infrared absorption spectroscopy (SEIRAS) to probe monolayers of membrane proteins. *Biochim. Biophys. Acta* 1828, 2283–2293.

[9] Seiça, A. F. S., Schimpf, J., Friedrich, T., Hellwig, P. 2020. Visualizing the movement of the amphipathic helix in the respiratory complex I using a nitrile infrared probe and SEIRAS. *FEBS Lett.* 594, 491–496.

[10] Chance B., Williams, G. 1956. *Advances in Enzymology and Related Areas of Molecular Biology*. *The respiratory chain and oxidative phosphorylation*. Interscience Publishers, INC., New York.

[11] Sherpherd, M., Poole, R. K. 2013. *Bacterial respiratory chain*. *Encyclopedia of Biophysics*.

[12] Mitchell, P., Moyle, J. 1967. Chemiosmotic hypothesis of oxidative phosphorylation. *Nature* 213, 137–139.

[13] Boyer, P. D. 1975. A model for conformational coupling of membrane potential and proton translocation to ATP synthesis and to active transport. *FEBS Lett.* 58.

[14] Anraku, Y., Gennis, R. B. 1987. The aerobic respiratory chain of *Escherichia coli*. *TIBS*, 262–266.

[15] Sousa, P. M. F., Silva, S. T. N., Hood, B. L., Charro, N., Charita, J. N., Vaz, F., Penque, D., Condrads, T. P., Melo, A. M. P. 2011. Supramolecular organizations in the aerobic respiratory chain of *Escherichia coli*. *Biochimie* 93, 418–425.

[16] Borisov, V. B., Muralib, R., Verkhovskaya, M. L., Bloch, D. A., Han, H., Gennis, R. B., Verkhovsky, M. I. 2011. Aerobic respiratory chain of *Escherichia coli* is not allowed to work in fully uncoupled mode. *Proc. Natl. Acad. Sci. U.S.A.* 108, 42, 17320–17324.

[17] Borisov, V. B., Verkhovsky, M. I. 2015. Oxygen as Acceptor. *EcoSalPlus* 3, 2.

[18] Unden, G., Bongaerts, J. 1997. Alternative respiratory pathways of *Escherichia coli*: energetics and transcriptional regulation in response to electron acceptors. *Biochim. Biophys. Acta* 1320, 217–234.

[19] Krebs, H. A., Johnson, W. A. 1980. The role of citric acid in intermediate metabolism in animal tissues. *FEBS Lett.* 117, 148–156.

[20] Kravchuk, V., Petrova, O., Kampjut, D., Wojciechowska-Bason, A., Breese, Z., Sazanov, L. 2022. A universal coupling mechanism of respiratory complex I. *Nature* 609, 7928.

[21] Feng, Y., Li, W., Li, J., Wang, J., Ge, J., Xu, D., Liu, Y., Wu, K., Zeng, Q., Wu, J.-W., Tian, C., Zhou, B., Yang, M. 2012. Structural insight into the type-II mitochondrial NADH dehydrogenases. *Nature* 491, 478–482.

[22] Yankovskaya, V., Horsefield, R., Törnroth, S., Luna-Chavez, C., Miyoshi, H. 2003. Architecture of succinate dehydrogenase and reactive oxygen species generation. *Science* 209, 700–704.

[23] Li, J., Han, L., Vallese, F., Dinge, Z., Choi, S. K., Hong, S., Luo, Y., Liu, B., Chan, C.K., Tajkhorshid, E., Zhua, J., Clarke, O., Zhang, K., Gennis, R. B. 2021. Cryo-EM structures of *Escherichia coli* cytochrome bo_3 reveal bound phospholipids and ubiquinone-8 in a dynamic substrate binding site. *Proc. Natl. Acad. Sci. U. S. A.* 118, 34, e2106750118.

[24] Theßeling, A., Rasmussen, T., Burschel, S., Kägi, J., Müller, R., Böttcher, B., Friedrich, T. 2019. Homologous *bd* oxidases share the same architecture but differ in mechanism. *Nat. Commun.* 10, 5138.

[25] Grauel, A., Kägi, J., Rasmussen, T., Makarchuk, I., Oppermann, S., Moumbock, A. F. A., Wohlwend, D., Müller, R., Melin, F., Günther, S., Hellwig, P., Böttcher, B., Friedrich, T. 2021. Structure of *Escherichia coli* cytochrome *bd*-II type oxidase with bound aurachin D. *Nat. Commun.* 12, 6498.

[26] Sobti, M., Walshe, J. L., Wu, D., Ishmukhametov, R., Zeng, Y.-C., Robinson, C. V., Berry, R. M., Stewart, A. G. 2020. Cryo-EM structures provide insight into how *E. coli* F_1F_o ATP synthase accommodates symmetry mismatch. *Nat. Commun.* 11, 2615.

[27] Puustinen, A., Fine, l. M., Haltia, T., Gennis, R. B., Wikström M. 1991. Properties of the two terminal oxidases of *Escherichia coli*. *Biochemistry* 30, 3936–3942.

[28] Weiss, H., Friedrich, T., Hofhaus, G., Preis, D. 1991. The respiratory-chain NADH dehydrogenase (complex I) of mitochondria. *Eur. J. Biochem.* 197, 563–576.

[29] Friedrich, T. 1998. The NADH: Ubiquinone Oxidoreductase (Complex I) from *Escherichia coli*. *Biochim. Biophys. Acta* 1608, 134–146.

[30] Brandt, U. 2006. Energy Converting NADH: Quinone Oxidoreductase (Complex I). *Annu. Rev. Biochem.* 75, 69–92.

[31] Friedrich, T., Weiss, H. 1997. Modular Evolution of the Respiratory NADH:Ubiquinone Oxidoreductase and the Origin of its Modules. *J. theor. Biol.* 187, 529–540.

[32] Matsushita, K., Ohnishi, T., Kaback, H. R. 1987. NADH-ubiquinone oxidoreductases of the *Escherichia coli* aerobic respiratory chain. *Biochemistry* 26, 24, 7732–7737.

[33] Blaza, J., Bridges, H. R., Aragão, D., Dunn, E. A., Heikal, A., Cook, G. M., Nakatani, Y., Hirst, J. 2016. The mechanism of catalysis by type-II NADH:quinone oxidoreductases. *Sci. Rep.* 7, 40165.

[34] Heikal, A., Nakatani, Y., Dunn, E., Weimar, M. R., Day, C. L., Baker, E. N., Lott, J. S. 2014. Structure of the bacterial type II NADH dehydrogenase: a monotopic membrane protein with an essential role in energy generation. *Mol. Microbiol.* 91, 950–964.

[35] Yano, T., Li, L.-S., Weinstein, E., Teh, J.-S., Rubin, H. 2006. Steady-state Kinetics and Inhibitory Action of Antitubercular Phenothiazines on *Mycobacterium tuberculosis* Type-II NADH-Menaquinone Oxidoreductase (NDH-2). *J. Biol. Chem.* 281, 17, 11456–11463.

[36] Unden, G., Becker, S., Bongaerts, J., Holighaus, G., Schirawski, J., Six, S. 1995. O_2-Sensing and O_2-dependent gene regulation in facultatively anaerobic bacteria. *Arch. Microbiol.* 164, 81–90.

[37] Neijssel, O. M., de Mattos, M. J. T. The energetics of bacterial growth: a reassessment. *Mol. Microbiol.* 13, 179–182.

[38] Zambrano, M. M., Kolter, R. 1993. *Escherichia coli* mutants lacking NADH dehydrogenase I have a competitive disadvantage in stationary phase. *J. Bacteriol.* 175, 5642–5647.

[39] Melo, A. M. P., Bandeiras, T. M., Teixeira, M. N. 2004. New Insights into Type II NAD(P)H: quinone oxidoreductases. *Microbiol. Mol. Biol. Rev.* 68, 603–616.

[40] Madej, M. G., Nasiri, H. R., Hilgendorff, N. S., Schwalbe, H., Unden, G., Lancaster, C. R. 2006. Experimental Evidence for Proton Motive Force-Dependent Catalysis by the Diheme-Containing Succinate:Menaquinone Oxidoreductase from the GramPositive Bacterium *Bacillus licheniformis*. *Biochemistry* 45, 15049–15055.

[41] Cecchini, G., Schröder, I., Gunsalus, R. P., Maklashina, E. 2002. Succinate dehydrogenase and fumarate reductase from *Escherichia coli*. *Biochim. Biophys. Acta* 1553, 140-157.

[42] Park, S. J., Tseng, C. P., Gunsalus, R. P. 1995. Regulation of succinate dehydrogenase (sdhCDAB) operon expression in *Escherichia coli* in response to carbon supply and anaerobiosis: role of ArcA and Fnr. *Mol. Microbiol.* 15, 473–482.

[43] Poole, R. K., Cook, G. M. 2000. Redundancy of aerobic respiratory chains in bacteria? Routes, reasons and regulation. *Adv. Microb. Physiol.* 43, 165–224.

[44] Yang, K., Borisov, V. B., Konstantinov, A. A., Gennis, R. B. 2008. The fully oxidized form of the cytochrome *bd* quinol oxidase from *E. coli* does not participate in the catalytic cycle: direct evidence from rapid kinetics studies. *FEBS Lett.* 582, 25-26, 3705–3709.

[45] Yap, L. L., Lin, M. T., Ouyang, H., Samoilova, R. I., Dikanov, S. A., Gennis, R. B. 2010. The quinone-binding sites of the cytochrome bo_3 ubiquinol oxidase from *Escherichia coli*. *Biochim. Biophys. Acta* 1797, 1924–1932.

[46] Puustinen, A., Finel, M., Virkki, M., Wikström M. 1989. Cytochrome o (bo) is a proton pump in *Paracoccus denitrificans* and *Escherichia coli*. *FEBS Lett.* 249, 2, 163–167.

[47] Abramson, J., Riistama, S., Larsson, G., Jasaitis, A., Svensson-Ek, M. 2000. The structure of the ubiquinol oxidase from *Escherichia coli* and its ubiquinone binding site. *Nat. Struct. Mol. Biol.* 7, 910–917.

[48] van der Oost, J., de Boer, A. P., de Gier, J. W., Zumft, W. G., Stouthamer, A. H., van Spanning, R. .J. 1994. The heme-copper oxidase family consists of three distinct types of terminal oxidases and is related to nitric oxide reductase. *FEMS Microbiology Lett.* 121, 1, 1–9.

[49] Sousa, P. M. F., Videira, M. A. M., Bohn, A., Hood, B. L., Conrads, T. P., Goulao, L. F., Melo, A. M. P. 2012. The aerobic respiratory chain of *Escherichia coli*: from genes to supercomplexes. *Microbiology* 158, 2408–2418.

[50] Hill, S., Viollet. S., Smith, A. T., Anthony, C. 1990. Roles for enteric d-type cytochrome oxidase in N_2 fixation and microaerobiosis. *J. Bacteriol.* 172, 2071–2078.

[51] Alexeeva, S., Hellingwerf, K. J., Teixeira de Mattos, J.K. 2002. Quantitative Assessment of Oxygen Availability: Perceived Aerobiosis and Its Effect on Flux Distribution in the Respiratory Chain of *Escherichia coli*. *J. Bacteriol.* 184, 1402–1406.

[52] Brøndsted, L., Atlung, T. 1996. Effect of growth conditions on expression of the acid phosphatase (cyx-appA) operon and the appY gene, which encodes a transcriptional activator of *Escherichia coli*. *J. Bacteriol.* 178, 6, 1556–1564.

[53] Dassa, J., Fsihi, H., Marck, C., Dion, M., Kieffer-Bontemps, M., Boquet, P.L. 1991. A new oxygen-regulated operon in *Escherichia coli* comprises the genes for a putative third cytochrome oxidase and for pH 2.5 acid phosphatase (appA). *Mol. Gen. Genet.* 229, 341–352.

[54] Grund, T. N., Radloff, M., Di, W., Goojani, H. G., Witte, L. F., Jösting, W., Buschmann, S., Müller, H., Elamri, E., Welsch, S., Schwalbe, H., Michel, H., Bald, D., Safarian, S. 2021. Mechanistic and structural diversity between cytochrome *bd* isoforms of *Escherichia coli*. *Proc. Natl. Acad. Sci. U. S. A.* 118, 50, e2114013118.

[55] Forte, E., Siletsky, S. A., Borisov, V. B. 2021. In *Escherichia coli* Ammonia Inhibits Cytochrome bo_3 But Activates Cytochrome *bd*-I. *Antioxidants* 10, 13.

[56] Meunier, B., Madgwick, S. A., Reil, E., Oettmeier, W., Rich, P. R. 1995. New inhibitors of the quinol oxidation sites of bacterial cytochromes bo_3 and *bd*. *Biochemistry* 34, 1076-1083.

[57] Maklashina, E., Berthold, D. A., Cecchine, G. 1998. Anaerobic Expression of *Escherichia coli* Succinate Dehydrogenase: Functional Replacement of Fumarate Reductase in the Respiratory Chain during Anaerobic Growth. *J. Bacteriol.* 180, 22, 5989–5996.

[58] Kashyap, D. R., Kowalczyk, D. A., Shan, Y., Yang, C.-K., Gupta, D., Dziarski, R. 2020. Formate dehydrogenase, ubiquinone, and cytochrome *bd*-I are required for peptidoglycan recognition protein-induced oxidative stress and killing in *Escherichia coli*. *Sci. Rep.* 10, 1, 1993.

[59] Agip, A. N. A., Blaza, J. N., Fedor, J. G., Hirst, J. 2019. Mammalian Respiratory Complex I Through the Lens of Cryo-EM. *Annu. Rev. Biophys.* 48, 165–184.

[60] Letts, J. A., Sazanov, L. A. 2015. Gaining mass: the structure of respiratory complex I-from bacterial towards mitochondrial versions. *Curr. Opin. Struct. Biol.* 33, 135–145.

[61] Hirst, J. 2013. Mitochondrial Complex I. *Annu. Rev. Biochem.* 82, 551–575.

[62] Padavannil, A., Ayala-Hernandez, M. G., Castellanos-Silva, E. A., Letts, J. A. 2022. The Mysterious Multitude: Structural Perspective on the Accessory Subunits of Respiratory Complex I. *Front. Mol. Biosci.* 8.

[63] Hirst, J. 2011. Why does mitochondrial complex I have so many subunits? *Biochem. J.* 437, e1-e3.

[64] Stroud, D. A., Surgenor, E. E., Formosa, L. E., Reljic, B., Frazier, A. E., Dibley, M. G., Osellame, L. D., Stait, T., Beilharz, T. H., Thorburn, D. R., Salim, A., Ryan, M. T. 2006.

Accessory subunits are integral for assembly and function of human mitochondrial complex I. *Nature* 538, 123–126.

[65] Kirby, D. M., Crawford, M., Cleary, M. A., Dahl, H. H. 1999. Respiratory chain complex I deficiency: an underdiagnosed energy generation disorder. *Neurology* 52, 1255–1264.

[66] Lin, M. T., Beal, M. F. 2006. Mitochondrial dysfunction and oxidative stress in neurodegenerative diseases. *Nature* 443, 787–795.

[67] Rhein, V., Song, X., Wiesner, A., Ittner, L. M., Baysang, G. 2009. Amyloid-beta and tau synergistically impair the oxidative phosphorylation system in triple transgenic Alzheimer's disease mice. *Proc. Natl. Acad. Sci. U. S. A.* 106, 47, 20057–20062.

[68] Baertling, F., Sánchez-Caballero, L., van den Brand, M., Wintjes, L., Brink, M. 2017. NDUFAF4 variants are associated with Leigh syndrome and cause a specific mitochondrial complex I assembly defect. *Eur. J. Hum. Genet.* 25, 1273–1277.

[69] Schapira, A. 1998. Human complex I defects in neurodegenerative diseases. *Biochim. Biophys. Acta* 1364, 2, 261–270.

[70] Cooper, J. M., Mann, V. M., Krige, D., Schapira, A. H. V. 1992. Human mitochondrial complex I dysfunction. *Biochim. Biophys. Acta* 1101, 198–203.

[71] Zhang, X., Jones, D., Gonzalez-Lima, F. 2002. Mouse model of optic neuropathy caused by mitochondrial complex I dysfunction. *Neurosci. Lett.* 326, 97–100.

[72] Dawson, T. M., Dawson, V. L. 203. Molecular pathways of neurodegeneration in Parkinson's disease. *Science* 302 (203), 819–822.

[73] Kussmaul, L., Hirst, J. 2006. The mechanism of superoxide production by NADH:ubiquinone oxidoreductase (complex I) from bovine heart mitochondria. *Proc. Natl. Acad. Sci. U. S. A.* 103, 7607–7612.

[74] Guo, R., Zong, S., Wu, M., Gu, J., Yang, M. 2017. Architecture of Human Mitochondrial Respiratory Megacomplex $I_2III_2IV_2$. *Cell* 170, 1247–1257.

[75] Degli Esposti, M. 1998. Inhibitors of NADH-ubiquinone reductase: an overview. *Biochim. Biophys. Acta* 1364, 2, 222–235.

[76] Braun, M., Bungert, S., Friedrich, T. 1998. Characterization of the overproduced NADH dehydrogenase fragment of the NADH:ubiquinone oxidoreductase (complex I) from *Escherichia coli*. *Biochemistry* 37, 1861–1867.

[77] Weidner, U., Geier, S., Ptock, A., Friedrich, T., Leif, H., Weiss, H. 1993. The gene locus of the proton-translocating NADH: ubiquinone oxidoreductase in *Escherichia coli*. Organization of the 14 genes and relationship between the derived proteins and subunits of mitochondrial complex I. *J. Mol. Biol.* 233, 109–122.

[78] Leif, H., Weidner, U., Berger, A., Spehr, V., Braun, M., van Heek, P., Friedrich, T. 1993. *Escherichia coli* NADH dehydrogenase I, a minimal form of the mitochondrial complex. *Biochem. Soc. Trans.* 21, 998–1001.

[79] Friedrich, T., Böttcher, B. 2004. The gross structure of the respiratory complex I: a Lego System. *Biochim. Biophys. Acta* 1608, 1, 1–9.

[80] Sazanov L. A. 2007. Respiratory complex I: mechanistic and structural insights provided by the crystal structure of the hydrophilic domain. *Biochemistry* 46, 9, 2275–2288.

[81] Guénebaut, V., Schlitt, A., Weiss, H., Leonard, K., Friedrich, T. 1998. Consistent structure between bacterial and mitochondrial NADH: ubiquinone oxidoreductase (Complex I). *J. Mol. Biol.* 276, 105–112.

[82] Baranova, E. A., Morgan, D. J., Sazanov, L. A. 2007. Single particle analysis confirms distal location of subunits NuoL and NuoM in *Escherichia coli* complex I. *J. Struct. Biol.* 159, 2, 238–242.

[83] Baradaran, R., Berrisford, J. M., Minhas, G. S., Sazanov, L. A. 2013. Crystal structure of the entire respiratory complex I. *Nature* 494, 443–448.

[84] Ohnishi, T. 1998. Iron–sulfur clusters/semiquinones in Complex I. *Biochim. Biophys. Acta* 1364, 186–206.

[85] Gnandt, E., Dörner, K., Strampraad, M. F. J., de Vries, S., Friedrich, T. 2016. The multitude of iron-sulfur clusters in respiratory complex I. *Biochim. Biophys. Acta* 1857, 1068–1072.

[86] Dörner, K., Vranas, M., Schimpf, J., Straub, I. R., Hoeser, J. 2017. Significance of [2Fe-2S] Cluster N1a for Electron Transfer and Assembly of *Escherichia coli* Respiratory Complex I. *Biochemistry* 56, 2770–2778.

[87] Birrell, J. A., Morina, K., Bridges, H. R., Friedrich, T., Hirst, J. 2013. Investigating the function of [2Fe-2S] cluster N1a, the off-pathway cluster in complex I, by manipulating its reduction potential. *Biochem. J.* 456, 139–146.

[88] Schulte, M., Frick, K., Gnandt, E., Jurkovic, S., Burschel, S., Labatzke, R., Aierstock, K., Fiegen, D., Wohlwend, D., Gerhardt, S., Einsle, O., Friedrich, T. 2019. A mechanism to prevent production of reactive oxygen species by *Escherichia coli* respiratory complex I. *Nat. Commun.*

[89] Page, C. C., Moser, C. C., Chen, X., Dutton, P. L. 1999. Natural engineering principles of electron tunnelling in biological oxidation-reduction. *Nature* 402, 47–52.

[90] Pohl, T., Bauer, T., Dörner, K., Stolpe, S., Sell, P., Zocher, G., Friedrich, T. 2007. Iron-sulfur cluster N7 of the NADH:ubiquinone oxidoreductase (complex I) is essential for stability but not involved in electron transfer. *Biochemistry* 46, 6588–6596.

[91] de Vries, S., Dörner, K., Strampraad, M. J. F., Friedrich, T. 2015. Electron tunneling rates in respiratory complex I are tuned for efficient energy conversion. *Angew. Chem. Int. Ed.* 54, 2844–2848.

[92] Bridges, H. R., Bill, E., Hirst, J. 2012. Mössbauer spectroscopy on respiratory complex I: the iron-sulfur cluster ensemble in the NADH-reduced enzyme is partially oxidized. *Biochemistry* 51, 149–158.

[93] Gnandt, E., Schimpf, J., Harter, C., Hoeser, J., Friedrich, T. 2017. Reduction of the off-pathway iron-sulphur cluster N1a of *Escherichia coli* respiratory complex I restrains NAD^+ dissociation. *Sci. Rep.* 7, 1, 8754.

[94] Euro, L., Bloch, D. A., Wikström, M., Verkhovsky, M. I., Verkhovskaya, M. 2008. Electrostatic interactions between FeS clusters in NADH:ubiquinone oxidoreductase (Complex I) from *Escherichia coli*. *Biochemistry* 47, 3185–3193.

[95] Ohnishi, T., Nakamaru-Ogiso, E. 2008. Were there any "misassignments" among iron-sulfur clusters N4, N5 and N6b in NADH-quinone oxidoreductase (complex I)? *Biochim. Biophys. Acta* 1777, 703–710.

[96] Wikström, M., Sharma, V., Kaila, V. R. I., Hosler, J. P., Hummer, G. 2015. New perspectives on proton pumping in cellular respiration. *Chem. Rev.* 115, 2196–2221.
[97] Flemming, D., Stolpe, S., Schneider, D., Hellwig, P., Friedrich, T. 2005. A possible role for iron-sulfur cluster N2 in proton translocation by the NADH: ubiquinone oxidoreductase (complex I). *J. Mol. Microbiol. Biotechnol.* 10, 2-4, 208–222.
[98] Berrisford, J. M., Sazanov, L. A. 2009. Structural Basis for the Mechanism of Respiratory Complex I. *J. Biol. Chem.* 284, 29773–29783.
[99] Moser, C. C., Farid, T. A., Chobot, S. E., Dutton, P. L. 2006. Electron tunneling chains of mitochondria. *Biochim. Biophys. Acta* 1757, 1096.
[100] Verkhovskaya, M. L., Belevich, N., Euro, L., Wikström, M., Verkhovsky, M. I. 2008. Real-time electron transfer in respiratory complex I. *Proc. Natl. Acad. Sci. U. S. A.* 105, 3763–3767.
[101] Sharma, V., Belevich, G., Gamiz-Hernandez, A. P., Róg, T., Vattulainen, I., Verkhovskaya, M. L., Wikström M., Hummer, G., Kaila V. R. I. 2015. Redox-induced activation of the proton pump in the respiratory complex I. *Proc. Natl. Acad. Sci. U. S. A.* 112, 37, 11571–11576.
[102] Friedrich, T. 2014. On the mechanism of respiratory complex I. *J. Bioenerg. Biomembr.* 46, 255–268.
[103] Sinha, P. K., Torres-Bacete, J., Nakamaru-Ogiso, E., Castro-Guerrero, N., Matsuno-Yagi, A., Yagi, T. 2009. Critical roles of subunit NuoH (ND1) in the assembly of peripheral subunits with the membrane domain of *Escherichia coli* NDH-1. *J. Biol. Chem.* 284, 15, 9814–9823.
[104] Haapanen, O., Djurabekova, A., Sharma, V. 2019. Role of Second Quinone Binding Site in Proton Pumping by Respiratory Complex I. *Front. Chem.* 7, 221.
[105] Warnau, J., Sharma, V., Gamiz-Hernandez, A. P., Di Luca, A., Haapanen, O., Vattulainen, I., Wikström, M., Hummer, G., Kaila, V. R. I. 2018. Redox-coupled quinone dynamics in the respiratory complex I. *Proc. Natl. Acad. Sci. U. S. A.* 115, 36, E8413–E8420.
[106] Fedor, J. G., Jones, A. J. Y., Di Luca, A., Kaila, V. R. I., Hirst, J. 2017. Correlating kinetic and structural data on ubiquinone binding and reduction by respiratory complex I. *Proc. Natl. Acad. Sci. U. S. A.* 114, 48, 12737–12742.
[107] Grgic, L., Zwicker, K., Kashani-Poor, N., Kerscher, S., Brandt, U. 2004. Functional significance of conserved histidines and arginines in the 49-kDa subunit of mitochondrial complex I. *J. Biol. Chem.* 279, 20, 21193–21199.
[108] Berrisford, J. M., Baradaran, R., Sazanov, L. A. 2016. Structure of bacterial respiratory complex I. *Biochim. Biophys. Acta Bioenerg.* 1857, 7, 892–901.
[109] Tocilescu, M. A., Zickermann, V., Zwicker, K., Brandt, U. 2010. Quinone binding and reduction by respiratory complex I. *Biochim. Biophys. Acta* 1797, 1883–1890.
[110] Tocilescu, M. A., Fendel, U., Zwicker, K., Kerscher, S., Brandt, U. 2007. Exploring the ubiquinone binding cavity of respiratory complex I. *J. Biol. Chem.* 282, 40, 29514–29520.
[111] Gutiérrez-Fernández, J., Kaszuba, K., Minhas, G. S., Baradaran, R., Tambalo, M., Gallagher, D. T., Sazanov, L. A. 2020. Key role of quinone in the mechanism of respiratory complex I. *Nat. Commun.* 11, 1, 4135.

[112] Grba, D., Hirst, J. 2020. Mitochondrial complex I structure reveals ordered water molecules for catalysis and proton translocation. *Nat. Struct. Mol. Biol.* 27, 10.
[113] Kaila, V. R. I. 2018. Long-range proton-coupled electron transfer in biological energy conversion: towards mechanistic understanding of respiratory complex I. *J. R. Soc. Interface* 15, 20170916.
[114] Haapanen, O., Sharma, V. 2017. Role of water and protein dynamics in proton pumping by respiratory complex I. *Sci. Rep.* 7, 7747.
[115] Wikström, M., Djurabekova, A., Sharma, V. 2023. On the role of ubiquinone in the proton translocation mechanism of respiratory complex I. *FEBS Lett.* 597, 224–236.
[116] Wikström, M. 1984. Two protons are pumped from the mitochondrial matrix per electron transferred between NADH and ubiquinone. *FEBS Lett.* 169, 300–304.
[117] Kikuno, R., Miyata, T. 1985. Sequence homologies among mitochondrial DNA-coded URF 2, URF 4 and URF 5. *FEBS Lett.* 189, 85–88.
[118] Di Luca, A., Gamiz-Hernandez, A. P., Kaila, V. R. I. 2017. Symmetry-related proton transfer pathways in respiratory complex I. *Proc. Natl. Acad. Sci. U. S. A.*, E6314–E6321.
[119] Efremov, R. G., Sazanov, L. A. 2011. Structure of the membrane domain of respiratory complex I. *Nature* 476, 414–420.
[120] Parey, K., Lasham, J., Mills, D. J., Djurabekova, A., Haapanen, O., Yoga, E. G., Xie, H., Külbrandt, W., Sharma, V., Vonck, J., Zickermann, V. 2021. High-resolution structure and dynamics of mitochondrial complex I—Insights into the proton pumping mechanism. *Sci. Adv.* 7, 46, eabj3221.
[121] Euro, L., Belevich, G., Verkhovsky, M. I., Wikström, M., Verkhovskaya, M. 2008. Conserved lysine residues of the membrane subunit NuoM are involved in energy conversion by the proton-pumping NADH:ubiquinone oxidoreductase (Complex I). *Biochim. Biophys. Acta Bioenerg.* 1777, 9, 1166–1172.
[122] Hoeser, F., Tausend, H., Götz, S., Wohlwend, D., Einsle, O., Günther, S., Friedrich, T. 2022. Respiratory complex I with charge symmetry in the membrane arm pumps protons. *Biochemistry* 119, 27, e2123090119.
[123] Michel, J., DeLeon-Rangel, J., Zhu, S., Van Ree, K., Vik, S. B. 2. Mutagenesis of the L, M, and N Subunits of Complex I from *Escherichia coli* Indicates a Common Role in Function. *PloS one* 6 (2), e17420.
[124] Efremov, R. G., Baradaran, R., Sazanov, L. A. 2010. The architecture of respiratory complex I. *Nature* 465, 7297, 441–445.
[125] Zickermann, V., Kerscher, S., Zwicker, K., Tocilescu, M.A., Radermacher, M., Brandt, U. 2009. Architecture of complex I and its implications for electron transfer and proton pumping. *Biochim. Biophys. Acta* 1787, 6, 574–583.
[126] Peng, G., Fritzsch, G., Zickermann, V., Schägger, H., Mentele, R., Lottspeich, F., Bostina, M., Radermacher, M., Huber, R., Stetter, K.O., Michel, H. 2003. Isolation, characterization and electron microscopic single particle analysis of the NADH:ubiquinone oxidoreductase (complex I) from the Hyperthermophilic Eubacterium *Aquifex aeolicus*. *Biochemistry* 42, 3032–3039.

[127] Cabrera-Orefice, A., Yoga, E. T., Wirth, C., Siegmund, K., Zwicker, K., Guerrero-Castillo, S., Zickermann, V., Hunte, C., Brandt, U. 2018. Locking loop movement in the ubiquinone pocket of complex I disengages the proton pumps. *Nat. Commun.* 9, 4500.

[128] Bridges, H. R., Fedor, J. G., Blaza, J. N., Di Luca, A., Jussupow, A., Jarman, O. D., Wright, J. J., Agip, A. N. A., Gamiz-Hernandez, A. P., Roessler, M. M., Kaila, V. R. I., Hirst, J. 2020. Structure of inhibitor-bound mammalian complex I. *Nat. Commun.* 11, 5261.

[129] Verkhovskaya, M., Bloch, D. A. 2013. Energy-converting respiratory Complex I: on the way to the molecular mechanism of the proton pump. *Int. J. Biochem. Cell. Biol.* 45, 2, 491–511.

[130] Ohnishi, T. 2010. Structural biology: Piston drives a proton pump. *Nature* 465, 7297, 428–429.

[131] Efremov, R. G., Sazanov, L. A. 2011. Respiratory complex I: 'steam engine' of the cell? *Curr. Opin. Struct. Biol.* 21, 4, 532–540.

[132] Gonzalez-Halphen, D., Ghelli, A., Iommarini, L., Carelli, V., Esposti, M. D. 2011. Mitochondrial complex I and cell death: a semi-automatic shotgun model. *Cell Death Dis.* 2, 10, e222.

[133] Treberg, J. R., Brand, M. D. 2011. A Model of the Proton Translocation Mechanism of Complex I. *J. Biol. Chem.* 286, 20, 17579–17584.

[134] Ohnishi, T., Nakamaru-Ogiso, E., Ohnishi, S.T. 2010. A new hypothesis on the simultaneous direct and indirect proton pump mechanisms in NADH-quinone oxidoreductase (complex I). *FEBS Lett.* 584, 19, 4131–4137.

[135] Kaila, V. R. I. 2021. Resolving Chemical Dynamics in Biological Energy Conversion: Long-Range Proton-Coupled Electron Transfer in Respiratory Complex I. *Acc. Chem. Res.* 54, 4462–4473.

[136] Mühlbauer, M. E., Saura, P., Nuber, F., Di Luca, A., Friedrich, T., Kaila, V. R. I. 2020. Water-Gated Proton Transfer Dynamics in Respiratory Complex I. *J. Am. Chem. Soc.* 142, 32, 13718–13728.

[137] Kaila, V. R. I., Wikström, M., Hummer, G. 2014. Electrostatics, hydration, and proton transfer dynamics in the membrane domain of respiratory complex I. *Proc. Natl. Acad. Sci. U. S. A.* 111, 19, 6988–6993.

[138] Röpke M., Saura, P., Riepl, D., Pöverlein, M. C., Kaila, V. R. I. 2020. Functional Water Wires Catalyze Long-Range Proton Pumping in the Mammalian Respiratory Complex I. *J. Am. Chem. Soc.* 142, 21758–21766.

[139] Steimle, S., Bajzath, C., Dörner, K, Schulte, M., Bothe, V., Friedrich, T. 2011. Role of subunit NuoL for proton translocation by respiratory complex I. *Biochemistry* 50, 16, 3386–3393.

[140] Kampjut, D., Sazanov, L. A. 2022. Structure of respiratory complex I – An emerging blueprint for the mechanism. *Curr. Opin. Struct. Biol.* 74, 102350.

[141] D'mello, R., Hill, S., Poole, R. K. 1996. The cytochrome bd quinol oxidase in *Escherichia coli* has an extremely high oxygen affinity and two oxygen-binding haems: implications for regulation of activity in vivo by oxygen inhibition. *Microbiology* 142, 755–763.

[142] Dröse, S., Krack, S., Sokolova, L., Zwicker, K., Barth, H. D., Morgner, N., Heide, H., Stege, M., Nübel, E., Zickermann, V., Kerscher, S., Brutschy, B., Radermacher, M., Brandt, U.

2011. Functional Dissection of the Proton Pumping Modules of Mitochondrial Complex I. *PLoS Biol.* 9, 8, e1001128.

[143] Borisov, V. B., Gennis, R. B., Hemp, J., Verkhovsky, M. I. 2011. The cytochrome *bd* respiratory oxygen reductases. *Biochim. et Biophys. Acta* 1807, 11, 1398–1413.

[144] Friedrich, T., Wohlwend, D., Borisov, V. B. 2022. Recent Advances in Structural Studies of Cytochrome *bd* and Its Potential Application as a Drug Target. *Int. J. Mol. Sci.* 23, 6.

[145] Forte, E., Borisov, V. B., Vicente, J. B., Giuffrè, A. 2011. The cytochrome *bd* respiratory oxygen reductases. *Biochim. Biophys. Acta* 1807, 1398–1413.

[146] Borisov, V. B., Forte, E., Davletshin, A., Mastronicola, D., Sarti, P., Giuffrè, A. 2013. Cytochrome *bd* oxidase from *Escherichia coli* displays high catalase activity: an additional defense against oxidative stress. *FEBS Lett.* 587, 14, 2214–2218.

[147] Forte, E., Nastasi, M.R., Borisov, V.B. 2022. Preparations of Terminal Oxidase Cytochrome bd-II Isolated from Escherichia coli Reveal Significant Hydrogen Peroxide Scavenging Activity. *Biochemistry (Moscow)* 87, 8, 720–730.

[148] Belevich, I., Borisov, V. B., Zhang, J., Konstantinov, A. A., Gennis, R. B., Verkhovsky, M. I. 2005. Time-resolved electrometric and optical studies on cytochrome *bd* suggest a mechanism of electron-proton coupling in the di-heme active site. *Proc. Natl. Acad. Sci. U. S. A.* 102, 10, 3657–3662.

[149] Safarian, S., Rajendran, C., Müller, H., Preu, J., Langer, J. D., Ovchinnikov, S., Hirose, T., Kusumoto, T., Sakamoto, J., Michel, H. 2016. Structure of a *bd* Oxidase Indicates Similar Mechanisms for Membrane-Integrated Oxygen Reductases. *Science* 352, 583–586.

[150] Grund, T. N., Kabashima, Y., Kusumoto, T., Di, W., Welsch, S., Sakamoto, J., Michel, H., Safarian, S. 2022. The cryoEM structure of cytochrome *bd* from *C. glutamicum* provides novel insights into structural properties of actinobacterial terminal oxidases. *Front. Chem.* 10, 1085463.

[151] Safarian, S., Opel-Reading, H. K., Di, W., Mehdipour, A. R., Hards, K., Harold, L. K., Radloff, M., Stewart, I., Welsch, S., Hummer, G., Cook, G. M., Krause, K. L., Michel, H. 2021. The cryo-EM structure of the *bd* oxidase from *M. tuberculosis* reveals a unique structural framework and enables rational drug design to combat TB. *Nat. Commun.* 12, 1, 5236.

[152] Wang, W., Gao, Y., Tang, Y., Zhou, X., Lai, Y., Zhou, S., Zhang, Y., Yang, X., Liu, F., Guddat, L. W., Wang, Q., Rao, Z., Gong, H. 2021. Cryo-EM structure of mycobacterial cytochrome *bd* reveals two oxygen access channels. *Nat. Commun.* 12, 1, 4621.

[153] Hoeser, J., Hong, S., Gehmann, G., Gennis, R., Friedrich, T. 2014. Subunit CydX of *Escherichia coli* cytochrome bd ubiquinol oxidase is essential for assembly and stability of the di-heme active site. *FEBS Lett.* 588.

[154] Safarian, S., Hahn, A., Mills, D. J., Radloff, M., Eisinger, M. L., Nikolaev, A., Meier-Credo, J., Melin, F., Miyoshi, H., Gennis, R. B., Sakamoto J., Langer J. D., Hellwig, P., Kühlbrandt, W., Michel, H. 2019. Active site rearrangement and structural divergence in prokaryotic respiratory oxidases. *Science* 366, 6461, 100–104.

[155] Dueweke, T. J., Gennis, R. B. 1991. Proteolysis of the cytochrome *d* complex with trypsin and chymotrypsin localizes a quinol oxidase domain. *Biochemistry* 30, 14, 3401–3406.

[156] Miyoshi, H., Takegami, K., Sakamoto, K., Mogi, T., Iwamura, H. 1999. Characterization of the ubiquinol oxidation sites in cytochromes *bo* and *bd* from *Escherichia coli* using aurachin C analogues. *J. Biochem.* 125, 1, 138–142.

[157] Hata-Tanaka, A., Matsuura, K., Itoh, S., Anraku, Y. 1987. Electron flow and heme-heme interaction between cytochromes *b*-558, *b*-595 and *d* in a terminal oxidase of *Escherichia coli*. *Biochim. Biophys. Acta Bioenerg.* 893, 2, 289–295.

[158] Jünemann, S., Wrigglesworth, J. M. 1994. Antimycin inhibition of the cytochrome *bd* complex from *Azotobacter vinelandii* indicates the presence of a branched electron transfer pathway for the oxidation of ubiquinol. *FEBS Lett.* 345, 2, 198–202.

[159] Kobayashi, K., Tagawa, S., Mogi, T. 1999. Electron Transfer Process in Cytochrome *bd*-Type Ubiquinol Oxidase from *Escherichia coli* Revealed by Pulse Radiolysis. *Biochemistry* 38, 18, 5913–5917.

[160] Borisov, V. B., Liebl, U., Rappaport, F., Martin, J.-L., Zhang, J., Gennis, R. B. 2002. Interactions between Heme *d* and Heme b_{595} in Quinol Oxidase bd from *Escherichia coli*: A Photoselection Study Using Femtosecond Spectroscopy. *Biochemistry* 41, 1654–1662.

[161] Murali, R., Gennis, R. B. 2018. Functional importance of Glutamate-445 and Glutamate-99 in proton-coupled electron transfer during oxygen reduction by cytochrome *bd* from *Escherichia coli*. *Biochim. Biophys. Acta* 1859, 8, 577–590.

[162] Fang, H. F., Lin, R.-J., Gennis, R. B. 1989. Location of heme axial ligands in the cytochrome *d* terminal oxidase complex of *Escherichia coli* determined by site-directed mutagenesis. *J. Biol. Chem.* 264, 8026–8032.

[163] Cao, Y.-C., Liao, R.-Z. 2023. QM Calculations Revealed that Outer-Sphere Electron Transfer Boosted O-O Bond Cleavage in the Multiheme-Dependent Cytochrome *bd* Oxygen Reductase. *Inorg. Chem.* 62, 10, 4066–4075.

[164] Zhang, J., Hellwig, P., Osborne, H.-W. Huang, J. P., Moënne-Loccoz, P., Konstantinov, A. A., Gennis, R. B. 2001. Site-Directed Mutation of the Highly Conserved Region near the Q-Loop of the Cytochrome *bd* Quinol Oxidase from Escherichia coli Specifically Perturbs Heme b_{595}. *Biochemistry* 40, 29, 8548–8556.

[165] Rappaport, F., Zhang, J., Vos, M. H., Gennis, R. B., Borisov, V. B. 2010. Heme-heme and heme-ligand interactions in the di-heme oxygen-reducing site of cytochrome *bd* from *Escherichia coli* revealed by nanosecond absorption spectroscopy. *Biochim. Biophys. Acta* 1797, 9, 1657–1664.

[166] Makarchuk, I., Gerasimova, T., Kägi, J., Wohlwend, D., Melin, F., Friedrich, T., Hellwig, P. 2023. Mutating the environment of heme b_{595} of *E. coli* cytochrome *bd*-I oxidase shifts its redox potential by 200 mV without inactivating the enzyme. *Bioelectrochemistry* 151, 108379.

[167] Mogi, T. 2009. Probing the haem *d*-binding site in cytochrome *bd* quinol oxidase by site-directed mutagenesis. *J. Biochem.* 145, 763–770.

[168] Yang, K., Zhang, J., Vakkasoglu, A. K., Hielscher, R., Osborne, J. P., Hemp, J., Miyoshi, H., Hellwig, P., Gennis, R. B. 2007. Glutamate 107 in Subunit I of the Cytochrome *bd* Quinol Oxidase from *Escherichia coli* Is Protonated and near the Heme *d*/Heme b_{595} Binuclear Center. *Biochemistry* 46, 11, 3270–3278.

[169] Mogi, T., Endou, S., Akimoto, S., Morimoto-Tadokoro, M., Miyoshi, H. 2006. Glutamates 99 and 107 in transmembrane helix III of subunit I of cytochrome *bd* are critical for binding of the heme b_{595}-*d* binuclear center and enzyme activity. *Biochemistry* 45, 51, 15785–15792.
[170] Lide, D. R. 1995. *CRC Handbook of Chemistry and Physics: A Ready-reference Book of Chemical and Physical Data*.
[171] Cyberphysics. *https://www.cyberphysics.co.uk/topics/light/emspect.htm*.
[172] Morais, C. L. M., Lima, K. M. G., Singh, M., Martin, F. L. 2020. Tutorial: multivariate classification for vibrational spectroscopy in biological samples 15, 2143–2162.
[173] Penner, M. H. 2017. *Food Analysis*. *Basic Principles of Spectroscopy*. Springer, Nielsen, S.S.
[174] Atkins, P., Paula, J. D. 2006. *Physical chemistry*. Oxford University Press.
[175] Perkampus, H.-H. 1992. *UV-VIS Spectroscopy and Its Applications*. Springer.
[176] Kalsi, P. K. 2005. *Spectroscopy of organic compounds*. New Age International Publishers, New Delhi.
[177] Prasad, S., Mandal, I., Singh, S., Paul, A., Mandal, B., Venkatramani, R., Swaminathan, R. 2017. Near UV-Visible electronic absorption originating from charged amino acids in a monomeric protein. *Chem. Sci.* 8, 5416–5433.
[178] Nienhaus, K., Nienhaus, G. U. 2005. Probing heme protein-ligand interactions by UV/visible absorption spectroscopy. *Methods Mol. Biol.* 305, 215–242.
[179] Williams M. A. 2013. Protein-ligand interactions: fundamentals. *Methods Mol. Biol.* 1008, 3–34.
[180] Everse, J. 2013. *Encyclopedia of Biological Chemistry*. *Heme Proteins*. Academic Press.
[181] Melin, F., Hellwig, P. 2020. Redox Properties of the Membrane Proteins from the Respiratory Chain. *Chem. Rev.* 120, 10244–10297.
[182] Chalmers, J. M., Griffiths, P. R. 2002. *Handbook of Vibrational Spectroscopy*. J. WIey, New York.
[183] Guenzler, H., Gremlich, H. U. 2002. *IR Spectroscopy An introduction*. Wiley-VCH, Weinheim (Germany).
[184] Dutta, A. 2017. *Spectroscopic Methods for Nanomaterials Characterization*. *Chapter 4 - Fourier Transform Infrared Spectroscopy*. Elsevier.
[185] Yoshikawa, M. 2023. *Advanced Optical Spectroscopy Techniques for Semiconductors*. Springer, Cham.
[186] Jesús, O., Dittrich, M. 2012. Fourier Transform Infrared Spectroscopy for Molecular Analysis of Microbial Cells. *Methods in molecular biology (Clifton, N.J.)* 881, 187–211.
[187] Analytical Procedures and General Directions. 2017. Infrared Spectroscopy. *ACS Reagent Chemicals*.
[188] Cameron, J. M., Bruno, C., Parachalil, D. R., Baker, M. J., Bonnier, F., Butler, H. J., Byrne, H. J. 2020. *Vibrational Spectroscopy in Protein Research*. *Vibrational spectroscopic analysis and quantification of proteins in human blood plasma and serum*. Academic Press.
[189] Kötting, C., Güldenhaupt, J., Gerwert, K. 2012. Time-Resolved FTIR Spectroscopy for Monitoring Protein Dynamics Exemplified by Functional Studies of Ras Protein Bound to a Lipid Bilayer. *Chem. Phys.* 13, 2649–2653.

[190] Stuart, B. H. 2021. Infrared Spectroscopy of Biological Applications: An Overview. *Biomolecules Analysis*.
[191] Siebert, F. 1995. Infrared spectroscopy applied to biochemical and biological problems. *Methods Enzymol.* 246, 501–526.
[192] Barth, A. 2007. Infrared spectroscopy of proteins. *Biochim. Biophys. Acta* 1767, 1073–1101.
[193] Singh, B. R. 2000. *Infrared Analysis of Peptides and Proteins*. *Principles and Applications*. American Chemical Society.
[194] Barth, A. 2000. The infrared absorption of amino acid side chains. *Prog. Biophys. Mol. Biol.* 74, 3, 141–173.
[195] Krimm, S., Bandekar, J. 1986. Vibrational spectroscopy and conformation of peptides, polypeptides, and proteins. *Adv. Protein. Chem.* 38, 181–364.
[196] Surewicz, W. K., Mantsch, H. H., Chapman, D. 1993. Determination of protein secondary structure by Fourier transform infrared spectroscopy: a critical assessment. *Biochemistry* 32, 2, 389–394.
[197] Ghimire, H., Venkataramani, M., Bian, Z., Liu, Y., Perera, A. 2017. ATR-FTIR spectral discrimination between normal and tumorous mouse models of lymphoma and melanoma from serum samples. *Sci. Rep.* 7, 1, 16993.
[198] Goormaghtigh, E., Cabiaux, V., Ruysschaert, J. M. 1994. Determination of soluble and membrane protein structure by Fourier transform infrared spectroscopy. III. Secondary structures. *Sub-Cell. Biochem.* 23, 405–450.
[199] Barth, A., Zscherp, C. 2002. What vibrations tell us about proteins. *Q. Rev. Biophys.* 35, 4, 369–430.
[200] Heimburg, T., Schünemann, J., Weber, K., Geisler, N. 1999. FTIR-Spectroscopy of multistranded coiled coil proteins. *Biochemistry* 38, 39, 12727–12734.
[201] Chellgren, B. W.,Trevor, P. C. 2004. Effects of H_2O and D_2O on Polyproline II Helical Structure. *J. Am. Chem. Soc.* 126, 45, 14734–14735.
[202] Griffiths, P., de Haseth, J. 2007. *Fourier Transform Infrared Spectrometry*. Wiley-Interscience.
[203] Tkachenko, N. V., Ed. 2006. *Optical Spectroscopy*. Elsevier Science, Amsterdam.
[204] Amigo, J. M., Grassi, S., Ed. 2019. *Hyperspectral Imaging*. Data Handling in Science and Technology. Elsevier.
[205] Jaggi, N., Vij, D.R. 2007. *Handbook of Applied Solid State Spectroscopy. Fourier Transform Infrared Spectroscopy*. Spring.
[206] Bacsik, Z., Mink, J. Keresztury, G. 2004. FTIR Spectroscopy of the Atmosphere. I. Principles and Methods. *Applied Spectroscopy Reviews* 39, 295–363.
[207] Patrizi, B., de Cumis, S. 2019. Dioxin and Related Compound Detection: Perspectives for Optical Monitoring. *Int. J. Mol. Sci.* 20, 11, 2671.
[208] Misra, N. N., Sullivan, C., Cullen, C. J. 2015. Process Analytical Technology (PAT) and Multivariate Methods for Downstream Processes. *Curr. Biochem. Eng.* 2, 2, 13.
[209] Tiernan, H., Byrne, B., Kazarian, S. G. 2020. ATR-FTIR spectroscopy and spectroscopic imaging for the analysis of biopharmaceuticals. *Spectrochim. Acta. A Mol. Biomol. Spectrosc.* 241, 118636.

[210] Heberle, J., Ataka, K. 2013. Surface Enhanced Infrared Absorption Spectroscopy. In *Encyclopedia of Biophysics*, G. C. K. Roberts, Ed. Springer Berlin Heidelberg, Berlin, Heidelberg, 2528–2531.

[211] Osawa, M., Ataka, K. 1992. Electromagnetic Mechanism of Enhanced Infrared-Absorption of Molecules Adsorbed on Metal Island Films. *Surf. Sci.* 262, 118−122.

[212] Osawa, M. 1997. Dynamic Processes in Electrochemical Reactions Studied by Surface-Enhanced Infrared Absorption Spectroscopy (SEIRAS). *Bullet. Chem. Soc. Jpn.* 70, 12, 2861–2880.

[213] Osawa, M. 2001. *Surface-Enhanced Infrared Absorption. In NearField Optics and Surface Plasmon Polaritons*. Springer, Berlin, Heidelberg.

[214] Lorenz-Fonfria, V. A. 2020. Infrared Difference Spectroscopy of Proteins: From Bands to Bonds. *Chem. Rev.* 120, 3466–3576.

[215] Merklin, G. T., Griffiths, P. R. 1997. Effect of Microscopic Surface Roughness in Surface-Enhanced Infrared Absorption Spectrometry. *J. Phys. Chem. B* 101, 30, 5810–5813.

[216] Seiça, A. F. S., Iqbal, M. H., Carvalho, A., Choe, J. Y., Boulmedais, F., Hellwig, P. 2021. Study of Membrane Protein Monolayers Using Surface-Enhanced Infrared Absorption Spectroscopy (SEIRAS): Critical Dependence of Nanostructured Gold Surface Morphology. *ACS Sens.* 6, 8, 2875–2882.

[217] Ataka, K., Heberle, J. 2007. Biochemical applications of surface-enhanced infrared absorption spectroscopy. *Anal. Bioanal. Chem.* 388, 1, 47–54.

[218] Ataka, K., Richter, B., Heberle, J. 2006. Orientational control of the physiological reaction of cytochrome *c* oxidase tethered to a gold electrode. *J. Phys. Chem. B.* 110, 18, 9339–9347.

[219] Kriegel, S., Uchida, T., Osawa, M., Friedrich, T., Hellwig, P. 2014. Biomimetic Environment to Study *E. coli* Complex I through Surface-Enhanced IR Absorption Spectroscopy. *Biochemistry* 53, 40, 6340–6347.

[220] Pinkerneil, P., Güldenhaupt, J., Gerwert, K., Kötting, C. 2012. Surface-attached polyhistidine-tag proteins characterized by FTIR difference spectroscopy. *Chemphyschem.* 13, 11, 2649–2653.

[221] Bornhorst, J. A., Falke, J. J. 2000. Purification of proteins using polyhistidine affinity tags. *Methods Enzymol.* 326, 245–254.

[222] Toseland, C. P. 2013. Fluorescent labeling and modification of proteins. *J. Chem. Biol.* 6, 3, 85–95.

[223] Getahun, Z., Huang, C. Y., Wang, T., De León, B., DeGrado, W. F., Gai, F. 2003. Using nitrile-derivatized amino acids as infrared probes of local environment. *J. Am. Chem. Soc.* 125, 2, 405–411.

[224] Levin, D. E., Schmitz, A. J., Hines, S. M., Hines, K. J., Tucker, M. J., Brewer, S. H., Fenlon, E. E. 2016. Synthesis and Evaluation of the Sensitivity and Vibrational Lifetimes of Thiocyanate and Selenocyanate Infrared Reporters. *RSC Adv.* 43, 6, 36231–36237.

[225] Kwang-Im, O., Jun-Ho, C., Joo-Hyun, L., Jae-Beom, H. 128. Nitrile and thiocyanate IR probes: molecular dynamics simulation studies. *J. Chem. Phys.* 2008 (128), 154504.

[226] Maienschein-Cline, M. G., Londergan, C. H. 2007. The CN stretching band of aliphatic thiocyanate is sensitive to solvent dynamics and specific solvation. *J. Phys. Chem. A* 111, 40.

[227] Reimers, J. R., Hall, L. E. 1999. The Solvation of Acetonitrile. *J. Am. Chem. Soc.* 121, 15, 3730–3744.
[228] Mukherjee, S., Chowdhury, P., DeGrado, W. F., Gai,F. 2007. Site-Specific Hydration Status of an Amphipathic Peptide in AOT Reverse Micelles. *Langmuir* 23, 11174–11179.
[229] Waegele, M. M., Tucker, M. J., Gai, F. 2009. 5-Cyanotryptophan as an infrared probe of local hydration status of proteins. *Chem. Phys. Lett.* 478, 4-6, 249–253.
[230] Suydam, I. T., Boxer, S. G. 2003. Vibrational Stark Effects Calibrate the Sensitivity of Vibrational Probes for Electric Fields in Proteins. *Biochemistry* 42, 12050–12055.
[231] Boxer, S. G. 2009. Stark Realities. *J. Phys. Chem.* 113, 10, 2972–2983.
[232] Schultz, K. C., Supekova, L., Ryu, Y. H., Xie, J. M., Perera, R. 2006. A Genetically Encoded Infrared Probe. *J. Am. Chem. Soc.* 128, 13984.
[233] Tucker, M. J., Getahun, Z., Nanda, V., DeGrado, W. F., Gai,F. 2004. A New Method for Determining the Local Environment and Orientation of Individual Side Chains of Membrane-Binding Peptides. *J. Am. Chem. Soc.* 126, 16, 5078–5079.
[234] Alfieri, K. N., Vienneau, A. R., Londergan, C. H. 2011. Using infrared spectroscopy of cyanylated cysteine to map the membrane binding structure and orientation of the hybrid antimicrobial peptide CM15. *Biochemistry* 50, 51, 11097–11108.
[235] Bischak, C. G., Longhi, S., Snead, D. M., Costanzo, S., Terrer, E., Londergan, C. H. 2010. Probing Structural Transitions in the Intrinsically Disordered C-Terminal Domain of the Measles Virus Nucleoprotein by Vibrational Spectroscopy of Cyanylated Cysteines. *Biophys J.* 99, 5, 1676–1683.
[236] Watson, M. D., Gai, X. S., Gillies, A. T., Brewer, S. H., Fenlon, E. E. 2008. A Vibrational Probe for Local Nucleic Acid Environments: 5-Cyano-2 '-deoxyuridine. *J. Phys. Chem. B* 112, 42, 13188–13191.
[237] Zhang, D., Decatur, S. M. 2007. Cyanophenylalanine as a vibrational probe for the aggregation of ABeta16-22 peptides. *Biophys. J.* 9650, 559A-559A.
[238] Zou, H., Liu, J., Blasie, J. K. 2009. Mechanism of interaction between the general anesthetic halothane and a model ion channel protein, III: Molecular dynamics simulation incorporating a cyanophenylalanine spectroscopic probe. *Biophys. J.* 96, 10, 4188–4199.
[239] Fang, C., Bauman, J. D., Das, K., Remorino, A., Arnold, E., Hochstrasser, R. M. 2008. Two-dimensional infrared spectra reveal relaxation of the nonnucleoside inhibitor TMC278 complexed with HIV-1 reverse transcriptase. *Proc. Natl. Acad. Sci. U. S. A.* 105, 5, 1472–1477.
[240] Krummel, A. T., Zanni, M. T. 2008. Evidence for Coupling between Nitrile Groups Using DNA Templates: A Promising New Method for Monitoring Structures with Infrared Spectroscopy. *J. Phys. Chem. B* 112, 5, 1336–1338.
[241] Fafarman, A. T., Webb, L. J., Chuang, J. I., Boxer, S. G. 2006. Site-Specific Conversion of Cysteine Thiols into Thiocyanate Creates an IR Probe for Electric Fields in Proteins. *J. Am. Chem. Soc.* 128, 41, 13356–13357.
[242] Degani, Y., Neumann, H., Patchornik, A. 1970. Selective cyanylation of sulfhydryl groups. *J. Am. Chem. Soc.* 92, 23, 6969–6971.
[243] Vanaman, T. C., Stark, G. R. 1970. A Study of the Sulfhydryl Groups of the Catalytic Subunit of *Escherichia coli* Aspartate Transcarbamylase: The use of enzyme--5-thio-2-nitrobenzoate

mixed disulfides as intermediates in modifying enzyme sulfhydryl groups. *J. Biol. Chem.* 245, 14, 3565–3573.

[244] Ellman, G. L. 1959. Tissue sulfhydryl groups. *Arch. Biochem. Biophys.* 82, 1, 70–77.

[245] Doherty, G. M., Motherway, R., Mayhew, S. G., Malthouse, J. P. 1992. ^{13}C NMR of cyanylated flavodoxin from *Megasphaera elsdenii* and of thiocyanate model compounds. *Biochemistry* 31, 34, 7922–7930.

[246] Kim, J.-Y., Park, J., Lim, M. 2010. Picosecond Dynamics of CN--Ligated Ferric Cytochrome c after Photoexcitation Using Time-Resolved Vibrational Spectroscopy. *Bull. Kor. Chem. Soc.* 31, 12, 3771–3776.

[247] McMahon, H. A., Alfieri, K. N., Clark, K. A. A., Londergan, C. H. 2010. Cyanylated Cysteine: A Covalently Attached Vibrational Probe of Protein−Lipid Contacts. *J. Phys. Chem. Lett.* 1, 5, 850–855.

[248] Londergan, C.H., Baskin, R., Bischak, C.G., Hoffman, K.W., Snead, D.M., Reynoso, C. 2015. Dynamic asymmetry and the role of the conserved active-site thiol in rabbit muscle creatine kinase. *Biochemistry* 54, 1, 83–95.

[249] Pohl, T., Uhlmann, M., Kaufenstein, M., Friedrich, T. 2007. Lambda Red-Mediated Mutagenesis and Efficient Large Scale Affinity Purification of the *Escherichia coli* NADH:Ubiquinone Oxidoreductase (Complex I). *Biochemistry* 46, 37, 10694–10702.

[250] Vranas, M. 2013. *Heterologous production, purification and characterization of respiratory proteins from Aquifex aeolicus in Escherichia coli strains,* Albert-Ludwigs-Universität Freiburg.

[251] Schägger, H., von Jagow, G. 1987. Tricine-sodium dodecyl sulfate-polyacrylamide gel electrophoresis for the separation of proteins in the range from 1 to 100 kDa. *Anal. Biochem.* 166, 2, 368–379.

[252] Gill, S. C., von Hippel, P. H. 1989. Calculation of protein extinction coefficients from amino acid sequence data. *Anal. Biochem.* 182, 2, 319–326.

[253] Friedrich, T., Hofhaus, G., Ise, W., Nehls, U., Schmitz, B., Weiss, H. 1989. A small isoform of NADH:ubiquinone oxidoreductase (complex I) without mitochondrially encoded subunits is made in chloramphenicol-treated *Neurospora crassa*. *Eur. J. Biochem.* 180, 1, 173–180.

[254] Weiss, R. F. 1970. The solubility of nitrogen, oxygen and argon in water and seawater. *Deep Sea Res. Oceanogr. Abstr.* 17, 4, 721–735.

[255] Friedrich, T., van Heek, P., Leif, H., Ohnishi, T., Forsche, E., Kunze, B., Jansen, R., Trowitzsch-Kienast, W., Höfle, G., Reichenmach, H., Weiss, H. 1994. Two binding sites of inhibitors in NADH:ubiquinone oxidoreductase (complex I). *Eur. J. Biochem.* 219, 691-698.

[256] Huang, C.-S., Kopacz, S. J., Lee, C.-P. 1983. Mechanistic differences in the energy-linked fluorescence decreases of 9-aminoacridine dyes associated with bovine heart submitochondrial membranes. *Biochim. Biophys. Acta Bioenerg.* 722, 1, 107–115.

[257] Sonn-Segev, A., Belacic, K., Bodrug, T., Young, G., VanderLinden, R. T., Schulman, B. A., Schimpf, J., Friedrich, T., Dip, P. V., Schwartz, T. U., Bauer, B., Peters, J.-M., Struwe, W.B., Benesch, J. L. P., Brown, N. G., Haselbach, D., Kukura, P. 2020. Quantifying the heterogeneity of macromolecular machines by mass photometry. *Nat. Commun.* 11, 1, 1772.

[258] Ataka, K., Heberle, J. 2006. Use of surface enhanced infrared absorption spectroscopy (SEIRA) to probe the functionality of a protein monolayer. *Biopolymers* 82, 4, 415–419.

[259] Vercellino, I., Sazanov, L. A. 2022. The assembly, regulation and function of the mitochondrial respiratory chain. *Nat. Rev. Mol. Cell Biol.* 23, 2, 141–161.

[260] Nuber, F., Schimpf, J., Di Rago, J.-P., Tribouillard-Tanvier, D., Procaccio, V., Martin-Negrier, M.-L., Trimouille, A., Biner, O., von Ballmoos, C., Friedrich, T. 2021. Biochemical consequences of two clinically relevant ND-gene mutations in *Escherichia coli* respiratory complex I. *Sci. Rep.* 11, 1, 12641.

[261] Birrell, J. A., Yakovlev, G., Hirst, J. 2009. Reactions of the flavin mononucleotide in complex I: a combined mechanism describes NADH oxidation coupled to the reduction of $APAD^+$, ferricyanide, or molecular oxygen. *Biochemistry* 48, 50, 12005–12013.

[262] Bungert, S., Krafft, B., Schlesinger, R., Friedrich, T. 1999. One-step purification of the NADH dehydrogenase fragment of the *Escherichia coli* complex I by means of Strep-tag affinity chromatography. *FEBS Lett.* 460, 2, 207–211.

[263] Ataka, K., Giess, F., Knoll, W., Naumann, R., Haber-Pohlmeier, S., Richter, B., Heberle, J. 2004. Oriented Attachment and Membrane Reconstitution of His-Tagged Cytochrome *c* Oxidase to a Gold Electrode: *In Situ* Monitoring by Surface-Enhanced Infrared Absorption Spectroscopy. *J. Am. Chem. Soc.* 126, 16199–16206.

[264] Steimle, S., Schnick, C., Burger, E. M., Nuber, F., Krämer, D., Dawitz, H., Brander, S., Matlosz, B., Schäfer, J., Maurer, K., Glessner, U., Friedrich, T. 2015. Cysteine scanning reveals minor local rearrangements of the horizontal helix of respiratory complex I. *Mol. Microbiol.* 98, 1, 151–161.

[265] Seiça, A. F. S. 2019. *Infrared spectroscopic study of the conformational movements in membrane proteins from respiratory chain by introducing a CN label in critical positions,* University Strasbourg.

[266] Torres-Bacete, J., Nakamaru-Ogiso, E., Matsuno-Yagi, A., Yagi, T. 2007. Characterization of the NuoM (ND4) subunit in *Escherichia coli* NDH-1: conserved charged residues essential for energy-coupled activities. *J. Biol. Chem.* 282, 51, 36914–36922.

[267] Leroi, G. E., Klemperer, W. 1961. Infrared Spectra of Sodium and Potassium Cyanide. *J. Chem. Phys.* 35, 774.

[268] Blankenburg, L., Schroeder, L., Habenstein, F., Błasiak, B., Kottke, T., Bredenbeck, J. 2019. Following local light-induced structure changes and dynamics of the photoreceptor PYP with the thiocyanate IR label. *Phys. Chem. Chem. Phys.* 21, 12, 6622–6634.

[269] Fafarman, A. T., Boxer, S. G. 2010. Nitrile Bonds as Infrared Probes of Electrostatics in Ribonuclease S. *J. Phys. Chem. B* 114, 42, 13536–13544.

[270] Dalton, S. R., Vienneau, A. R., Burstein, S. R., Xu, R. J., Linse, S., Londergan, C. H. 2018. Cyanylated Cysteine Reports Site-Specific Changes at Protein–Protein-Binding Interfaces Without Perturbation. *Biochemistry* 57, 26, 3702–3712.

[271] Edelstein, L., Stetz, M. A., McMahon, H. A., Londergan, C. H. 2010. The effects of alpha-helical structure and cyanylated cysteine on each other. *J. Phys. Chem. B.* 114, 14, 4931–4936.

[272] Valentine, J. S., Sheridan, R. P., Allen, L. C., Kahn, P. C. 1979. Coupling between oxidation state and hydrogen bond conformation in heme proteins. *Proc. Natl. Acad. Sci. U. S. A.* 76, 3, 1009–1013.

[273] Melin, F., Xie, H., Meyer, T., Ahn, Y. O., Gennis, R. B., Michel, H., Hellwig, P. 2016. The unusual redox properties of C-type oxidases. *Biochimica et Biophysica Acta (BBA) - Bioenergetics* 1857, 12, 1892–1899.

[274] Steward, K. *Essential Amino Acids: Chart, Abbreviations and Structure*. https://www.technologynetworks.com/applied-sciences/articles/essential-amino-acids-chart-abbreviations-and-structure-324357.

7 Appendix

7.1 Nomenclature

Table 7.1: List of homologous subunits of complex I in *E. coli*, *T. Thermophilus*, *Y. lipolytica* and *H. sapiens*.

E. coli	*T. thermophilus*	*Y. lipolitica*	*H. sapiens*
NuoA	Nqo7	NU3M	ND3
NuoB	Nqo6	NUKM	NDUFS7
NuoCD	Nqo4	NUCM	NDUFS2
	Nqo5	NUGM	NDUFS3
NuoE	Nqo2	NUHM	NDUFV2
NuoF	Nqo1	NUBM	NDUFV1
NuoG	Nqo3	NUAM	NDUFS1
NuoH	Nqo8	NU1M	ND1
NuoI	Nqo9	NUIM	NDUFS8
NuoJ	Nqo10	NU6M	ND6
NuoK	Nqo11	NULM	ND4L
NuoL	Nqo12	NU5M	ND5
NuoM	Nqo13	NU4M	ND4
NuoN	Nqo14	NU2M	ND2

Table 7.2: Location of cofactors and functions of complex I.

Location	Module	*E. coli* subunit	Cofactor/function
Peripheral arm	NADH binding	NuoF	FMN N3
		NuoE	N1a
		NuoG	N1b
			N4
			N5
			N7
	Quinone binding	NuoI	N6a
			N6b
		NuoCD	Quinone binding
		NuoB	N2
Membrane arm	Antiporter-like	NuoL	Proton pathways
		NuoM	
		NuoN	
	E-channel	NuoH	Coupling mechanism/ proton pathways
		NuoA	
		NuoJ	
		NuoK	

7.2 Structures of 20 amino acids

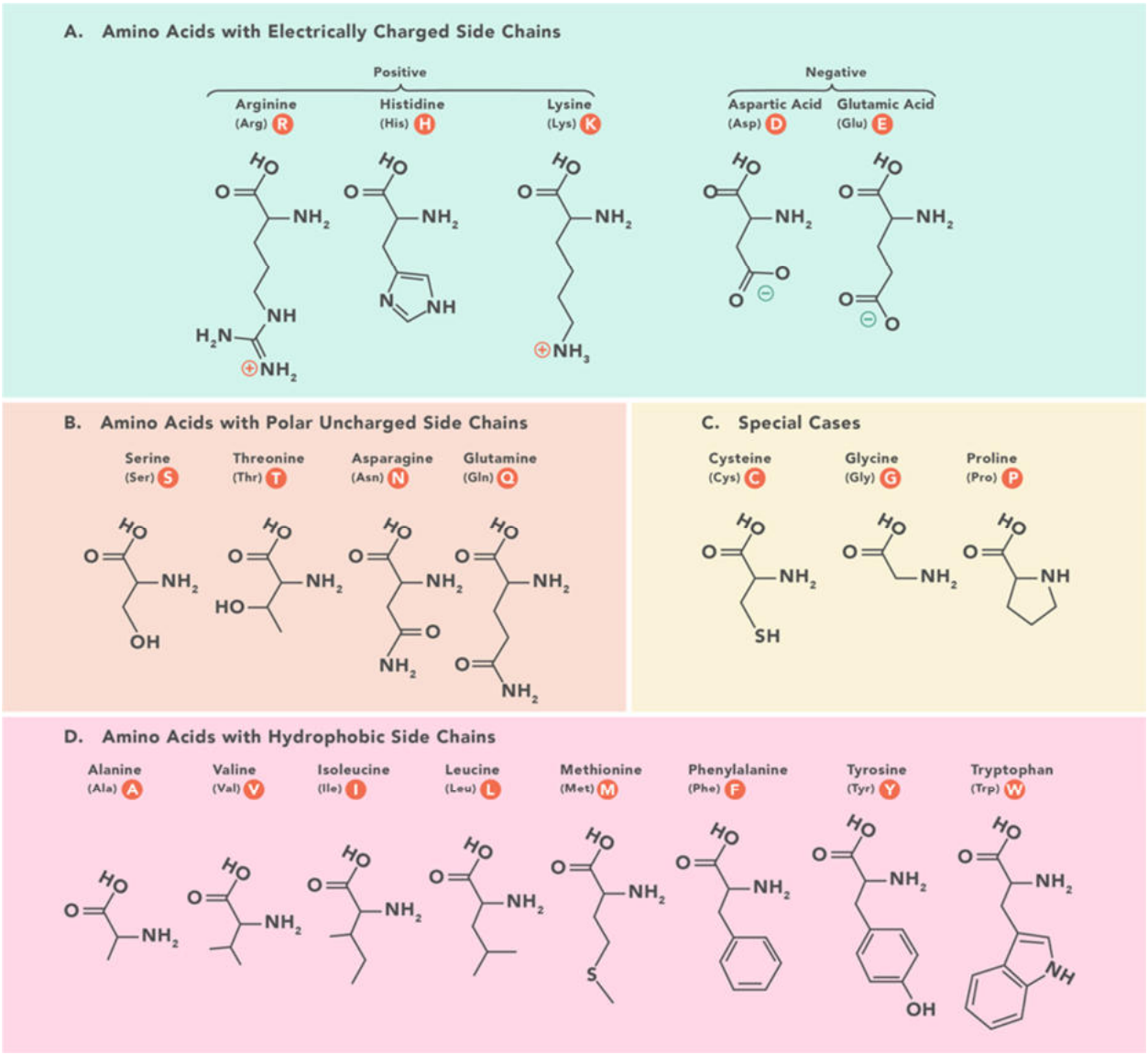

Figure 7.1: 20 amino acids [274].

7.3 Labelling efficiency calculation example

To calculate label efficiency, absorbance of the peak at 278 nm is compared with the one at 412 nm. An example of calculation for one the Complex I variant is presented:

$$A_{278} = 0.18$$
$$A_{412} = 0.023$$

$$[TNB] = \frac{A_{412}}{\varepsilon_{TNB}} = \frac{0.023 \times DF}{14150} \times 10^6 = 3.25\ \mu M$$

$$[E108C] = \frac{[A_{278}]}{\varepsilon_{KI}} = \frac{0.18 \times DF}{781} \times 10^6 = 4.60\ \mu M$$

$$\%_{labeling\ efficiency} = \left(\frac{[TNB]}{[E108C]}\right) \times 100\% = \left(\frac{3.25}{4.60}\right) \times 100 \approx 71\ \%$$

7.4. Spectral shifts of NuoM variants

Table 7.3. Behaviour of the spectral changes compared to the initial state.

Variant	Location	CN (cm^{-1})	+NADH	+Q_2
E108C	cytoplasmatic	2125	-	hydrophilic
H159C	cytoplasmatic	2123	hydrophobic	hydrophilic
S105C	cytoplasmatic	2127	hydrophobic	hydrophilic
H117C	cytoplasmatic	2127	hydrophobic	hydrophilic
S414C	periplasmatic	2123	-	hydrophilic
T332C	periplasmatic	2127	hydrophobic	-
T442C	periplasmatic	2123	-	hydrophilic
S425C	periplasmatic	2129	hydrophobic	hydrophilic
T178C	cavity	2133	hydrophobic	-
K234C	cavity	2131	hydrophobic	-
D258C	cavity	2125	hydrophilic	hydrophilic

7.5. Orientation of complex I variant on Ni-NTA modified gold surface

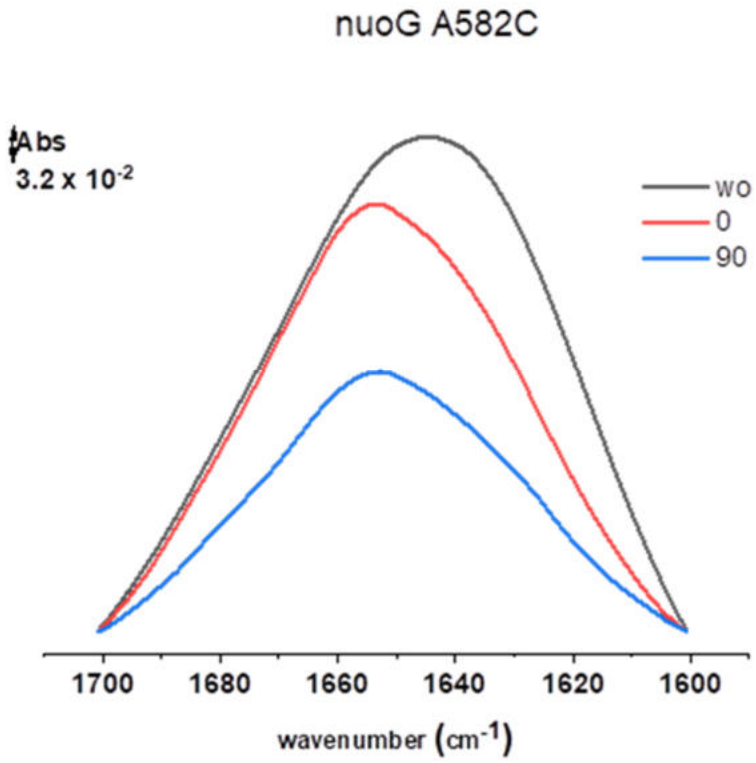

Figure 7.2: MID IR spectrum of complex I A582C^{G} variant recorded with polarization 0° (red), 90° (blue) and without polarization (black).

Acknowledgements

This work was carried out from November 2019 to June 2023 at the Institute of Biochemistry, Albert-Ludwigs-University Freiburg (DE) and Laboratory of Bioelectrochemistry, University of Strasbourg (FR). Here, I would like to express my gratitude to all people involved.

First of all, I would like to thank my both supervisors Prof. Dr. Thorsten Friedrich and Prof. Dr. Petra Hellwig for giving me an opportunity to work on this interesting project. Thank you for the mentorship, support, helpful advice, scientific discussions, corrections, remarks and all the expertise I have learnt all these years. At this point, I would like also to thank Dr. Frédéric Melin for his kindness, helpfulness, support and corrections of this work.

I would like to thank Prof. Dr. Sophie Lecomte and Prof. Dr. Christoph von Ballmoos for kindly accepting my request to be part of the thesis committee, and expressing interest in this work.

Funding was provided by DFG, Region Alsace, DFH-UFA and is gratefully acknowledged. I would like to thank PDI in Strasbourg and RTG 1976 in Freiburg. Acknowledgement goes to Christiane Zähringer and Sabine Richter for the great coordination and excellent organizational work.

My gratitude goes to my AK Friedrich collegues: Jan, Caroline, Luca, Sanaz. Vielen Dank für einfach alles! Ich danke euch für eure Unterstützung, Hilfe, die nette Arbeitsatmosphäre mit der richtigen Dosis Wahnsinn. Ohne euch hätte ich die Arbeit nicht schaffen können! An dieser Stelle möchte ich mich ganz herzlich bei Franziska Hoeser bedanken, die mir immer mit Rat und Tat zur Seite stand. Ein ganz besonderes Dankeschön geht an meine ehemalige Betreuerin Sabrina Oppermann. Danke für deine Hilfsbereitschaft und Unterstützung. Ich möchte hier auch meinem ersten Praktikumsbetreuer Johannes Schimpf sowie Alexander Theßeling für die witzige Atmosphäre danken. Des Weitern geht meine Danksagung an Dörte Thiel für ihre Hilfe und Unterstützung im Labor. Rebecca Mößner-Hornberger, die mir ständig im letzen Jahr geholfen hat, gebührt mein Dank. Vielen Dank Rebecca für die Unterstützung, für tolle Gespräche und Unterhaltung und Danke an Maximilian Weiß, der diese nette Atmosphäre immer unterstützt hat.

I would to thank Dr. Daniel Wohlwend for creating nice pictures. Gratitude to AK Einsle, AK Andrade and all Institute of Biochemistry for creating nice working environment.

This time would not be so enjoyable without the part of my life I have spent on the other side of the Rhine. And I would like to thank all people there. I want to thank Soumia Hnini for her help and support. Merci Soumia pour ton aide et soutien.

My sincere gratitude goes to Zahia Boubegtiten for her endless help, constant support, encouragement, ability to deal with unexpected problems, for giving me motivation to learn French. Merci pour tout Zahia. Sans toi, mon séjour à Strasbourg n'aurait pas été si spécial.

I would like to thank the research team of the Laboratory of Bioelectrochemistry and Spectroscopy. My gratitude goes to Dr. Frédéric Melin, Dr. Youssef El Khoury, Dr. Nicolas Javahiraly. Thank you for your objectivity and advice. I would like to thank present PhD students Krongkarn Sirinukunwattana, Raaif Siddeeque and Ariadna Murillo Bello. Thank you for creating a nice working atmosphere. Here, I want to thank my colleague Iryna Makarchuk. Thank you my dear French sister for being part of my life, for guiding me in Strasbourg, for the crazy moments we shared, for the unforgettable memories we created, for all the fun we had, for great trips and amazing adventures. Ти мій друг на все життя.

I would like to thank former colleagues Filipa Santos Seiça and Fatima Omeis. Thank you my sweetie Filipa for your help, support, guidance and all the great moments we shared. Thank you Fatima for your kindness and that you are always ready to lend an ear. Thank you, lab girls, for these beautiful moments of our réunions, they mean a lot.

Here I want to thank Renato and Michael for all the crazy times and memories we shared. This is unforgettable and will stay with us. I want to thank my friends in Strasbourg whom I have met during these years. Diana, Anna, Andrei, Guido and Renata, thank you guys, without you my time in Strasbourg would never be so fulfilled and memorable.

On behalf of the social committee, I really want to thank the international team of StrasAIR for making these years more enjoyable with organized trips, events and cafés lingistiques. Thank you Rokas for joining, thank you El President Nizami, thank you Ivan and Sven.

I also want to thank my friends in Germany who supported me on my way. Thank you Erzhena and Tatiana for the funny moments, thank you Taimoor for believing in me, thank you Vladislav for starting this journey to Freiburg and thank you Hans Peter for providing entertainment. I would like to thank my friend Anna for her support and our meetings in different countries.

Here I want to thank my dearest friends in Latvia who I miss a lot: Olga and Karina, thank you for being my friends for life!

Finally, I want to thank my parents and my aunt. Thank you for your unconditional love, care patience and support. Without you I would not be able to achieve this. Я вас люблю, спасибо за все!

Université de Strasbourg

Tatjana Gerasimova

universität freiburg

Décryptage des mécanismes des complexes de la chaîne respiratoire par marquage IR et approches exaltées de surface

Résumé

La chaîne respiratoire aérobie d'*E. coli* se compose de plusieurs déshydrogénases primaires et de réductases terminales. Le complexe I est la plus grande enzyme de la chaîne respiratoire qui catalyse le transfert de deux électrons du NADH à la quinone, couplé à la translocation de quatre protons à travers la membrane. Il a une structure en forme de L composée d'un bras périphérique et d'un bras membranaire. Le couplage des deux processus fait encore l'objet de débats. Un marqueur nitrile a été inséré à proximité de l'une des voies protoniques putatives dans NuoM du complexe I. Des positions individuelles ont été génétiquement changées en cystéines et marquées avec des cyanures. Les marqueurs nitrile sont des marqueurs IR intéressantes car elles peuvent fournir des informations précieuses sur l'environnement local de la sonde dans un environnement protéique défini. Les changements de conformation dans ces positions ont été visualisés avec SEIRAS lors de l'ajout de substrats.

La cytochrome *bd*-I oxydase appartient aux réductases terminales des chaînes respiratoires. Les résidus d'acide glutamique conservés à proximité des hèmes sont importants pour les fonctions de la *bd*-I oxydase. Ces résidus sont discutés en relation avec le rôle physiologique de l'enzyme.

Mot-clés: complexe I, SEIRAS, marqueur nitrile, spectroscopie infrarouge, *bd*-I oxydase

Résumé en anglais

The aerobic respiratory chain of *E. coli* consists of several primary dehydrogenases and terminal reductases. Complex I is the largest enzyme in the respiratory chain that catalyzes the transfer of two electrons from NADH to quinone coupled with the translocation of four protons across the membrane. It has an L-shape structure consisting of a peripheral and a membrane arm. The coupling of both processes is still under debate. A nitrile label was inserted in the proximity of one of the putative proton pathways in NuoM of complex I. Individual positions were genetically changed to cysteines and labelled with cyanides. Nitrile labels are attractive IR labels as they can provide valuable information about the local environment of the probe in a defined protein environment. Conformational changes in these positions were visualized with SEIRAS upon addition of substrates.

Cytochrome *bd*-I oxidase belongs to terminal reductases of respiratory chains. Conserved glutamic acid residues in proximity of hemes are important for functions of *bd*-I oxidase. These findings are discussed in relation to the physiological role of the enzyme.

Keywords: complex I, SEIRAS, nitrile label, infrared spectroscopy, *bd*-I oxidase